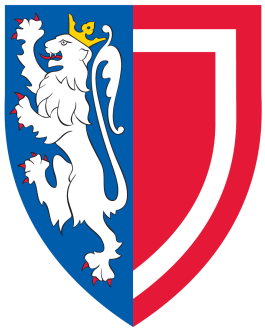
A Search for the Direct Detection of Dark Matter via Annual Modulation with the Full XMASS-I Dataset





Alexander Mason

Balliol College

University of Oxford

A thesis submitted for the degree of

Doctor of Philosophy

Hillary 2021

Acknowledgements

First of all I would like to thank my supervisor Kai Martens. His guidance, insight and friendship over the past 4.5 years made the work presented in this thesis possible. The generous hospitality of both him and the friends I made during my 2 years based at the Kamioka observatory helped keep me sane and got me through my time there.

I am indebted to my colleagues and friends at Oxford University, in particular my fellow Balliolite particle physicists Thomas Hancock and Hannah Pullen, without whose coding expertise ROOT would have defeated me. I am also very thankful to Sue Geddes and Kim Proudfoot without whom the particle physics department could not function.

I am grateful to Oxford University and Kavli IPMU for funding my studies and I would additionally like to thank the XMASS collaboration, in particular the members of the analysis group that helped me no end throughout my studies: M. Yamashita, K. Abe, Y. Kishimoto, H. Ogawa, K. Hiraide, K. Ichimura and B. Xu.

I would also like to thank my friends from home and Cambridge University. In particular Holly Pacey who was there by my side throughout undergrad and knew just how to cheer me up whenever I wavered. The support she provided during the 2 years I spent living in Japan was essential.

Finally, I would like to thank my parents Toni and Sheelagh, they will never truly know how grateful I am for the unwavering support and love they have always shown me.

Abstract

Astrophysical observations indicate that the observable matter that forms the stars, planets and life as we know it only constitutes 5% to the total energy density of our universe. Dark matter and dark energy make up the remainder, 26% and 69% respectively. While the nature of dark energy is still largely speculative, gravitational effects of dark matter have been widely observed and place constraints on its nature. Many candidates that could form dark matter have been ruled out over the years due to the lack of astrophysical signatures they would imply or lack of production, annihilation and direct detection signals in experiments or instruments that have sensitivity for these signals.

XMASS is a single-phase dark matter direct detection experiment. The detector houses 832 kg of liquid Xenon within its active volume and has been operational for over 5 years (the current longest for any noble liquid experiment), resulting in a 3.53 ton year exposure. Two annual modulation analyses are presented in this thesis, one based on the previous XMASS modulation analysis and then my own one that introduces a new classification technique and a new approach to χ^2 minimisation that is less reliant on Monte Carlo based evaluation of systematic uncertainty. The obtained 90% confidence level upper limit for the spin independent interaction cross section ($\sigma_{SI}^{90\%}$) between Weakly Interacting Massive Particle (WIMP) dark matter and standard model nucleons has been halved to 3.6×10^{-39} cm^2 for a WIMP of mass 4 GeV with respect to the previous XMASS modulation analysis and has a minimal value of 1.2×10^{-43} cm^2 for a WIMP of mass 40 GeV.

Contents

1 Introduction **1**

1.1 Evidence for dark matter 2

1.1.1 Indirect observations of missing mass 2

1.1.2 The bullet cluster and DM self-interaction strength 5

1.1.3 Why DM is necessary for structure formation in the early universe 6

1.1.4 General relativity and ΛCDM precision astronomy 9

1.2 Beyond the standard model and dark matter candidates 14

1.2.1 Beyond the standard model 14

1.2.2 Dark matter candidates 16

1.3 Dark matter detection techniques 22

1.3.1 Dark matter collider detection searches 23

1.3.2 Dark matter indirect detection searches 23

1.3.3 Dark matter direct detection searches 25

2 The Direct Detection of Dark Matter **29**

2.1 Simplified model: fermionic DM-SM nucleon interaction 30

2.1.1 DM-SM mediator 30

2.1.2 Simplified scalar model 30

2.1.3 The DM-nucleon interaction coefficient 32

2.2 Non-relativistic reduction and event rates 34

2.2.1 Direct detection operators 34

2.2.2 The DM direct detection event rate 37

2.3 Annual modulation of the DM nuclear recoil event rate 39

3 The XMASS Experiment 43

3.1 Liquid xenon 45

3.1.1 Xe base properties 45

3.1.2 Xe isotopes 46

3.1.3 LXe scintillation mechanism 47

3.1.4 LXe relative scintillation yield efficiency 50

3.1.5 LXe optical properties 53

3.2 The XMASS detector 54

3.2.1 The inner detector 56

3.2.2 The outer detector 57

3.2.3 Distillation, circulation and purification 57

3.2.4 Data acquisition and PMT response 59

3.2.5 XMASS detector simulation 62

3.3 XMASS calibration techniques 64

3.3.1 LED calibration 65

3.3.2 Inner calibration 66

3.3.3 Hose calibration 71

3.4 Backgrounds 73

3.4.1 External backgrounds 73

3.4.2 Internal backgrounds 74

4 High Energy Alpha Calibration 81

4.1 Waveform theory 82

4.1.1 A waveform's constituent parts 82

4.1.2 Waveform convolution properties 83

4.1.3 Deconvolution and discrete Fourier transform 85

4.2 High energy alpha events for calibration 86

4.2.1 Alpha source, event symmetry and azimuthal orientation . . . 87

4.2.2 Bright and dark hemispheres: NPEs and waveforms 88
4.2.3 Bright and dark hemispheres: MC timing information 89
4.3 Extracting the optical parameters 92
4.3.1 Deconvolution 92
4.3.2 Comparison between bright side and dark side 94
4.3.3 Exponential decay fit 94
4.3.4 Further complications 97
4.4 Outlook 98

5 Event Classification 99
5.1 Traditional XMASS event selection 99
5.1.1 The XMASS standard cut 99
5.1.2 Likelihood cut 104
5.2 New PDF classification of signal and BG events 106
5.2.1 MC datasets 107
5.2.2 Event hit information 108
5.2.3 PDF generation 110
5.2.4 Classification parameter 117
5.2.5 MC classification: CDFs, ROC curves and signal/$\sqrt{\mathrm{BG}}$ 121
5.2.6 Classification power 125
5.3 ^{55}Fe low energy calibration crosscheck 128
5.4 Outlook 131

6 Data Selection, Time Periods, LY and Event Rates 133
6.1 Run selection and period structure 134
6.1.1 Normal threshold periods 134
6.1.2 Additional run selection criteria for low threshold data 135
6.2 Light yield history 142
6.2.1 Hose data LY ratio 143
6.2.2 Hose LY ratio Vs Inner ^{57}Co -30 cm LY 146

6.2.3 Normal threshold and low threshold LY 149
6.3 Light yield dependence of observed event rate 152

7 Signal Spectra **163**
7.1 WIMP SI energy spectra 164
7.1.1 Xe NR MC energy spectra 164
7.1.2 Xe NR energy spectra relative efficiencies 170
7.2 Electron signal spectra for the model independent search 174
7.2.1 Electron signal relative efficiencies 175
7.3 Previous analysis spectra and relative efficiencies 176

8 χ^2 Minimisation, Cross Section Scans and Dummy Samples **177**
8.1 Expected event rate and χ^2 formulae 177
8.1.1 General χ^2 variables 178
8.1.2 Formulae and variables for the expected event rate 180
8.1.3 Null signal fit and MI search 181
8.1.4 WIMP SI search 183
8.2 Null signal best fit parameters 184
8.3 Dummy sample event rates 189
8.4 MI best fit amplitudes 190
8.5 Cross section scan and 90% confidence limit 195

9 Modulation Analyses Results **199**
9.1 MI and $\sigma_{SI}^{90\%}$ results for the previous XMASS modulation analysis . . 201
9.2 MI and $\sigma_{SI}^{90\%}$ results for the complete dataset likelihood cut modulation analysis 203
9.3 MI and $\sigma_{SI}^{90\%}$ results for the stable LY dataset PDF cut modulation analysis 205
9.4 $\sigma_{SI}^{90\%}$ results comparison 207
9.5 MI variable phase analysis checks 210

10 Conclusion **213**

10.1 Summary of the WIMP search results 213

10.2 Discussion for future analyses 216

A Period Structure and LY Systematics **219**

A.1 Period structure 219

A.2 Event rate systematics from LY uncertainties 220

References **223**

Chapter 1

Introduction

Astrophysical observations indicate that ordinary matter - the stuff that constitutes the stars, the earth we stand on and everything we currently understand - represents only a small fraction of the total energy density of the universe. The standard cosmological model that at present explains the observed large scale structure of the universe - discussed in the following section - is the ΛCDM model. This asserts that the universe is composed of 3 main constituents, dark energy ~ 68.9% associated with the cosmological constant (Λ) in the Einstein field equations, cold dark matter (CDM) ~ 26.2% relevant for the structure formation observed throughout the universe, and ordinary matter ~ 4.9% only, less than $\frac{1}{5}$ that of DM.

Ordinary matter is currently pretty well understood in the context of both particle physics and astrophysics. DM on the other hand is very much not well understood. This thesis explores the direct detection of DM and its expected modulation signal, the data utilised for analysis was captured using the liquid Xenon single-phase detector XMASS. Its astrophysical affects have been observed and they are documented in section 1.1, the possible candidates for DM are discussed in section 1.2 and detection techniques are outlined in section 1.3. Dark energy is not understood in any way, shape or form and more information is needed before we can establish a good theoretical framework to explain it.

1.1 Evidence for dark matter

This section is broken down into 4 subsections. The first 1.1.1 outlines the initial astrophysical observations of missing mass in both galaxies and galaxy clusters and hence where the term DM comes from. The second 1.1.2 discusses the bullet cluster, a perfect example that highlights the differences between matter and DM interactions or lack thereof, more measurements of colliding galaxies like this one could produce the first indirect measurements of DM's self-interaction strength. The third 1.1.3 discusses the important part that DM plays in structure formation throughout the evolution of the universe. And finally 1.1.4 details up to date precision astronomy measurements that have been used to determine the proportions of Λ, DM and ordinary matter present within the universe.

1.1.1 Indirect observations of missing mass

The term "dark matter" was coined in 1933 by F. Zwicky in reference to the Coma cluster [1, 2]. He calculated the galaxy cluster's mass using two distinct methods, one using the luminosity of galaxies present within the cluster and another using their velocity by applying the virial theorem of a gravitationally bound system ($\langle \mathrm{KE} \rangle = -\frac{1}{2}\langle \mathrm{PE} \rangle$), which for spherical symmetry ($\langle \mathrm{KE} \rangle = \frac{1}{2}\mathrm{M}\langle \mathrm{v}^2 \rangle$ and $\langle \mathrm{PE} \rangle = -\frac{\mathrm{GM}^2}{\langle \mathrm{R} \rangle}$) implies: $\mathrm{M} = \frac{\langle \mathrm{v}^2 \rangle \langle \mathrm{R} \rangle}{\mathrm{G}}$. Zwicky found that the mass obtained using the virial theorem suggested there was 500 times more mass than that predicted by looking at the galaxies' luminosity and hence there was mass present that was not being observed directly. Recent observations reduce this discrepancy to a factor 50, however the missing mass problem remains.

The most widely reported evidence for DM is likely galaxy rotation curves. Spiral galaxies are composed of a bulge in the centre where the majority of the galaxy's stars reside and a semi-flat disk that is composed of spiralling arms made up of more stars and gas. According to Kepler's laws the rotational velocity of an object of any given mass is only dependent on the radius (R) that object is located at and the mass

(M) that is contained within that radius: $v_{\text{rot}} = \sqrt{\frac{GM}{R}}$, where G is the gravitational constant. The neutral hydrogen present in the gas clouds and stars within the disk emit 21 cm wavelength radio waves, by measuring the Doppler shift of this line one can infer their rotational speed. As the vast majority of the galaxy's luminous matter is concentrated at the centre one would assume the rotational velocity of stars to reduce $\propto\sim R^{-\frac{1}{2}}$ from the centre. However this is not observed, instead the rotational speed of galaxies tends to a constant at large R as the data for spiral galaxy NGC 3198 depicts in figure 1.1. There is not enough luminous matter at large R to produce such a velocity distribution and additional matter which is not being directly observed is required. This is referred to as the DM halo surrounding all galaxies and makes up the majority of a galaxies' mass.

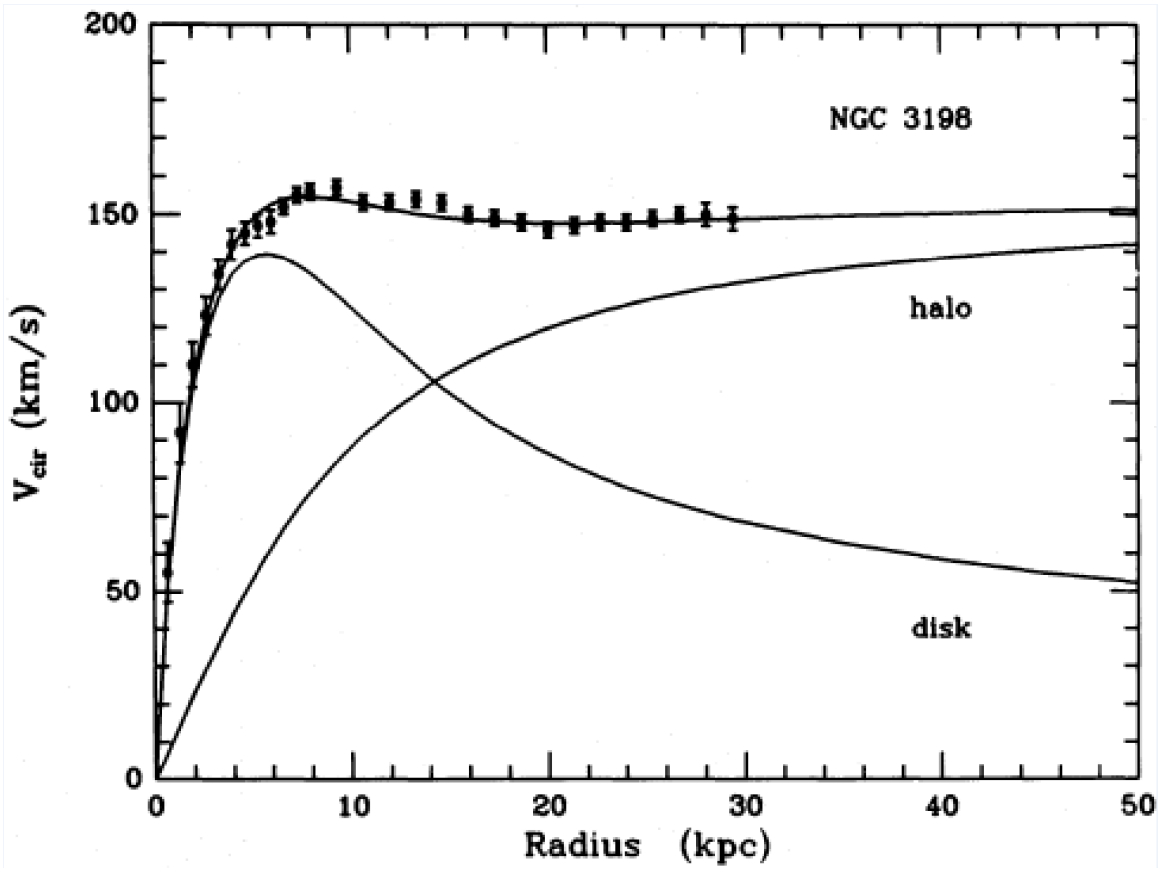


Figure 1.1: Rotation curve of NGC 3198. The line marked "disk" shows the expected rotation curve if the only mass in the galaxy were that in the visible stars. The line marked "halo" is the extra dark matter needed to reproduce the observed rotation curve [3].

The above examples demonstrate that although DM has not been observed directly, it does interact via gravity and its indirect effects on ordinary matter can be observed. John Wheeler famously outlined general relativity in 12 words: "Spacetime tells matter how to move; matter tells spacetime how to curve". This results in matter no longer travelling in straight lines, instead they follow geodesics dictated by spacetime which itself is dictated by the matter within it. Therefore a large collection of matter, i.e. a galaxy cluster can warp spacetime so photons emitted from a source behind it are bent around said matter. The matter acts as a lens magnifying the brightness of the emitting source and allows us to view objects that would otherwise be out of view. The matter distribution necessary for the observed gravitational lensing of a source can be reconstructed using the image's position and magnification. Gravitational lensing is not reliant on DM, however DM makes up a large portion of galaxies and galaxy clusters and gravitational lensing examples - as in figure 1.2 - infer additional mass that is non-luminous and missing from direct observation.

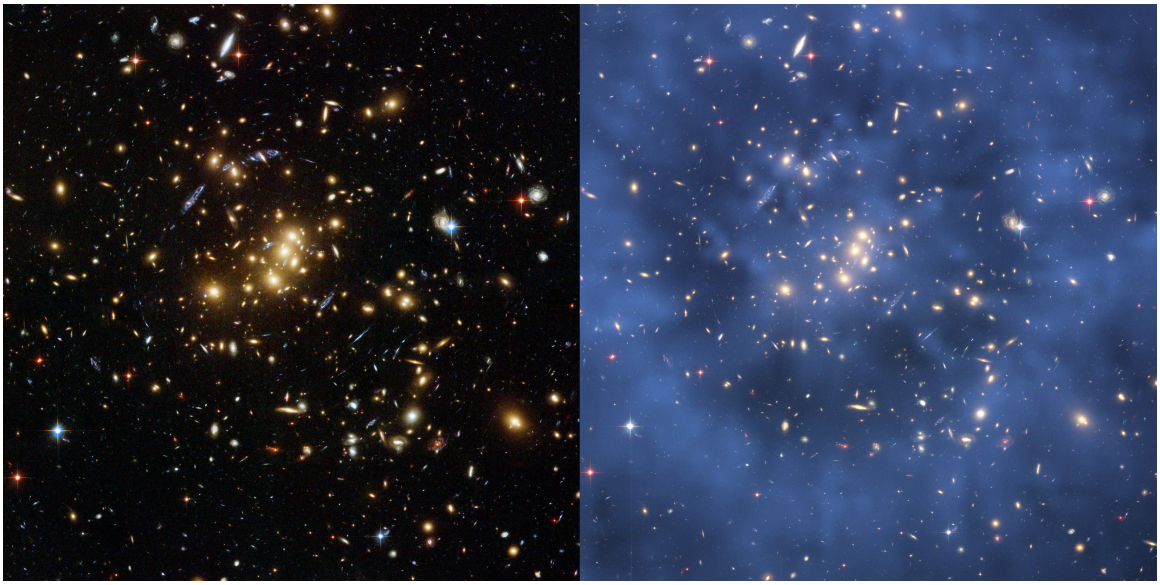


Figure 1.2: Hubble's view of massive galaxy cluster Cl 0024+17 (ZwCl 0024+1652). The optical image data only is displayed on the left: odd-looking blue arcs appearing among the yellowish galaxies are magnified and distorted images of galaxies located far behind the cluster. The image on the right includes a blue shading map to indicate the dark matter necessary to account for the gravitationally lensed galaxies (Credits: NASA, ESA, M.J. Jee and H. Ford (Johns Hopkins University)) [4].

1.1.2 The bullet cluster and DM self-interaction strength

Figure 1.3 is a composite image of the remnants of the collision between two galaxy clusters, famously termed the bullet cluster. It shows optical data of the galaxies, x-ray data (highlighted in red) observed by the Chandra observatory [5], and a DM map (highlighted in blue) reconstructed using gravitational lensing. The optical data and DM map overlap while the x-ray map does not. The stars and celestial bodies in the colliding galaxies pass through one another - interacting gravitationally but without colliding - while the interstellar gas is confined to the centre of the collision due to the strong level of interactions that reduce momentum, heat the gas and releases x-rays in the process. The DM moving through unimpeded implies that DM is either formed from celestial bodies or particles that are both weakly interacting with visible matter and also weakly self-interacting. Galaxy cluster collisions like this one observed with greater sensitivity and coupled with simulation could allow us to infer the DM self-interaction strength. Some level of DM self-interaction is predicted by most theories and a limit would severely reduce the allowed set of theories.

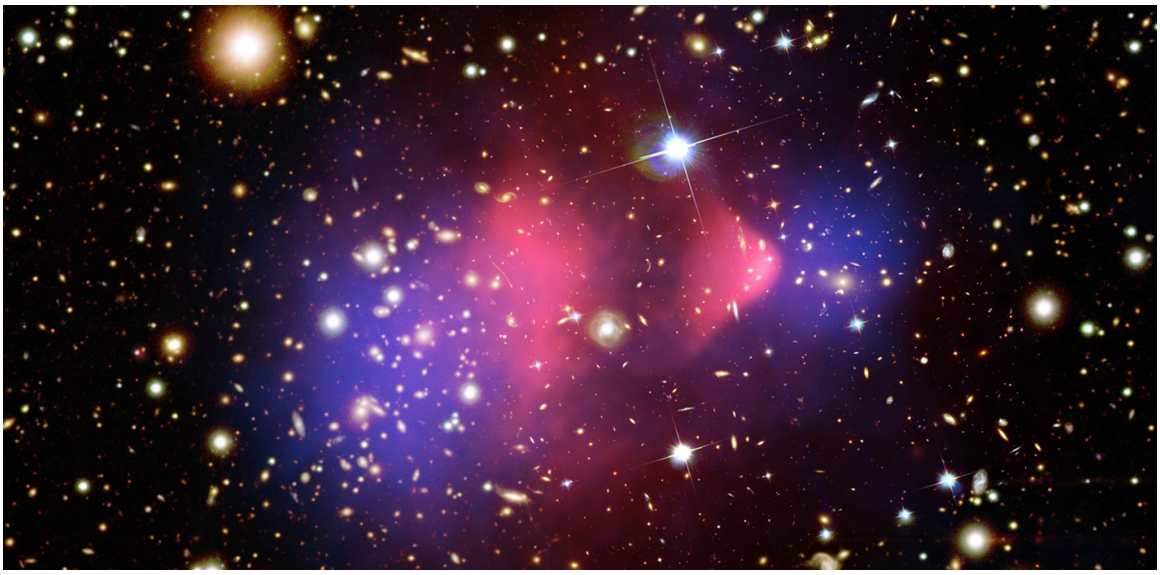


Figure 1.3: Bullet cluster 1E-0657-56, composite image, optical, x-ray (red) and gravitational lensing dark matter map (blue) [5] (Credit: X-ray: NASA/CXC/CfA/M.Markevitch et al.; Optical: NASA/STScI; Magellan/U.Arizona/D.Clowe et al.; Lensing Map: NASA/STScI; ESO WFI; Magellan/U.Arizona/D.Clowe et al.)

1.1.3 Why DM is necessary for structure formation in the early universe

During recombination small fluctuations are present throughout the universe, these are predicted to originate from quantum fluctuations that occurred during inflation. These result in anisotropies present in the Cosmic Microwave Background (CMB) and are observed as temperature fluctuations ($\frac{\Delta T}{T} \sim 10^{-5}$). Figure 1.4 shows the data taken by the Planck satellite.

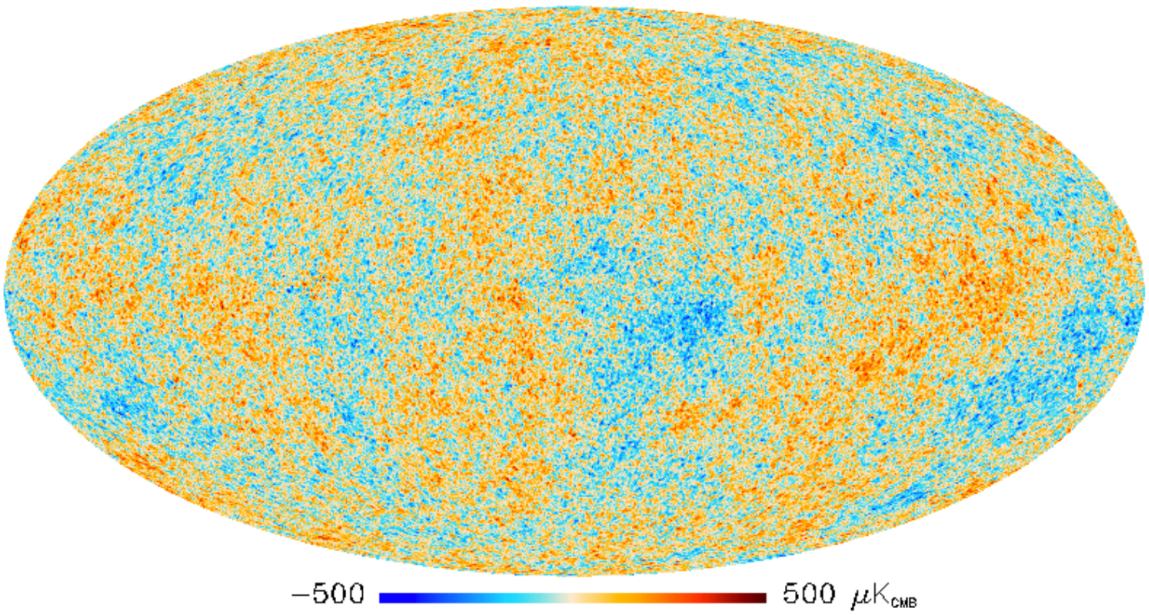


Figure 1.4: Temperature fluctuation of the CMB at recombination - with the dipole effects induced by our galaxy removed - measured by the Planck satellite [6].

As the universe expands, overdense and underdense regions expand faster and more slowly respectively due to their stronger gravity or lack thereof, this amplifies the magnitude of the fluctuations. Overdense regions eventually reach inflection points where they stop expanding and contract under gravity. A consequence of the lack of strong DM self-interaction is that DM is pressureless, the lack of pressure results in continued concentration in overdense regions. This produces a network of filaments where matter clumps together interspersed with bubbles and voids where matter is lacking. These overdense gravitational wells attract ordinary matter in the form of Baryon/photon plasma, which was smoothly distributed after recombination. On the

largest scale the universe appears both isotropic and homogeneous. However on the scale of galaxies and galaxy clusters the universe is structured like a foam as the 2dF redshift survey demonstrates in figure 1.5. To obtain the structure observed throughout the universe, DM needs to clump together under gravity and hence needs to be cold (non-relativistic); hot (relativistic) DM would not coalesce under gravity as proficiently and would resultant in less pronounced clustering as the universe evolved. N-body-simulations compare the structure formation in the early universe both with and without DM [7].

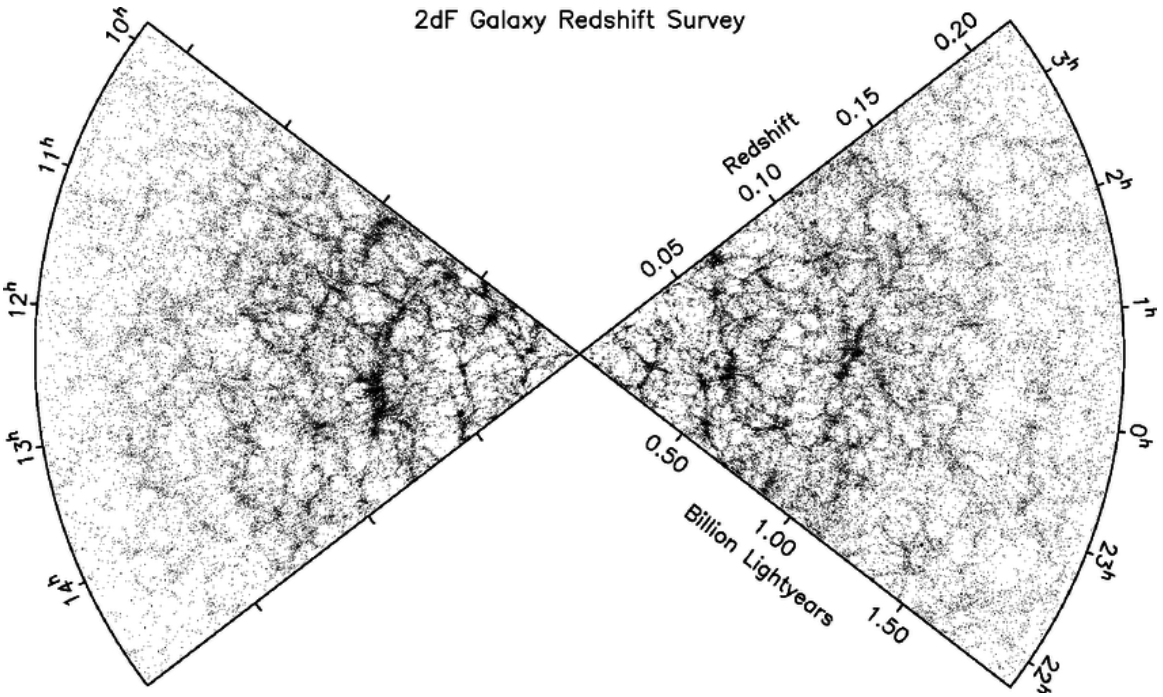


Figure 1.5: The distribution of galaxies measured by the 2dF galaxy redshift survey [8], each galaxy is represented by a point. The structure resembles that of a foam composed of filaments and voids.

Because ordinary matter does self-interact, an inflection point occurs where the gravitational force is matched by the force of the plasma's pressure and the plasma rebounds, propagating at the speed of sound. The characteristic speed of sound in plasma is $\sim \frac{c}{2}$ and these Baryon Acoustic Oscillations (BAO) creates a characteristic size $\sim$ 500 Mly for the Baryon over dense regions. Figure 1.6 demonstrates the redshift-space correlation function for the SDSS luminous red galaxies (LRG) sample [9], the

BAO acoustic peak is present where expected. A variety of ΛCDM models are also displayed. BAO information is used to extract the relative proportions of DM and ordinary matter.

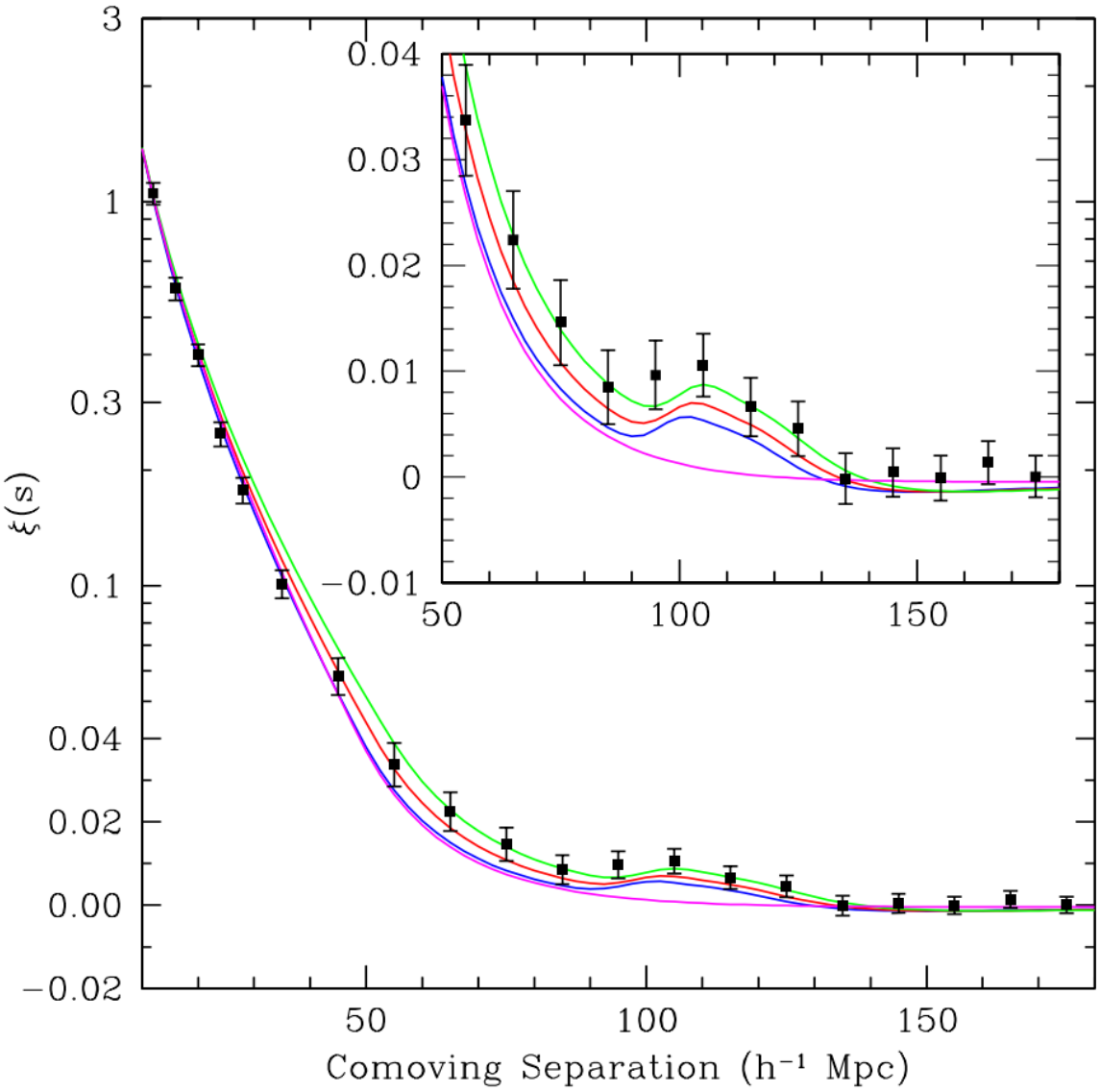


Figure 1.6: The large-scale redshift-space correlation function of the SDSS LRG sample [9]. With Ω_M, Ω_b and Ω_c are the matter, baryonic and DM densities respectively - discussed in the next section - the ΛCDM models are $\Omega_M h^2$= 0.12 (green), 0.13 (red), and 0.14 (blue), all with $\Omega_b h^2$ = 0.024, spectral index n = 0.98, and with a mild non-linear prescription folded in. The magenta line shows a pure CDM model ($\Omega_M h^2$= 0.105), which lacks the acoustic peak at 105 $h^{-}1$ Mpc present in the other models.

The CMB is a blueprint for structure formation throughout the universe, the power spectrum of the CMB temperature fluctuations is displayed in figure 1.7. The

data, which exhibits 7 acoustic peaks, is fit using a flat ΛCDM model with only six-parameters: $\Omega_b h^2$, $\Omega_c h^2$, a scalar spectral index n_s, an optical depth τ, a primordial amplitude A_S and an acoustic scale angle θ_{MC} [10]. The first peak represents the first compression of the baryonic plasma, the second represents its first refraction and the other peaks originate from matter that is attracted to the gravitational well from greater distances, hence a reduced effect. The relative heights and positions of said peaks are dictated by the relative proportions of baryonic matter and dark matter with other early time cosmological parameters necessary for accurate modelling. Ω_M, H_0 and other cosmological parameters are then inferred from these 6.

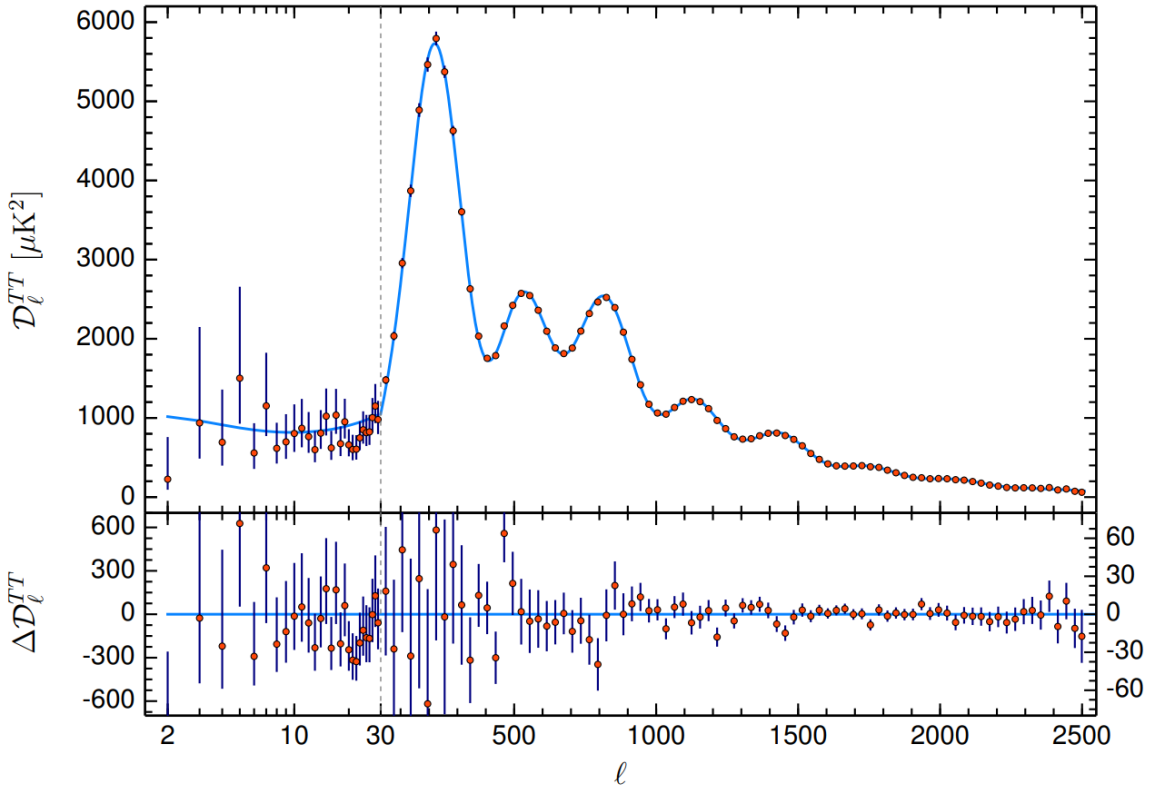


Figure 1.7: Power spectrum of the CMB temperature fluctuations measured by the Planck satellite, the blue line is the six-parameter flat ΛCDM model best fit [10].

1.1.4 General relativity and ΛCDM precision astronomy

In general relativity the metric tensor $g_{\mu\nu}$ defines the geometry of spacetime, it is a 4 dimensional symmetric tensor where the spacetime interval $ds^2 = g_{\mu\nu}dx^\mu dx^\nu$.

In curved space parallel transport of a vector gives different results around different paths. The Ricci curvature tensor measures how much a shape is deformed, essentially characterising the extent to which the metric varies from ordinary Euclidean space. Equation 1.1 demonstrates how it is calculated using the metric. The Ricci curvature scalar $R = g^{\mu\nu}R_{\mu\nu}$.

$$\begin{aligned} R_{\mu\nu} &= \frac{\partial\Gamma^{\lambda}_{\mu\lambda}}{\partial x^{\nu}} - \frac{\partial\Gamma^{\lambda}_{\mu\nu}}{\partial x^{\lambda}} + \Gamma^{\eta}_{\mu\lambda}\Gamma^{\lambda}_{\eta\nu} - \Gamma^{\eta}_{\mu\nu}\Gamma^{\lambda}_{\eta\lambda} \quad \text{where} \\ \Gamma^{\alpha}_{\beta\gamma} &= \frac{1}{2}g^{\alpha\kappa}\left[\frac{\partial g_{\kappa\gamma}}{\partial x^{\beta}} + \frac{\partial g_{\beta\kappa}}{\partial x^{\gamma}} - \frac{\partial g_{\beta\gamma}}{\partial x^{\kappa}}\right]. \end{aligned} \tag{1.1}$$

The Einstein field equations (EFE) define how the distribution of matter is related to spacetime geometry:

$$R_{\mu\nu} - \frac{1}{2}g_{\mu\nu}R = -8\pi G T_{\mu\nu} - \Lambda g_{\mu\nu}. \tag{1.2}$$

$T_{\mu\nu}$ is the energy-momentum tensor and defines the matter and energy content of the universe, Λ is the cosmological constant, a constant of integration. As previously stated the tensors are symmetric and hence there are 10 differential equations, this is greatly simplified if homogeneity and isotropy are assumed. The Friedmann-Robertson-Walker (FRW) solution considers a maximally symmetric 3D space embedded within a 4D spacetime, the model for a simple universe:

$$ds^2 = c^2dt^2 - R^2(t)\left[\frac{dr^2}{1-Kr^2} + r^2d\theta^2 + r^2sin^2\theta d\phi^2\right]. \tag{1.3}$$

$R(t)$ is the scale factor containing the spatial dimensions and K is the curvature constant which tells us about the overall curvature of the 3D space. $K > 0$ represents a closed 3D space (similar to a spherical 2D surface represented in 3D), $K < 0$ represents an open 3D space (similar to a saddle structure for a 2D space represented in 3D) and $K = 0$ represents a flat 3D space.

If the matter content is considered a perfect fluid - assuming no internal forces - the resulting energy-momentum tensor is diagonal: $T_{00} = (\rho c^2)$ and $T_{11} = T_{22} = T_{33} = P$, where ρ is the density of said matter and P is the pressure it exerts through random

thermal motion. $T_{\mu\nu}$ is constructed from multiple components: dark matter, ordinary matter, radiation - all of which act as perfect fluids. Solving the EFE with the FRW metric and $T_{\mu\nu}$ defined above, an equality is obtained that relates K and $R(t)$ with the Hubble constant (H) and the proportion of energy-momentum critical density (ρ_c) that is a result of the matter component (Ω_M) and the cosmologic constant dark energy component (Ω_Λ) within the universe at any given time:

$$\frac{K}{R^2(t)} = H^2(\Omega_M + \Omega_\Lambda - 1). \tag{1.4}$$

Astrophysical observations such as the previously mentioned CMB Data or BAO data have results that are degenerate for some values of Ω_M and Ω_Λ. Figure 1.8 plots these results along with additional astrophysical observation data: such as Type 1A supernovae (SNe). By combining these results the true Ω_M and Ω_Λ values that satisfy all the astrophysical observations can be extracted, a line representing a flat universe ($K = 0$ according to equation 1.4) is included in the plot [11]. The combined results indicate that the universe is both likely flat and predominantly composed of dark energy (~ 70%) with matter being a subdominant component (~ 30%). The dark energy drives the acceleration of our ever expanding universe.

Early big bang nucleosynthesis (BBN) data indicated that in order to produce the proportions of ^{4}He, ^{3}He, ^{7}Li and D relative to H measured in the universe today, baryonic matter could only make up ~ 4% of ρ_c [12]. This was one of the first sources of corollary information that supported the missing mass paradigm from the mid-1900s. There is currently a cosmological lithium problem where only $\frac{1}{3}$ of the ^{7}Li predicted by BBN is observed. The ratios of the other elements relative to H predict an Ω_b value that agrees with that extracted from the CMB data. Therefore it is more likely that there is an additional currently unknown process which accounts for this discrepancy, rather than the smaller ^{7}Li H ratio indicating a smaller Ω_b value. Possible astrophysical, nuclear and Beyond the SM solutions are reported in [13].

The ~ 30% matter content and ~ 4% baryonic content imply that a large pro-

portion of matter present in the universe today is non-baryonic. Furthermore this non-baryonic component called DM is observed to be weekly interacting with both ordinary matter and itself as highlighted in section 1.1.1 and 1.1.2 respectively. It also needs to be cold (non-relativistic) to produce the structure formation born from quantum fluctuations during inflation discussed in section 1.1.3. This defines the ΛCDM standard cosmological model. The latest Planck results [10] that incorporate additional astrophysical observations find $\Omega_\Lambda \sim 68.9\%$ and $\Omega_M \sim 31.1\%$. The best fit DM and baryonic matter proportions are $\Omega_c \sim 26.2\%$ and $\Omega_b \sim 4.9\%$ respectively.

Section 1.1.1 outlined the initial indirect observations of missing mass in the Coma cluster and in galaxy rotation curves. While the presence of additional matter that was not being observed directly (DM) is a solution, it is not the only solution proposed for these observational problems. Modified Newtonian Dynamics (MOND) [14] postulates that all the matter is accounted for and instead it is gravity that behaves differently. This is formally expressed by modifying $F = ma$ with an additional unspecified function $\mu(x)$: $F = m\mu(\frac{a}{a_0})a$. In the high acceleration extreme ($x \gg 1$) $\mu(x) \to 1$ and at low accelerations ($x \ll 1$) in the deep-MOND regime $\mu(x) \to x$, which makes $F = m\frac{a^2}{a_0}$. The deep-MOND regime leads to rotational velocities independent of the radius: $\frac{GMm}{r^2} = m\frac{(\frac{v^2}{r})^2}{a_0}$ which implies $v^4 = GMa_0$. MOND can be made to agree with most galaxy rotation curves by selecting a suitable a_0. However, this fixes the scale and when applied to galaxy clusters or considered with respect to gravitational lensing the whole paradigm falls apart. It was a simple solution which is no longer supported by the wealth of cosmological observations discussed in this section.

This thesis focuses on DM and from here on in there will be no further mention of MOND. The following sections will outline the possible DM candidates and the currently employed experimental detection techniques will be fleshed out.

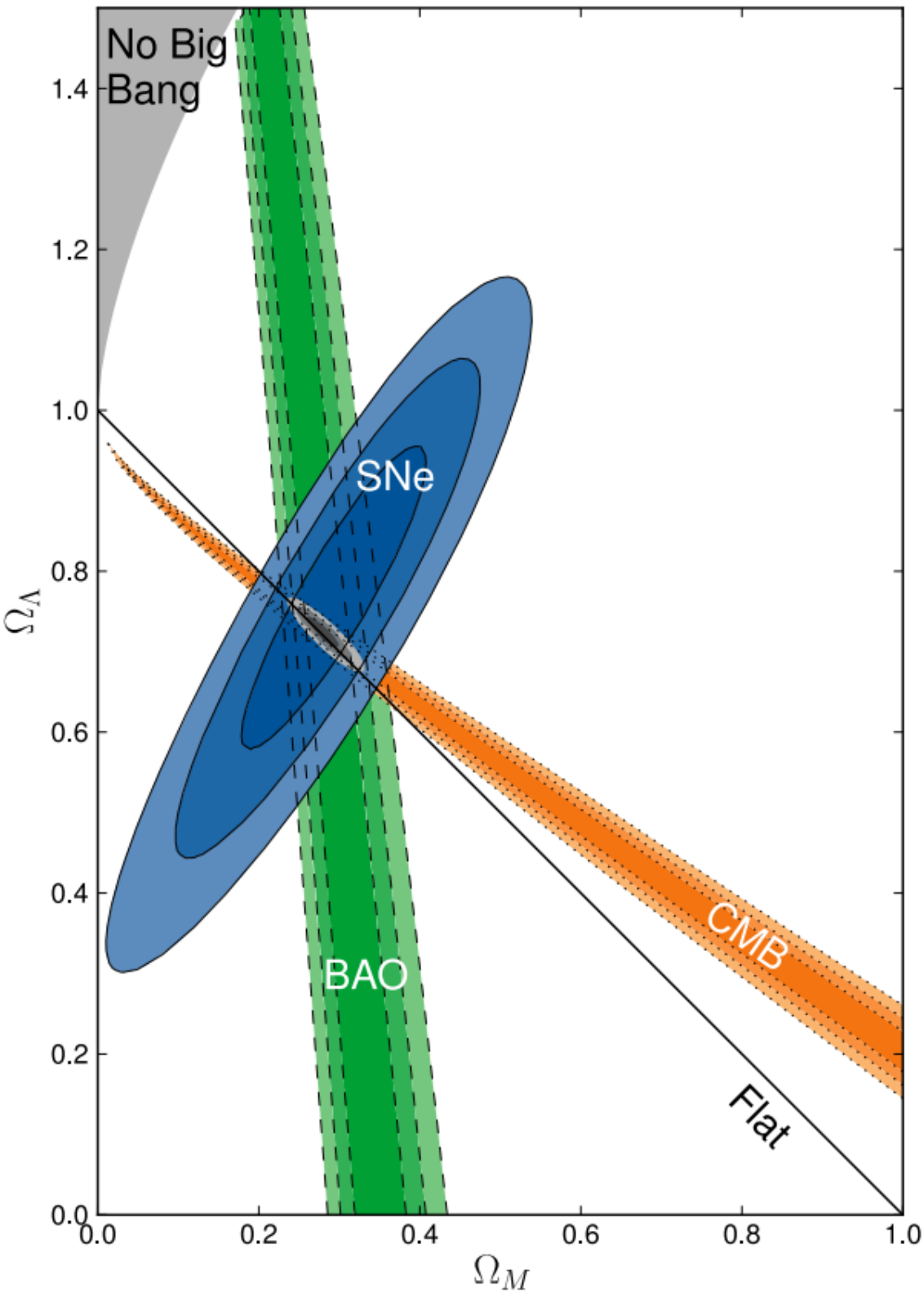


Figure 1.8: 68.3%, 95.4%, and 99.7% confidence regions in the (Ω_M , Ω_Λ) plane from SNe combined with the constraints from BAO and CMB [11].

1.2 Beyond the standard model and dark matter candidates

A few astrophysical candidates for DM have been considered over the years, however most have been excluded by observational data or dismissed due to conflictions with what is required by observations. As particle physics is able to explain the baryonic astrophysical observations, perhaps it is the best place to start when considering particle forms of DM.

1.2.1 Beyond the standard model

The standard model (SM) of particle physics is our current best means of accurately describing the enormous amount of data on particles and their interactions. The last piece of the SM came in 2012 when the Higgs Boson was discovered, a central prediction of the Higgs mechanism that gives all other particles their mass - the culmination of a 50 year journey from theoretical prediction to experimental validation.

We know that the SM is incomplete as there are many things it leaves out or fails to explain. Neutrinos are massless in the SM and hence the observed neutrino oscillations directly contradict this assertion. Why is there something rather than nothing? There is not enough CP violation present in the SM to produce the matter antimatter asymmetry ($\sim 10^{-10}$) required to form the universe that we observe. Additionally, why are there 3 generations of fermions, 3 generations are required for said CP violation, is this a coincidence? We wouldn't exist in a universe with < 3 generations to postulate such a question, but why aren't there > 3, is there an underlying reason? Why is the Higgs mass so small? A naive assumption would place it around the Plank scale, however it is many orders of magnitude smaller, what mechanism suppresses its mass? The SU(3)×SU(2)×U(1) group describes the symmetry groups of the observed strong, weak and electromagnetic forces that the elementary particle interactions obey. Why is this the case? How do we incorporate gravity? And is there a larger grand unified theory - SU(5) or SO(10) perhaps - that packages these symmetry groups

in a simplified manner, explains the observed particle interactions and incorporates some new ones? Similarly, why are the 19 free parameters of the SM what they are? Are they constructed from fewer more fundamental parameters?

Multiple beyond the standard model (BSM) theories have been proposed that answer one or a few of these unknowns simultaneously by incorporating additional interactions or particles. As noted previously, grand unified theories (GUT) attempt to bundle the SM symmetry groups together. These larger symmetry groups introduce additional interactions that often violate baryon/lepton conservation which could explain the matter antimatter asymmetry. GUTs are predominantly constrained by proton decay - SU(5) has been all but ruled out while SO(10) is still possible.

Supersymmetry (SUSY) attempts to explain the hierarchy problem by introducing an additional symmetry that connects fermions (spin $\frac{1}{2}$ particles) and bosons (integer spin particles) by an operator that allows for direct interactions/conversions. This operator doubles the number of particles that are currently present in the SM - the fermions and bosons have oppositely signed loop corrections to the Higgs mass and cancel out the largest components, thus helping to explain the low Higgs mass.

The coupling constants for the 3 SM forces can be made to converge at high energy by invoking GUT/SUSY, however gravity works on a completely different scale with its coupling constant, 10s of orders of magnitude smaller. String theory attempts to incorporate gravity into a model which so far excludes it and in doing so predicts very few observables except for an abundance of pseudo scalar axions in most models. Axions were originally proposed as a solution to the strong CP problem: QCD conserves CP even though there is a CP violating term in the Lagrangian, which can have values from $0 \rightarrow 2\pi$, for a CP violating term of $\mathcal{O}(1)$ the electric dipole moment of the neutron should be $\sim 10^{-18}$ em, it is experimentally verified to be $< 10^{-26}$ em [15]. This is a major fine-tuning problem. However the problem can be solved by promoting the CP violating term into a field and applying a new global symmetry which is then spontaneously broken. This results in a new particle known as the QCD axion. Axions are currently considered one of the best DM candidates.

1.2.2 Dark matter candidates

Discussed above are a subset of BSM theories that offer plausible candidates for DM. Here we attempt to survey the field of candidates that have been put forward and have been/are actively searched for. In particular we will discuss astrophysical candidates like MACHOs and primordial black holes, and particle candidates like Neutrinos (SM and sterile), WIMPs, asymmetric DM, axions and electrophilic DM.

- **MACHOs:** Massive Compact Halo Objects (MACHOs) where one of the first astrophysical candidates considered as a solution to the missing mass problem. A celestial body that is very heavy and is incapable of being directly observed. The main problem with this hypothesis is that the known mechanisms that produces dense celestial bodies require strong self-interactions. This is a baryonic process and this solution contradicts evidence from the requirements of DM needed for structure formation. Additionally, they should be observable indirectly via a "micro-lensing" gravitational effect. The process of gravitational lensing magnifies the surface brightness of the image. Hence, if a MACHO transits in front of a star the star's light brightens and dims in a predictable manner, from which the mass of the MACHO can be extracted. MACHOs have been observed by the MACHO experiment [16], however the more sensitive EROS-2 experiment [17] finds that MACHOs cannot form the abundance of DM predicted in the Milky Way halo unless their mass (M_C) is very much smaller or much larger than that of our sun ($M_\odot \sim 2\times10^{30}$ kg): $M_C < 10^{-8}\ M_\odot$ or $M_C > 100\ M_\odot$.

- **PBHs:** Primordial Black Holes (PBHs) were hypothesised to have formed from sufficiently dense regions arising from heterogeneous conditions soon after the big bang [18]. Their masses (M_{PBH}) are not constrained by the stellar gravitational collapse mechanism and hence masses $M_{PBH} \ll M_\odot$ are quite plausible. Hawking radiation places a lower bound on their theoretically allowed masses at $M_{PBH} > 10^{11}$ kg ($5\times10^{-20}\ M_\odot$); any smaller than this and their matter would

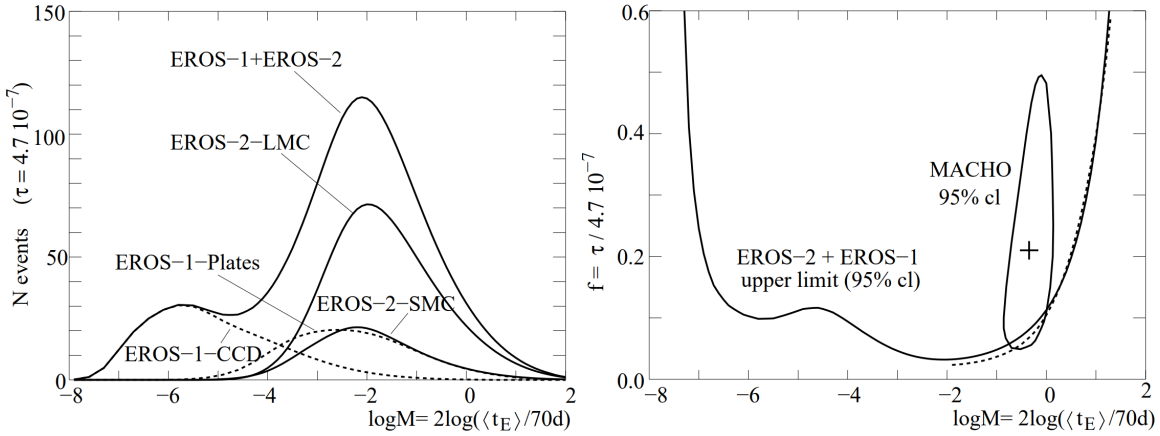


Figure 1.9: EROS-1 and EROS-2 Number of events and Limits. MACHOs cannot form the abundance of DM predicted in the Milky Way halo between 10^{-8} $M_\odot < M_C < 100$ $M_\odot$ [17].

have evaporated off and they would not have survived over the lifetime of the universe. This allows masses $\sim 10^{-19}$ $M_\odot < M_{PBH} < 10^{-8}$ $M_\odot$ and $M_{PBH} > 100$ $M_\odot$ where PBHs could exist. They are a perfect DM candidate in that they are non-baryonic, non-relativistic, stable and collision-less. Unfortunately, additional astrophysical and cosmological observations undermine PBHs forming the majority of DM in almost the entirety of the lower mass range: Lensing of gamma-ray bursts [19], Capture of primordial black holes by neutron stars [20] and the survival of white dwarfs and the supernova rate [21]. Temperature anisotropies in the cosmic microwave background also rule out PBHs above the gravitational lensing limit in the range of 100 $M_\odot < M_{PBH} < 10^4$ $M_\odot$ [22].

- **SM and Sterile Neutrinos:** Neutrinos are the only long-lived SM particles that are not charged under either the electromagnetic or strong interactions. Additionally they have been observed to oscillate between flavour states meaning they have mass, therefore it is possible they could form the observed DM. However there are problems with both their mass and their abundance. The mass of the electron neutrino $m_{\nu_e} < 1.1$ eV according to the KATRIN tritium β-decay experiment [23], and the mass differences between the neutrino mass states is $\Delta m^2_{21} = (7.53 \pm 0.18) \times 10^{-5}\text{eV}^2$ with $\Delta m^2_{31} = (2.453 \pm 0.034) \times 10^{-3}\text{eV}^2$ for normal ordering or $\Delta m^2_{31} = -2.546^{+0.034}_{-0.040} \times 10^{-3}\text{eV}^2$ for inverted ordering [24].

These masses make SM neutrinos relativistic and thus they would be a hot form of DM. Density fluctuations smaller than ~100 Mpc cannot gravitationally confine neutrinos due to their relativistic speeds (depending on their exact mass). This is larger than galaxy clusters and could therefore not form the structure observed throughout the universe. Additionally they have an abundance problem, e^+e^- annihilate after the neutrinos decouple $\rightarrow T_\nu = \left(\frac{4}{11}\right)^{1/3} T_\gamma$. Their number density relation is $n_\nu = \frac{3}{4}\left(\frac{T_\nu}{T_\gamma}\right)^3 n_\gamma$ and this implies $\frac{\rho_\nu}{\rho_c} = \frac{3}{11}\frac{n_\gamma m_\nu}{\rho_c}$, therefore the sum of all SM neutrino masses needs to be ~ 11.5 eV to form the required abundance of DM [25], which is ruled out by the directly measured mass limit and differences already listed.

Sterile neutrinos would be the right handed counterparts of the left handed SM neutrinos. They are a solution to the problem of the very small SM neutrino masses via the see-saw mechanism which mixes sterile and SM neutrinos. Sterile neutrinos are predicted to be both heavy and uncharged under the entire SM gauge group SU(3)×SU(2)×U(1) (SM-singlet), therefore sterile neutrinos make a good DM candidate. However, astrophysical implications of their existence are highly dependent on their mass (M), they are a viable DM candidates if M ~ few keV, as outlined in figure 1.10 [25].

- **WIMPs:** Weakly Interacting Massive Particles (WIMPs) is a generic term and these theorised particles have historically been the most favoured DM candidate. Their high mass allows them to account for DM in its entirety. They are cold (non-relativistic) which means they could reproduce the necessary structure formation observed throughout the universe. No SM particle has all the necessary characteristics and the 2 major BSM candidates are the fermionic lightest neutralino generated in SUSY, which could be the WIMP or the bosonic axions generated prolifically in string theories and offering a solution to the strong CP problem. Axions are discussed later.

  SUSY partners of the neutral photon (bino), Z-boson (zino) and 2 from the

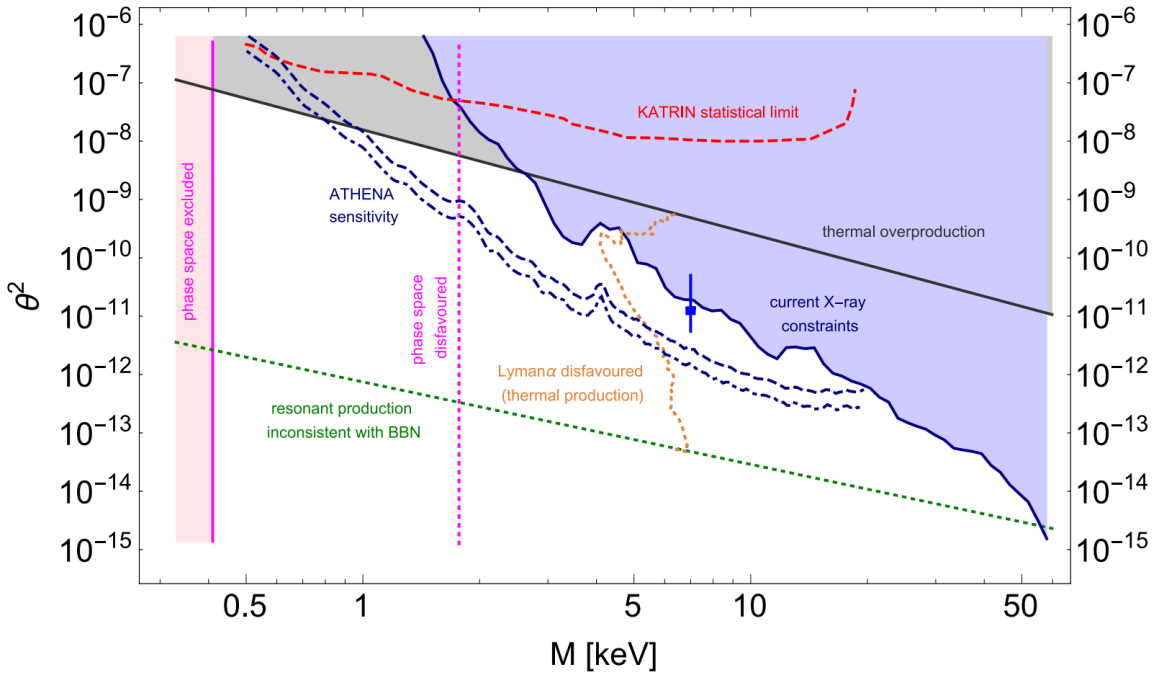


Figure 1.10: Generic SM-singlet fermion of mass M and a mixing angle θ with the SM neutrinos. The correct DM density is produced along the black solid line due to θ-suppressed weak interactions alone [25], mechanisms with resonances allow θ to have smaller values, down to the dashed green line. The other lines indicate theoretical or observed experimental/astrophysical limits.

Higgs doublet (Higgsinos) result in 4 neutral weakly interacting fermions which have identical quantum numbers and hence mix, resulting in 4 weakly interacting massive particles (WIMPs) referred to as neutralinos. If an additional quantum number R-parity (+1 for SM particles, -1 for their SUSY partners) is conserved the lightest SUSY particle (LSP) cannot decay into a SM particle and hence is stable. If an LSP does exist it has to be a neutralino. If the LSP was another SUSY particle - charged under the SM gauge groups - it would interact strongly.

One of the main reasons SUSY WIMPs are highly favoured as a DM candidate is the so-called "WIMP miracle". Stable particles such as the posited DM WIMPs remain in equilibrium at early times in the evolution of the universe until they freeze out when the rate of expansion becomes too large and collisions too rare. WIMPs with masses within the GeV-TeV range - predicted by most

supersymmetry models - produce the required abundance of DM with interaction cross sections that are very weak $< 10^{-36}$, a very good DM candidate. A plot of the current experimental limits is displayed in the next section where the different possible detection techniques are discussed.

- **Asymmetric DM:** If distinct processes underpin the formation of visible matter - made from SM particles - and dark matter - formed from an entirely unrelated sector - one would naively assume one to dominate by many orders of magnitude, not a factor of 5. Why is the quantity of visible matter and dark matter as similar as it is? This underlying quandary gave rise to the notion that DM could be formed from a sector related to but separate from that of the SM. Initial concepts postulated an unconnected mirrored sector that obeyed identical physics to that of the SM, each producing matter in equal quantities. This was expanded upon to allow for limited levels of interactions between the two sectors which could lead to the observed imbalance. There is a rich phenomenology associated with asymmetric DM models, with most predicting a DM particle of mass $\mathcal{O}(\text{GeV})$ [26]. These DM particles are subject to constraints from the usual cosmological observations and can be verified experimentally via conventional particle physics detection techniques, discussed in more detail in the following section.

- **Axions:** Axions are bosons predicted by many string theories and are a solution to the strong CP problem. Although axions are light particles ($\sim 1 - 100$ μev) they are not hot DM. The fact they are bosons means they form a Bose-Einstein condensate. The energy density is not stored in the small axion mass, but instead in oscillations of the axion field around its minimum. Therefore axions are an effective cold DM solution. They are also pseudoscalars and their interaction vertices are intrinsically different to the fermionic DM listed above. The strong CP axion mass is proportional to its coupling constant $g_{a\gamma\gamma}$ by virtue of the symmetry it helps solve. The strong CP problem can be solved with two

different approaches to coupling, the KSVZ axion via hadronic coupling [27,28] and the DFSZ axion via minimum coupling [29,30], this results in slightly offset mass coupling relations. These relations are outlined in figure 1.11, the left plot shows the Axion Dark Matter Experiment's (ADMX) expected sensitivity in the coming years, the right hand plot shows the ADMX recent results [31] in narrow mass (frequency) bands that support this expectation.

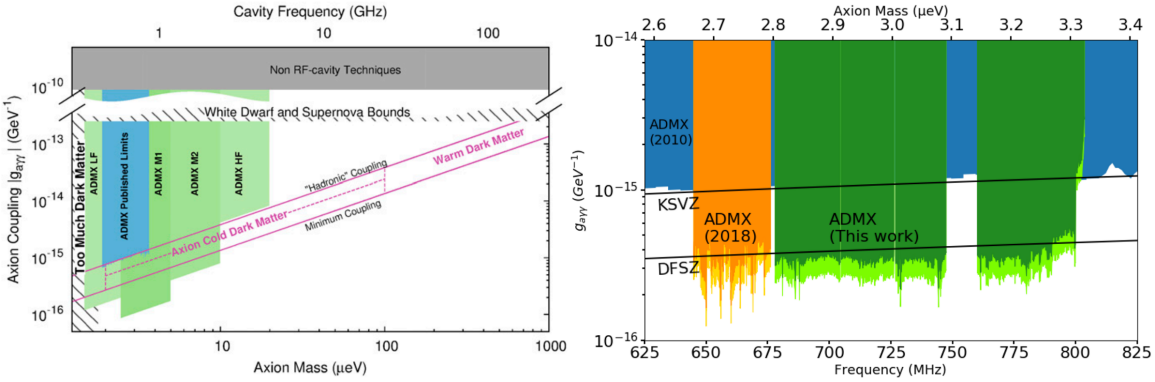


Figure 1.11: ADMX are probing the axion coupling vs axion mass available phase space predicted for the KSVZ and DFSZ axions. The expected experiment sensitivity (left) [32] and recent results (right) [31].

- **Electrophilic DM:** In [33] the DAMPE collaboration reported observation of an electron positron excess at ~ 1.4 TeV. A 1.4 TeV fermionic DM particle, accompanied by a dark photon scalar mediator, both charged under a new dark $U(1)_X$ gauge symmetry and coupled to the SM right-handed leptons, could produce the reported DM annihilation excess [34] but neutrino flavour mixing constrains coupling to the left-handed SM lepton doublets. Dark photon coupling to SM fermions via $U(1)$ kinetic mixing minimally affects the DM annihilation rates while introducing Yukawa tree level DM-nucleon interactions, greatly increasing the expected direct detection event rates. Unfortunately this simple addition to the SM only attempts to solve the particular problem of DM and does not help with any other particle physics problems; for example this theory contributes only minimally to the anomalous magnetic moment $(g-2)$ of the muon.

1.3 Dark matter detection techniques

There are three methods that particle physicists and astrophysicists can use to search for interactions between SM and DM particles as displayed in figure 1.12. Collider detection (production) searches use particle accelerators in an attempt to produce DM out of SM particles, however in most complete models (i.e. SUSY or asymmetric DM) it is unlikely that the first particles observed at colliders would be the DM that populates the universe. Indirect detection (annihilation) searches look for potential SM decay products of DM, producing an observable beyond what is predicted from known astrophysical processes. This in principle works for all the particle DM candidates considered here, however some are best searched for via other means - such as axions with resonant microwave cavities as in the ADMX experiment. Direct detection searches look for nuclear recoil or electron recoil interactions induced by DM particles - present in our galaxies DM halo - with the detector's target material. This would work for the axion, electrophilic DM, asymmetric DM and WIMPs. This thesis is predominantly focused on WIMPs and chapter 2 outlines how such nuclear recoil interactions could arise by using a simplified model in section 2.1 and generalising to an effective field theory Lagrangian in section 2.2.

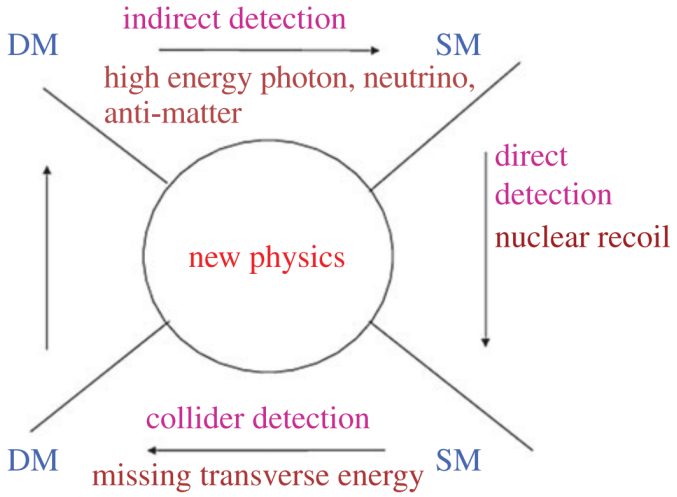


Figure 1.12: The three search methodologies for DM-SM interactions [35]. Indirect: DM→SM. Direct: DM+SM→DM+SM. Collider: SM→DM.

There are pros and cons with all of these searches, however if DM is discovered in the future all three techniques should be utilised to verify results for consistency and to fully understand its characteristics via additional processes. The following subsections outline these three techniques in turn, most emphasis is placed on direct detection as that is the methodology employed in this thesis.

1.3.1 Dark matter collider detection searches

Collider detection searches use particle accelerators to smash SM particles together at very high energies to produce particles with masses larger than that of said SM particles. This technique has been used to great effect in the past when discovering new SM particles, however BSM particles have so far evaded detection. This approach will not exclusively produce DM, most BSM theories attempt to rectify the SM's inherent problems, not solve the DM problem, hence these theories don't exclusively predict one extra particle that is DM, but a plethora of particles that make up an entirely new sector, one of which could be DM. Therefore the first new particles to be produced and discovered using this methodology may not be the DM present throughout the universe but instead additional particles in said sector. However most non-DM particles predicted in these new sectors are usually somewhat charged under the SM gauge groups and hence will interact in the detector and be observed directly. The way to search for DM production in colliders is to search for missing transverse energy as the DM particles won't be observed in the detectors nor decay into something else that can be observed - DM is both long-lived and weakly interacting with the SM. A summary of the ATLAS searches for different SUSY models and varied final state particles is presented in figure 1.13.

1.3.2 Dark matter indirect detection searches

Indirect detection searches look predominantly for an excess of high-energy photons, neutrinos or anti-matter, dependent on the specific DM model. The SM astrophysical processes and cosmic ray models that produce these particles have relatively small

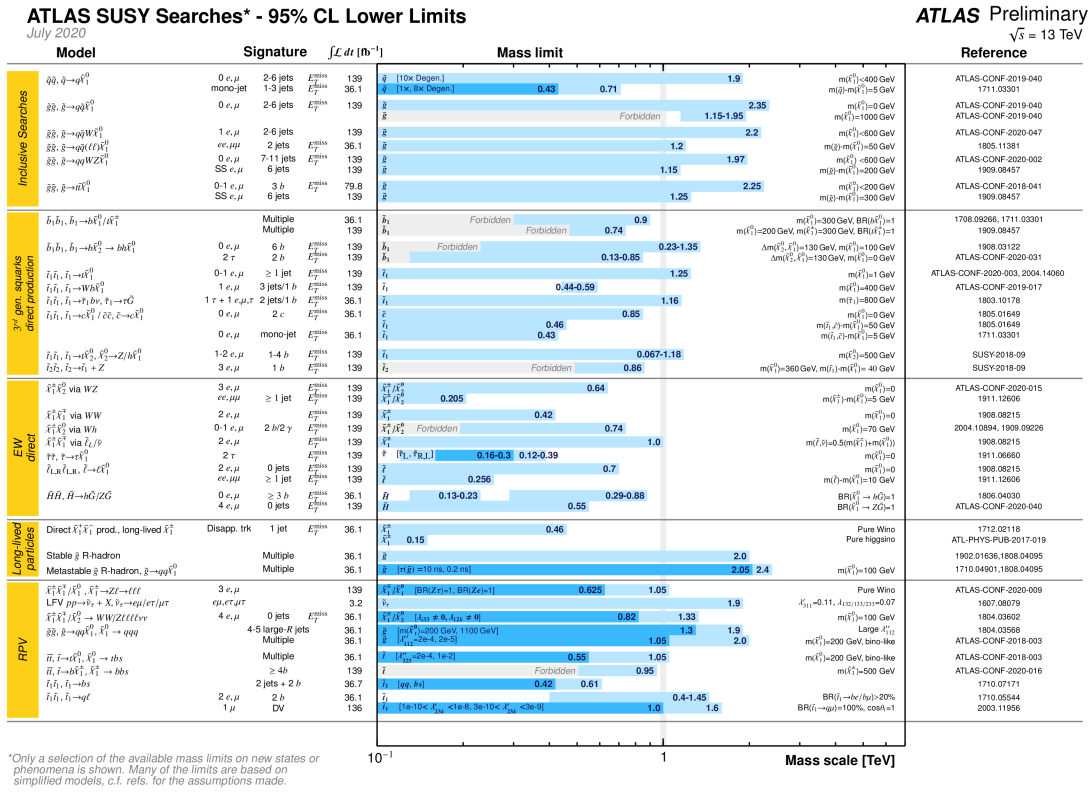


Figure 1.13: Overview of the ATLAS analyses results for multiple SUSY models with different final state particles [36].

and well understood fluxes. Therefore a deviation from the SM theoretical values by a new DM driven mechanism can be discovered. A sizeable portion of DM is predicted to be trapped in local gravitational wells, i.e. at the gravitational centre of our milky way but also inside of individual stars. The Dark Energy Survey (DES) collaboration examines the size, population and distribution of dwarf galaxies surrounding the Milky Way. The mass-to-light ratio in such dwarf galaxies is 100 times larger than in an average galaxy due to heavily supressed star formation; this makes them prime candidates to search for DM. Observations of dwarf galaxies support the CDM paradigm and place stringent limits on warm DM, interacting DM and fuzzy dark matter [37]. The Fermi Large Area Telescope (Fermi-LAT) utilised a similar sample of dwarf galaxies to search for an excess of γ-ray emission; some dwarf galaxies exhibited an excess above expected BG levels, but no globally significant excess was observed given the sample size [38]. The Alpha Magnetic Spectrometer (AMS) exper-

iment located on the international space station (ISS) measures cosmic-ray fluxes of positrons, electrons, antiprotons, protons, and nuclei. An excess of positrons at high energy supports the expected SM diffuse BG plus an additional source term which could be DM [39]. Additional space based experiments like PAMELA also compare the ratio of matter to anti-matter for electron and proton fluxes. While PAMELA did not observe a significant excess that indicates DM, it has set strong constrains on exotic DM processes and discovered an antiproton radiation belt that surrounds Earth [40]. Underground experiments like Super-Kamiokande [41] are attempting to observe high energy neutrinos formed from DM pair annihilation, so far no significant signals have been discovered.

1.3.3 Dark matter direct detection searches

Direct detection experiments are attempting to observe non-relativistic DM-SM nuclear recoil interactions with recoil energies of only a few keV. This energy is converted into three different types of signal: scintillation light, phonons and ionisation. Some detectors are only sensitive to a single type while others can simultaneously record two different types. Figure 1.14 associates some recent experiments with the respective signal types they exploit. The experiments themselves fall into three main camps, each of which is outlined below: those that use monocrystalline crystals, semiconductors or noble liquids. As the predicted DM-SM interaction cross sections are very small ($< 10^{-36}$ cm^2) these experiments are conducted deep underground to reduce backgrounds and the materials used are heavily assayed to reject materials that are contaminated with radioisotopes.

- **NaI(Tl) and $CaWO_3$ crystals:** DAMA/LIBRA, ANIAS and CoSINE-100 use NaI(Tl) crystals while CRESST's crystals are made from $CaWO_3$, both can measure scintillation photons however CRESST has the advantage of additionally measuring phonons. The DAMA/LIBRA experiment claims to observe an annual modulation in their event rate with a 12.9σ confidence level that

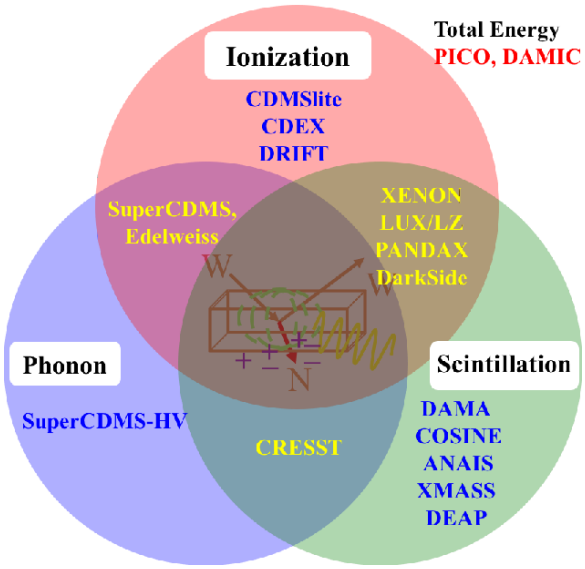


Figure 1.14: Direct detection DM experiments sensitive to scintillation light, phonons and ionisation signals [42].

is consistent with a DM induced annual modulation signal expected from the Earth's motion around the Sun as the Sun traverses the DM halo [43–45]. However no other experiment has been able to validate these results, including the model independent modulation results from the XMASS detector that are the subject of this thesis. The best fit modulation amplitude and phase reported by the CoSINE-100 experiment are both consistent with the null hypothesis and results reported by DAMA/LIBRA [46]. The ANAIS experiment was designed using the same target material to confirm or refute the positive results reported by DAMA/LIBRA; no modulation signal was found and the results are incompatible with those reported by DAMA/LIBRA at 3.3 σ [47].

- **Ge and Si semiconductors:** Ge and Si semiconductor detectors have much better energy resolution than other direct detection experiments, hence they probe lower nuclear recoil energies and lower WIMP masses. The super-CDMS group uses Ge and Si crystals with a detector sensitive to both ionisation and phonon signals. Correlating an event's respective ionisation and phonon signals allow them to discriminate between nuclear recoil and electron recoil events.

- **Noble liquids:** Noble liquid detectors use either Xe or Ar for their target mass and contain a large liquid target with a gaseous layer above. Single-phase detectors like XMASS and DEAP utilise only the liquid and are optically isolated from the gas layer, only registering scintillation photon signals. The UK based ZEPLIN collaboration began humbly with ZEPLIN-I - a single-phase detector with 3 kg liquid Xenon (LXe) - before pioneering dual-phase LXe detectors in their following ZEPLIN-II and ZEPLIN-III experiments. The ZEPLIN and LUX collaborations then merged to form the LUX-ZEPLIN (LZ) collaboration that is currently competing with the XENON collaboration. These dual-phase detectors utilise the gas layer by applying a vertical electric field to additionally extract and independently measure the associated ionisation signal alongside the scintillation photon signals. The Electric field does reduce the number of scintillation photons observed, however this loss is worth the increase in event position determination and classification capabilities gained with the inclusion of the ionisation signal. The difference in pulse shape discrimination between LXe and LAr is discussed in section 3.1.3. Dual phase detectors outperform single-phase detectors at discrimination between electron recoil and nuclear recoil events. Noble liquid detectors have one large advantage over the others and it's their scalability: sensitivity $\propto$ target mass. The largest Xenon detectors contain several tons of target material and one massive collaborative effort with an even larger detector is a possibility in the future [48]. The many advantages to using LXe as a detector material and are listed in section 3.1.1; a key advantage is its large atomic number (A) and lack of intrinsic radioactive isotopes. Ar is cheaper but has a smaller A and ^{39}Ar has a half-life $\sim$ 200 years, Ar without this RI is more expensive than Xe. The spin independent (SI) interaction outlined in section 2.2 - is a first order level interaction: no spin, transferred momentum or relative velocity factors supress the interaction. Additionally it is $\propto A^2$, making it ideally suited for investigation in LXe detectors and is the main focus of the analyses carried out in this thesis.

- **Current limits:** Figure 1.15 shows the WIMP-nucleon SI cross section limits set by multiple direct detection experiments: XMASS Modulation 2018 [49, 50], XMASS fiducial volume 2018 [51], DAMA NaI 2017 [43–45], CDMS-Si 2013 [52], SuperCDMS 2014 [53], CDMS-Lite 2018 [54], CREST-II 2016 [55], DarkSide 50 2018 [56, 57], NEWS-G 2018 [58], DEAP-3600 2019 [59], PandaX-II 2021 [60], LUX 2017 [61], Xenon1T 2018 [62]. Coherent neutrino scattering (dashed orange line) originates from ^{7}Be and ^{8}B solar neutrinos inducing a small nuclear recoil energy ~ few keV (WIMP mass below ~ 10 GeV) and low energy atmospheric neutrinos that induce nuclear recoil energies > 20 keV (WIMP mass above ~ 10 GeV). This neutrino background can only be reduced by annual modulation or with directional event information - very difficult at the scale needed. This results in a neutrino floor (blocked out yellow) that will hamper direct detection WIMP SI searches.

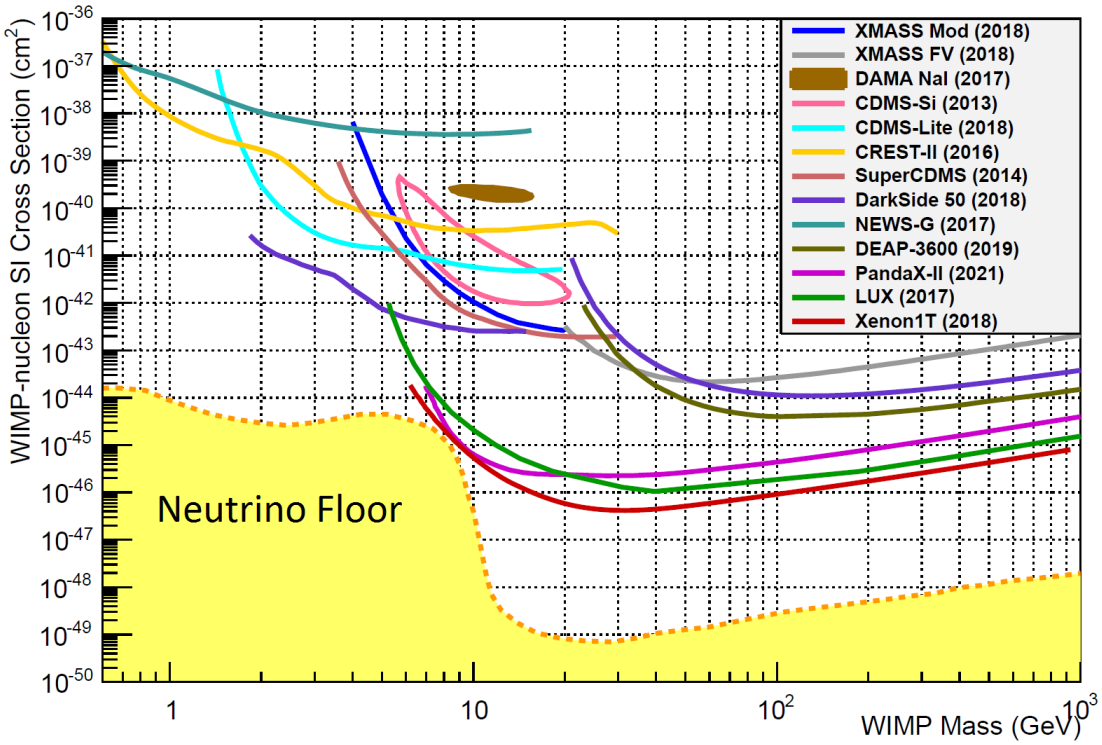


Figure 1.15: Multiple direct detection experiments: WIMP-nucleon SI cross section limits. The Ge and Si semiconductor detectors cover the low WIMP mass region while the noble liquid detectors cover the high WIMP mass region. The largest experiments are getting ever closer to the neutrino floor.

Chapter 2

The Direct Detection of Dark Matter

As mentioned in section 1.2.1 extensions to the SM can lead to additional particles that could form the DM observed throughout the universe. Section 2.1 outlines a simplified scalar model where SM fermions can interact with a DM fermion through a scalar mediator that mixes with the SM Higgs. An electron recoil (ER) interaction can occur from the DM fermion interacting with the multitude of SM fermion electrons present in atoms, these electrons can be considered in isolation and hence there are no residual multi-body interactions that need to be considered. The nuclear recoil (NR) interaction on the other hand occurs from the DM fermion interacting with the quarks and gluons present in the nucleons; this calculation is more involved and the nucleon interaction coefficient is derived explicitly by considering the contributions from both. Section 2.2 generalises this approach to the general Dirac fermion DM-SM quark effective field theory interaction Lagrangian and examines the non-relativistic analogues of the interaction terms. The relationship between the nucleon and nuclei cross sections is discussed and finally the expected differential event rate is calculated. This is work I undertook in my first year separate from the calibration study and modulation analyses I performed as a member of the XMASS collaboration. Section 2.3 discusses how the Earth orbiting the Sun induces an annual modulation effect on the expected event rate: this is the main focus of this thesis.

2.1 Simplified model: fermionic DM-SM nucleon interaction

2.1.1 DM-SM mediator

For DM χ to have escaped experimental detection so far, it must be a singlet under all SM gauge groups (G_{SM}) [63] or have a very large mass >> TeV. For the SM Lagrangian ($\mathcal{L}_{\mathrm{SM}}$) or any beyond the SM (BSM) Lagrangian ($\mathcal{L}_{\mathrm{BSM}}$) extensions to be gauge invariant, all the terms must be singlets for all of the theories' gauge groups. Therefore all $\mathcal{L}_{\mathrm{BSM}}$ terms must be G_{SM} singlets, including the interaction piece involving DM particles and a spin-0 or spin-1 mediator S: $\mathcal{L}_{\mathrm{BSM}} \supset \bar{\chi}\chi\mathcal{S}$. S links the SM and DM sectors and given this interaction term it must also be a G_{SM} singlet.

The only G_{SM} singlet that can be exploited to construct a new renormalisable Lagrangian that can incorporate the new mediator is within the Higgs field Φ. $\Phi^\dagger\Phi$ is a SM singlet with a mass dimension of 2, hence $m_{\Phi^\dagger\Phi S}\Phi^\dagger\Phi S$ and $g_{\Phi^\dagger\Phi S^2}\Phi^\dagger\Phi S^2$ are perfectly valid terms as neither violate gauge invariance, Lorentz invariance or locality.

2.1.2 Simplified scalar model

In the simplest case [63], a scalar mediator S mixes with the SM Higgs via their interacting potentials. Equation 2.1 outlines the relevant Lagrangain terms in both the SM and the BSM extension. $\mathcal{L}_{\mathrm{SM}}$ includes the terms governing the Higgs potential: $\mu^2 < 0$ and $\lambda > 0$ with degenerate minima located at $\Phi = \frac{-\mu^2}{2\lambda} = \frac{v}{2}$ away from zero, where v is the vacuum expectation value (VEV). And $\mathcal{L}_{\mathrm{SM}}$ includes the interaction terms between the Higgs and the SM leptons and quarks: u_R, d_R, e_R, Q_L and L_L, where $Q_L = \begin{pmatrix} u \\ d \end{pmatrix}_L$ and $L_L = \begin{pmatrix} \nu_e \\ e \end{pmatrix}_L$ are the left handed SM doublets for the quarks and leptons respectively. There is an implied sum over all 3 generations within the Lagrangian and Hermitian conjugate terms forcing the Lagrangian to be real. $\mathcal{L}_{\mathrm{BSM}}$ includes the kinetic terms for the additional fields S (Klein-Gordon) and χ (Dirac), the interaction term between these two new fields and the interaction potential (V_{int}). V_{int} includes

self-interaction terms for S and the interaction terms with the Higgs field. M_{SS} and m_χ are mass terms for the two new fields, μ_{HS} and μ_S are coupling constants with mass dimension 1 and λ_{HS}, λ_S and y_χ are coupling constants with mass dimension 0:

$$\begin{aligned}
&\mathcal{L}_{SM} \supset -\bar{Q}_L\Phi^\dagger u_R - \bar{Q}_L\Phi d_R - \bar{L}_L\Phi e_R - \mu^2\Phi^\dagger\Phi - \lambda(\Phi^\dagger\Phi)^2 \quad \text{and} \\
&\mathcal{L}_{BSM} \supset \frac{1}{2}\partial_\mu S\partial^\mu S - V_{int} + \bar{\chi}(i\not{\partial} - m_\chi)\chi - y_\chi\bar{\chi}\chi S, \quad \text{where} \\
&V_{int} = -\frac{1}{2}M_{SS}^2S^2 + \mu_{HS}\Phi^\dagger\Phi S + \frac{1}{2}\lambda_{HS}\Phi^\dagger\Phi S^2 + \frac{1}{3!}\mu_S S^3 + \frac{1}{4!}\lambda_S S^4.
\end{aligned} \tag{2.1}$$

For simplicity the S^3 and $\Phi^\dagger\Phi S$ terms are removed by imposing a Z_2 symmetry. For S to couple with the Higgs after electroweak symmetry breaking (EWSB), λ_{HS} must be non-zero and S must also acquire a VEV $\langle S\rangle = w$. After symmetry breaking, the fields and their mass matrix are:

$$\Phi = \begin{pmatrix} 0 \\ \frac{h'+v}{\sqrt{2}} \end{pmatrix} \quad \text{and} \quad S = s' + w, \quad \text{with} \quad M^2 = \begin{pmatrix} 2\lambda v^2 & \lambda_{SH}vw \\ \lambda_{SH}vw & \frac{1}{3}\lambda_S w^2 \end{pmatrix}. \tag{2.2}$$

By rotating the fields by mixing angle ϵ the mass matrix can be diagonalised and the fields transformed into their mass eigenstate bases: $h = h'\cos\epsilon + s'\sin\epsilon$ and $s = -h'\sin\epsilon + s'\cos\epsilon$. The Higgs has been observed to behave as predicted by the SM and LHC constraints require $\epsilon \leq 0.4$. By taking ϵ and λ_{SH} to be small, the masses and mixing angle can be simplified [63], only the first order components included:

$$M_h^2 = 2\lambda v^2 \quad \text{and} \quad M_s^2 = \frac{1}{3}\lambda_S w^2, \quad \text{where} \quad \tan\epsilon \approx \frac{\lambda_{SH}vw}{M_h^2 - M_s^2} \approx \sin\epsilon. \tag{2.3}$$

Equation 2.1 included interaction terms between S and χ and Yukawa interaction terms between Φ and the SM fermions. The SM sector and the DM sector separate. However the mixing between S and Φ opens a portal between the two sectors, the new mass eigenstate fields h and s can both interact with both the SM fermions (f) and χ. By expanding the Lagrangian one obtains the new set of interactions:

$$\begin{aligned}
&\mathcal{L} \supset -h'\sum_i \frac{y_i}{\sqrt{2}}\bar{f}_i f_i - y_\chi s'\bar{\chi}\chi \quad \text{becomes} \\
&\mathcal{L} \supset -(h\cos\epsilon - s\sin\epsilon)\sum_i \frac{m_i}{v}\bar{f}_i f_i - y_\chi(h\sin\epsilon + s\cos\epsilon)\bar{\chi}\chi.
\end{aligned} \tag{2.4}$$

The Yukawa interaction terms are related to the fermions mass via $\frac{y_i}{\sqrt{2}} = \frac{m_i}{v}$ where i represents any SM fermion of any generation.

2.1.3 The DM-nucleon interaction coefficient

The DM-nucleon operator can be represented using an effective field theory (EFT) with higher mass dimension (> 4) operators: $O_N = C_N \bar{\chi}\chi\bar{N}N$ [63]. The contributions to this DM-nucleon EFT operator can be separated into the quark and gluon components, $O_q = C_q \bar{\chi}\chi\bar{q}q$ and $O_g = C_g \frac{\alpha_s}{12\pi}\bar{\chi}\chi G^{a\mu\nu}G^a_{\mu\nu}$ respectively. The 4-momentum of the incoming and outgoing χ particle is P_1 and P_1' respectively, likewise the 4-momentum of the incoming and outgoing SM quark or gluon is P_2 and P_2' respectively. The spins of the incoming and outgoing χ and SM particles are denoted s_1, s_1', s_2 and s_2' in the same way. Figure 2.1 illustrates the Feynman diagrams for these interactions, the left and middle diagrams demonstrate quarks interacting with χ via scalar mediator particles h and s respectively, the right diagram demonstrates gluons interacting with χ via an intermediary top quark loop.

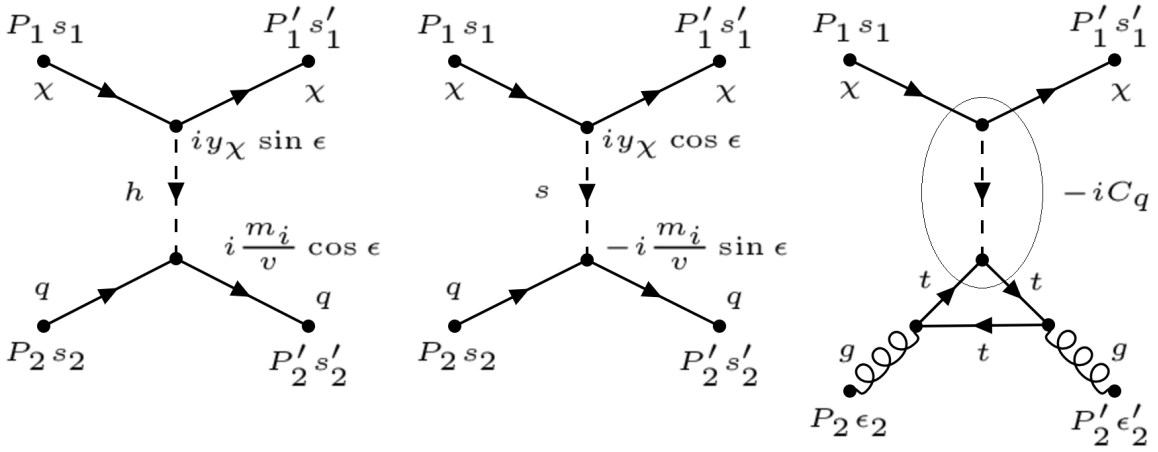


Figure 2.1: Contributing Feynman diagrams to DM-nucleon interaction. Left: q-χ via mediator particle h. Middle: q-χ via mediator particle s. Right: g-χ via an intermediary top quark loop. The interaction vertex factors and momentum/spin labels are included.

The EFT approach to represent the DM-nucleon interaction via a single operator is accomplished by integrating out the two scalar mediators, the transferred energy $q^2 = (P_1 - P_1')^2 \ll m_h^2$ or m_s^2 so the propagator terms become constant $\frac{1}{q^2 - m_h^2} \to \frac{-1}{m_h^2}$. This is

similar to the how the electroweak force was initially considered a 4 fermion interaction vertex EFT with an interaction constant supressed by m_W^2. The quark interaction coefficient (C_q) arising from the quark-χ interaction Feynman diagrams calculated in equation 2.5 is embedded within the gluon-χ interaction Feynman diagram, indicated by the ellipse in figure 2.1.

$$C_q = \sin\epsilon\cos\epsilon y_\chi \frac{m_q}{v}\left(\frac{1}{m_h^2} - \frac{1}{m_s^2}\right) = \frac{\sin\epsilon\cos\epsilon y_q y_\chi}{\sqrt{2}}\left(\frac{1}{m_h^2} - \frac{1}{m_s^2}\right). \tag{2.5}$$

The gluon interaction with a top-quark loop is what facilitates the interaction with the scalar mediator particles as demonstrated in figure 2.2.

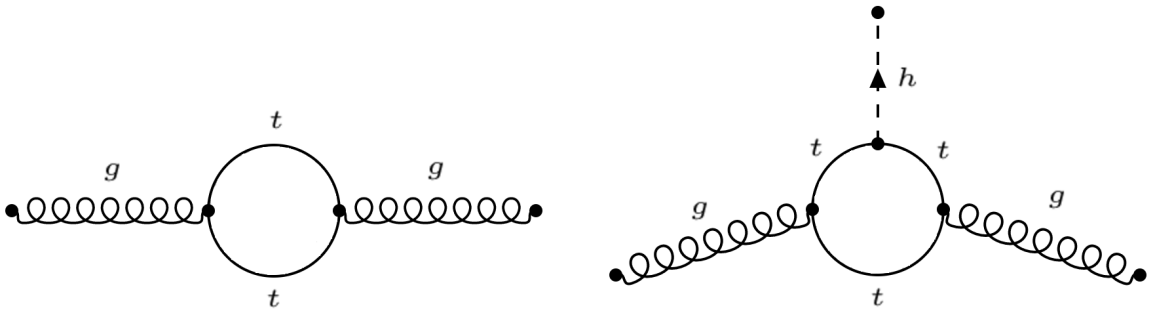


Figure 2.2: Gluon self-energy top-loop contribution and interaction with scalar mediators.

The gluon interaction can be calculated by considering the gluon self-energy and the additional contribution arising from such a top quark loop ($\Omega_{gg}^t(0)$) [64]:

$$\begin{aligned} \mathcal{L}_{gg} &= -\frac{1}{4}G^{a\mu\nu}G^a_{\mu\nu}[1 + \Omega_{gg}^t(0)], \quad \text{where} \\ \Omega_{gg}^t(0) &= \frac{\alpha_s}{6\pi}\left[\frac{4\pi\mu^2}{m_t^2}\right]^\xi \Gamma(1+\xi)\frac{1}{\xi}. \end{aligned} \tag{2.6}$$

α_s is the strong coefficient and ξ is the dimensional regularisation parameter arising from the loop integral: $\xi \to 0$.

The mediator's 4-momentum (P_s) in a direct detection interaction is very small ($P_s^2 = q^2 \ll m_s^2$) and effectively tends to the soft limit ($P_s \to 0$). A theorem exists that relates the amplitudes of an arbitrary process X with the same process plus the addition of a soft scalar $X + s$ [64], which can be generalised to pseudoscalars, vectors and axial-vectors. The coefficient of the $G^{a\mu\nu}G^a_{\mu\nu}s$ EFT interaction Lagrangian can

be calculated by applying said theorem to the top quark contribution to the gluon self-energy:

$$\lim_{P_s \to 0} A(X+s) = \frac{m_0}{v}\frac{\partial}{\partial m_0}A(X) \quad \rightarrow \quad \mathcal{L}_{ggs} = \frac{\alpha_s}{12\pi}G^{a\mu\nu}G^a_{\mu\nu}\frac{s}{v}\sin\epsilon. \tag{2.7}$$

The $G^{a\mu\nu}G^a_{\mu\nu}s$ vertex compared to the $\bar{q}qs$ vertex is of opposite sign and suppressed by a factor of m_q. An equivalent result holds for X+h and the DM part of the gluon interaction is identical, hence $C_g = -\frac{C_q}{m_q}$.

Nucleons (N) have mass $m_N = 0.938$ GeV and low energy nucleons are described via non-perturbative QCD. How strongly each of their components couple for each type of interaction is defined by their Wilson coefficients, $f^N_{T_q}$ and $f^N_{T_g}$ for each of the light quarks and gluons respectively [65]. Taking this into account, the quark and gluon contributions can be combined to calculate the total nucleon coefficient C_N:

$$\begin{aligned} C_N &= \sum_{q=u,d,s}\frac{m_N}{m_q}f^N_{T_q}C_q - \frac{2}{27}f^N_{T_g}\sum_{q=c,b,t}m_N C_g \\ &= \frac{m_N}{v}y_\chi\cos\epsilon\sin\epsilon\left(\frac{1}{m_h^2}-\frac{1}{m_s^2}\right)\left(\sum_{q=u,d,s}f^N_{T_q}+\frac{2}{9}f^N_{T_g}\right). \end{aligned} \tag{2.8}$$

2.2 Non-relativistic reduction and event rates

2.2.1 Direct detection operators

Outlined above is a simple BSM extension where a scalar mediator mixes with the SM Higgs. Of course, there are many different sorts of theories concerning different types of mediators and different forms of DM [66]. For instance, in supersymmetry one generates a second Higgs doublet, and after EWSB five physical degrees of freedom (d.o.f.) remain and five particles emerge; two neutral scalars (one light SM Higgs, and one heavy Higgs), two oppositely charged scalars, and one pseudoscalar. In this model both scalar and pseudoscalar mediators could convey information between the two sectors [63, 67]. There are also theories that allow for vector, axial vector and mediators with spin larger than 1. The Lagrangians governing these for many

different types of DM are listed in [68]. Equation 2.9 is the most general Dirac fermion DM-SM quark EFT interaction Lagrangian, that incorporates the traditional scalar, pseudoscalar, vector and axial vector mediators for both the SM and DM sectors. The coefficients of which are S_χ and S_q, P_χ and P_q, V_χ and V_q and A_χ and A_q respectively. The interaction terms are supressed by the energy scale Λ (mediator mass) of said theories.

$$\begin{aligned} L_\chi \supset & \frac{1}{\Lambda^3}\bar{\chi}(S_\chi + i\gamma^5 P_\chi)\psi\bar{q}m_q(S_q + i\gamma^5 P_q)q \\ & + \frac{1}{\Lambda^2}\bar{\chi}\gamma_\mu(V_\chi + \gamma^5 A_\chi)\chi\,\bar{q}\gamma^\mu(V_q + \gamma^5 A_q)q. \end{aligned} \tag{2.9}$$

DM has a local velocity of $\sim 10^{-3}$ c and at low momentum the particle and antiparticle Dirac spinors reduce to the simple form represented by the Pauli spinors (ϕ_χ and ϕ_N) and where $\vec{\sigma}$ and $\vec{p}$ are the 3-vector Pauli matrices and DM momentum respectively [69]:

$$u_\chi(p) = \sqrt{\frac{E + m_\chi}{2m_\chi}}\begin{pmatrix} \phi_\chi \\ \frac{\vec{\sigma}\cdot\vec{p}}{E+m_\chi}\phi_\chi \end{pmatrix} \to \begin{pmatrix} \phi_\chi \\ \frac{\vec{\sigma}\cdot\vec{p}}{2m_\chi}\phi_\chi \end{pmatrix}. \tag{2.10}$$

Consequently one can consider the non-relativistic analogues of the interaction terms in equation 2.9 where the spatial components of the gamma matrices dominate [69, 70]. The scalar interaction $\bar{\chi}\chi\bar{N}N$ to leading order in $\frac{p}{m_\chi}$ becomes $1_\chi 1_N$ and is spin independent (SI), as is the vector interaction. Whereas the axial vector interaction $\bar{\chi}\gamma_\mu\gamma^5\chi\bar{N}\gamma^\mu\gamma^5 N$ becomes $\bar{\chi}\gamma_i\gamma^5\chi\bar{N}\gamma^i\gamma^5 N \to \phi_\chi^\dagger\sigma^i\phi_\chi\phi_N^\dagger\sigma^i\phi_N \to 4\vec{S}_\chi\cdot\vec{S}_N$ is spin dependent (SD).

Additional relevant 3-vectors can be constructed from the non-relativistic incoming and outgoing 3-momentum of both particles, $\vec{p}$ and $\vec{p}'$ respectively for χ and $\vec{k}$ and $\vec{k}'$ respectively for N. Figure 2.3 displays the kinematics of the elastic scattering interaction in the lab frame.

The transferred momentum $\vec{q}$ and relative velocity $\vec{v} \equiv \vec{v}_{\chi_{in}} - \vec{v}_{N_{in}}$ are both frame independent. However it is more useful to construct a frame independent term $\vec{v}^\perp$ that is perpendicular to $\vec{q}$ ($\vec{v}^\perp\cdot\vec{q} = 0$) so terms cancel more simply [69]. This is constructed

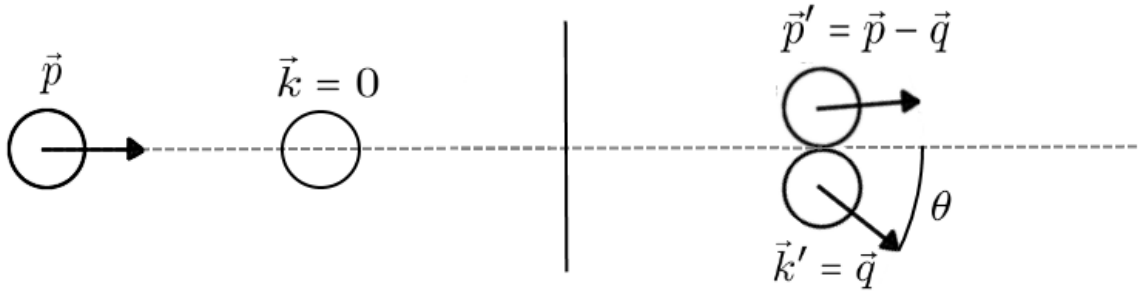


Figure 2.3: Non-relativistic DM particle and nucleon scattering in the lab frame with the momentum variables included.

in equation 2.11 below where $\mu_N = \frac{m_\chi m_N}{m_\chi + m_N}$ is the DM-nucleon reduced mass:

$$\vec{v}^{\perp} = \vec{v} + \frac{\vec{q}}{2\mu_N} = \frac{1}{2}(\vec{v}_{\chi_{in}} + \vec{v}_{\chi_{out}} - \vec{v}_{N_{in}} - \vec{v}_{N_{out}}) = \frac{1}{2}\left(\frac{\vec{p}}{m_\chi} + \frac{\vec{p}'}{m_\chi} - \frac{\vec{k}}{m_N} - \frac{\vec{k}'}{m_N}\right). \quad (2.11)$$

It is shown in [70] that $\frac{i\vec{q}}{m_N}$, $\vec{v}^{\perp}$, $\vec{S}_\chi$ and $\vec{S}_N$ are the only 3-vectors required to construct the Hermitian non-relativistic operators concerning the interaction Lagrangian equation 2.9 and all 8 are listed in table 2.1 [69]. There are higher order operators related to mediators with tensor interactors but these are not considered.

Table 2.1: Relativistic $\mathcal{L}_{int}$ terms reduced to non-relativistic operators (spin-0 and spin-1 only), including how they act under parity and time reversal (E=even, O=odd) and their order: corresponding to how many powers of $\vec{v}^{\perp}$ or $\frac{\vec{q}}{m_N}$ they contain [69].

$\mathcal{L}_{int}$	Non-Relativistic Reduction	P/T	Order
$\bar{\chi}\chi\bar{N}N$	$1_\chi 1_N$	E/E	LO
$i\bar{\chi}\chi\bar{N}\gamma^5 N$	$i\vec{S}_N \cdot \frac{\vec{q}}{m_N}$	O/O	NLO
$i\bar{\chi}\gamma^5\chi\bar{N}N$	$-i\vec{S}_\chi \cdot \frac{\vec{q}}{m_\chi}$	O/O	NLO
$\bar{\chi}\gamma^5\chi\bar{N}\gamma^5 N$	$-(\vec{S}_\chi \cdot \frac{\vec{q}}{m_\chi})(\vec{S}_N \cdot \frac{\vec{q}}{m_N})$	E/E	N^2LO
$\bar{\chi}\gamma_\mu\chi\bar{N}\gamma^\mu N$	$1_\chi 1_N$	E/E	LO
$\bar{\chi}\gamma_\mu\chi\bar{N}\gamma^\mu\gamma^5 N$	$-2\vec{S}_N \cdot \vec{v}^{\perp} + 2i\vec{S}_\chi \cdot (\vec{S}_N \times \frac{\vec{q}}{m_\chi})$	O/E	NLO
$\bar{\chi}\gamma_\mu\gamma^5\chi\bar{N}\gamma^\mu N$	$2\vec{S}_\chi \cdot \vec{v}^{\perp} + 2i\vec{S}_\chi \cdot (\vec{S}_N \times \frac{\vec{q}}{m_N})$	O/E	NLO
$\bar{\chi}\gamma_\mu\gamma^5\chi\bar{N}\gamma^\mu\gamma^5 N$	$-4\vec{S}_\chi \cdot \vec{S}_N$	E/E	LO

A target nucleus has atomic number Z and mass number A with mass $m_T = Am_N$ and DM-nucleus reduced mass μ_T. The operators in table 2.1 only consider χ interacting with a nucleon. When considering the interaction between χ and a nucleus for a SI (scalar or vector) interaction the contributions from both the protons and

neutrons need to be taken into account $[Zf_p + (A-Z)f_n]^2$ [68, 71]. Where f_p and f_n are the proton and neutron nucleon DM coupling coefficients, these are equivalent to the $C_{N=p,n}$ from equation 2.8. To be model independent f_p and f_n should be treated separately, their Wilson coefficients do not need to be the same, and BSM theories naturally arise which treat up quarks and down quarks differently. However as DM has not yet been directly observed they are often considered identical for simplicity. The cross sections for the SI χ-p (σ_p^{SI}) and χ-nucleus (σ_T^{SI}) interactions are related in equation 2.12 with the addition of a nuclear form factor $F(q)$, which in its bare form is a simple exponential however more complicated expressions are implemented [69].

$$\sigma_T^{\mathrm{SI}} = \frac{\mu_T^2}{\mu_N^2}\left[Z + (A-Z)\frac{f_n}{f_p}\right]^2 F^2(q)\sigma_p^{\mathrm{SI}}. \tag{2.12}$$

The spin dependent (SD) cross section is more complicated to generalise to a target nucleus. The relation requires the spin of the nucleus S_T and the average proton and neutron spins, $\langle S_p\rangle$ and $\langle S_n\rangle$ respectively. These are coupled with the axial vector proton and neutron nucleon DM coupling coefficients a_p and a_n respectively. Most of the nucleons contribute only slightly while the main contribution comes from a singular unpaired proton or neutron as demonstrated by the lack of Z or A terms in the relation:

$$\sigma_T^{\mathrm{SD}} = \frac{\mu_T^2}{\mu_N^2}\frac{4(S_T+1)}{3S_T}\left[\langle S_p\rangle + \langle S_n\rangle\frac{a_n}{a_p}\right]^2 \sigma_p^{\mathrm{SD}}. \tag{2.13}$$

Therefore σ_p^{SI} has a factor A^2 detection advantage over σ_p^{SD} as we use nuclei, not unpaired nucleons, for our detector targets.

2.2.2 The DM direct detection event rate

The kinematics of a lab frame collision demonstrated in figure 2.3 require $\vec{p}' = \vec{p} - \vec{q}$ and $\vec{k}' = \vec{q}$ with the target recoiling at angle θ from the initial DM particle's trajectory. Equation 2.14 conserves kinetic energy, which gives us an upper bound on the transferred momentum $\vec{q}_{max}^2 = 4\mu_T^2 v^2$ (generalised to a nucleus of mass m_T) [69]. v is

the relative velocity which is simply the DM velocity in the lab frame.

$$\frac{\vec{p}^2}{2m_\chi} = \frac{(\vec{p}-\vec{q})^2}{2m_\chi} + \frac{\vec{q}^2}{2m_T} \rightarrow \vec{v}\cdot\vec{q} = \frac{\vec{q}^2}{2\mu_T} \rightarrow \frac{|\vec{q}|^2}{4\mu_T^2|\vec{v}|^2} = \cos^2\theta = \frac{1}{2}(1+\cos 2\theta). \quad (2.14)$$

The differential cross section for such a scattering can be considered in terms of $\vec{q}$, nuclear recoil energy $E_R = \frac{\vec{q}^2}{2m_T}$ or $\cos 2\theta$. All approaches are equivalent, however E_R is most convenient for experimentalists as energy is what is measured. By combining the Galilean invariant amplitude ($\mathcal{M}$) and the nuclear response into one term labelled the transition probability ($P(v,\vec{q}^2)$) - dependent on both v and $\vec{q}^2$ - the differential cross section is [69]:

$$\frac{d\sigma}{dE_R} = \frac{m_T}{2\pi v^2} P(v,\vec{q}^2). \quad (2.15)$$

Equation 2.16 has converted the cross section into an expected event rate within a given detector (R_D) by considering the total number of target nuclei within said detector (N_T), the local density of DM ρ_χ, the DM mass and averaging over the local DM velocity distribution (represented by $\langle\ldots\rangle$) [69]. Values for the local DM density ρ_χ vary between 0.2 and 0.6 GeV cm^{-3}. ρ_χ does not affect the recoil spectra in any way, it simply linearly scales the overall flux, therefore interpreting limits with different values of ρ_χ is trivial and as such direct detection experiments by convention set $\rho_\chi = 0.3$ GeV cm^{-3} to simplify comparisons [72].

$$\frac{dR_D}{dE_R} = N_T \frac{\rho_\chi m_T}{2\pi m_\chi} \left\langle \frac{1}{v} P(v,\vec{q}^2) \right\rangle. \quad (2.16)$$

The velocity distribution of the DM halo is required to analyse this differential cross section. Although N-body simulations are progressing there remain large uncertainties due to the lack of direct observations. Therefore a simple Maxwell-Boltzmann distribution is taken as an adequate approximation and used throughout the direct

detection community [69]:

$$f_v(\vec{v}) = \frac{1}{\pi^{\frac{3}{2}} v_0^3} e^{-\frac{v^2}{v_0^2}}. \tag{2.17}$$

v_0 is the velocity dispersion of DM in the local galactic neighbourhood and is taken to be ~ 232 km s^{-1}, the same as in the previous XMASS modulation analysis [49,50]. Equation 2.18 integrates over said function alongside $P(v, \vec{q}^2)$, to do so three additional factors are important. The lower bound on the DM velocity, this is the minimum velocity required for an elastic scattering interaction ($v_{\min} = \frac{|q|}{2\mu_T}$). The upper bound on the dark matter velocity is taken to be the escape velocity of the milky way, 544 km/s is used, the same as in [49,50]; this is the most commonly used value among direct detection experiments. And the velocity of earth in the galactic rest frame ($\vec{v_e}$) [69]. Thus:

$$\left\langle \frac{1}{v} P(v, \vec{q}^2) \right\rangle = \int_{v_{\min}}^{v_{\max}} v^2 dv \int d^2\Omega f_v(\vec{v} + \vec{v_e}) \frac{1}{v} P(v, \vec{q}^2). \tag{2.18}$$

2.3 Annual modulation of the DM nuclear recoil event rate

The relative velocity between a DM particle χ and the target nuclei confined in a direct detection experiment is not only dependent on the velocity of DM particles in the solar system. The Earth orbits the Sun and hence the relative velocity needs to take both into account: $\vec{v} = \vec{v_0} + \vec{v_e}$. Velocity corrections from the Earth's daily rotation on its axis are minimal and hence not included. The mean orbital velocity of the earth around the sun is $\frac{2\pi \times 1 \text{ AU}}{1 \text{ year}} = 29.8$ km/s, where 1 AU $= 1.496 \times 10^8$ km and 1 year $= 3.16 \times 10^7$ s.

However the orbital ellipse that the earth traverses is at a 60 degree angle with $\vec{v_0}$. This halves the absolute effect that the orbital velocity has on the relative velocity between DM particles and the earth. The relative velocity can be written as an average velocity ($|\vec{v_0}|$ km/s) with a sinusoidal function superimposed on top with

amplitude $|\vec{v_e}| = 15$ km/s, period $T = 1$ year and a maximal phase t_0 that occurs in June, 152.5 days from the start of the year:

$$|v| = |\vec{v_0}| + |\vec{v_e}| \cos\left(\frac{t - t_0}{T}\right). \tag{2.19}$$

As discussed above the expected event rates vary as a function of m_χ and $|v|$. Without the effect of the Earth orbiting the sun the expected differential event rate ($C_0(E_R)$) would have an energy spectrum dependent on the particular theory in question and m_χ, however it would be a constant over time. This annual orbit changes $|v|$ and makes the event rate time dependent. However to first order the induced time corrections to the event rate can be collected into a single sinusoidal term with the same period and phase as $|v|$ with the amplitude of said annual modulation in the event rate $A_{\text{annual}}(E_R)$ considered time independent. The expected differential event rate can be represented as:

$$\frac{dR_D}{dE_R} = C_0(E_R) + A_{\text{annual}}(E_R) \cos\left(\frac{t - t_0}{T}\right). \tag{2.20}$$

The nuclear recoil energy spectra between WIMP DM and Xe nuclei with a SI proton cross section $\sigma_p^{SI} = 1$ pb in 1kg of LXe were calculated for a range of WIMP masses when the first XMASS modulation analysis was conducted [73,74]. These were calculated for the average relative velocity $|\vec{v_0}|$, maximum relative velocity ($|\vec{v_{max}}| = |\vec{v_0}| + |\vec{v_e}|$) and minimum relative velocity ($|\vec{v_{min}}| = |\vec{v_0}| - |\vec{v_e}|$). In chapter 7 the nuclear recoil energy spectra using $|\vec{v_0}|$ are shown in figure 7.1 with the residual spectra shown in figure 7.2 being the difference between the nuclear recoil spectra calculated using $|\vec{v_{max}}|$ and $|\vec{v_{min}}|$. These are displayed in chapter 7 for easier referral because that is where they are explicitly used to generate the theoretically expected $C_0(E_R)$ and $A_{\text{annual}}(E_R)$ spectra within XMASS. This is hard to discuss in detail here as it requires applying cuts developed in chapter 5, which are based on the backgrounds and detector characteristics outlined in chapter 3.

The backgrounds present in the detector materials can emit α-rays, β-rays or

γ-rays which can induce the production of scintillation photons within the LXe contained within XMASS and are recorded as events. Scintillation light emission is isotropic, so that the light recorded by the individual PMTs in the detector - the so-called hit pattern - and timing characteristics depend on the event location and the nature of the recoiling particle as well as its energy. Event classification is discussed in chapter refchap:EventClassification.

In addition to the nuclear recoil based WIMP search conducted in this thesis a model independent search is undertaken where the measured event rates are used to obtain modulation amplitudes that are then compared directly against those measured by DAMA/LIBRA [45]. If the observed annual modulation of the event rate is caused by DM that doesn't specifically - for some unknown reason - interact strongly with NaI crystals and not Xe, the observed event rate amplitude by DAMA/LIBRA should also be observed by XMASS.

Chapter 3

The XMASS Experiment

The analyses conducted in this thesis - outlined in the following chapters - utilise the full dataset recorded by the direct detection experiment XMASS. XMASS is a single-phase liquid Xenon (LXe) detector located in Japan under the mountain Ikenoyama at a water equivalent depth of 2700m; depths of multiple deep underground laboratories are displayed in figure 3.1. XMASS is a multipurpose detector and as such its name stands for multiple things: "Xenon neutrino MASS detector", "Xenon MASSive detector for solar neutrino" and finally "Xenon detector for weakly interactive MASSive particles". XMASS was initially envisaged as a multistage project, its first iteration XMASS-I housing ~ 1 ton of LXe with a 100kg fiducial volume (FV), XMASS-I.5 (~ 5 ton, 1 ton FV) and culminating in XMASS-II (~ 25 ton, 10 ton FV). XMASS-I and XMASS-I.5 would be housed in the same water tank outer detector and use the same experimental setup, hence the nomenclature. The XMASS-I experiment was constructed in 2010 and took commissioning data up until 2012. The detector was then refurbished to mitigate the impact of its main source of radioactive background and XMASS-RFB began data taking in November 2013 and concluded in February 2019 after achieving more than 5 years of data taking; the longest for any noble liquid based detector to date. As XMASS was decommissioned and no further iterations are anticipated, from here on out the experiment and the detector will simply be referred to as the XMASS. This chapter explains the experimental setup of the XMASS detector and the relevant information necessary for said analyses.

Section 3.1 outlines why Xe is a good SM target candidate for a direct detection experiment, listing its base properties and outlining its scintillation mechanisms. Section 3.2 details the experimental setup, data acquisition and MC simulation. Section 3.3 explains the different types of calibration undertaken to better understand the internal conditions and detector response. And finally section 3.4 discusses the backgrounds observed within XMASS, both external and internal.

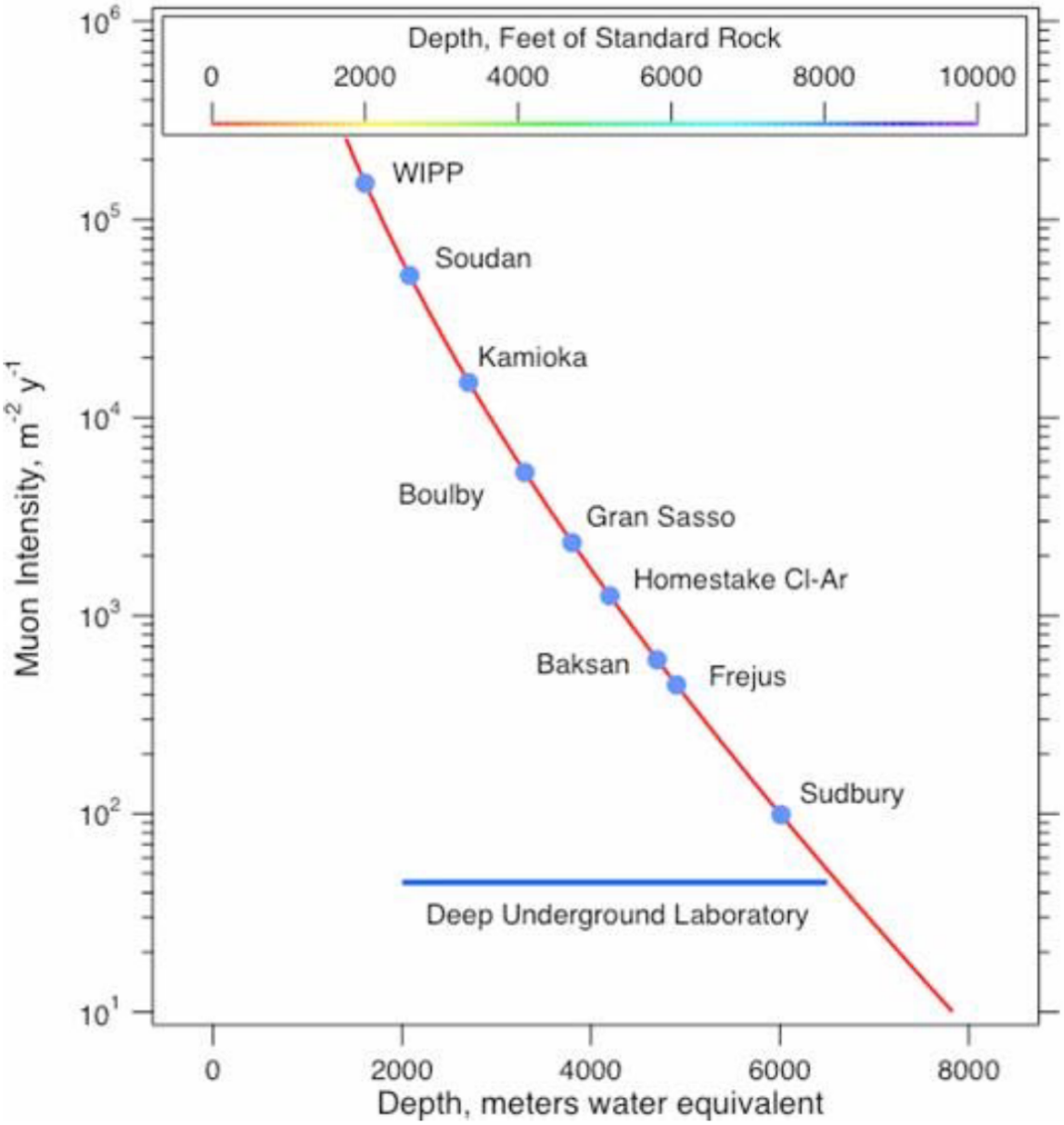


Figure 3.1: Depth of multiple deep underground laboratories (DUL) and their respective muon intensity [75], XMASS resides in the Kamioka DUL.

3.1 Liquid xenon

As discussed in section 1.3.3 many DM direct detection experiments use LXe as the target matter. Its base properties and radioactive Isotopes outlined in sections 3.1.1 and 3.1.2 respectively indicate why this is the case. The following subsections detail how it performs in practise, its scintillation mechanisms, scintillation yield efficiency and optical properties are explained in sections 3.1.3, 3.1.4 and 3.1.5 respectively.

3.1.1 Xe base properties

Xe's base elemental properties are listed below.

- **A noble element:** Xe is a noble element with complete shells of electrons ($5s^2 4d^{10} 5p^6$), as such it is chemically inert, which allows for the efficient removal of chemically reactive contaminants. Therefore the chemical makeup of the target material won't change over time, which is advantageous for long-run experiments requiring it to be held in situ for extended periods of time.

- **Large mass number:** Xe has an atomic number (Z) of 54 with several stable isotopes resulting in an average mass number (A) of 131.29 ($^{131.29}_{54}$Xe). As outlined in section 2.2.1 the spin-independent (SI) WIMP-nucleus cross section is $\sigma_T^{\mathrm{SI}} = \frac{\mu_T^2}{\mu_N^2}\left[Z + (A-Z)\frac{f_n}{f_p}\right]^2 F^2(q)\sigma_p^{\mathrm{SI}}$. If one assumes the contributions from both the protons (f_p) and neutrons (f_n) to be equal, the sensitivity increases for $\sigma_p^{\mathrm{SI}} \propto A^2$ - ignoring the contribution from the nuclear form factor $F(q)$.

- **Large density:** In the liquid phase Xe has a density of ~ 2.98 g/cm^3 [76], which has two benefits. Firstly, a more compact detector and secondly, self-shielding against external photons. Figure 3.2 displays how Xe interacts strongly with electromagnetic radiation resulting in the rapid attenuation of low energy γ-rays within relatively short distances (~ 5.7 cm for a 1MeV γ) [74, 77]. This reduces background radiation emanating from the detector's inner surface materials from entering a central fiducial volume.

- **Cryogenic liquid:** Xe is relatively easily contained as a liquid, at 1 atm Xe melts at 161.4 K and boils at 165.1 K [76]. This simplifies the required distillation and purification processes and makes the detector size highly scalable.

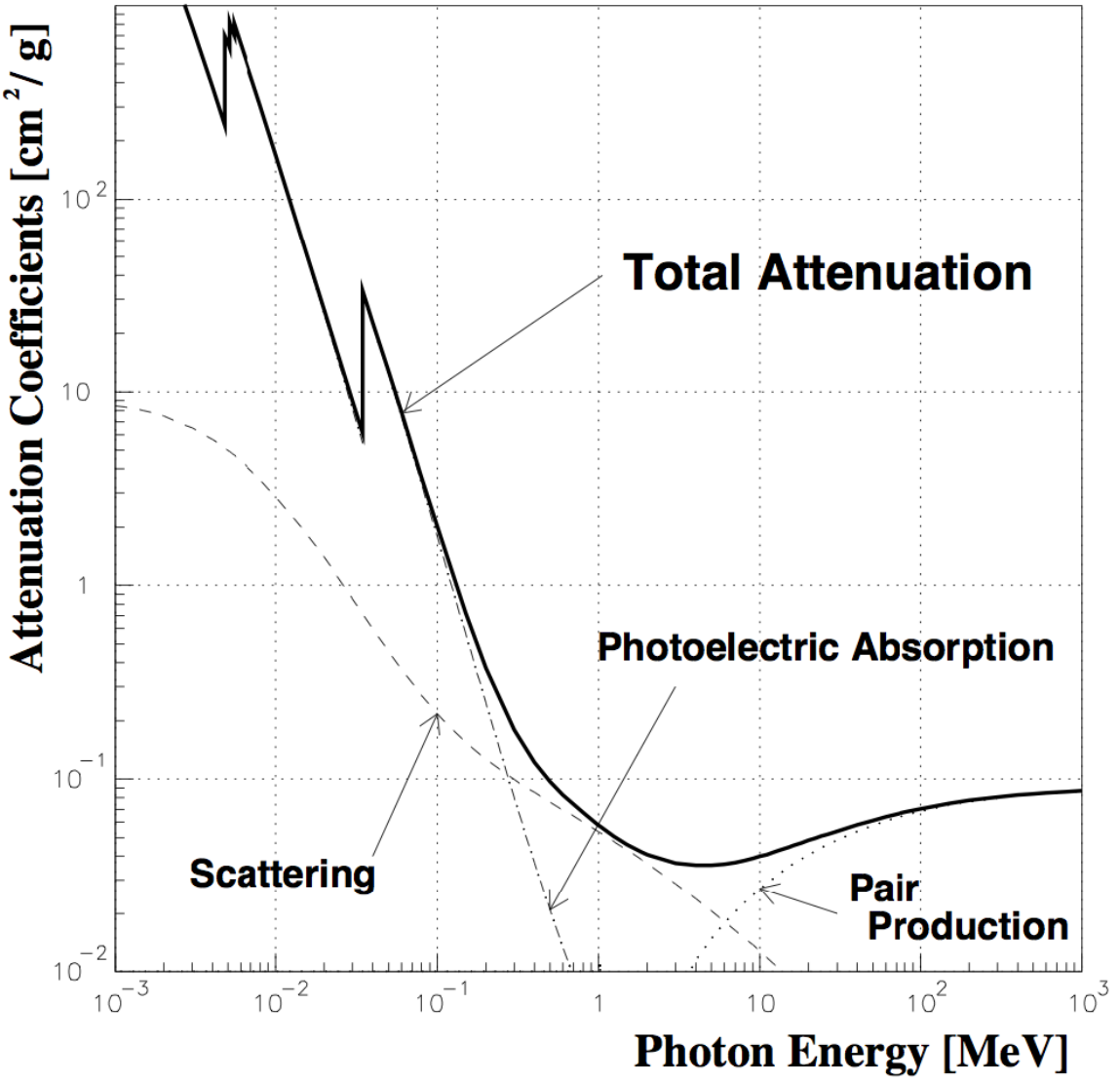


Figure 3.2: Attenuation coefficient of xenon for γ-rays [77] with the multiple contributing effects and the combined total.

3.1.2 Xe isotopes

All of the non-synthetic isotopes of Xe are listed in table 3.1 [74, 76]. Xenon is comprised of stable isotopes except for 2 ultra-long lived RIs (^{124}Xe and ^{136}Xe) which

have half-lives ($t_{0.5}$) roughly the lifetime of the universe (t_{universe}) making it an ideal candidate to probe for ultra-rare interactions. ^{136}Xe has a relatively large abundance (8.87 %), undergoes double-beta decay [78] and is an important isotope for testing neutrinoless double-beta decay. Experiments like EXO and NEXT search for this but also DM experiments like LZ, XENONnT and PandaX-II [79]. Two of the isotopes (^{129}Xe and ^{131}Xe) have non-zero spin owing to single unpaired neutrons (n). This allows the spin dependent (SD) cross section (σ_n^{SD}) to be evaluated using ~ half the total Xe.

Table 3.1: Isotopes of Xenon (synthetic isotopes not listed), values taken from [74, 76]. ^{136}Xe is an important neutrinoless double-beta decay candidate.

Isotope	Abundance (%)	Half Life ($t_{0.5}$)	Spin	Decay mode
^{124}Xe	0.096	1.8×10^{22} yrs	0	double e^- capture
^{126}Xe	0.090	stable	0	n.a.
^{128}Xe	1.92	stable	0	n.a.
^{129}Xe	26.44	stable	1/2 (unpaired n)	n.a.
^{130}Xe	4.08	stable	0	n.a.
^{131}Xe	21.18	stable	1/2 (unpaired n)	n.a.
^{132}Xe	26.89	stable	0	n.a.
^{134}Xe	10.44	stable	0	n.a.
^{136}Xe	8.87	2.165×10^{21} yrs	0	$\beta^-\beta^-$

Some direct detection experiments use Argon (Ar) as their target material. Ar is cheaper in its raw form, however it has a smaller A and a long lived radioactive isotope (RI) $^{39}_{18}$Ar with $t_{0.5}$ = 269 years which is problematic. Deep mine reserves do exist where the Argon has had the time necessary for this RI to become depleted, unfortunately this useful form of Argon is rarer and hence more expensive.

3.1.3 LXe scintillation mechanism

LXe is a scintillator that emits scintillation light via two processes: direct excitation and ionisation and recombination outlined below [80, 81]. The scintillation light Xe produces has a peak wavelength λ_{Scint} ~ 175 nm [76] which can be observed by appropriately selected photomultiplier tubes (PMTs). Xe has a large scintillation yield, which is evaluated to be ~ 96 photons/keV within XMASS. Scintillation photons

are the only signal XMASS can measure but due to the high quantum efficiency of its PMTs it measures an observed light yield of 14.5 – 16.2 photons/keV allowing sub-keV energies to be probed.

1. **Direct excitation:** Where a Xe atom is excited into a metastable state Xe^*, forms an excited dimer with another Xe atom, which then de-excites emitting scintillation light:
$$\begin{aligned} Xe^* + Xe &\rightarrow Xe_2^*, \\ Xe_2^* &\rightarrow 2Xe + \gamma. \end{aligned} \tag{3.1}$$

2. **Ionisation and recombination:** Where a Xe atom gets ionised (Xe^+), combines with another Xe atom to that then captures an electron and splits, leaving one of its constituents in its second excited state Xe^{**}. This de-excites into Xe^* releasing the energy as heat and then follows the same procedure as above to return to its ground state and emit scintillation light:
$$\begin{aligned} Xe^+ + Xe &\rightarrow Xe_2^+, \\ Xe_2^+ + e^- &\rightarrow Xe^{**} + Xe, \\ Xe^{**} &\rightarrow Xe^* + \text{heat}, \\ Xe^* + Xe &\rightarrow Xe_2^*, \\ Xe_2^* &\rightarrow 2Xe + \gamma. \end{aligned} \tag{3.2}$$

The excited dimer (Xe_2^*) that releases the scintillation photons has both a singlet and a triplet state, each with their own decay constant and branching fraction (τ_S, F_S) and (τ_T, F_T) respectively, where $F_S + F_T = 1$. $\tau_S \sim 2 - 4$ ns and $\tau_T \sim 20$ ns [80, 81], the component fractions depend on the incident particle and its energy. The recombination process on the other hand takes even longer as there are more initial steps and ions must find free electrons.

Figure 3.3 [80] demonstrates the scintillation emission spectra measured for different incident particles with their fitted decay constants noted alongside. β-rays (and γ-rays) predominantly ionise the Xe atoms (Xe^+) resulting in a large singular

decay constant as recombination dominates. XMASS observed a scintillation emission decay constant ~ 45 ns [82], which is very similar to that quoted in the figure. Neutrons can't ionise, they can only scatter on a Xe nucleus producing a nuclear recoil, hence the emission profile displays both short and long decay constants. Values measured for nuclear recoil events at XMASS are $\tau_S = 4.3 \pm 0.6$ ns, $\tau_T = 26.9^{+0.7}_{-1.1}$ ns and $F_S = 0.252^{+0.027}_{-0.019}$ [83], the singlet decay time is very similar to that quoted in the plot however the singlet/triplet fraction is smaller and the triplet decay time is longer. Time delays (> 30 ns) introduced by recombination processes where not incorporated into the fit as they occur < 10% of the time. The previous modulation analysis [49,50] simulated nuclear recoil events - to construct WIMP spectra - using a nuclear recoil long decay constant of DC = 27.5 ± 2 ns. The analyses presented in this thesis build on the previous work and use the same value. The work on the previous XMASS modulation analysis began before the values in [83] were finalised, to compensate for this a more conservative error of 2 ns was implemented.

Direct excitation scintillation emission is not influenced by impurities present in the LXe or free electrons and hence shouldn't vary over time. However for the recombination scintillation mechanism to work Xe ions must find free electrons. Xe has full shells of electrons and hence the free electrons likely originate more often than not from said impurities within the LXe. Therefore the fewer impurities present the longer the recombination process could take increasing that processes decay constant. However the extent of such decay time changing effects are unknown and are not considered within XMASS. The LXe absorption length is highly dependent on the level of impurities, this is measured by XMASS and varies over time as reported in section 3.1.5.

XMASS also studied scintillation-only pulse shape discrimination [82] (PSD) by comparing the ratio of early (0 – 20 ns) to total (0 – 200 ns) scintillation light emission to reduce electron recoil events while retaining nuclear recoil events. This PSD is not incorporated in my analyses. Scintillation emission in liquid argon (LAr) is emitted from an excited dimer similarly to that of LXe, here the singlet component is only ~ 6

ns though, while the triplet component is ~ 1500 ns and can thus mostly be discounted as such scintillation photons will be detected individually over an extended period. There is an additional intermediate component in Ar with 30 – 100 ns decay time that was reported by some experiments [84]. Specific pulse shape timing characteristics sufficient to discriminate between ER and NR are thus available in LAr [85].

3.1.4 LXe relative scintillation yield efficiency

Scintillation efficiency is the proportion of the deposited energy that gets converted into scintillation photons. This varies greatly based on both the deposited energy and on the particle causing this deposition.

α-rays have a greater scintillation efficiency when compared to γ-rays because of their higher density of ionisation. Nuclear recoils; similar to α-rays have a high density of ionisation, however they interact with multiple Xe nuclei with a smaller energy-momentum transfer producing excess heat; reducing the remaining energy, resulting in fewer scintillation photons and a worse scintillation efficiency than both α-rays and γ-rays.

The 122 keV γ-ray ^{57}Co calibration source is both well understood and in widespread use amongst many low energy threshold physics experiments. This makes it the ideal point of reference when comparing energies and scintillation yields. Hence, the nuclear recoil scintillation efficiency (L_{Eff}) is often taken from the literature and most commonly expressed as the ratio:

$$L_{Eff} = \frac{\text{Scintillation yield induced by nuclear recoil}}{\text{Scintillation yield induced by } \gamma\text{-rays at 122 keV}}. \tag{3.3}$$

Measurements of L_{Eff} above 3 keV$_{nr}$ from multiple collaborations are consolidated in figure 3.4, the central value and the ± 1 and 2 σ bands are shown using the red line and 2 purple bands respectively, values below 3 keV$_{nr}$ are extrapolated from higher energy measurements [86]. The first modulation analysis [73, 74] used these L_{Eff} values. Figure 3.5 shows the result of a more recent study by the LUX group which includes measurements below 3 keV$_{nr}$ [87]. The previous modulation analysis

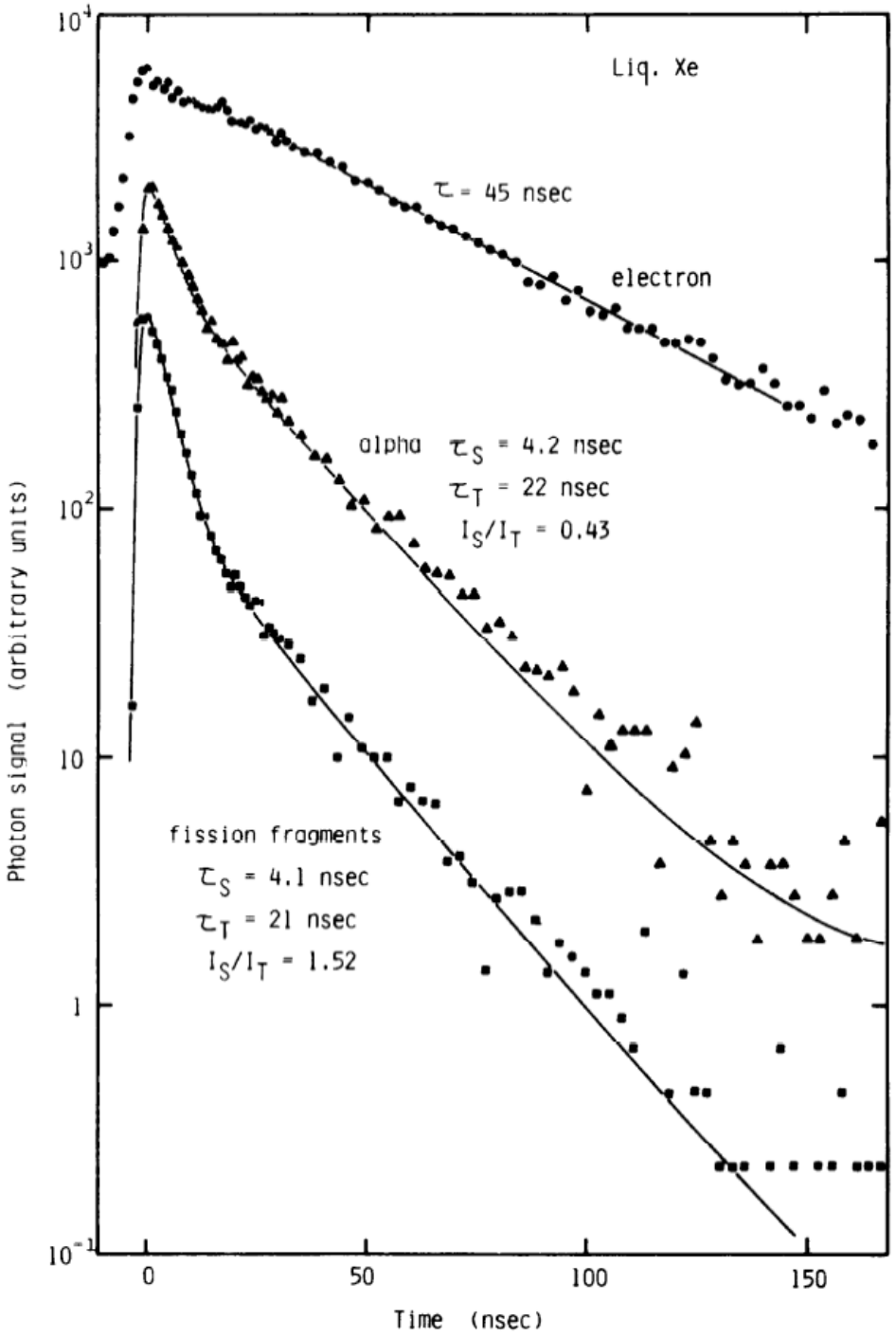


Figure 3.3: LXe scintillation decay time constants and ratios for different incident particles: electrons, alphas and fission fragments (nuclear recoil) [80].

[49,50] additionally implemented these L_{Eff} values for energies < 3 keV_{nr}, the analyses presented in this thesis use the same L_{Eff} values.

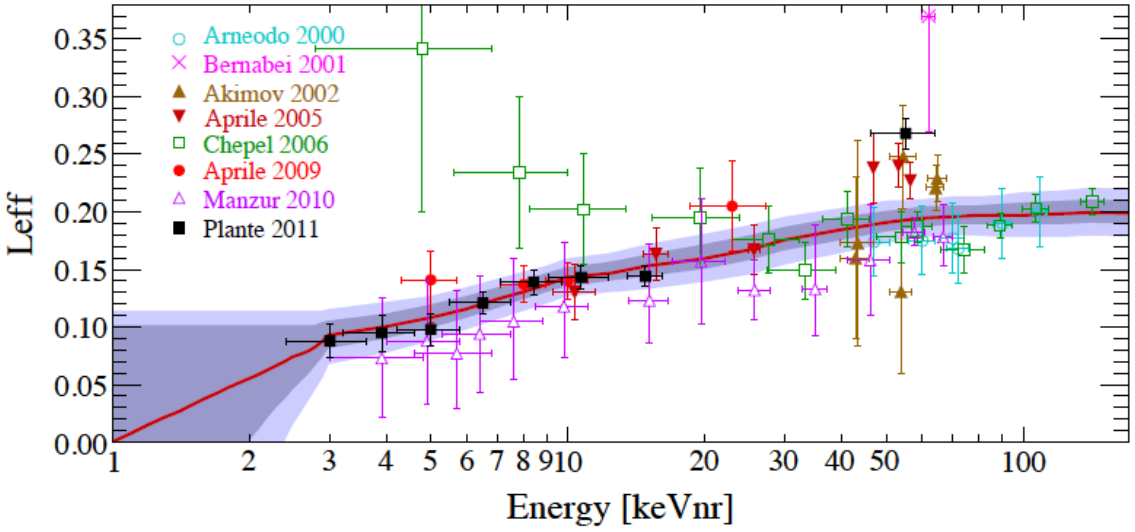


Figure 3.4: L_{Eff} measurements consolidated from multiple collaborations above 3 keV_{nr}. The Red line is the central fit and the dark and light purple regions represent the ± 1 σ and ± 2 σ bands, respectively [86].

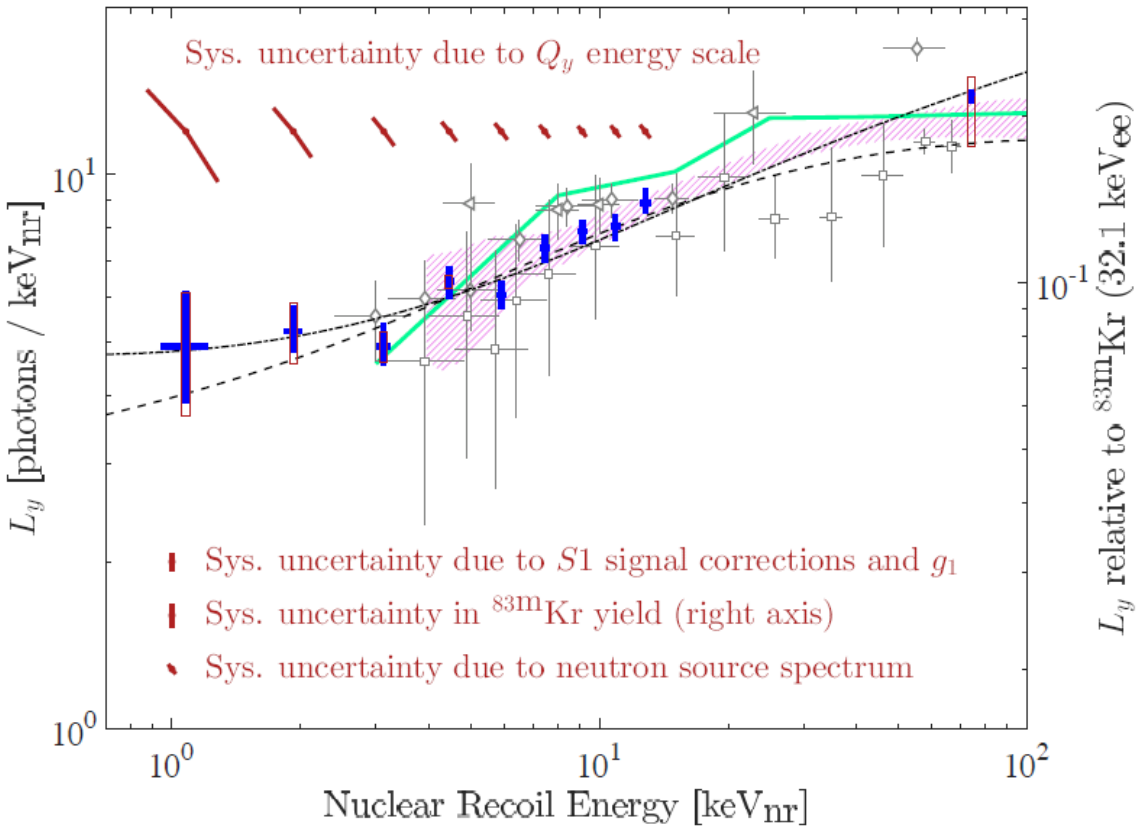


Figure 3.5: LUX collaboration's measurements of L_{Eff} including points < 3 keVnr [87]. Blue points are obtained using a DD generator to produce a mono-energetic neutron beam.

Most of the experiments that measured the L_{Eff} values present in figures 3.4 and 3.5 apply an electric field under normal detector operation. However their definitions of L_{Eff} separate out the effects the electric field has on scintillation efficiency into distinct additional factors. Therefore the extracted L_{Eff} function is equally applicable to detectors that apply electric fields and those that don't.

3.1.5 LXe optical properties

When scintillation photons are emitted they have to traverse the LXe before they can potentially induce a photoelectron (PE) in a PMT and register a signal. Three main optical properties dictate how the scintillation photon's path is affected, these are heavily influenced by the Xe purity, which is discussed in section 3.2.3 and generally improves over time. Scintillation photons can be absorbed by the impurities in the LXe, the probability that the scintillation photons have not been absorbed is $P = e^{-\frac{l}{l_A}}$, where l is the distance the scintillation photon has travelled and l_A is the absorption length. Scintillation photons can also Rayleigh scatter within the LXe changing their direction of travel. The angular (θ) distribution of said scattering is $\propto 1 + \cos^2(\theta)$, peaked both forward and back. The scattering length (l_S) is defined in the same way as l_A. Scintillation photons can also change direction if reflected off of the inner detector's inner surface. In XMASS reflection off the inner surface is considered purely specular with a reflectivity of 25% and all inner surfaces are considered flat.

The LXe's optical properties at the Xe scintillation wavelength is measured indirectly by comparing inner calibration data with MC simulation, outlined in section 3.3.2. The optical properties obtained by this method are displayed over time in figure 3.6. l_A ranges from 4 m at the start of XMASS data taking to ~ 30 m by the end and l_S varies between 52 cm - 53.5 cm. The optical photon yield within XMASS is found to be ~ 96 photons/keV, however the observed number of photons is significantly less because of scintillation photon absorption, reflectivity and the fact that photocathode coverage is only 62%. The resultant observed light yield (LY) initially fluctuates between 14.6 PE/keV and 15.8 PE/keV but eventually settles ~ 16 PE/keV. The

conditions that led to the specific shape of the l_A and LY curves displayed in 3.6 are outlined in section 3.2.3. The previous modulation analysis used equation 3.4 [50] to convert between LY and l_A and so do the analyses presented in this thesis.

$$\mathrm{LY} = 16.42 - \frac{764.39}{l_A/cm}. \tag{3.4}$$

Chapter 4 outlines an attempted new form of calibration, the aim of which was to cross-check these parameters by using a completely different type of event where the effects of scattering and reflection can be disentangled due to the event's geometry.

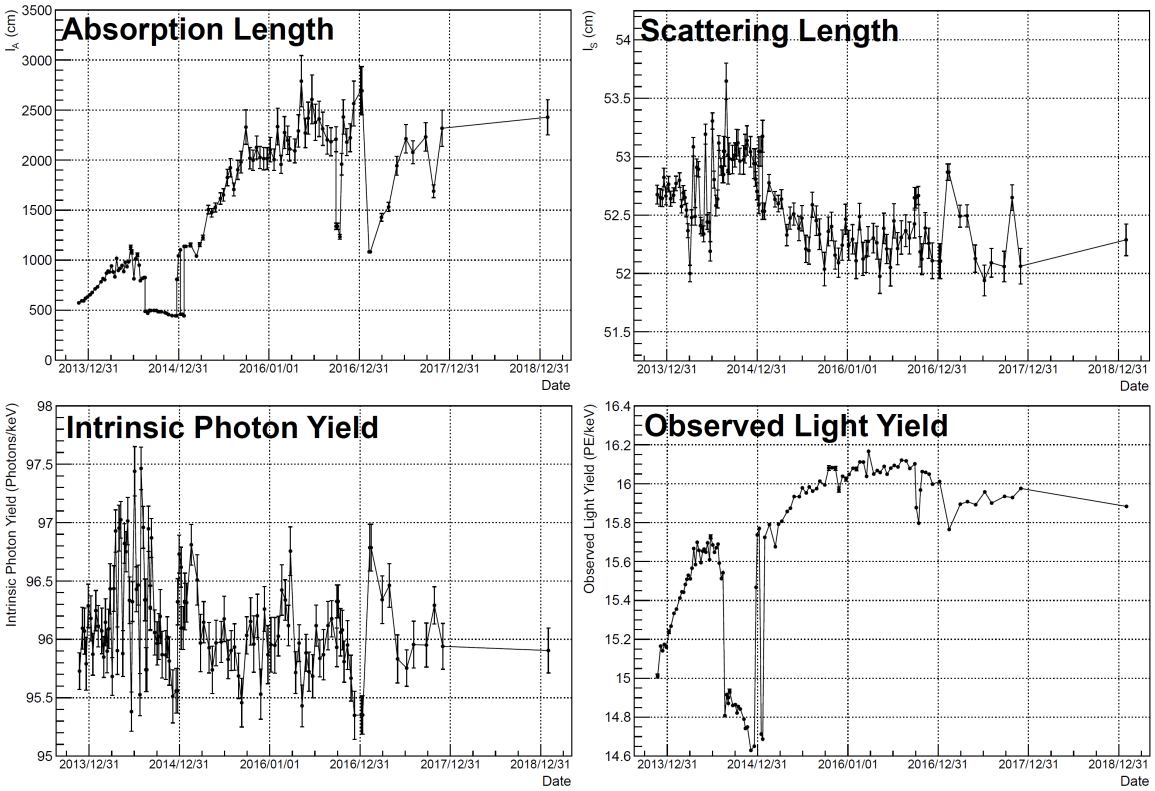


Figure 3.6: The optical parameters of the XMASS Detector obtained by minimising a chi squared comparison of calibration ^{57}Co data and MC simulated data. The variation/dips in l_A and LY over time is explained by impurities and detector operational changes.

3.2 The XMASS detector

The previous section outlined why most direct detection experiments use LXe as a target material and its properties that affect detector performance and design. All

of the data used in this thesis was recorded with the XMASS detector, this section outlines the detector's design as it is important to understanding the data.

Figure 1.5 displays a schematic view of the XMASS detector. The central vessel is where the Inner detector (ID) is located, this is outlined in sections 3.2.1. The water tank and the 20-inch PMTs form the outer detector (OD), which is detailed in section 3.2.2. The electronics hut located on top of the water tank houses the data acquisition (DAQ) system, how this works is explained in section 3.2.4. The Monte Carlo (MC) simulation of the XMASS detector is described in section 3.2.5.

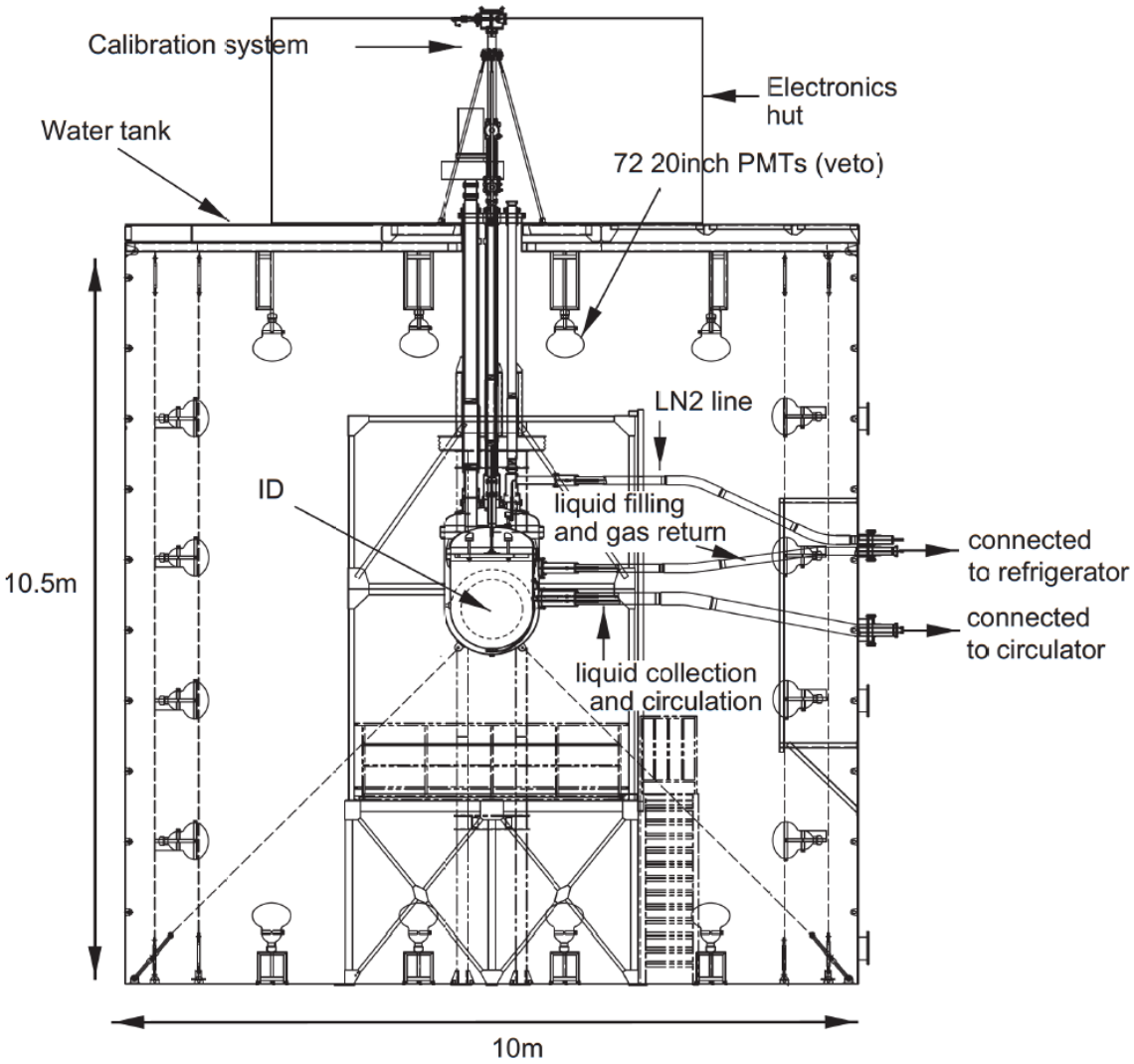


Figure 3.7: XMASS detector schematic [88]. A 10.5 m × 10 m water tank and 72 20 inch PMTs make up the outer detector, the inner detector is located at the centre of the water tank while the calibration system and electronics hut is located on top.

3.2.1 The inner detector

An outer vacuum chamber (OVC) and an inner vacuum chamber (IVC) form the Oxygen-free high conductivity (OFHC) Cu vessel that insulates the 1.114 tons of LXe and the ID contained within. The ID consists of a OFHC Cu PMT holder with a pentakis-dodecahedron structure that has an average radius of ~ 40 cm. This structure holds in place 642 inward facing 2 inch PMTs (630 Hexagonal Hamamatsu R10789-11 and 12 Round Hamamatsu R10789-11MOD) that are closely packed to achieve a photo-cathode coverage of 62% as displayed in figure 3.8. The PMTs and the structure's OFHC Cu surround 832 kg[1] of LXe present within this active volume and they have a quantum efficiency of more than 28% at the scintillation wavelength of liquid xenon (~175 nm) [88]. Embedded into the holder surface alongside the PMTs are 8 blue LEDs used for waveform gain and PE calibration discussed in section 3.3.1 and utilised in section 6.1.2.

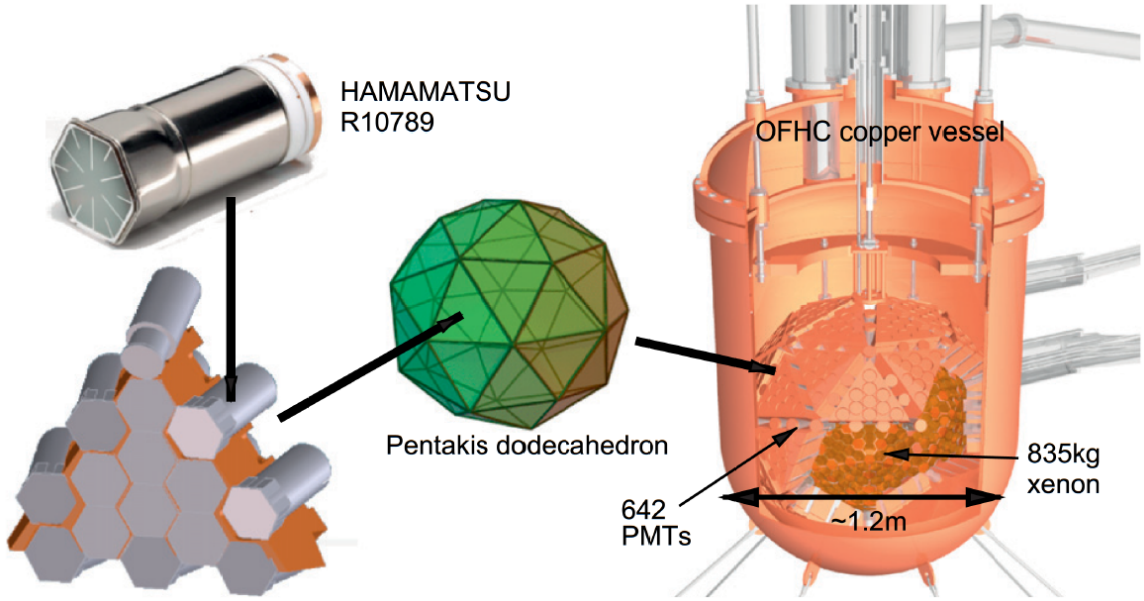


Figure 3.8: XMASS inner detector: OFHC Cu vessel and the OFHC Cu PMT holder with a pentakis-dodecahedron structure which houses 642 Hamamatsu PMTs [88].

[1]There was previously 835kg of LXe present in the active volume before the inner surface of the ID was refurbished using OFHC Cu plates to cover the Al-seal located at the PMT photo-cathode edges, which was a major source of background and is discussed further in section 3.4.2.

3.2.2 The outer detector

The OD is a stainless steel cylindrical water tank with a height of 10.5 m and a diameter of 10 m. The OFHC Cu vessel is located at the centre of this configuration surrounded by more than 4 m of purified water in every direction which acts as a passive shield from neutrons and γ-rays for the ID. The 72 HAMAMATSU R3600 20inch PMTs detect Cherenkov light emitted in the water, thus providing an active veto against cosmic-ray muons.

3.2.3 Distillation, circulation and purification

Commercial Xe contains Kr, and unfortunately ^{85}Kr has a half-life of 10.76 years and thus becomes a source of target intrinsic background (BG) if not removed. The 1.2 tons of Xe acquired for use in the XMASS detector had a Kr/Xe content of 340 ppb and with the natural ^{85}Kr/Kr ratio of $(0.6 \pm 0.2) \times 10^{-11}$. The distillation tower employed is 2915 mm long with a diameter of 40 mm. Xe was processed at a flow rate of 4.7 kg/h with all the Xe processed in 10 days. The system was 99% efficient at collecting purified Xe and a krypton contamination upper limit of 2.7 ppt was achieved [88].

The XMASS detector's xenon circulation and purification system flow map is displayed in figure 3.9. The LXe was stored in a 700 L reservoir tank before filling the ID. Vacuum insulation and a 200 W pulse tube refrigerator (PTR) (PC105U, IWATANI) liquefied the Xe before it entered the detector with < 50 W of heat leakage. A 300 W rod heater helped evaporate the LXe in the reservoir tank and the gaseous Xe was subsequently passed through and purified by 2 getters (PS4-MT15, SAES), connected in series with a 30 L/min flow rate. The first getter operates at high temperatures and the second at room temperature to better remove hydrogen impurities. A frost point meter (FPM) measured < 0.09 ppb water in the Xe before it was liquefied at the PTR's cold finger [88].

Xe was liquefied by two PTRs and the ID was filled with LXe over the course of

5 days. After filling, the LXe was then returned back to the reservoir tank in 3 hours at a flow rate of 2 L/min. The ID was emptied and refilled 2 more times increasing the observed LY by ~ 16% compared to the first filling. The concentration of ^{222}Rn and ^{220}Rn was measured to be 8.2 ± 0.5 mBq and < 0.28 mBq respectively [88].

Evaporated Xe from above the LXe surface in the ID passes through a different getter before it gets liquefied by one of the PTRs and delivered back into the ID. Only 35 W of cooling power is required to compensate for the ID's heat leakage. After 8 months of use, the other PTR was used to cool the LXe with the first PTR warming up; this coincided with a sharp decrease in the observed LY with a coincidentally decreasing l_A as displayed in figure 3.6. This was understood to be precipitated by impurities frozen out at the previously used PTR's cold finger - released while warming up - and transported into the target volume along with the newly liquefied Xe evaporate. XMASS rectified the problem by emptying the LXe held in the ID back into the 700 L reservoir tank, then heating up the cold fingers to bake them out at ~ 30 $°C$. When refilling the ID the Xe evaporated from the 700L reservoir was again passed through a high temperature getter before reaching the PTR's cold finger to be liquefied again. A sharp increase in both the LY and l_A occurred, returning to similar values measured just before the refrigerator swap. Over time the impurities were removed - similarly to before the initial refrigerator swap - which resulted in the observed LY and l_A increasing and eventually stabilising. The other drop in LY at the end of 2016 coincided with a change in the xenon gas flow and the drop in LY at the start of 2017 occurred after the LXe had been removed to be distilled again to if the procedure would reduce the levels of Ar and Kr present. Ar is one of main BGs in the FV energy spectrum (> 30 keV).

Dual-phase LXe detectors apply an electric field to drift electrons and extract the ionisation signal of an event after first recording the interactions scintillation signal. The drifting electrons can attach to impurities, which would remove them from the bunch of fast drifting "free electrons on their way to being recorded as the ionisation signal. To maximise the observed ionisation signal, the electron absorption length

needs to be maximised by minimising the presence of said impurities. In single-phase detectors with no applied electric field this is a not an issue. All we require is a large LY to maximise the only recorded immediate scintillation signal. The level and type of impurities in XMASS are not measured during normal run conditions. The impurities present affect the LY and l_A, parameters that are tracked in fortnightly calibrations and are accounted for in every XMASS analysis. As in the analyses presented in this thesis, LY and l_A are used to normalise the recorded event rates as outlined in chapter 8 and the MC simulated signal event rates in chapter 7.

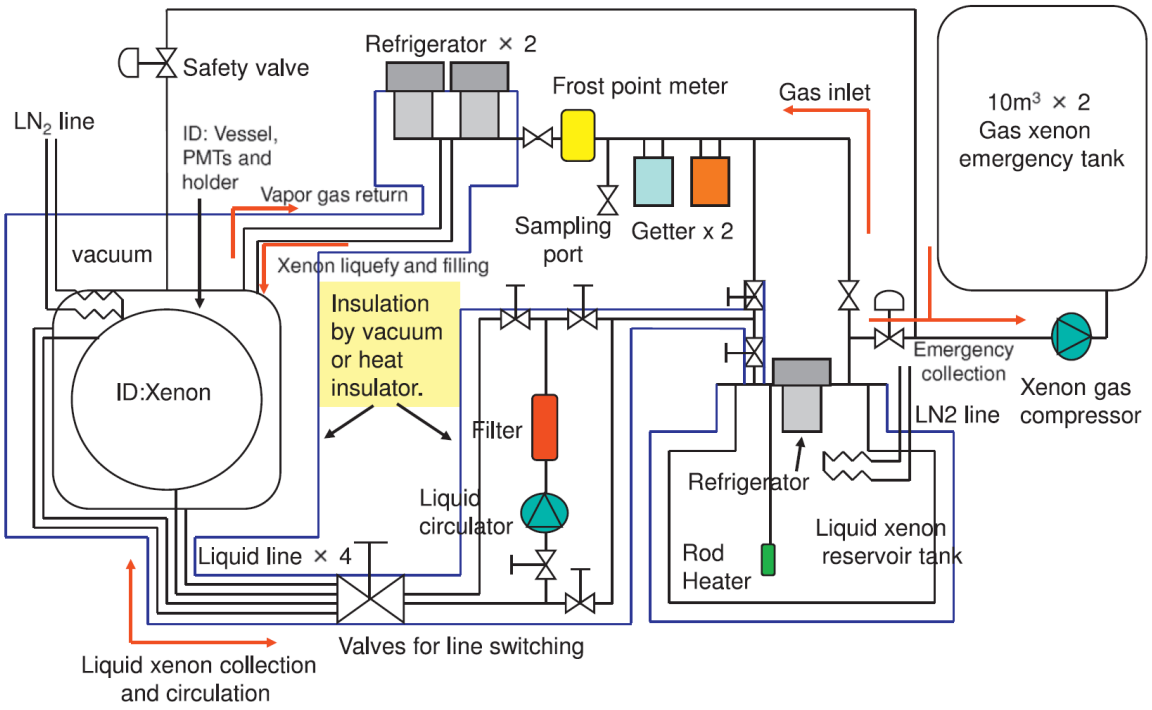


Figure 3.9: XMASS detector's Xe circulation and purification system flow map [88].

3.2.4 Data acquisition and PMT response

This section outlines how PMTs register a signal, how events are triggered upon and what data is extracted and recorded for further analysis.

When a scintillation photon strikes a PMT's photo-cathode, it can be reflected, absorbed or register a signal. The PMTs have a quantum efficiency of 28% (at ~ 175 nm) which is a great achievement but still means that many scintillation photons do

not register signals. If a scintillation photon registers a signal it is usually because a single photoelectron (PE) was produced at the PMTs photo-cathode, however the energy of 175 nm photons is large enough that 10% of the time two PEs are produced. The electric field within the PMT guides these PEs towards the first and subsequent dynodes where on each dynode a single incoming electron produces ~ 10 secondary electrons. This process continues over all the dynodes, amplifying the photoelectron signal. The random nature of this process means a single induced PE will not be amplified by the same amount each time, a measurement of 1 NPEs (number of PEs) corresponds to the average signal induced by a single PE. The probability distribution function of the measured signals' NPEs is displayed in figure 3.10. The second peak at 2 NPEs is because 10% of the time two PEs are produced at the photo-cathode - 175 nm Xe scintillation photons have enough energy to liberate more than one photon.

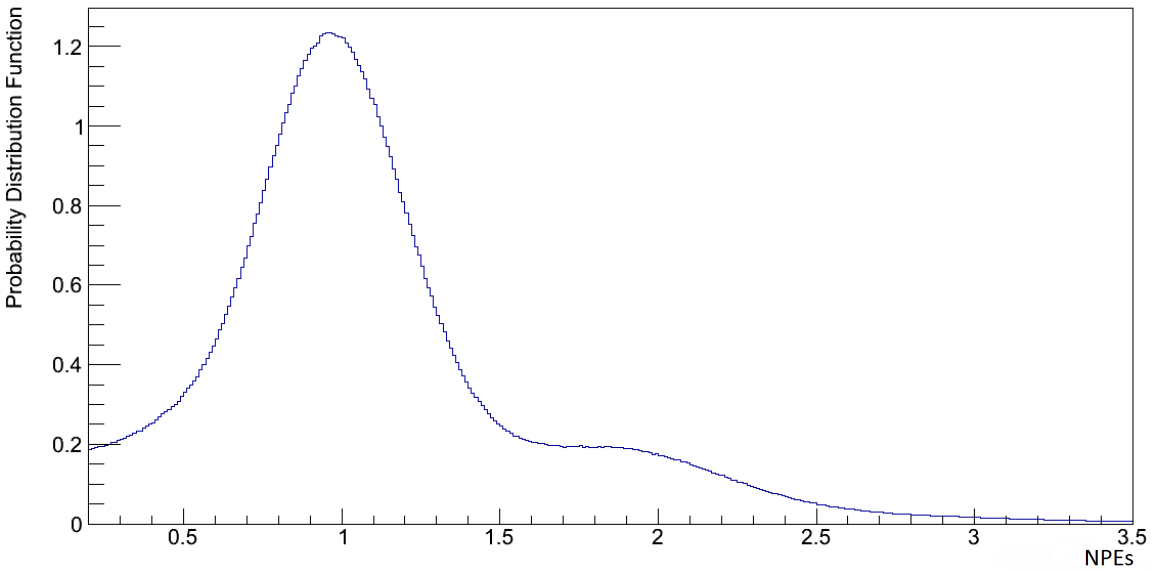


Figure 3.10: Probability distribution function of measured NPEs. Peaks at 1 and 2 NPEs are observed because 10% of the time 2 PEs are produced at the photo-cathode instead of 1 by 175 nm scintillation photons.

These signals travel to the DAQ along ~ 11 m of coaxial cables. Preamplifier cards amplify the signals by a factor 11 and feed the information into analogue timing modules (ATMs) and flash analogue to digital converters (FADCs) [88].

The ATMs - used previously in the Super Kamiokande (SK) experiment [89, 90] -

simultaneously function as analogue-to-digital converters (ADCs) and time-to-digital converters (TDCs) recording the signal's NPEs and the signal's threshold-crossing time. The TDC has 0.4 ns resolution for recording a threshold-crossing time and the ADC integrates the charge in the following 1300 ns with a range of 450 pC and 0.2 pC (~ 1 mV) resolution - corresponding to 120 NPEs and 0.05 NPEs respectively.

After FADCs for each individual PMT channel were installed after refurbishment, the ATMs were used exclusively to trigger the readout of the FADCs. If any PMT's ATM input signal crosses the -5 mV (~ 0.2 PE) threshold, the ATM produces a rectangular output pulse 200 ns wide and 15 mV (~ 0.6 PE) high. Analogue fan-in units add these pulses over all ATM channels, and a trigger is produced if the analogue sum of all ID channels crosses a prescribed threshold. If for example the ID trigger threshold is set to 40 mV a minimum of 3 separate PMTs registering signals within 200 ns of each other are required to pass the 40 mV trigger, as each individual rectangular 200 ns signal is only 15 mV (~ 0.6 PE) high.

- **Normal 40 mV ID trigger:** > 3 hit ID PMTs.
- **Low-threshold 25 mV ID trigger:** > 2 hit ID PMTs (from Dec 2015).
- **OD trigger:** > 7 hit OD PMTs.

Additional special triggers are issued for calibration purposes, i.e. the GPS PPS trigger for the LED calibration events is issued every 1 s. The modulation analyses presented in this thesis only utilise events that result from a normal or low-threshold ID trigger when not accompanied by an OD trigger. For calibration purposes other triggers are utilised.

The FADC (CAEN V1751) has a dynamic range of 1 V with 1 mV resolution corresponding to 50 NPEs and 0.05 NPEs respectively. The voltage is sampled at a rate of 1 GHz and the waveforms of the signals are recorded in the timing window -1 μs to 10 μs with respect to the event's trigger time. Most analyses conducted by XMASS only utilise information recorded within -200 ns to +300 ns. However, shortly after

an event there likely are afterpulses in the contributing PMTs, and these are dealt with by excluding events within 10 ms of a preceding event. The primary purpose of the additionally recorded 10 μs is to study these artefacts. The -1 μs recorded prior to the trigger being issued is used to measure the rate of spontaneous hits - referred to as dark hits - investigated in section 6.1.2 utilising the LED calibration events.

The waveform of an average 1 PE pulse is demonstrated in figure 3.11. Figure 3.12 displays an example of a raw recorded FADC output (black line) for one particular PMT contributing to a ^{57}Co calibration event. 3 individual pulses are clearly evident, these are fit (red dashed line) using a peak finding algorithm based on a SavitzkyGolay filter which applies a convolution of 1 PE pulse waveforms. The procedure extracts the peak time for each pulse (pink triangle); the application of this algorithm is limited to roughly ~10 hits per individual PMT waveform [91]. β-ray events exhibit a longer decay time of ~ 45 ns and hence the pulses are well spread out which simplifies the fitting procedure. Cherenkov light on the other hand is emitted instantaneously, resulting in the individual recorded photons separated in time by only the difference in photon travel time - within the LXe - and the transit time spread (TTS) of the PMT. This means that multiple recorded PE pulses by the same PMT are overlapping, this makes discriminating between them more difficult. However the low energy of these events results in only $\sim 0-100$ pulses spread out over multiple PMTs (642 PMTs in XMASS) so peak fitting is still effective. The transit time of a PE transitioning to the first dynode inside a PMT is the largest source of uncertainty on the time of a fitted waveform, with the TTS of the XMASS PMTs being ~3 ns.

3.2.5 XMASS detector simulation

Figure 3.13 depicts a model of the XMASS detector realistically rendered as implemented in Geant4 [88, 92, 93]. Events are simulated by generating incident particles that interact with the LXe and other detector components. The resulting scintillation photons traverse the detector according to the optical parameters set for the simulation, they can scatter or be reflected until they either get detected by a PMT and

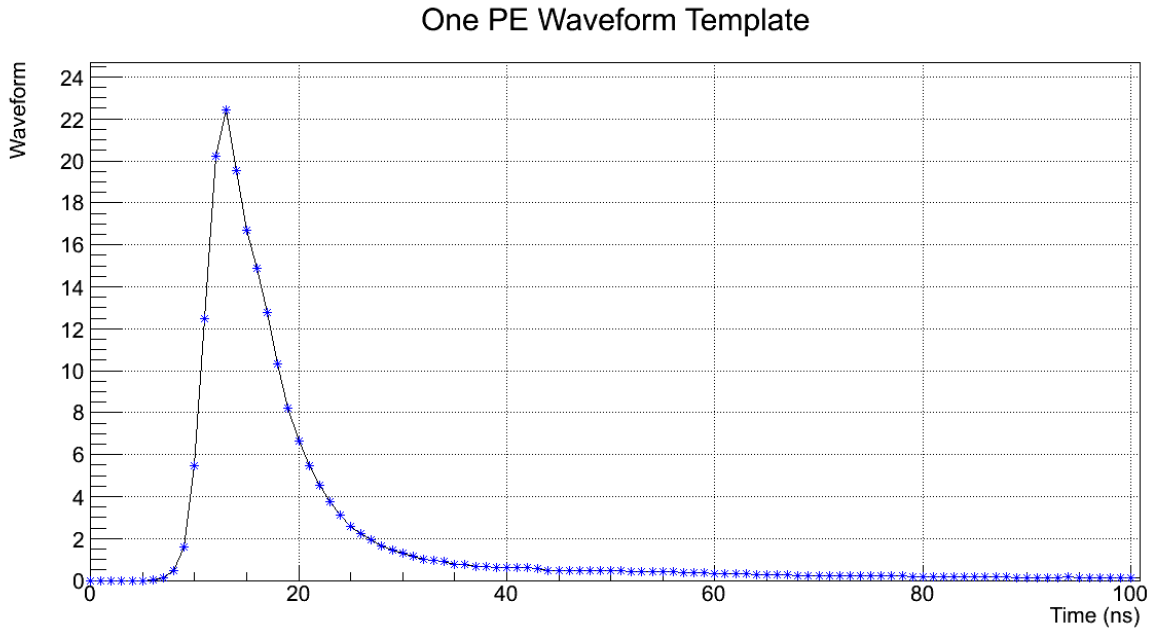


Figure 3.11: 1 PE waveform pulse averaged over many pulses recorded during LED calibration taking. Rises steeply and then exhibits exponential decay (capacitor discharge).

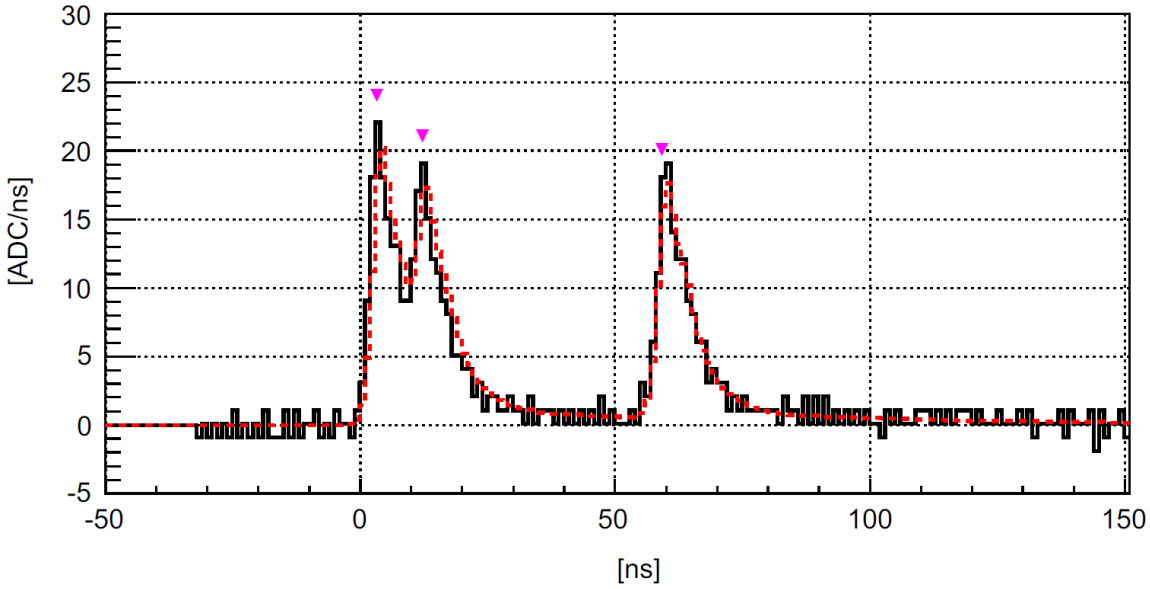


Figure 3.12: The raw FADC output waveform (black line) from 1 PMT in a ^{57}Co calibration event, fit using a SavitzkyGolay filter (red dashed line) with the peak times extracted (pink triangles) [91].

initiate a signal or get absorbed/fail to initiate a signal. A simulation file records the hit time and hit PMT's identification number (PMTid) of each signal in each simulated event. These files are then converted into root files equivalent to those obtained

during normal detector operations, accounting for the response of the electronics to the generated raw signals. The simulations conditions are set and conducted for each individual run after the optical parameters are measured using fortnightly ^{57}Co inner calibration data discussed in section 3.3.

All simulated pulses are of size 1 PE and the intrinsic electronic noise observed in the waveforms recorded under normal detector operations - present in figure 3.12 - is not simulated. The majority of the physics analyses conducted by XMASS don't use the raw recorded waveforms and instead use the peak times extracted for each individual pulse as outlined in the previous section. As is also evident in figure 3.12 the size of the pulses is much larger than the noise and hence the presence of the noise or lack thereof doesn't impact fitting to a significant degree to warrant the simulation of said noise. Additionally, XMASS analyses apply a noise cut which removes events that are suspect of being affected by excessive noise; this cut is discussed in section 5.1.1. Similarly dark hits are also not simulated. As this affects low energy events and most XMASS analyses apply a FV cut - which essentially renders the lowest energy bins unusable - dark hits have only been considered in the previous XMASS modulation analysis [49, 50] and the analyses presented in this thesis. These are discussed further in section 6.1.2.

3.3 XMASS calibration techniques

This section outlines the multiple calibration techniques and sources XMASS uses to calibrate the detector. LED calibration is used to keep PE stable by correcting for variations in the PMT waveform gain, this is detailed in section 3.3.1 and was utilised in reference to additional run selection criteria for low threshold data in section 6.1.2. Inner calibration outlined in section 3.3.2 is used to fine-tune optical parameters and obtain the energy-scale (PE $\rightarrow$ keV$_{ee}$) relation using multiple sources of known energies. External hose calibration explained in section 3.3.3 was used as a cross check and in section 6.2 to obtain the LY once inner calibration data taking ceased.

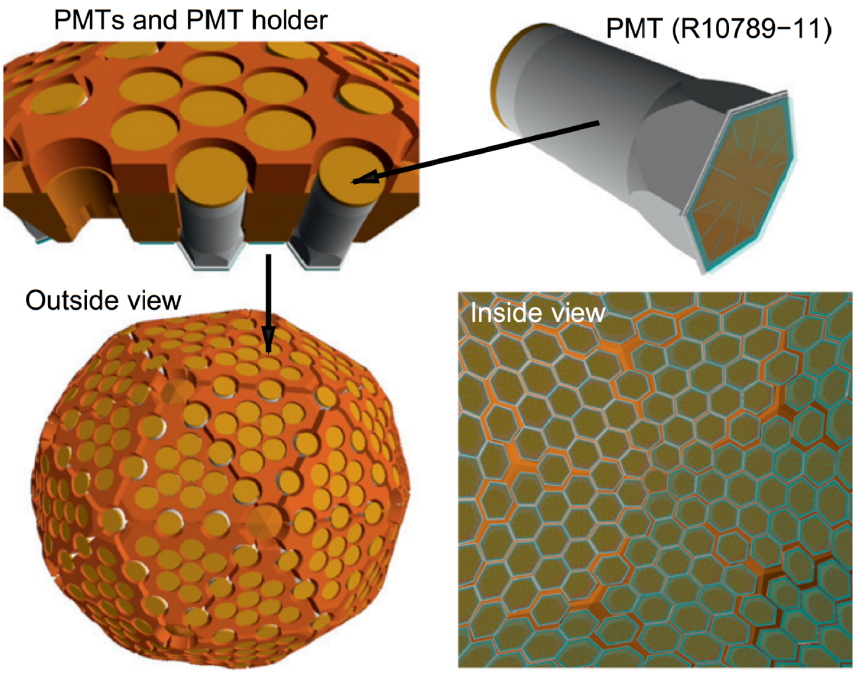


Figure 3.13: A model of the XMASS inner detector and PMTs realistically rendered as implemented in Geant4 [88].

3.3.1 LED calibration

8 blue LEDs are located on the ID PMT holder's inner surface. A GPS PPS event trigger initiates the flash of the LEDs once a second; there is a ~40 ns delay between the event trigger and the LED flash. The wavelength of the blue light is larger than normal LXe scintillation light. Therefore these photons have a lower energy and can only produce 1 PE maximum when they strike the PMT's photo cathode.

The LED calibration events are used to monitor the single PE waveform gain of each individual PMT over the entire lifetime of the detector and to measure the prevalence of dark hits, these are accidental hits - caused largely by the thermal emission of electrons from the photocathode - that can be measured in the 1 μs that is recorded before the 8 blue LEDs flash. Gain correction is conducted weekly to keep PE consistent over time. The WF gain of all PMTs reduced over time - most steeply at the beginning of data taking and then tailed off towards the end. The maximum decrease for a single PMT was ~ 10% over the entirety of data taking, however most PMTs reduced by $\mathcal{O}(1)$%. Section 6.1.2 outlines how both of these measures are used

to apply additional run selection criteria with respect to the low threshold data due to the necessity for increased PE and event rate stability.

3.3.2 Inner calibration

The XMASS detector is primarily calibrated via internal RI source measurements. Figure 3.14 displays the calibration system, comprised of a stepping motor that guides a RI source down into the active volume along the detector's central z-axis with ~1 mm position resolution. Data is recorded at 10cm increments: -40 cm to +40 cm.

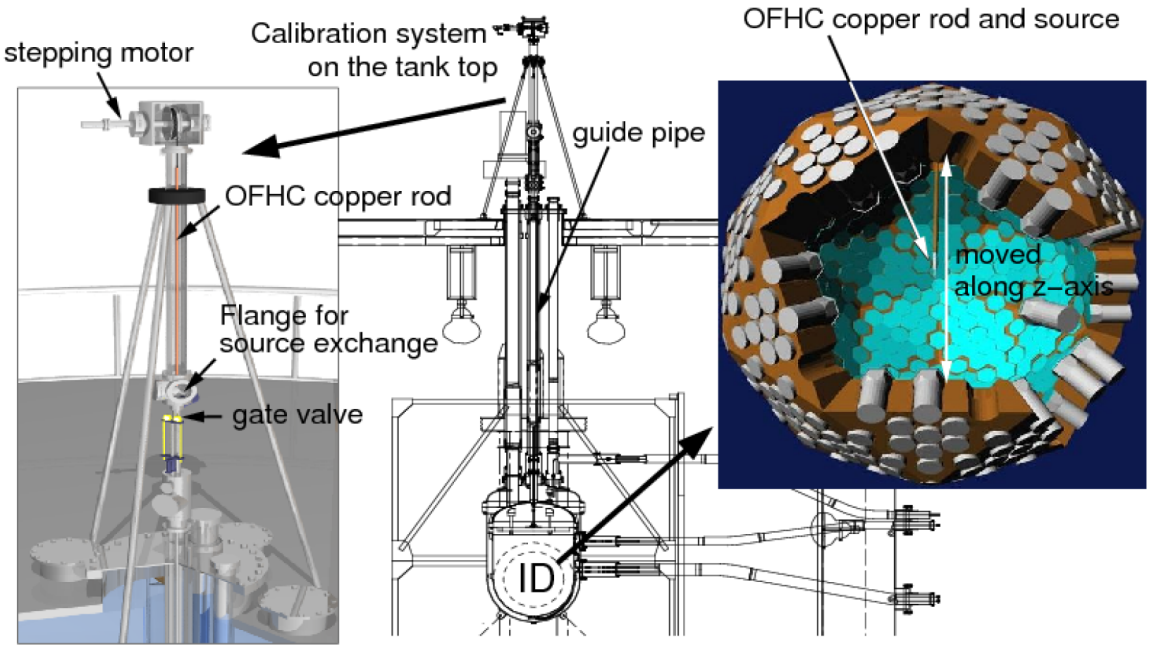


Figure 3.14: XMASS inner calibration system: stepping motor and guide pipe to lower the calibration source into the ID with 1mm position resolution [88].

- **RI calibration sources:** The XMASS detector's energy scale is calibrated using multiple RI sources, listed in table 3.2. Some of the RI sources listed undergo α decay (^{241}Am: 5.486 keV) or β decay (^{137}Cs: 512 keV) or electron capture (^{57}Co) etc prior to emitting a γ-ray of a specific energy at a later time measured as a standalone event. Only the relevant γ-rays are listed in table 3.2. The range in energy they span is sufficient for DM analyses as nuclear recoil energies are small (~ few keV). The listed 8 keV and 59.3 keV energy events are

a result of K_α X-rays from copper and tungsten present in the ^{109}Cd and ^{57}Co sources respectively [88]. The 30 keV peak observed during ^{241}Am calibration is a result of the 59.5 keV γ-ray being absorbed by the LXe, which then emits a 25.0 keV electron, a ~ 30 keV X-ray and low energy Auger electrons. In the case of the 2π source this ~ 30 keV X-ray is sometimes absorbed back into the source on account of the source's large solid angle, only to be re-emitted at a later time and be measured as a standalone event [91]. 1.65 keV events are observed from the ^{55}Fe calibration source [49]: The 5.9 keV photon is emitted from the source into the LXe, the Photoelectric effect (L-shell) occurs in the LXe with a 1.5 or 1.8 keV electron emitted while the X-ray from the L-shell (4.4 or 4.1 keV respectively) is reabsorbed by the source. The previous modulation analysis [49, 50] utilised these as a low energy calibration source, the 1.65 keV peak is compared to MC simulation in figure 3.15. They were additionally used to cross check the PDF classifier developed in chapter 5. Figure 3.18 shows the measured ^{57}Co spectrum, the 122 keV peak is fit for LY and l_A evaluation.

Table 3.2: XMASS inner calibration sources and their respective γ event energies [50]. The origin for each γ-ray is detailed, the energies used for energy calibration are in italics and the ^{57}Co 122 keV γ-ray events are additionally in bold as these are used to measure the optical parameters and LY.

Source	Type	Energy (keV)	Origin
^{55}Fe	2π	*1.65*	L-shell escape peaks [49]
		5.9	K_α X-ray from ^{55}Mn [91]
^{109}Cd	2π	*8*	K_α X-ray from Copper (contained in the source) [88, 94]
		22	^{109}Ag X-rays [94]
		58	Xe L, K escape peaks for X-rays [94]
		88	^{109}Cd γ-rays [94]
^{241}Am	4π	*17.8*	^{237}Np X-rays [91]
		59.5	^{237}Np γ-rays [91]
	2π	30	59.5 keV $\gamma \xrightarrow[\text{in LXe}]{\text{absorbed}}$ 25.0 keV e^- + low E Auger e^-s + ~ 30 keV X-ray ($\xrightarrow[\text{by source}]{\text{absorbed}}$ 30 keV escape peak) [91]
		59.5	^{241}Am γ-rays [91]
^{57}Co	4π	14, ***122***, 136	^{57}Co γ-rays [95]
		59.3	K_α X-ray from Tungsten (contained in the source) [88, 91]
^{137}Cs	2π	*662*	^{137}Cs γ-rays [88]

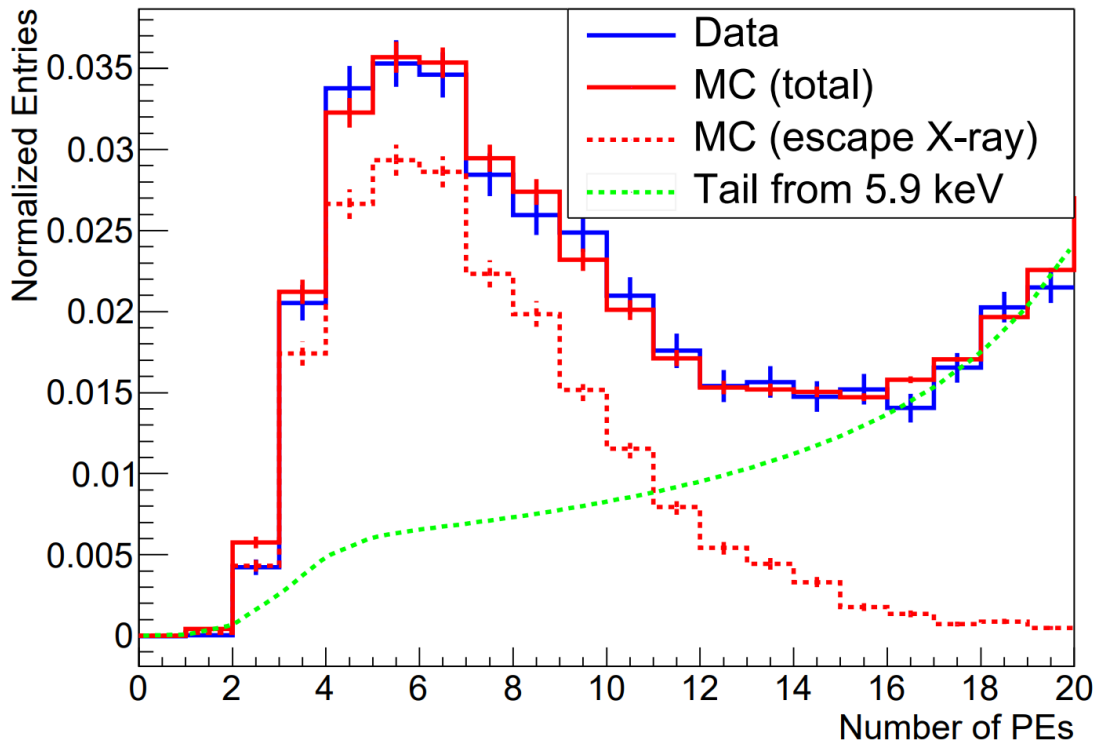


Figure 3.15: The energy spectrum of ^{55}Fe events centred around the 1.65 keV L-shell escape peak. Data (solid blue line) is compared to MC simulation (solid red line) - composed of the 1.65keV events (dashed red line) and the 5.9 keV events tail (dashed green line) [49].

XMASS RI sources are produced by KRISS [95], and come either as needle (4π) or flat (2π) sources. These RI sources are attached to the end of a copper rod to be inserted into the detector, figure 3.16 demonstrates this for the ^{57}Co source. The relation between electron equivalent energy (keV$_{ee}$) and keV$_{\mathrm{Co}}$ (keV$_{\mathrm{Co}}$ = $\frac{\mathrm{NPEs}}{\mathrm{LY}}$) is taken from the previous modulation analysis [49, 50] and displayed in figure 3.17.



Figure 3.16: XMASS ^{57}Co source mounted on the OFHC Cu source holder rod.

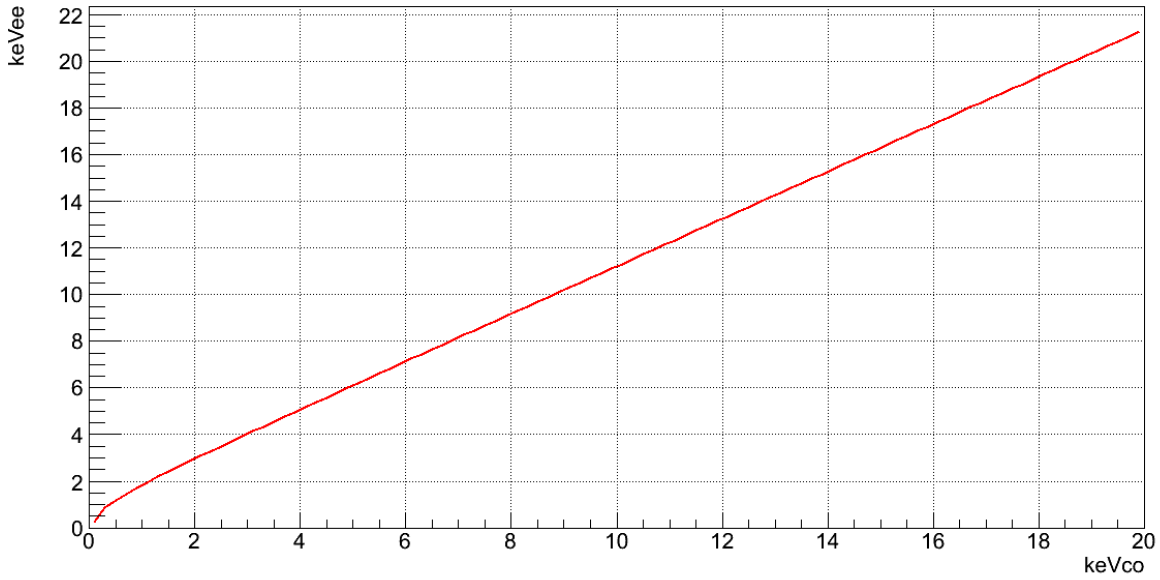


Figure 3.17: The relation between keV_{ee} and $\mathrm{keV}_{\mathrm{Co}}$ ($\mathrm{keV}_{\mathrm{Co}} = \frac{\mathrm{NPEs}}{\mathrm{LY}}$) used for mapping event energies using the γ-ray calibration sources to electron equivalent energies [49,50]. The LY is that obtained using ^{57}Co calibration hence the Co Index.

- **Light yield:** Figure 3.18 displays the NPEs distribution of ^{57}Co events recorded with the source located at the centre of the detector (z = 0 cm). There are 3 peaks at ~ 800, 1800 and 2000 NPEs corresponding to the 3 γ-ray energies 59.3, 122 and 136 respectively - listed in table 3.2. The two higher energies are fit with Gaussian's and the central (mean) NPE value of the 122 keV peak is scaled by 122 to obtain the LY. The error on the extracted LY corresponds to the error of this mean value similarly scaled by 122. This is a fitted parameter that roughly corresponds to the standard deviation of the 122 keV peak divided by $\sqrt{\mathrm{Entries}}$ (corresponding to that peak). Most XMASS analyses perform a fiducial volume (FV) cut - reconstructed event radius < 20 cm - and hence use this 0 cm LY value. However the modulation analyses use events throughout the entire active volume as lower energies are probed and the FV cut becomes ineffective at lower energies. Therefore the modulation analyses use inner calibration data taken at z = −30 cm to measure the LY. This is paired with hose data to obtain LY measurements throughout the entire lifetime of the detector, discussed in section 6.2.

As outlined above the energy is calculated not by using the integer number of recorded pulses but the total NPEs of an event scaled by the LY measured at that point in time. The NPEs of each individual pulse is intrinsically random as displayed in figure 3.10 and hence so is the total NPEs (NPEs of all pulses summed up) for any given event. Due to the high observed LY that XMASS measures, ~ 16 PEs/keV, these random effects become negligible at a ~ few keV. The effect is important for the lowest energies with only a handful of recorded pulses though. The minimum energy used in the analyses is 0.5 keV_{ee}, which corresponds to ~ 3.5 – 4 total NPEs. However, after the introduction of the low-threshold trigger the LY changes by only ~ ±1% and this has a negligible effect when compared to the width of the energy bins (0.5 keV_{ee}) at these low energies.

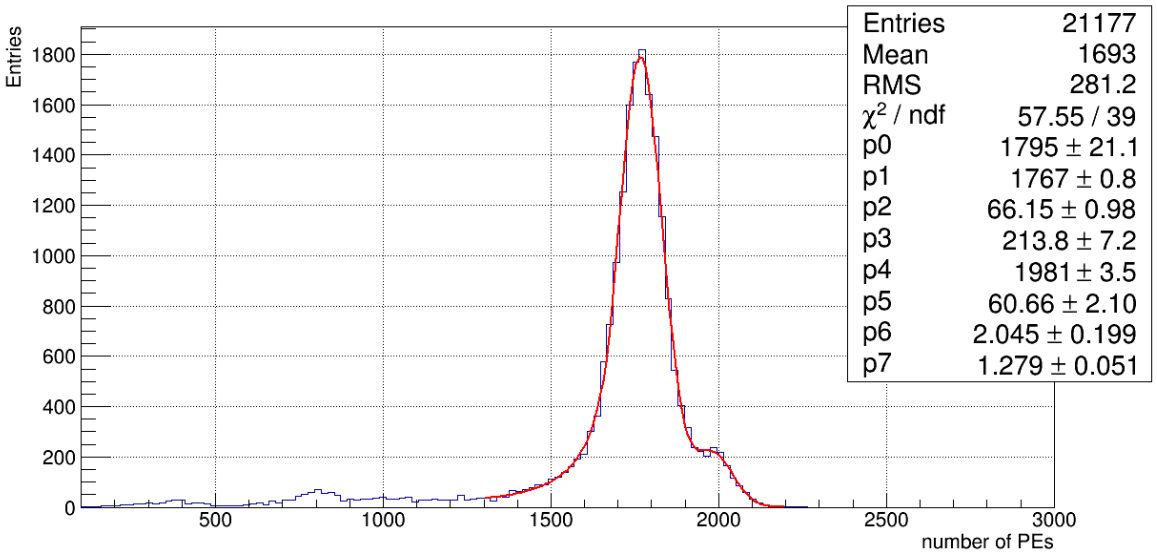


Figure 3.18: The observed ^{57}Co z = 0 cm NPEs spectrum from the last ^{57}Co dataset recorded on 2019/01/31. The 122 keV and 136 keV peak are Gaussian fitted. The 122 keV peak mean value: 1767 ± 0.8 is used to obtain the LY by scaling by 122.

- **Optical parameters:** The average NPEs/event is obtained for each PMT for each internal calibration position using events within the Gaussian-fit 1σ of the ^{57}Co 122 keV γ-ray peak. Equivalent ^{57}Co 122 keV γ-ray events are simulated at each of the nine internal calibration positions using the XMASS

MC over a l_A and l_S optical parameter grid. A χ^2 comparison of the measured PE distributions between data and MC is performed using all nine calibration positions and all functioning hexagonal PMTs simultaneously. The minimal chi squared and best fit optical parameters are extracted by interpolating between l_A and l_S grid points. The reflectivity (specular) of the PMT OFHC Cu holder was obtained and fixed similarly. Chapter 4 outlines a new calibration technique that attempted to cross check these optical parameters using alpha particles that originate on the surface of the source holder and incorporates timing.

3.3.3 Hose calibration

Attached to the outside of the outer OFHC Cu cryostat vessel in the water are $\frac{1}{4}$ inch stainless steel vacuum tubes intended to reliably and reproducibly position external calibration sources as close as possible to the detector's active volume as displayed in figure 3.19. The U-shaped (Hirano) hose tube was initially used. The other two tubes curve further out but terminate on the wall of the OFHC Cu vessel at the level of the centre of the ID; after December 2013 one of these tubes was settled on to acquire all further Hose calibration datasets. This tube was not used prior to December 2013 and that's why there is no comparable Hose calibration data in the first ~2 months of data taking.

A RI source of ^{60}Co is inserted into this hose via stiff stainless steel stranded wire (fish tape) that fits snugly into the vacuum tube. This allows the source at its end to be pushed against the far end of the stainless steel tubing at the outside of the outer cryostat vessel - and retrieve it after calibration. As figure 3.20 displays the source is attached to the end of said tubing and is guided down to the outer wall of the OFHC Cu vessel. This allows for the study of the detector's response to external radiation. It is explained in section 6.2 how this external hose data is used to determine the LY during the period where inner calibration data taking ceased.

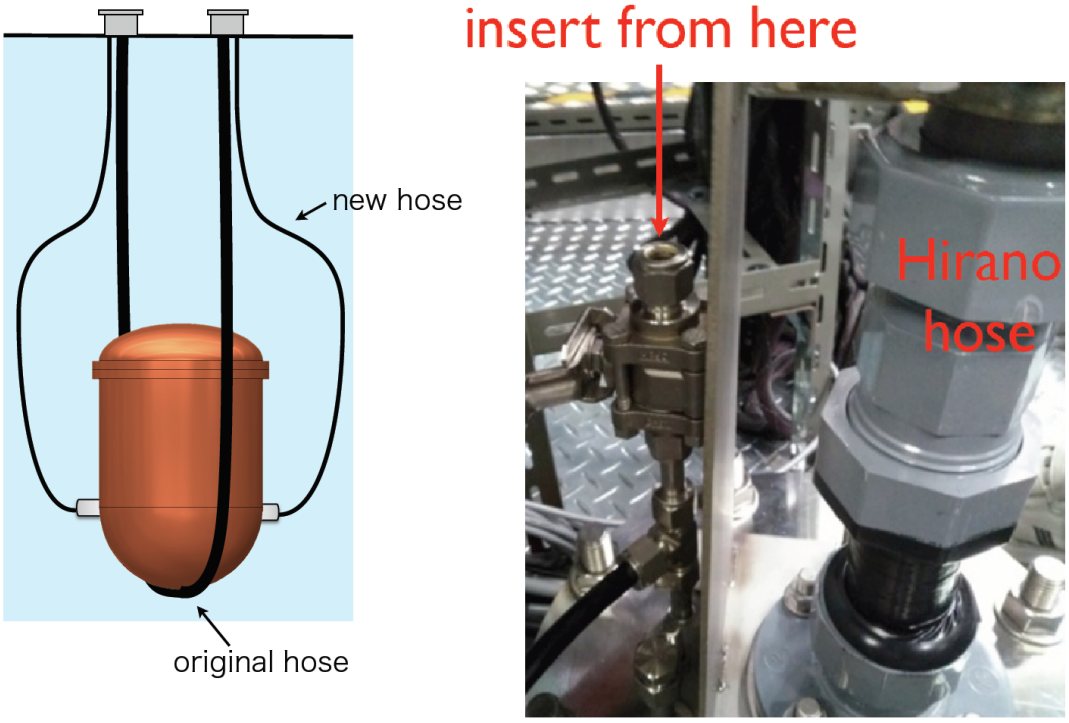


Figure 3.19: The stainless steel vacuum tubes running outside/along the outer OFHC Cu vessel in the water. These are used for external hose calibration.

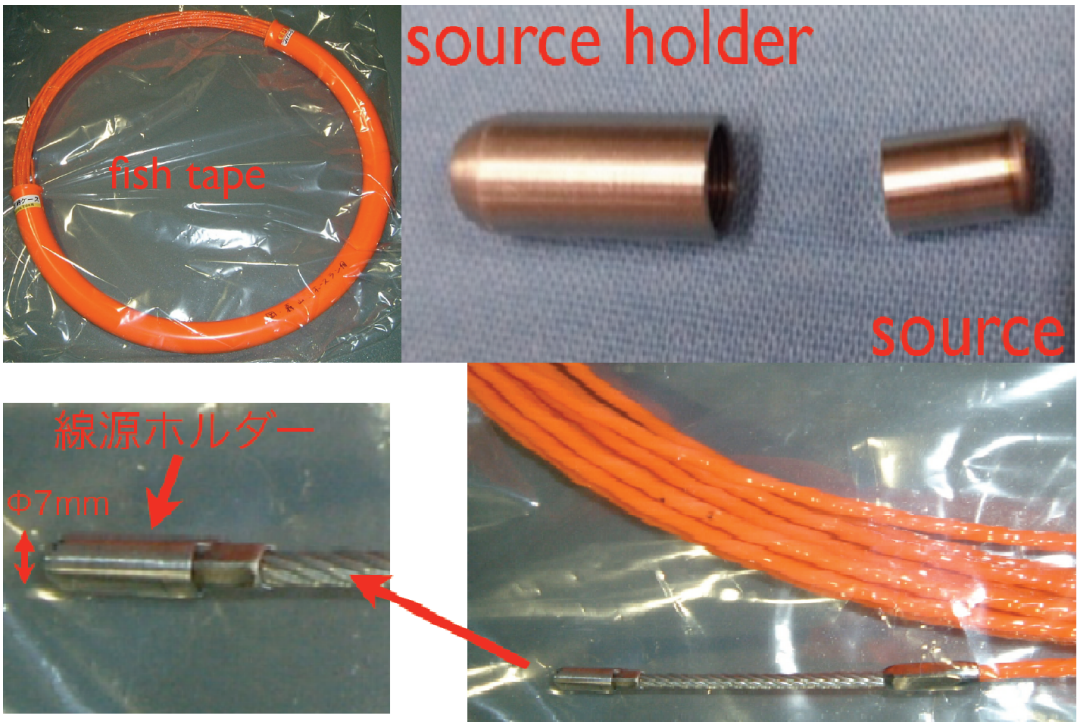


Figure 3.20: The ^{60}Co source is attached to the end of a stiff stainless steel stranded wire (fish tape) which is inserted along the stainless steel vacuum tube in figure 3.19 to perform external hose calibration.

3.4 Backgrounds

This section outlines the sources of background (BG) that induce events within the XMASS detector. These include both external and internal sources of BG, detailed in sections 3.4.1 and 3.4.2 respectively. The main source of BG is the PMTs Al-seal, specifically β emitters in the ^{238}U and ^{210}Pb decay chains which deposit only small fractions of their energy in the LXe just besides the PMT entrance window. Additionally, Cherenkov events resulting from ^{40}K decays in the photocathode are numerous, however these are easily identifiable. Understanding the BG is critical to optimise analysis sensitivity and reduce the σ_{SI} limits. Chapter 5 outlines a newly developed PDF based classification technique.

3.4.1 External backgrounds

The external BG sources are mitigated by conducting the experiment deep underground and utilising the OD as a water shield and muon tagger - a technology now routinely deployed in large scale DM experiments. All external BG sources negligibly effect the event rate, these our outlined below.

- **Cosmic-ray muons:** The laboratory resides within a mountain that shields the experiment from cosmic-ray muons reducing their flux by 5 orders of magnitude from 1.1×10^{-2} cm^{2}s^{-1} above ground to $\sim 10^{-7}$ cm^{2}s^{-1} [74]. When cosmic-ray muons pass through the OD water tank they emit Cherenkov light which the 72 OD PMTs can detect. The OD acts as an active veto against cosmic-ray muons. Cosmic-ray muons pass through the OD and ID at a rate of 0.14 events day^{-1}kg^{-1}. The energy range of spallation products is $\mathcal{O}$(MeV) corresponding to an event rate $\sim 10^{-4}$ day^{-1} kg^{-1}keV$_{ee}^{-1}$. This is negligible compared to the recorded event rate and a conservative estimate considering not all spallation products result in background events.

- **γ-rays and neutrons:** Radioactive isotopes from the ^{238}U and ^{232}Th decay series in the mine rocks produce both γ-rays and neutrons. The estimated

neutron flux for E < 10 MeV and E > 10 MeV is 10^{-9} cm^{-2}s^{-1} and 10^{-8} cm^{-2}s^{-1} respectively [50]. The OD water tank has a surface area of 4.5×10^6 cm^2 which results in a conservative estimate of 3.9×10^3 n day^{-1} entering the water tank. The OD water tank acts as a passive shield against γ-rays and neutrons, a MC study calculated that 2 m of water should reduce the event rate by $\sim 10^{-7}$, resulting in a negligible effect on the ID event rate from neutrons and γ-rays from the surrounding rock: 4.7×10^{-7} day^{-1}kg^{-1}. This level of reduction is expected given the attenuation length of γ-rays in water is $\sim$ 10 cm (at 1 MeV) and $e^{-\frac{2\text{m}}{0.1\text{m}}} = 2 \times 10^{-9}$; the attenuation length is even shorter at lower energies.

- **Radon:** Rn is present in the air in the Kamioka mine and was measured to be 2000 Bq/m^3 in summer and 40 Bq/m^3 in winter, depending on the direction of the air flow in the main access tunnel to the underground lab [96]. The XENON collaboration measured a similar Rn concentration in the air underground at LNGS - emanating from the surrounding rock - of $\sim$ 320 Bq/m^3 in the XENON room [97]. A Rn detector on top of the water tank constantly measures the concentration of Rn present in the water. This is accomplished by bubbling N2 through water taken from the water tank to extract Rn from it (at a calibrated efficiency). Rn progeny are then measured (at a calibrated efficiency) and the concentration of Rn present in the water is inferred. The maximum ^{222}Rn measured was $(1.4 \pm 0.2) \times 10^{-1}$ Bq m^{-3}. MC simulations [50] indicate that this is a negligible contribution to the event rate: $(1.4 \pm 0.2) \times 10^{-5}$ day^{-1}kg^{-1}keV$_{ee}^{-1}$ [50, 98].

3.4.2 Internal backgrounds

Table 3.3 lists all of the internal BG types that originate from the different detector components / materials within XMASS. The Al-seal contains relatively high levels of ^{238}U and ^{210}Pb (BG Types 15 and 16 respectively), faces the LXe and is the dominant source of background events. The detector was refurbished with OFHC

Cu plates and rings to encapsulate the Al-seal, cut the direct optical path into the detector's sensitive volume, and improve the situation as demonstrated in figure 3.21. The observed event rate reduced by an order of magnitude, however BG types 15 and 16 remain dominant and problematic. The relevant decay chains in the Al-seal are: the Uranium series for ^{238}U and ^{210}Pb, the Actinium series for ^{235}U and the Thorium series for ^{232}Th. They are displayed in figure 3.22. While α particles normally stop in the seal and do not cause scintillation emission in the LXe surrounding the seal, β-rays have enough range to emerge from the seal and deposit an arbitrary fraction of their energy in the LXe, causing scintillation light emission at the seal. While the copper rings and plates cut the amount of light that reaches the inner detector volume, they cannot fully prevent light leakage into the active volume causing BG events that are hard to identify as they originate behind the ID surface; typically they reconstruct even inside the fiducial volume. With potassium being a crucial ingredient to high quantum efficiency photocathodes of our PMTs, β-rays from 40K decays (BG type 2) in the thin photocathode produce Cherenkov light in the PMT entrance window. This is the dominant source of BG events below 3.5 keV$_{ee}$. However, although they are dominant they are less problematic compared to the previously mentioned Al-seal RI sources. This is because the Cherenkov radiation is emitted instantaneously and hence these events have very distinct short timing characteristic and are therefore easily identifiable.

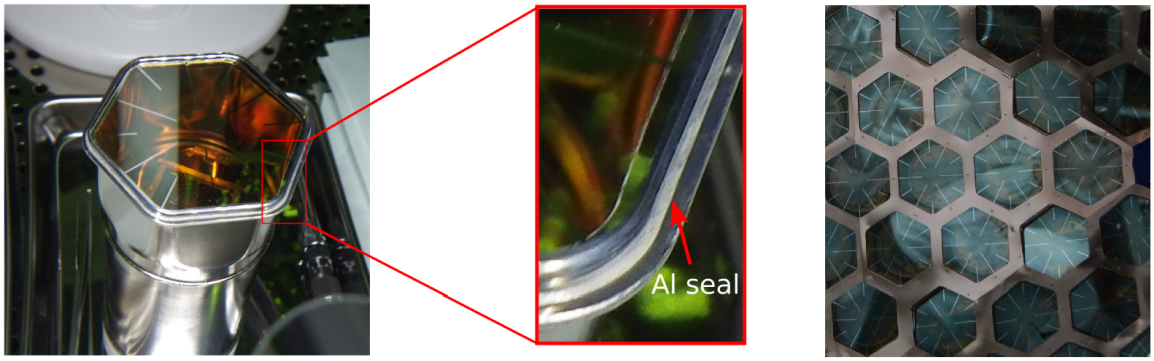


Figure 3.21: XMASS PMT Al-seal and Copper plate/ring coverings applied when the XMASS detector was refurbished to mitigate the largest source of BG by an order of magnitude [74].

Table 3.3: All individual internal BG sources in the XMASS experiment. Each one is simulated for every run using the optical parameters measured during ^{57}Co calibration and given a specific BG type number to identify it.

BG Type	Component	Element / Signal
0	PMT Body	^{232}Th
1	PMT Body	^{60}Co
2	PMT Body	^{40}K
3	PMT Base	^{238}U
4	PMT Base	^{232}Th
5	PMT Base	^{210}Pb
6	IVC (Welded by Amagasaki)	^{232}Th
7	IVC (Welded by Tohoku-Oe)	^{232}Th
8	IVC (Welded by Tohoku-Oe)	^{238}U
9	OVC (Welded by Amagasaki)	^{232}Th
10	OVC (Welded by Tohoku-Oe)	^{232}Th
11	OVC (Welded by Tohoku-Oe)	^{238}U
12	OFHC Cu Holder	^{60}Co
13	OFHC Cu Holder	^{210}Pb
14	Filler	^{210}Pb
15	Al-Seal	^{238}U
16	Al-Seal	^{210}Pb
17	Al-Seal	^{232}Th
18	Al-Seal	^{235}U
19	OFHC Cu Plate Bulk	^{210}Pb
20	OFHC Cu Ring Bulk	^{210}Pb
21	OFHC Cu Plate Surface	^{210}Pb
22	OFHC Cu Ring Surface	^{210}Pb
23	PMT Window Surface	^{210}Pb
24	LXe	^{214}Pb
25	LXe	^{214}Bi
26	LXe	^{85}Kr
27	LXe	^{14}C
28	LXe	^{39}Ar
29	LXe	$2\nu\beta\beta$

Normal runs are runs recorded not for the purposes of calibration but under normal detector operational conditions which XMASS uses in its physics analyses. The optical parameters of a given run are obtained by linearly interpolating the optical parameters extracted during fortnightly ^{57}Co calibration either side of said run. These are then used to simulate the BGMC accounting for each individual source of internal BG listed in table 3.3. Figure 3.23 compares the conventional XMASS standard cut

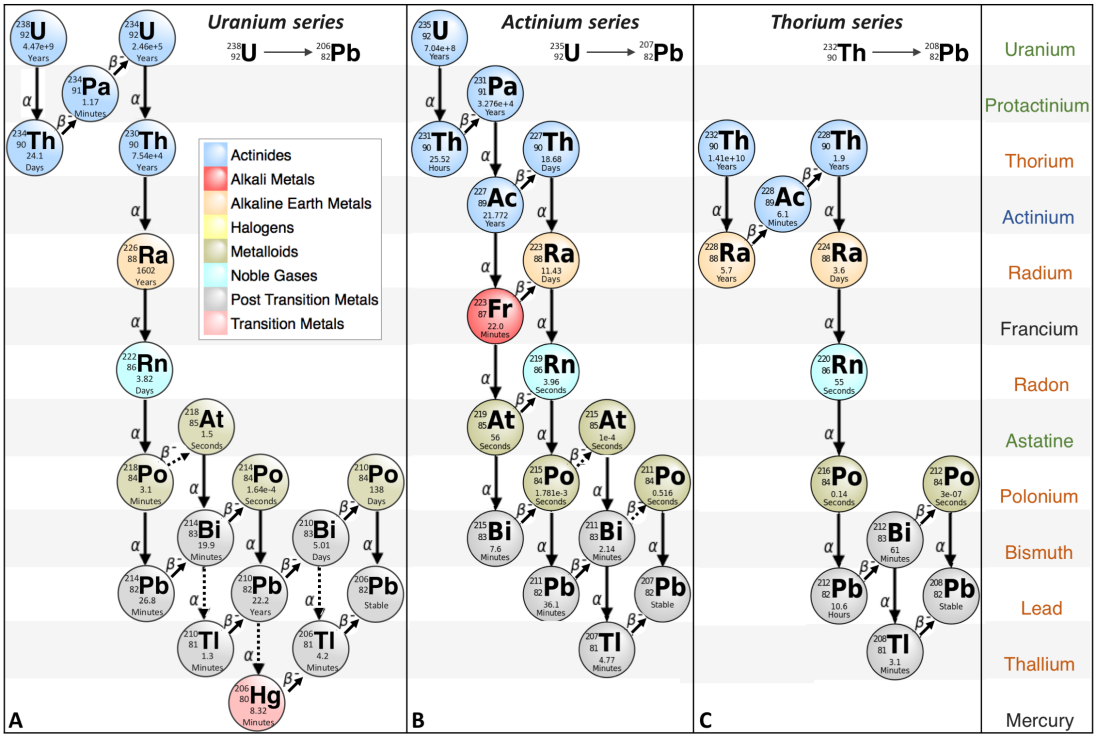


Figure 3.22: Uranium, Actinium and Thorium series decay chains [99].

(StdCut: detailed in section 5.1.1) event rate (events/day/keV$_{ee}$/kg) of normal run data (red) and combined internal BGMC (blue) for the first 100 days following the start of low threshold data taking (Dec 2015). The top plot shows the absolute event rates while the bottom plot shows the ratio, there is a clear disparity at low energy (< 7 keV$_{ee}$). The current best hypothesis for this discrepancy is a mismatch between the positions / geometry of the OFHC Cu plates and rings between what's simulated in the XMASS MC and reality. This is because there are tiny crevices between these newly added components which could allow additional BG components to emanate to varying degrees. Events which cause scintillation emission in the LXe within these crevices would result in low energy events as only a few scintillation photons would find their way out and be detected. Figures 3.24 and 3.25 display the BGMC event rate for XENON1T and XMASS respectively, with the contribution from each experiment's main BG components. Both have applied a fiducial volume cut; XMASS however has also applied the previously mentioned StdCut. XENON1T's event rate is smaller by multiple magnitudes even before applying any specifically designed cuts.

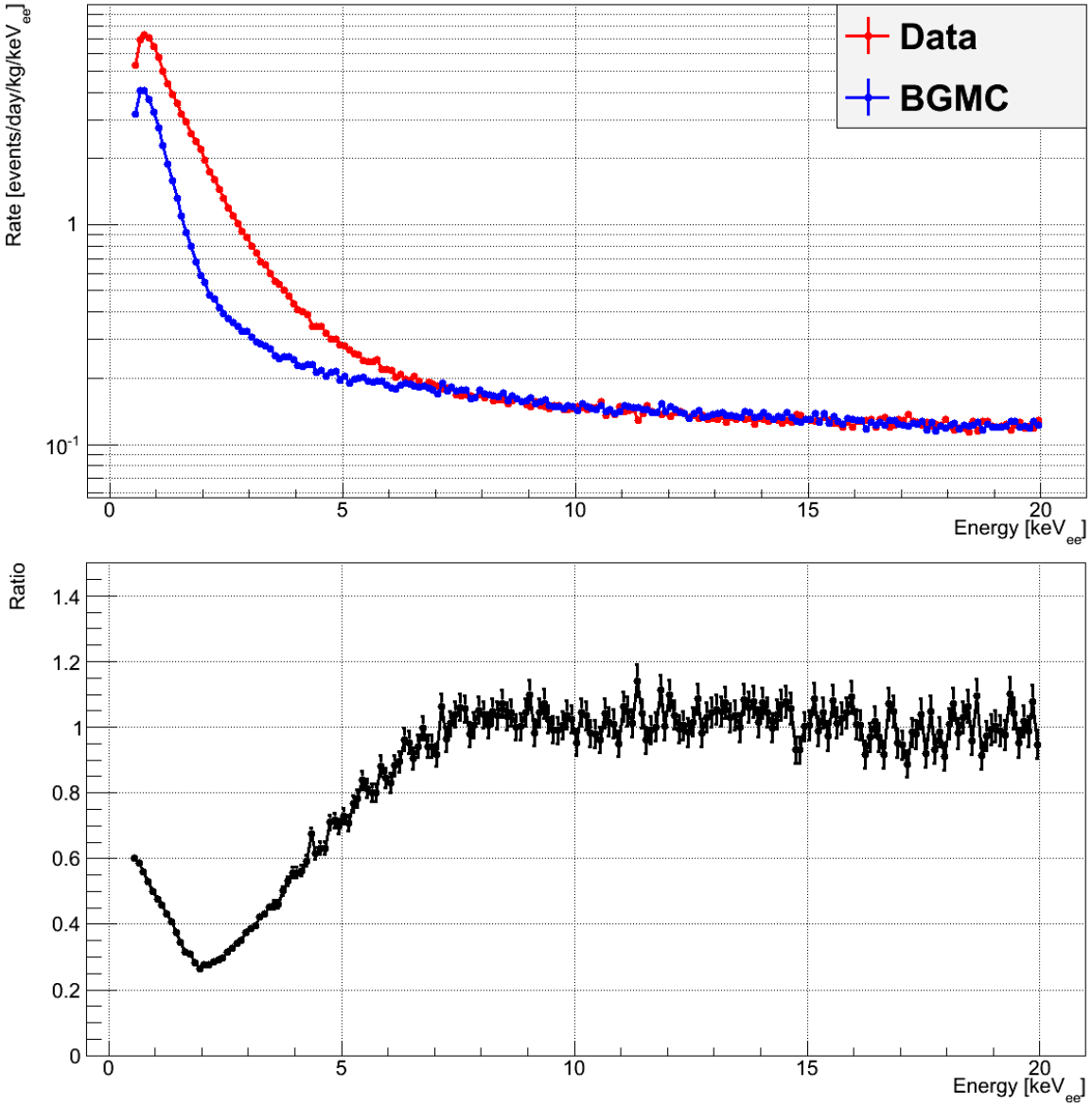


Figure 3.23: Event rate (StdCut) for the combined internal BGMC and the data in the first 100days following the start of low threshold data taking. Top: Comparison. Bottom: Ratio. The discrepancy is thought to arise form a mismatch between the MC simulations and the true position / geometry of the OFHC Cu plates and rings - installed to prevent light leakage from the Al seal radioactivity induced scintillation emission.

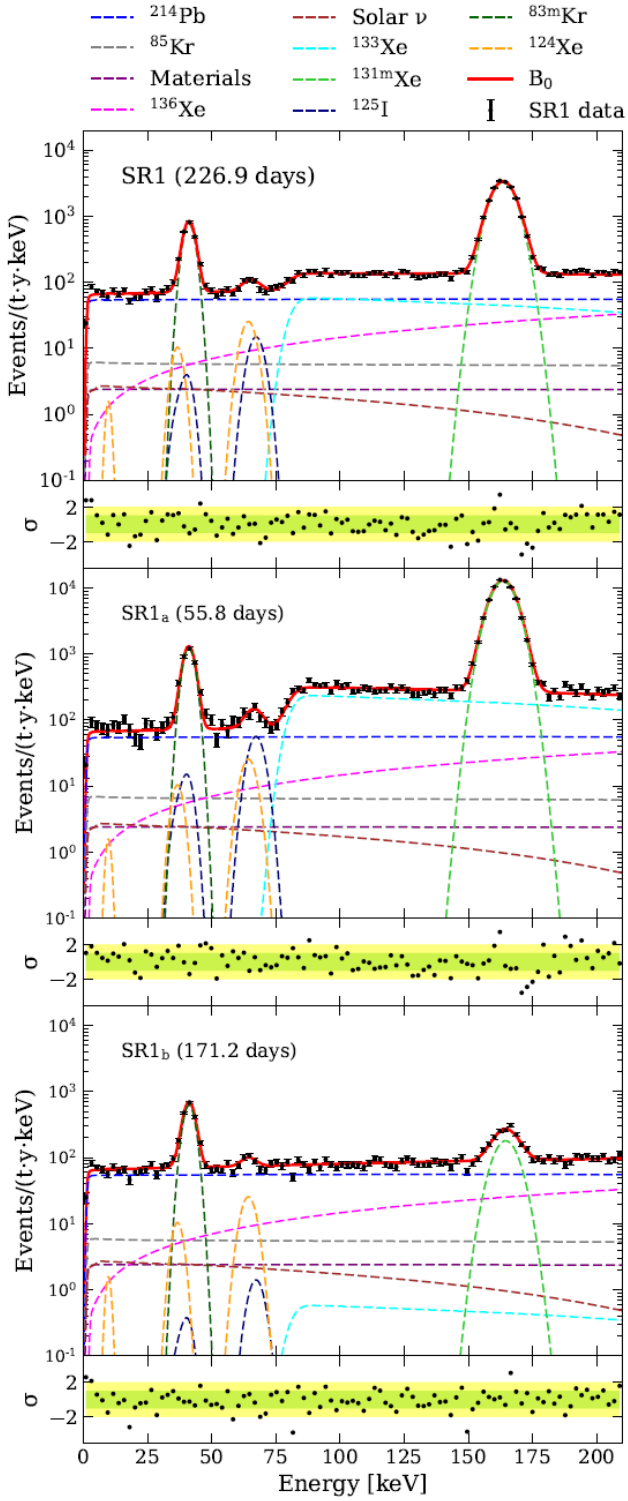


Figure 3.24: The electronic recoil energy spectrum observed in XENON1T for its 3 distinct run periods SR1, $SR1_a$ and $SR1_b$. The data is compared to a MC simulation of the total background (solid red line) with the other dashed lines representing individual backgrounds from various sources (colours) [100].

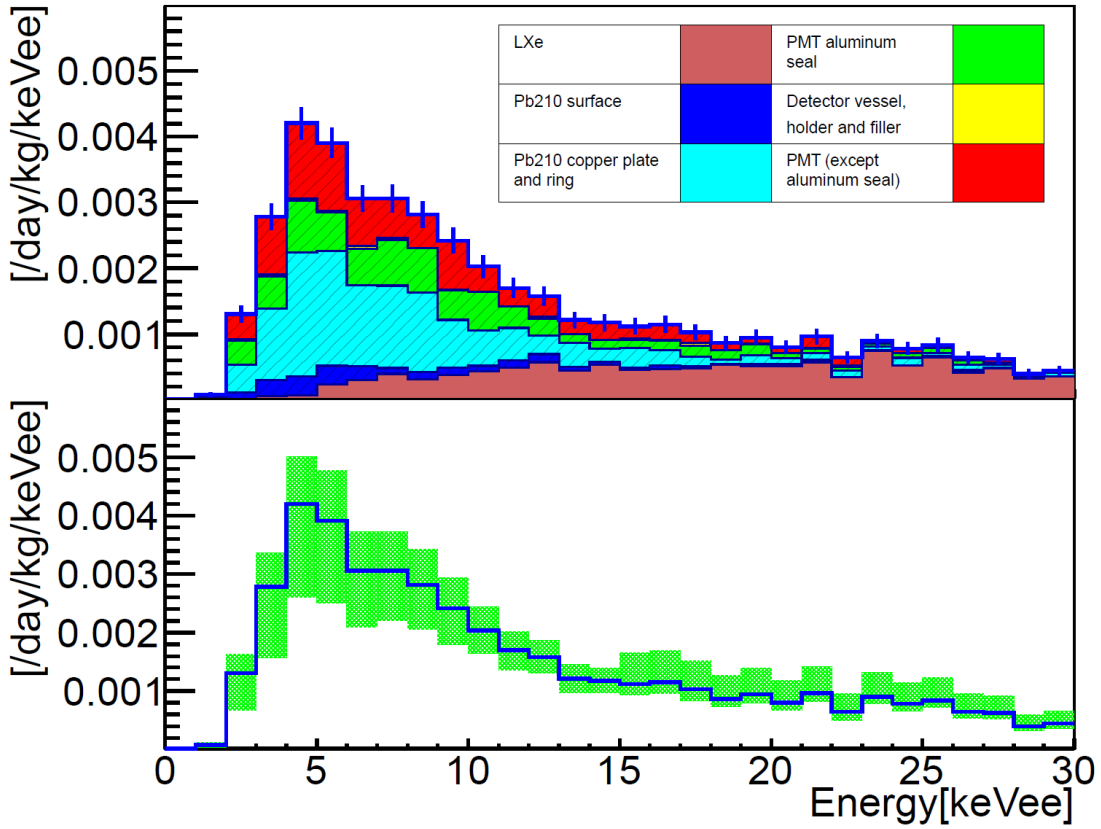


Figure 3.25: (Top) BG estimate for events in the XMASS FV. The coloured stacked histograms show the various contributions to this estimate. (Bottom) Energy spectrum with the green region covering its systematic and statistical errors [51].

Two modulation analyses are presented in this thesis. The first is an update to the previous modulation analysis [49,50], in which the BGMC is used to generate BG LY relative efficiency curves. However, the uncertainties that arise from this technique are large, especially at low energy where the disparity is clear. The second analysis does not generate BG LY relative efficiency curves, instead it fits the data directly with a LY gradient incorporated into the fit, hence removing this source of systematic error. Instead the BGMC is used in this analysis - see chapter 5 - to develop a new PDF based classification technique.

Chapter 4

High Energy Alpha Calibration

XMASS extracts the optical parameters - governing how scintillation photons traverse the detector - by performing a χ^2 comparison of internal ^{57}Co calibration data with equivalent MC simulated events, scanning the parameter space for the scintillation light's absorption and scattering lengths l_A and l_S respectively, as outlined in section 3.3.2. The values for l_A range from 4 m to 30 m, with l_S consistently found between 52 cm and 53 cm. Thus l_A is much larger than the detectors inner diameter and the ascertained l_S much larger than the 35 cm expected for the Rayleigh scattering length [101]. The reflectivity of the OFHC Cu PMT holder is considered purely specular.

This chapter outlines a new proposed calibration technique that attempted to cross check these optical parameters via a completely novel approach that utilised time information in calibration for the first time within XMASS. It exploited high energy alpha events that emit their light into 2π steradians (sr) illuminating half the detector's inner surface directly. The other half of the detector receives only indirect - scattered or reflected - light.

Section 4.1 outlines the theory underpinning said calibration technique. Section 4.2 describes the alpha events used, their high degree of spatial asymmetry and the MC simulated time information. Section 4.3 details how the alpha events and the MC time information can be compared using a Kolmogorov-Smirnov test to extract the optical parameters and explains why this technique failed to extract the optical

parameters. Finally section 4.4 outlines how its approach could be adapted in the future.

4.1 Waveform theory

A waveform is how the readout electronics' FADC boards record the response of a single PMT in the detector to scintillation light. The timing distribution of these waveforms recorded in an event is dictated by the scintillation emission profile, photon propagation profiles and a common time offset, this is discussed along with the shape of said waveforms in section 4.1.1. Section 4.1.2 defines the convolution properties of said waveform and applies them to superimpose many waveforms and rewrite this summation in a more useful way, extracting the important components. Section 4.1.3 outlines discrete Fourier transformation formulae which are necessary to apply the technique in practise.

4.1.1 A waveform's constituent parts

The cumulative waveform $\Psi_{ei}(t, \underline{x}, \underline{\tau}, \underline{o}, \underline{j}, t_e)$ recorded in event (e) by PMT (i) is the convolution of three main contributions and a common time shift:

$$\Psi_{ei}(t, \underline{\tau}, \underline{o}, \underline{j}, t_e) = D(t, \underline{\tau}) * P_i(t, \underline{x}, \underline{o}) * W(t, \underline{j}) * T_e(t, t_e). \tag{4.1}$$

- $D(t, \underline{\tau})$**:** is the scintillation photon production time profile with $t = 0$ defined against the parent particle initiating the event. It is dependent on both the parent particle and the event energy; the LXe scintillation mechanisms governing $D(t, \underline{\tau})$ are defined in section 3.1.3. The excited Xe dimer (Xe_2^*) has both a singlet and a triplet state each with its own decay constant and branching fraction (τ_1, F_1) and (τ_2, F_2) respectively, where $F_2 = 1 - F_1$. These three parameters define $\underline{\tau}$ and determine the number of scintillation photons produced over time. $D(t, \underline{\tau})$ does not impact how the photons traverse the detector and is PMT independent.

- $P_i(t, \underline{x}, \underline{o})$**:** is the photon propagation profile, constructed from the travel time of individual photons registering a signal in a distinct PMT i at time t. $t = 0$ and $\underline{x}$ are defined as the scintillation photon production time and position respectively. The path scintillation photons traverse within the LXe is dependent on the optical parameters ($\underline{o}$): l_A, l_S, the OFHC Cu PMT holder's reflectivity (c_R) and the proportion of this reflection that is specular (c_S).

- $W(t, \underline{j})$**:** is the recorded waveform response to a scintillation photon registering a signal in a PMT, $t = 0$ is defined as the time the scintillation photon strikes the PMTs photocathode. This produces 1 or 2 photoelectrons which go on to strike the first dynode, after signal amplification in the dynode chain the anode current is recorded by the FADC[1]. The shape of a 1 PE waveform response is displayed in figure 3.11 and the NPEs PDF is displayed in figure 3.10. The transit time spread of a PE transitioning from the photocathode to the first dynode inside a PMT is ~ 3 ns.

- $T_e(t, t_e)$**:** is a common time shift $(t - t_e)$ for an event, where t_e is the time offset between the incident particle instigating the event ($t = 0$ for $D(t, \underline{\tau})$) and the event being triggered upon by the DAQ, discussed in section 3.2.4. This varies between events due to statistical fluctuations in the transit time.

4.1.2 Waveform convolution properties

Outlined below is how individual PMT or event waveforms can be combined and why the overall scale of MC simulated photons used to construct $P_i(t, \underline{x}, \underline{o})$ is unimportant.

- **Associative and commutative:** Convolution is both associative and commutative. Therefore all of the components besides $P_i(t, \underline{x}, \underline{o})$ in equation 4.1 can

[1]Occasionally photons hit the 1st dynode directly registering a smaller waveform much earlier

be extracted and combined into a single unknown time profile $U_e(t, \underline{\tau}, \underline{j}, t_e)$.

$$\begin{aligned}\Psi_{ei}(t, \underline{x}, \underline{\tau}, \underline{o}, \underline{j}, t_e) &= [D(t, \underline{\tau}) * W(t, \underline{j}) * T_e(t, t_e)] * P_i(t, \underline{x}, \underline{o}) \\ &= U_e(t, \underline{\tau}, \underline{j}, t_e) * P_i(t, \underline{x}, \underline{o}), \quad \text{where} \\ U_e(t, \underline{\tau}, \underline{j}, t_e) &= D(t, \underline{\tau}) * W(t, \underline{j}) * T_e(t, t_e).\end{aligned} \tag{4.2}$$

- **Summation:** Convolution between two functions $f(t)$ and $g(t)$ is defined as:

$$\begin{aligned}(f * g)(t) &= \int_{-\infty}^{\infty} f(\tau) g(t - \tau) d\tau \\ &= \int_{-\infty}^{\infty} f(t - \tau) g(\tau) d\tau.\end{aligned} \tag{4.3}$$

In a sum of convolutions over i, where one component is independent of i, said component can be removed to the outside of the summation as outlined below:

$$\begin{aligned}\sum_i [f(t) * g_i(t)] &= \sum_i \left[\int_{-\infty}^{\infty} f(t - \tau) g_i(\tau) d\tau \right] \\ &= \int_{-\infty}^{\infty} \sum_i [f(t - \tau) g_i(\tau)] d\tau \\ &= \int_{-\infty}^{\infty} f(t - \tau) \sum_i [g_i(\tau)] d\tau \\ &= f(t) * \sum_i [g_i(t)].\end{aligned} \tag{4.4}$$

This summation technique can be applied to our resultant waveform. Summing over a group of PMTs within an individual event - where $U_e(t, \underline{\tau}, \underline{j}, t_e)$ by definition does not vary - results in a convolution between $U_e(t, \underline{\tau}, \underline{j}, t_e)$ and a sum over individual PMT photon propagation profiles $P_i(t, \underline{x}, \underline{o})$:

$$\begin{aligned}\sum_i [\Psi_{ei}(t, \underline{x}, \underline{\tau}, \underline{o}, \underline{j}, t_e)] &= \sum_i [U_e(t, \underline{\tau}, \underline{j}, t_e) * P_i(t, \underline{x}, \underline{o})] \\ &= U_e(t, \underline{\tau}, \underline{j}, t_e) * \sum_i [P_i(t, \underline{x}, \underline{o})].\end{aligned} \tag{4.5}$$

This summation technique can also be applied to multiple events when three requirements are met:

1. The events must have the same parent particle/energy, this fixes the scintillation emission time profile $D(t, \underline{\tau})$ between events.

2. The events' point of origin ($\underline{x}$) must be the same or $P_i(t, \underline{x}, \underline{o})$ a superposition of simulations with these different $\underline{x}$ positions.

3. The event time offset (t_e) needs to be the same and can be accounted for by time shifting individual events so they line up.

- **Scaling:** The convolution of two functions remains the same if one of those functions is scaled by a and the other inversely scaled by a:

$$f(t) * g(t) = \left[\frac{1}{a} f(t)\right] * [a g(t)]. \tag{4.6}$$

This implies that the number of photons simulated to construct $P_i(t, \underline{x}, \underline{o})$ is irrelevant. If you simulate too many or too few photons $U_e(t, \underline{\tau}, \underline{j}, t_e)$ will simply scale by the inverse amount:

$$\begin{aligned} \sum_i [\Psi_{ei}(t, \underline{x}, \underline{\tau}, \underline{o}, \underline{j}, t_e)] &= U_e(t, \underline{\tau}, \underline{j}, t_e) * \sum_i [P_i(t, \underline{x}, \underline{o})] \\ &= \left[\frac{1}{a} U_e(t, \underline{\tau}, \underline{j}, t_e)\right] * \sum_i [a P_i(t, \underline{x}, \underline{o})]. \end{aligned} \tag{4.7}$$

4.1.3 Deconvolution and discrete Fourier transform

- **Fourier transform and convolution theorem:** The continuous Fourier transform (FT) and its inverse are defined respectively as:

$$\begin{aligned} f(\xi) &= \int_{-\infty}^{\infty} f(x) e^{-2\pi i x \xi} dx \quad \text{and} \\ f(x) &= \int_{-\infty}^{\infty} f(\xi) e^{2\pi i x \xi} d\xi. \end{aligned} \tag{4.8}$$

The FT of the convolution of two functions is equivalent to the product of the FT of each function and vice versa:

$$\begin{aligned} \mathcal{F}[f * g] &= \mathcal{F}[f]\mathcal{F}[g] \quad \text{and} \\ \mathcal{F}[fg] &= \mathcal{F}[f] * \mathcal{F}[g]. \end{aligned} \tag{4.9}$$

- **Deconvolution using discrete Fourier transforms:** Taking the resultant waveform form equation 4.7 and applying equation 4.9, the unknown time profile $U_e(t, \underline{\tau}, \underline{j}, t_e)$ can be obtained by deconvoluting out $P_i(t, \underline{x}, \underline{o})$:

$$\frac{1}{a} U_e(t, \underline{\tau}, \underline{j}, t_e) = \mathcal{F}^{-1}\left(\frac{\mathcal{F}(\sum_i [\Psi_{ei}(t, \underline{x}, \underline{\tau}, \underline{o}, \underline{j}, t_e)])}{\mathcal{F}(\sum_i [a P_i(t, \underline{x}, \underline{o})])} \right). \tag{4.10}$$

The recorded waveforms are discrete time series with a resolution of 1ns. A complex time series $x_n \coloneqq x_0, x_1, ..., x_n, ..., x_{N-1}$ of length N can be converted into a complex sequence of N discrete frequencies $X_k \coloneqq X_0, X_1, ..., X_k, ..., X_{N-1}$ by taking the discrete FT:

$$X_k = \sum_{n=0}^{N-1} \left[x_n e^{-\frac{2\pi i}{N} nk} \right]. \tag{4.11}$$

$P_i(t, \underline{x}, \underline{o})$ is obtained by simulating scintillation photons. The travel time of these scintillation photons from production to registering a signal at a PMTs photo-cathode are recorded with a resolution $\ll$ 1 ns. However the FT of $\Psi_{ei}(t, \underline{x}, \underline{\tau}, \underline{o}, \underline{j}, t_e)$ is calculated at specific discrete frequencies and the same frequencies must be used for $P_i(t, \underline{x}, \underline{o})$. Therefore $P_i(t, \underline{x}, \underline{o})$ should be binned with a resolution of 1 ns and its discrete FT calculated equivalently. $U_e(t, \underline{\tau}, \underline{j}, t_e)$ can then be calculated by obtaining the ratio of these FTs as outlined in equation 4.10 and applying the discrete inverse FT:

$$x_n = \frac{1}{N} \sum_{k=0}^{N-1} \left[X_k e^{\frac{2\pi i}{N} nk} \right]. \tag{4.12}$$

4.2 High energy alpha events for calibration

In section 4.2.1 the source of the alpha events and their geometric properties of interest are explained. Section 4.2.2 and 4.2.3 outline the waveforms $\Psi_{ei}(t, \underline{x}, \underline{\tau}, \underline{o}, \underline{j}, t_e)$ and the MC generated photon propagation profiles $P_i(t, \underline{x}, \underline{o})$ respectively. The asymmetry

is clearly evident in said timing profiles and these could be used to extract $\underline{o}$ and $\underline{\tau}$ in order to optimise the MC.

4.2.1 Alpha source, event symmetry and azimuthal orientation

The ^{57}Co source used for internal calibration was produced by KRISS in Korea [95] and is displayed in figure 3.16. The source holder's surface (25 – 45 mm) was found to be contaminated with ^{241}Am, presumably during fabrication. ^{241}Am decays primarily via alpha decay with $t_{\frac{1}{2}}$ = 432.2 years and emits at 4 discrete energies 5.486 MeV, 5.443 MeV, 5.389 MeV and 5.545 MeV occurring 86%, 12.5%, 1% and 0.3% of the time respectively [102]:

$$^{241}_{95}\mathrm{Am} \rightarrow {}^{237}_{93}\mathrm{Np} + {}^{4}_{2}\alpha^{2+} + \gamma\,(59.5409\mathrm{keV}). \tag{4.13}$$

The high energy alpha particles are emitted from the surface of the source holder into the LXe. They lose their energy in the LXe almost instantaneously, travelling a very short distance. Therefore an abundance of scintillation photons are produced at a point very close to the surface of the cylindrical source holder. Scintillation photons are emitted isotropically and with the source holder's curvature much larger than the alpha's range in LXe the source holder blocks half of the scintillation light resulting in only one half of the detector receiving direct light from the scintillation emission. Figure 4.1 is the Mollweide projection of the number of photoelectrons (NPEs) in each PMT for one of these alpha events. There is a clearly visible vertical divide between the two hemispheres of high and low NPEs, a bright side and a dark side.

These alpha events can occur at any position on the source holder and hence can have any azimuthal orientation B_ϕ (bright side centre azimuth). The dark side azimuthal orientation is $D_\phi = B_\phi - 180$ deg. B_ϕ can be obtained using the angular position (θ, ϕ) of each PMT along with the recorded NPEs to calculate spherical harmonic (SH) coefficients for the event. By rotating the coordinate system around the z-axis until the SH xy-plane dipole coefficients become purely real one can extract

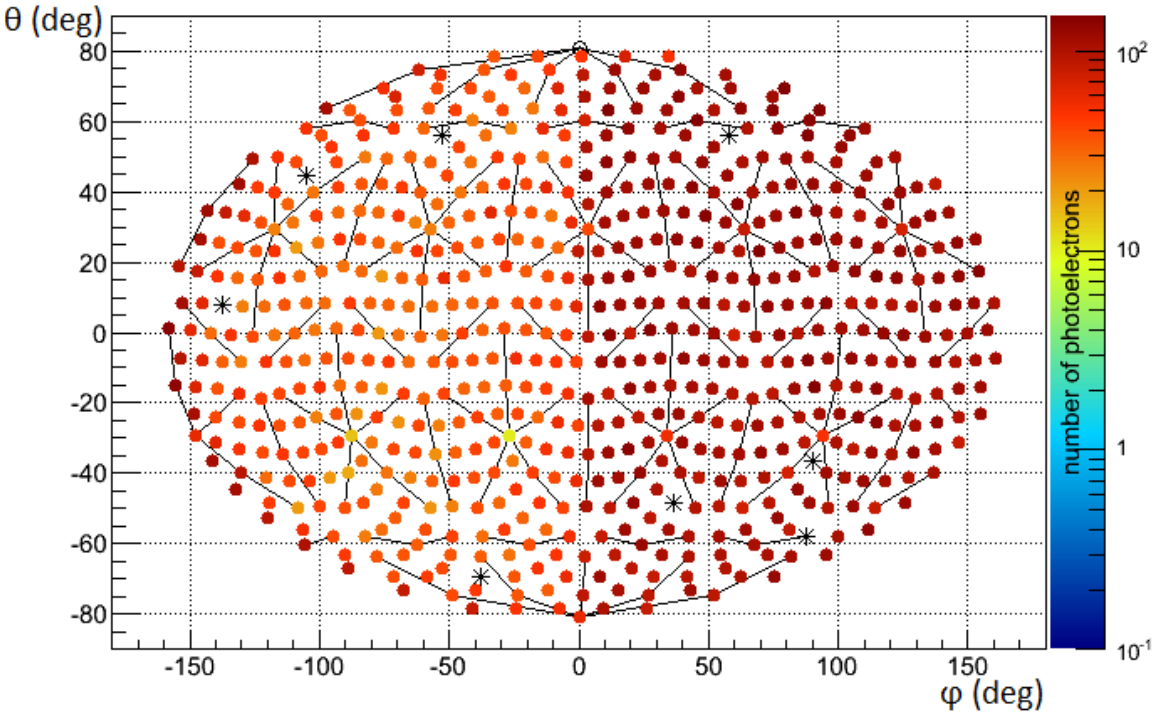


Figure 4.1: ^{57}Co calibration height $Z = 0$ cm alpha event: Mollweide projection of XMASS inner detector PMTs' integrated charge, each dot is an individual PMT with its colour indicating its recorded NPEs. The stars are PMTs that have been turned off and hence no information is available. The lines simply indicate the detector's pentakis-dodecahedron structure: Individual pentagons at the top and bottom of the detector with 2 sets of 5 pentagons offset along the detectors equator are visible.

B_ϕ with a precision ~ few deg (half a PMT's width at the detectors equator).

4.2.2 Bright and dark hemispheres: NPEs and waveforms

As outlined above, the calibration source holder blocks scintillation light emitted into exactly one hemisphere. This results in a sharp divide between one hemisphere of the detector which receives a large amount of direct scintillation light and the other hemisphere which can only observe scintillation light that is scattered within the LXe or reflected off of the ID's inner surface. The side that receives direct scintillation light records ~ 100 NPEs per PMT while the other receives ~ 40 NPEs per PMT (~ 2.5 times less), hence being coined the bright side and dark side respectively. The scattering and reflection mechanisms that affect light propagation occur over different time scales as they are governed by the LXe's optical properties and detector geometry

respectively. This leads to distinctive characteristics not only in the NPE distributions but also in the FADC recorded waveforms.

All current calibration techniques look solely at the NPEs distribution. A direct comparison of the NPEs recorded in each PMT between these recorded and MC simulated alpha events is flawed as the exact energy of the event is unknown. A possible technique that would work irrespective of event energy is to take an NPEs ratio. This could be a ratio of individual PMTs, i.e. ones directly opposite or well-defined groups of PMTs.

However, these events possess large stores of timing information that is independent of event energy and should be made use of. Figure 4.2 shows the summed up waveforms of the PMTs on the bright side $\Psi_{eB}(t, \underline{x}, \underline{\tau}, \underline{o}, \underline{j}, t_e)$ and dark side $\Psi_{eD}(t, \underline{x}, \underline{\tau}, \underline{o}, \underline{j}, t_e)$ of the detector in blue and green respectively. The superimposed PMTs in this figure are located in the central portion of the detector -35 cm $\leq \text{PMT}_Z \leq 35$ cm and away from the hemispherical divide $-80° \leq \text{Side}_\phi - \text{PMT}_\phi \leq 80°$), where $\text{Side}_\phi = B_\phi$ or D_ϕ for $\Psi_{eB}(t, \underline{x}, \underline{\tau}, \underline{o}, \underline{j}, t_e)$ and $\Psi_{eD}(t, \underline{x}, \underline{\tau}, \underline{o}, \underline{j}, t_e)$ respectively. Some PMTs are disabled and saturated PMTs are ignored.

$\Psi_{eB}(t, \underline{x}, \underline{\tau}, \underline{o}, \underline{j}, t_e)$ and $\Psi_{eD}(t, \underline{x}, \underline{\tau}, \underline{o}, \underline{j}, t_e)$ display very different timing profiles, the reason for this is explained in the following section. The absolute scale of said waveforms is unimportant, only relative information is relevant.

4.2.3 Bright and dark hemispheres: MC timing information

The majority of scintillation photons that register signals in the PMTs located on the bright side of the detector don't scatter or reflect, they simply travel directly from their point of origin and strike a PMT's photocathode. Therefore $P_i(t, \underline{x}, \underline{o})$ for the bright side PMTs has a singular peak at early time, the scintillation photons that induce signals at later times have been scattered or reflected. For the PMTs located on the dark side of the detector, no scintillation photon can reach said PMTs without first scattering in the LXe or reflecting off of the ID's bright side's inner surface. These processes work on different length scales and induce two peaks in $P_i(t, \underline{x}, \underline{o})$ for

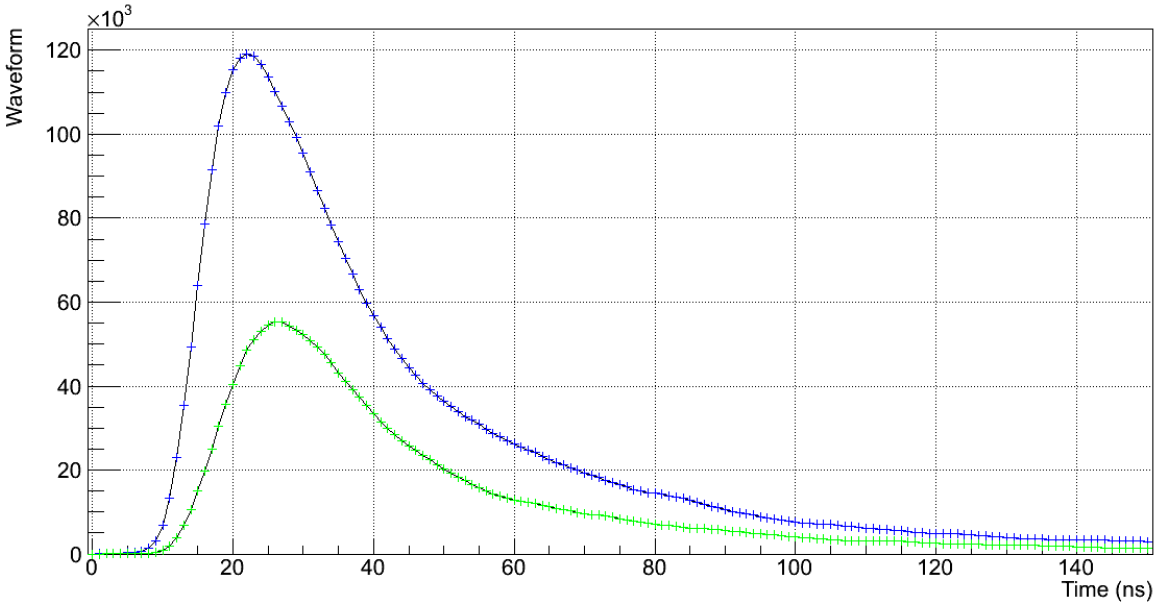


Figure 4.2: Calibration (Z = 0 cm) alpha event. The recorded waveforms for the bright and dark sides: $\Psi_{eB}(t, \underline{x}, \underline{\tau}, \underline{o}, \underline{j}, t_e)$ (blue) and $\Psi_{eD}(t, \underline{x}, \underline{\tau}, \underline{o}, \underline{j}, t_e)$ (green) respectively. The dark side has a wider time profile due to the scattering and reflecting mechanisms.

the dark side PMTs. The first peak occurs from scintillation photons that scatter soon after being produced and are directed towards said dark side PMTs. The second peak occurs because scintillation photons reflected off of the ID's inner surface are directed towards the dark side PMTs, these travel further and arrive later.

Such events were simulated at a point on the surface of the ^{57}Co source holder using the MXASS MC [88, 92, 93], the generated scintillation photon's traversal time throughout the ID and the PMT in which they register a signal was extracted. The generation position was calculated using the azimuthal orientation of the alpha event displayed in figures 4.1 and 4.2. This procedure was undertaken for a range of $\underline{o}$. The summed up bright side and dark side photon propagation profiles $P_B(t, \underline{x}, \underline{o})$ and $P_D(t, \underline{x}, \underline{o})$ respectively, are obtained by superimposing $P_i(t, \underline{x}, \underline{o})$ for PMTs located on the bright side and on the dark side respectively - same PMT positional conditions as before. Figures 4.3 and 4.4 display examples of $P_B(t, \underline{x}, \underline{o})$ and $P_D(t, \underline{x}, \underline{o})$ respectively - normalised by the total number of registered signals - simulated with the following optical parameters (l_A, l_S): (200 cm, 41 cm), (200 cm, 56 cm), (800 cm, 41 cm) and (800 cm, 56 cm), fixed c_R = 0.3 and c_S = 1.0.

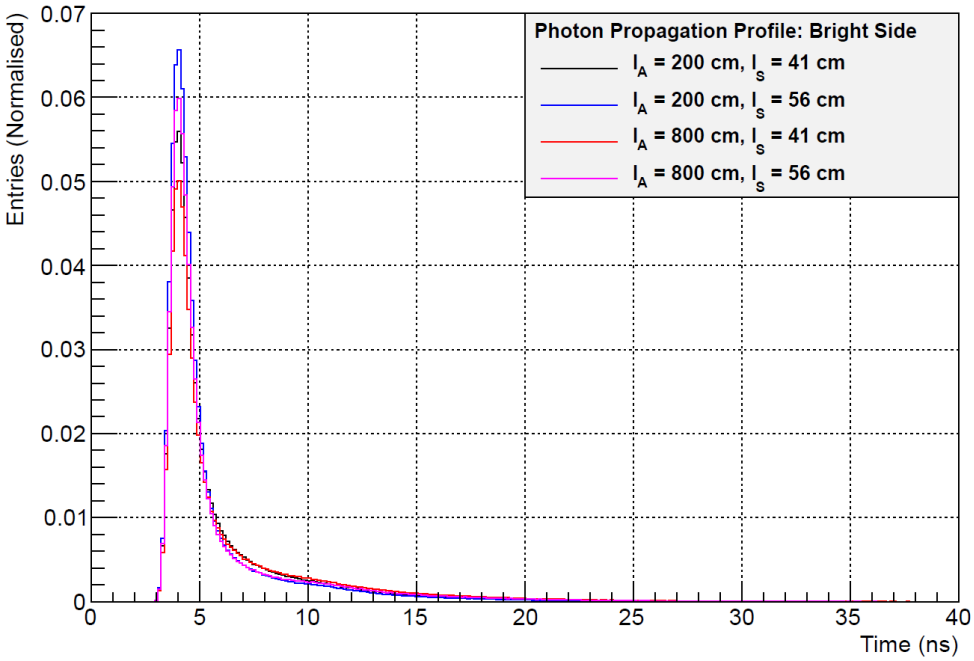


Figure 4.3: MC generated $P_B(t, \underline{x}, \underline{o})$ for fixed $c_R = 0.3$ and $c_S = 1.0$, and varied l_A and l_S. The bombardment of direct scintillation light results in a single clear peak.

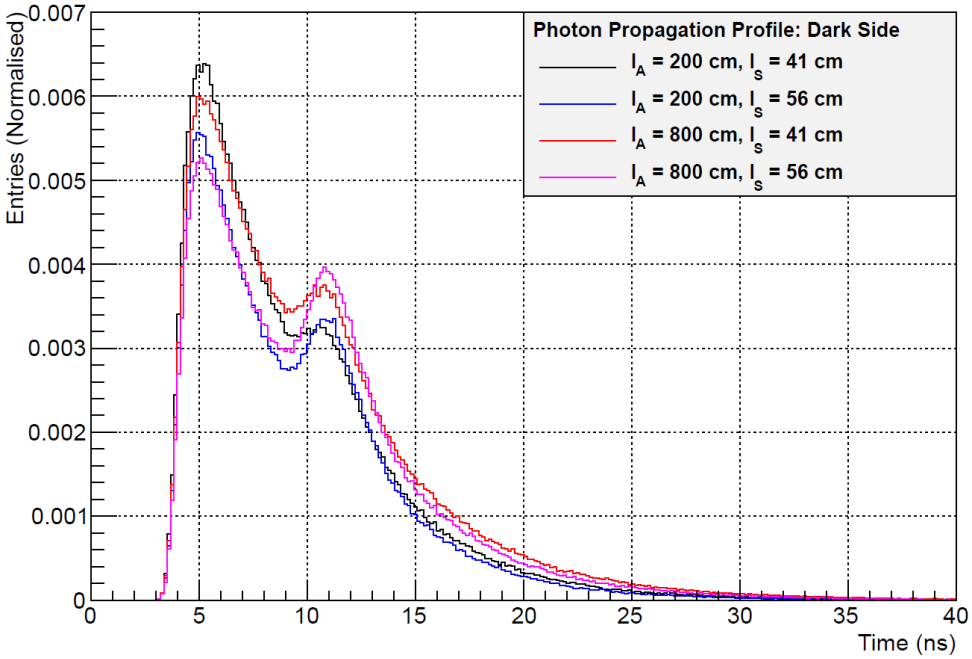


Figure 4.4: MC generated $P_D(t, \underline{x}, \underline{o})$ for fixed $c_R = 0.3$ and $c_S = 1.0$, and varied l_A and l_S. The two peaks observed are a consequence of the scintillation light propagation mechanisms that can induce a change of direction - resulting in light reaching the dark side. The first peak stems from scintillation light scattered backwards soon after production - before the light reaches the ID's inner surface. While the second peak stems from scintillation light reflected backwards off of the ID's inner surface. The reflected scintillation light travels further and hence arrives later.

4.3 Extracting the optical parameters

This section outlines how the time information contained with $\Psi_{eB}(t, \underline{x}, \underline{\tau}, \underline{o}, \underline{j}, t_e)$ and $\Psi_{eD}(t, \underline{x}, \underline{\tau}, \underline{o}, \underline{j}, t_e)$ can be used along with $P_B(t, \underline{x}, \underline{o})$ and $P_D(t, \underline{x}, \underline{o})$ for the purposes of calibration. Section 4.3.1 outlines the necessary deconvolution, section 4.3.2 discusses how the resultant profiles can be compared effectively and section 4.3.4 explains additional complications.

4.3.1 Deconvolution

As stated previously the unknown time profile $U_e(t, \underline{\tau}, \underline{j}, t_e)$ is by definition independent of PMT and optical parameters. Therefore in a single event any calculation of $U_e(t, \underline{\tau}, \underline{j}, t_e)$ using any group of PMTs should yield the same result. This holds irrespective of the number of scintillation photons used to form $P_i(t, \underline{x}, \underline{o})$. If equation 4.10 is implemented for an alpha event's bright side ($\Psi_{eB}(t, \underline{x}, \underline{\tau}, \underline{o}, \underline{j}, t_e)$, $P_B(t, \underline{x}, \underline{o})$) and dark side ($\Psi_{eD}(t, \underline{x}, \underline{\tau}, \underline{o}, \underline{j}, t_e)$, $P_D(t, \underline{x}, \underline{o})$) separately, one obtains $U_{eB}(t, \underline{\tau}, \underline{j}, t_e)$ and $U_{eD}(t, \underline{\tau}, \underline{j}, t_e)$ respectively. These should be identical if the optical parameters used to construct $P_B(t, \underline{x}, \underline{o})$ and $P_D(t, \underline{x}, \underline{o})$ are correct.

$U_{eB}(t, \underline{\tau}, \underline{j}, t_e)$ (blue) and $U_{eD}(t, \underline{\tau}, \underline{j}, t_e)$ (green) constructed using the waveforms displayed in figure 4.2 and the photon propagation profiles displayed in figures 4.3 and 4.4 with optical parameters (l_A, l_S): (200 cm, 41 cm), (200 cm, 56 cm), (800 cm, 41 cm) and (800 cm, 56 cm) are displayed in figures 4.5, 4.6, 4.7 and 4.8 respectively. The left hand plots show 0 – 300 ns and the right hand plots 0 – 100 ns.

The level of statistics in $\Psi_{eB}(t, \underline{x}, \underline{\tau}, \underline{o}, \underline{j}, t_e)$ and $P_B(t, \underline{x}, \underline{o})$ is much greater than in $\Psi_{eD}(t, \underline{x}, \underline{\tau}, \underline{o}, \underline{j}, t_e)$ and $P_D(t, \underline{x}, \underline{o})$. As a consequence $U_{eB}(t, \underline{\tau}, \underline{j}, t_e)$ is much smoother than $U_{eD}(t, \underline{\tau}, \underline{j}, t_e)$ with a smaller degree of fluctuation. All alpha events that occur on the ^{57}Co source holder have similar statistics. It is necessary to combine the waveforms and photon propagation profiles of multiple events to obtain $U_{eD}(t, \underline{\tau}, \underline{j}, t_e)$ profiles smooth enough to perform a direct comparison with $U_{eB}(t, \underline{\tau}, \underline{j}, t_e)$. This will be discussed further in section 4.4.

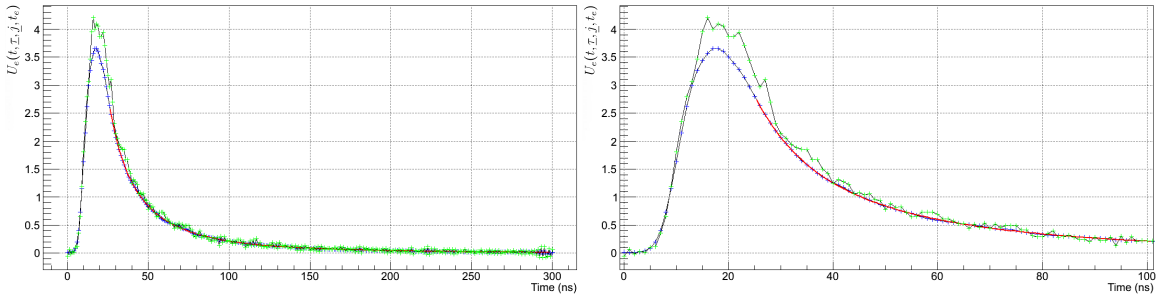


Figure 4.5: $U_{eB}(t, \underline{\tau}, \underline{j}, t_e)$ (blue) and $U_{eD}(t, \underline{\tau}, \underline{j}, t_e)$ (green) for $c_R = 0.3$, $c_S = 1.0$, $l_A = 200$ cm and $l_S = 41$ cm. Left: $0 - 300$ ns, right: $0 - 100$ ns.

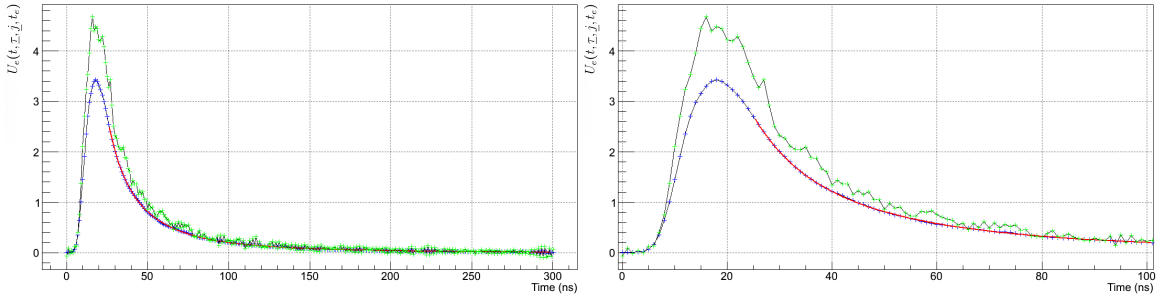


Figure 4.6: $U_{eB}(t, \underline{\tau}, \underline{j}, t_e)$ (blue) and $U_{eD}(t, \underline{\tau}, \underline{j}, t_e)$ (green) for $c_R = 0.3$, $c_S = 1.0$, $l_A = 200$ cm and $l_S = 56$ cm. Left: $0 - 300$ ns, right: $0 - 100$ ns.

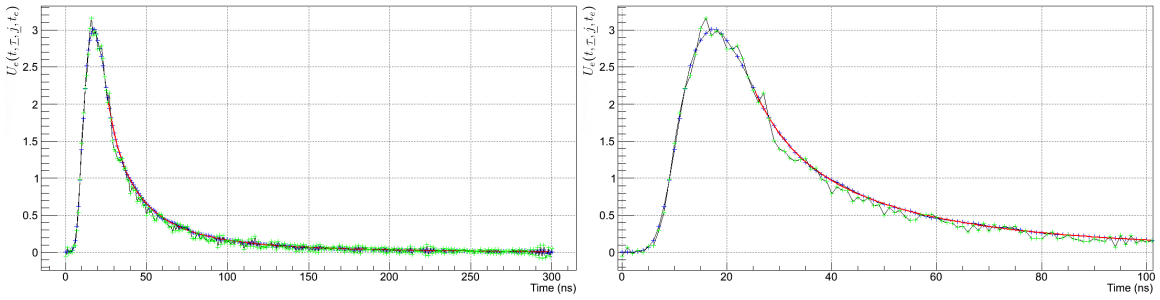


Figure 4.7: $U_{eB}(t, \underline{\tau}, \underline{j}, t_e)$ (blue) and $U_{eD}(t, \underline{\tau}, \underline{j}, t_e)$ (green) for $c_R = 0.3$, $c_S = 1.0$, $l_A = 800$ cm and $l_S = 41$ cm. Left: $0 - 300$ ns, right: $0 - 100$ ns.

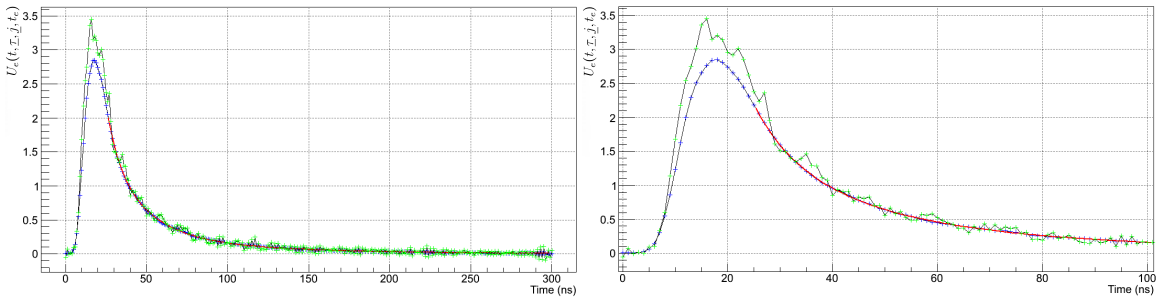


Figure 4.8: $U_{eB}(t, \underline{\tau}, \underline{j}, t_e)$ (blue) and $U_{eD}(t, \underline{\tau}, \underline{j}, t_e)$ (green) for $c_R = 0.3$, $c_S = 1.0$, $l_A = 800$ cm and $l_S = 56$ cm. Left: $0 - 300$ ns, right: $0 - 100$ ns.

4.3.2 Comparison between bright side and dark side

There are two metrics necessary to perform a comparison between $U_{eB}(t, \underline{\tau}, \underline{j}, t_e)$ and $U_{eD}(t, \underline{\tau}, \underline{j}, t_e)$. The first is not time related while the second measures the disparity between said profiles over time.

- **NPEs ratio (R):** The ratio of the integrals of $U_{eB}(t, \underline{\tau}, \underline{j}, t_e)$ and $U_{eD}(t, \underline{\tau}, \underline{j}, t_e)$. As demonstrated in equation 4.14 this is equivalent to a comparison between data and MC of the NPEs ratio of the bright and dark sides:

$$R = \frac{\int_{0\text{ ns}}^{300\text{ ns}} U_{eB}(t, \underline{\tau}, \underline{j}, t_e)dt}{\int_{0\text{ ns}}^{300\text{ ns}} U_{eD}(t, \underline{\tau}, \underline{j}, t_e)dt}. \tag{4.14}$$

- **KS max distance (D):** A Kolmogorov-Smirnov (KS) test of the $U_{eB}(t, \underline{\tau}, \underline{j}, t_e)$ and $U_{eD}(t, \underline{\tau}, \underline{j}, t_e)$ time series. This normalises both profiles, obtains the cumulative distribution function (CDF) of both profiles and finds the maximum distance between said CDFs as outlined in equation 4.15:

$$D = \underset{t}{\text{SUP}} \left| \frac{\int_{0\text{ ns}}^{t\text{ ns}} U_{eD}(t, \underline{\tau}, \underline{j}, t_e)dt}{\int_{0\text{ ns}}^{300\text{ ns}} U_{eD}(t, \underline{\tau}, \underline{j}, t_e)dt} - \frac{\int_{0\text{ ns}}^{t\text{ ns}} U_{eB}(t, \underline{\tau}, \underline{j}, t_e)dt}{\int_{0\text{ ns}}^{300\text{ ns}} U_{eB}(t, \underline{\tau}, \underline{j}, t_e)dt} \right|. \tag{4.15}$$

These two metrics together measure whether the correct proportion of scintillation photons reach each side of the detector and whether their timing profiles correctly reconstruct that contained with the recorded waveforms.

4.3.3 Exponential decay fit

The scintillation emission profile $D(t, \underline{\tau})$ discussed in section 4.1.1 and 3.1.3 is defined by three parameters τ_1, τ_2 and F_1 via equation 4.16:

$$y = \frac{F_1}{\tau_1} e^{-\frac{t}{\tau_1}} + \frac{1 - F_1}{\tau_2} e^{-\frac{t}{\tau_2}}. \tag{4.16}$$

However this simple double exponential does not correspond to the observed $U_{eB}(t, \underline{\tau}, \underline{j}, t_e)$ profile for a few reasons. Firstly a proportion of scintillation emission will occur via the recombination mechanism which introduces additional time

delays and longer decay constants into $D(t,\underline{\tau})$. Secondly $U_{eB}(t,\underline{\tau},\underline{j},t_e)$ is not only constructed from $D(t,\underline{\tau})$ but also the PMTs' waveform response to a signal $W(t,\underline{j})$ - displayed in figure 3.11. Thirdly all profile features are broadened due to a ~ 3 ns uncertainty in the transit time spread for a photoelectron to transition from the photocathode to the 1st dynode.

All of these time effects complicate matters and make fitting $U_{eB}(t,\underline{\tau},\underline{j},t_e)$ difficult. However, the convolution of an exponential with the sum of two exponentials results in the sum of 3 exponentials. Therefore it is possible that certain longer decay constants may remain relatively unaffected by all of the additional processes mentioned above. Equation 4.17 outlines this generally, where $h(t)$ is the Heaviside step function:

$$\begin{aligned} ae^{bt}h(t) * \left[ce^{dt} + fe^{gt}\right]h(t) &= \int_{-\infty}^{\infty} ae^{b\tau}h(\tau)\left[ce^{d(t-\tau)} + fe^{g(t-\tau)}\right]h(t-\tau)d\tau \\ &= h(t)\int_0^t ae^{b\tau}\left[ce^{d(t-\tau)} + fe^{g(t-\tau)}\right]d\tau \\ &= ah(t)\left[\frac{c}{b-d}e^{dt}\left[e^{(b-d)t} - 1\right] + \frac{f}{b-g}e^{gt}\left[e^{(b-g)t} - 1\right]\right] \\ &= ah(t)\left[\frac{c(b-g)+f(b-d)}{(b-d)(b-g)}e^{bt} - \frac{c}{b-d}e^{dt} - \frac{f}{b-g}e^{gt}\right]. \end{aligned} \tag{4.17}$$

$W(t,\underline{j})$ exhibits an initial rise followed by an exponential decay as the PMT signal is deposited onto a capacitor that is discharged into the FADC input. The effects of the initial rise and peak are broadened in the $U_{eB}(t,\underline{\tau},\underline{j},t_e)$ profile due to the transit time spread and the peak is maximal at ~ 18 ns. The short decay constants associated with both the scintillation mechanism and $W(t,\underline{j})$ will be heavily affected by the transit time spread and can't be extracted, the precise form of the function to fit in the region < 25 ns is unknown.

Figure 4.9 displays the left hand plot of figure 4.7 but with a log scale. After 25ns one can clearly observe 3 regions of differing exponential decay: 25 – 40 ns, 40 – 90 ns and 90 – 300 ns. This should be fully characterised by equation 4.18 which contains

7 free parameters:

$$y = c_1 e^{-\frac{t-t_e}{\tau_1}} + c_2 e^{-\frac{t-t_e}{\tau_2}} + c_3 e^{-\frac{t-t_e}{\tau_3}} . \tag{4.18}$$

$U_{eB}(t, \underline{\tau}, \underline{j}, t_e)$ is fitted (red) using the above equation; however, by looking at the graph, one can extract these decay constants directly.

- ~ **18 ns:** $U_{eB}(t, \underline{\tau}, \underline{j}, t_e)$ reduces from 2 to 1 between 27 - 39 ns.
- ~ **36 ns:** $U_{eB}(t, \underline{\tau}, \underline{j}, t_e)$ reduces from 0.5 to 0.2 between 59 - 92 ns.
- ~ **70 ns:** $U_{eB}(t, \underline{\tau}, \underline{j}, t_e)$ reduces from 0.07 to 0.02 between 147 - 234 ns.

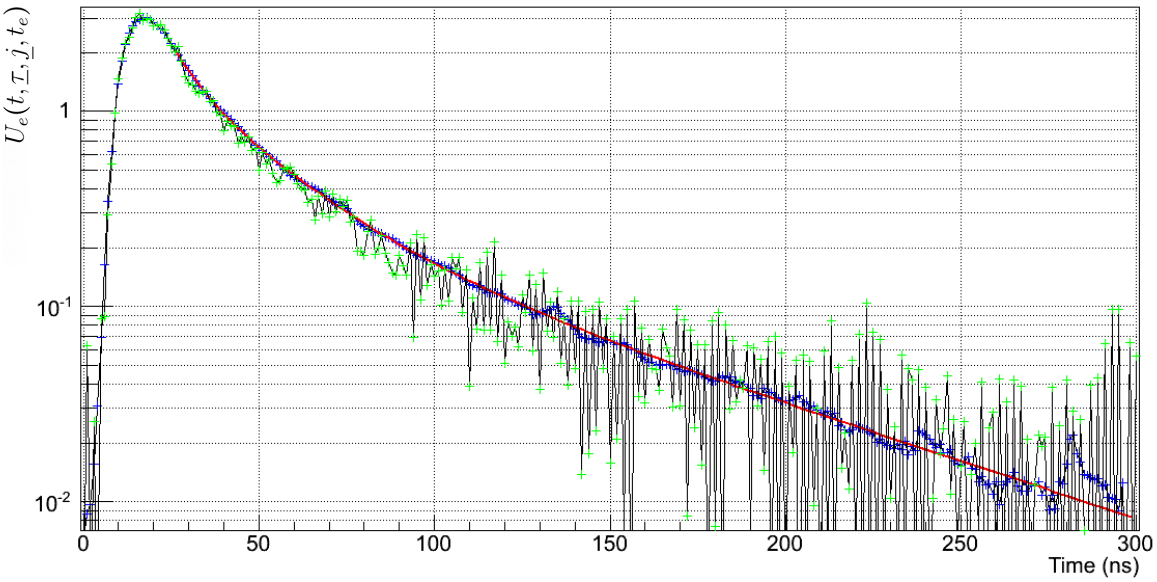


Figure 4.9: $U_{eB}(t, \underline{\tau}, \underline{j}, t_e)$ (blue) and $U_{eD}(t, \underline{\tau}, \underline{j}, t_e)$ (green) for c_R = 0.3, c_S = 1.0, l_A = 800 cm and l_S = 41 cm. Log scale, 0 – 300 ns, exponential fit (red) according to equation 4.18. Decay time constants of values 18 ns, 36 ns and 70 ns are extracted.

Many different processes shape the $U_{eB}(t, \underline{\tau}, \underline{j}, t_e)$ profile, therefore it is unlikely that the extracted decay constants can be attributed 100% to any specific distinct mechanism. Additionally here, these values were obtained from only one event and hence have an unknown degree of uncertainty, which can't be established from the fitting parameters' errors. More work is needed before an effective uncertainty can be attributed to these values. However the two smaller decay constants are similar to

values for the scintillation emission triplet decay constant ~ 20 ns and recombination decay constant ~ 40 ns discussed in section 3.1.3 and are likely at least partially attributable to these mechanisms. There is no such correspondence for the longest extracted decay constant and we know of no additional mechanism to explain it.

4.3.4 Further complications

The non-linear behaviour of the FADC readout electronics complicates the calibration technique even further. The FADC's have an upper limit of 1 V for each PMT, this equates to 50 NPEs if the scintillation photons register signals at identical times - pulses stacked on top of one another. However, due to scintillation emission mechanisms these signals arrive over an extended time period, hence the actual limit is somewhat larger. While no saturated PMTs where observed on the dark side, the level of signal recorded on the bright side is so large that some events result in many saturated FADC channels. One could remove the set of PMTs that are saturated but then you bias the sample of individual PMT waveforms to those that registered fewer signals; and thus no longer truly reflect the arriving light and its time evolution. Therefore neither $\underline{\tau}$ nor $\underline{o}$ can be extracted by looking at the waveforms of such high energy events.

A possible solution to these problems initially considered was to utilise alpha events recorded when the calibration source is located away from the centre (±20 cm). PMTs would no longer be located an equal distance from the source of the event and hence those further away would receive fewer PEs. Therefore if a subset of those PMTs where selected all saturated PMT effects could be removed. In the +20 cm (−20 cm) case only PMTs located below (above) the z = 0 cm line should be utilised. Unfortunately the very solution that solves one problem induces another. The fact that PMTs are now differing distances away from the source smears out the observed time effects by a few ns which reduces the potential of this calibration technique. Essentially the events used are too high in energy to be utilised by the calibration technique outlined in this chapter.

4.4 Outlook

The calibration technique presented in this chapter could work by superimposing many events of lower energy to overcome this non-linearity problem, however this introduces problems of its own.

- **Lower energy alpha events:** The lowest energy alpha events have energies ~ 2 MeV which is still relatively high and they are produced by radioactive isotopes (RI) that are long lived $t_{\frac{1}{2}} \sim 10^{15}$ years e.g. ^{144}Nd. Therefore a large amount of RI material would be needed to obtain the statistics necessary for a smooth $U_{eD}(t, \underline{\tau}, \underline{j}, t_e)$ profile. An entirely new source and source holder with a few flat planes rather than a cylinder would simplify the superposition of events and MC generation for $P_i(t, \underline{x}, \underline{o})$.

- **β-rays, γ-rays and neutrons:** These incident particles travel a few cm within the LXe before interacting, hence the emitted scintillation light won't originate directly next to the source and therefore this highly asymmetric pattern is not visible. A comparison between the upper and lower half of the detector - $U_{eU}(t, \underline{\tau}, \underline{j}, t_e)$ and $U_{eL}(t, \underline{\tau}, \underline{j}, t_e)$ respectively - could work if the source is located at different positions along the z-axis. However, this is suboptimal in comparison to the highly asymmetric events the alpha particles produce. Additionally, $P_i(t, \underline{x}, \underline{o})$ would be constructed from many scintillation photons originating from a diffuse region rather than a point and t_e would need to be accounted for by applying a time shift when superposing over many events.

- **LED (λ_{Scint}):** Currently no LED device exists that emits photons at the same wavelength as LXe scintillation photons isotropically into 2π steradians. However, theoretically this would be a very good replacement if searching for $\underline{o}$. Additionally, it would be of no help in obtaining $\underline{\tau}$ and these LED events would also require t_e be accounted for.

Chapter 5

Event Classification

XMASS struggles at discriminating between signal and background events when compared to dual-phase detectors; the latter have an inherent advantage by measuring additional information in the form of deposited charge. Outlined below are the specific cuts that make up the XMASS Standard Cuts (StdCuts) and the additionally implemented likelihood cuts used in the previous modulation analyses. These currently employed XMASS classification techniques utilise spatial PE and time information separately, however the event classifier that I developed uses these in tandem via a 2D probability density function (PDF).

5.1 Traditional XMASS event selection

5.1.1 The XMASS standard cut

- **1. Trigger Id cut:** In section 3.2.4 the conditions necessary to trigger the ID and OD are discussed. The OD acts as an active veto against Cosmic-ray muons, as such only ID events where the OD is not triggered are used for analysis.

- **2. $\mathbf{N_{HitPMTs}}$ cut:** Most XMASS analyses require a minimum number of 4 PMTs registering a signal before an event is triggered upon. However, since the introduction of the Low-Threshold trigger that minimum has been reduced to 3 PMTs to investigate energies down to 0.5 keV_{ee}. This was pioneered in the previous modulation analysis [49, 50]. Analyses that attempt to reconstruct

events' positions to apply a fiducial volume cut require a greater number of hits.

- **3. Noise cut:** PMTs record hits by registering a signal in the form of a negative current. Electronic noise is occasionally observed within events, if a positive current > 0.1 PE/ns is measured such events are rejected.

- **4. Afterpulse cut:** Afterpulses are caused by gases present within the PMTs. During the cascade of electrons from one dynode to another an electron can be knocked off of one of these gases producing a positively charged heavy ion. This is more likely to occur towards the back of the PMT due to the increased quantity of secondary electrons produced at each subsequent dynode. The electric field guiding the electrons pushes the heavy ion in the opposite direction towards the photocathode. Once it reaches the photocathode it produces a photoelectron which induces a signal similar to that of a normal event. However, because of the ion's increased weight compared to electrons the ion's journey takes much longer and the actual time delay with respect to the original PMT pulse - induced by scintillation photons - correlates with the mass of the ion. Most XMASS analyses utilise signals recorded in the -200 to 300 ns window with respect to the trigger. Afterpulses caused by He gas present in the PMT usually occur ~ 400 to 600 ns after the trigger, which is one of the limiting factors for this chosen time window. In several LXe experiments it was found that Xe can enter individual PMTs over time, most likely by weakening the seal between the PMT's entrance window and body in repeated cooling cycles.

  Two timing based cuts (dt and t_{rms}) are implemented to reject such afterpulse events and others that are correlated in time with the previously recorded event. dt is the difference in trigger time between an event and the previous event and t_{rms} is the root mean square of the individual pulse timings. One of the first things XMASS investigated - even before it had installed the FADC waveform digitizers - was event correlation. Events appeared correlated in time when dt < 10 ms, after 10 ms this observed correlation disappeared. Hence XMASS rejects

events that occur less than 10 ms after the previous event: dt < 10 ms events are cut. Additionally XMASS rejects events where the individual pulse timings appear random and hence have a large timing profile: t_{rms} > 100 ns events are cut. These combined cuts are illustrated in figure 5.1. The dt cut reduces the time in which events can occur, a run's livetime takes this into account and is less than the actual run time.

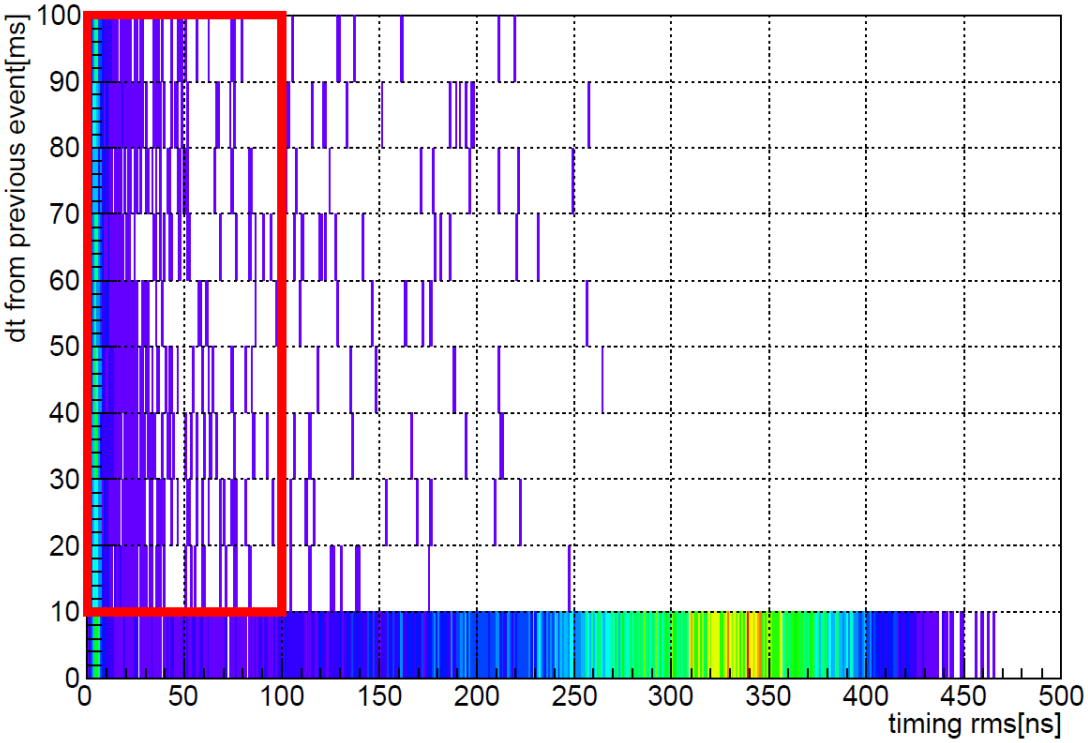


Figure 5.1: Observed events in a normal run. Afterpulse events rejected using two timing based cuts: dt < 10 ms and t_{rms} > 100 ns. These cuts remove events outside of the red box. Events within the red box survive and are used for physics analyses [50].

- **5. Cherenkov cut ($N_{HitPMTs}$ < 200):** Cherenkov light can be generated within the PMTs' quartz window (predominantly BG type 2: β-rays from ^{40}K) and its emission profile is instantaneous in contrast to light produced via scintillation. Therefore a large proportion of the hits are observed initially within a very short time frame: short time structure. This characteristic can be quan-

tified for any event by looking at the Cherenkov variable:

$$C = \frac{\text{Number of hit PMTs in the first 20 ns } (\mathrm{N}_{\mathrm{HitPMTs}}^{t<20\text{ ns}})}{\text{Total number of hit PMTs } (\mathrm{N}_{\mathrm{HitPMTs}})}. \tag{5.1}$$

Figure 5.2 shows the Cherenkov variable distribution for all internal detector component BG types 0-23 ($\mathrm{N}_{\mathrm{HitPMTs}} < 200$). While the higher energy events predominantly exhibit long time structures (low C), at low energy short time structure events (high C) are prevalent. The Cherenkov events are predominantly clustered in the top left of figure 5.2 and the Cherenkov cut deals with them by requiring $C \leq 0.6$. The Cherenkov cut is only applied to events that have $\mathrm{N}_{\mathrm{HitPMTs}} < 200$ as Cherenkov events make up a progressively smaller proportion of the BG as energy increases and hence the effectiveness of this cut diminishes.

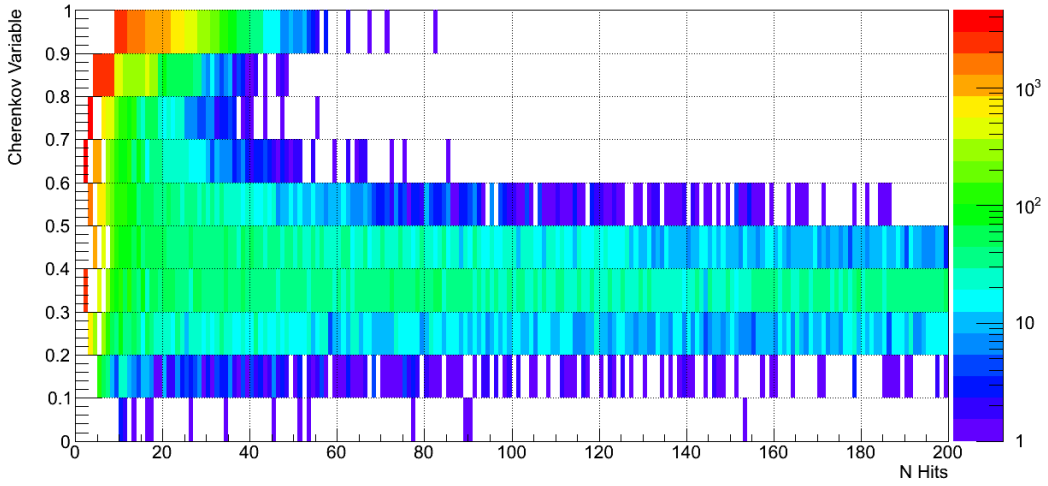


Figure 5.2: Cherenkov variable distribution for all internal BGMC types 0-23. A large number of events at low energy have a very short time structure (Cherenkov variable → 1).

- **6. Flasher cut ($\mathbf{N_{Hits}} = 3$):** Weak flashing behaviour was observed within individual PMTs in an after pulse study of PMT R10789. Flashes that occur close to the PMTs' anode can inadvertently produce a single photoelectron with a probability of 0.3 - 1.0%, these are detected by the same PMT with a transit time delay of ~ 40-50 ns. The previous modulation analysis [50] postulated that

these flashes can escape the initial PMT and induce hits in other PMTs. As reported in [103] such weak flashing behaviour and induced flasher events have been observed by multiple other experiments that utilise PMTs. Unfortunately the origin of such flashes is not completely understood and no systematic study has been published to explain this light emission mechanism. One hypothesis is simply that an electrical breakdown within the PMT occurs which results in light being emitted. To study these effects random 2 hit events were obtained via a special clock trigger.

These 2 hit events have 2 distinct PMTs registering signals where one registers a signal after the other and two variables (dt and $d\theta_N$) where used to analyse such events. We have postulated that light is emitted from the PMT which registered the first hit and one would presume that light is more likely to be emitted along the axis normal to the PMT's photocathode and less likely parallel to the PMT's photocathode. The positional information (photocathode centre) for both PMTs is known and hence we can obtain $d\theta_N$: the angular deviation of the second PMT away from the first PMTs normal axis (origin at first PMT's photocathode centre), and dt: the time separation between the 2 distinct hits.

Two plots are displayed in figure 5.3. The plot on the left shows the $d\theta_N$ variable calculated for every possible PMT pairing in the detector, it is then normalised into a probability density distribution. This probability is minimal along the normal axis (0 deg) as there is only one PMT located directly opposite, there is also only a small number of PMTs parallel to the normal axis (90 deg) surrounding said PMT and it is maximal at 45deg as many PMTs are located within the 40 - 50 deg cone region. Among the 2 hit events a timing peak was observed at dt $\sim$ 50 ns and only the events with $35 <$ dt < 200 ns are utilised to ascertain the $d\theta_N$ distribution. The $d\theta_N$ distribution for the raw data is plotted in black in the right hand plot. The red line within the same plot shows said raw data scaled (divided) by the $d\theta_N$ probability density distribution (in the left

hand plot), this corrects for the quantity of PMTs present in any given angular region.

The flashes emit predominantly along the PMT's normal direction as indicated by the linear increase from 50 deg to 0 deg. Entries above 50 deg are flat and unrelated to such flasher events. Only 3 hit events are subject to the following flasher cut: if any combination of 2 hits has dt > 35 ns and $d\theta_N < 50$ deg the event is considered a flasher event and is rejected.

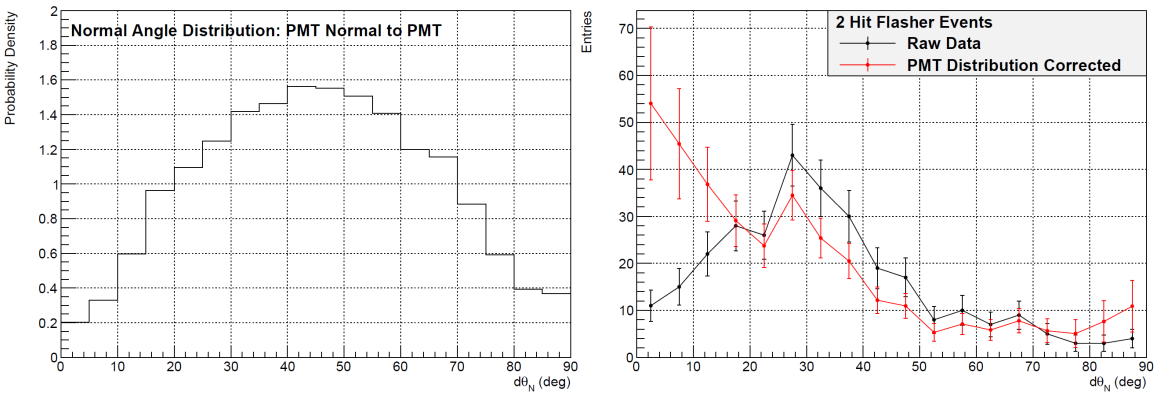


Figure 5.3: Left: Distribution of all other PMTs' locations in terms of its angle to the normal on the PMT's photocathode centre. The high symmetry of the almost spherical detector's inner surface makes this a universal distribution, applicable to every PMT in the detector. Right: Distribution of PMT locations that may have recorded a flash originating from the PMT with respect to which the direction is measured. The red distribution is derived from the black one by normalization with the overall PMT location distribution shown on the left. See text for more detail.

5.1.2 Likelihood cut

The first modulation analysis conducted by XMASS utilised a MaxPE/TotalPE likelihood cut [73, 74]. This was an attempt at spatial clustering by asserting that if a large proportion of hits are observed in a single PMT then the event most likely originates from the detector's internal surface. The previous modulation analysis [49, 50] introduced 2 additional variables, sphericity and aplanarity, which are outlined below. The likelihood (L) is calculated via:

$$L = f_{sph}(S(\boldsymbol{q})) \times f_{apl}(A(\boldsymbol{q})) \times f_{max}(M(\boldsymbol{q})). \tag{5.2}$$

Where $\boldsymbol{q} = (q_1, ..., q_{642})$ is the PE recorded in each PMT, $S(\boldsymbol{q})$ with f_{sph}, $A(\boldsymbol{q})$ with f_{apl} and $M(\boldsymbol{q})$ with f_{max} are the sphericity, aplanarity and MaxPE/TotalPE parameters coupled with their probability density functions respectively.

Applying a Cartesian coordinate system to the XMASS detector with the origin at the centre of the detector, the position of each PMT can be used to weight the PE observed in each PMT along each Cartesian direction: q^i_α where $i = 1, 2, 3$ corresponds to the x, y and z components (α is the PMTid). The sphericity tensor is:

$$S^{ij} = \frac{\sum_\alpha q^i_\alpha q^j_\alpha}{\sum_\alpha q^2_\alpha}. \tag{5.3}$$

S^{ij} has 3 eigenvalues $\lambda_1 \geq \lambda_2 \geq \lambda_3$ ($\lambda_1 + \lambda_2 + \lambda_3 = 1$). The sphericity parameter for an event is defined as $S(\boldsymbol{q}) = \frac{3}{2}(\lambda_2 + \lambda_3)$ and the aplanarity parameter is defined as $A(\boldsymbol{q}) = \frac{3}{2}\lambda_3$. If an event is perfectly spherical $S(\boldsymbol{q})$ becomes 1 and $A(\boldsymbol{q})$ becomes $\frac{1}{2}$. If the event topology resembles a line $S(\boldsymbol{q})$ becomes 1 and if it resembles a plane $A(\boldsymbol{q})$ becomes 0. The major deficiency with this approach is that it does not generalise the axis orientation, so a plane is only considered a plane when normal to an axis. This could be improved by orientating the z-axis around the maximum $\sum_\alpha q^\Omega_\alpha$ where Ω is any angular orientation. Finally, $M(\boldsymbol{q}) = \frac{q_{max}}{\sum_\alpha q_\alpha}$ is the MaxPE/TotalPE parameter, the largest fraction of PEs in the respective event recorded on a contributing PMT.

Figure 5.4 includes 4 plots, the first 3 from left to right are the probability density functions for the sphericity, aplanarity and MaxPE/TotalPE parameters respectively, while the plot on the right shows the combined signal to background log likelihood ratio: $-\text{Ln}(\frac{L_s}{L_b})$. They include signal events (blue = electron events distributed uniformly throughout the ID), background events (red = electron events simulated on the inner surface of the ID and normal run data events (black). The likelihood ($-\text{Ln}(\frac{L_s}{L_b})$) cut position is chosen to retain 50% signal efficiency.

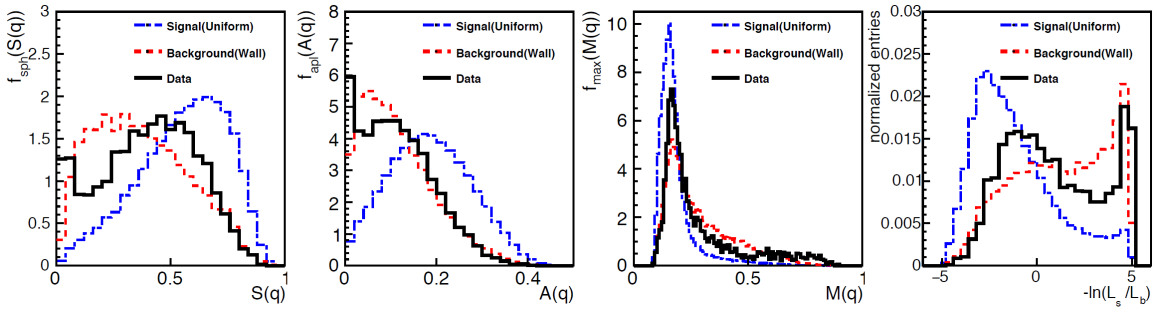


Figure 5.4: The four plots from left to right demonstrate f_{sph}, f_{apl}, f_{max} and $-\mathrm{Ln}(\frac{L_s}{L_b})$. Signal events (blue) and background events (red) simulated using l_A = 6 m are compared to data (black) in the 2.0 ± 0.1 keV$_{ee}$ energy region.

5.2 New PDF classification of signal and BG events

The StdCuts primarily consider event timings and use very general measures of the hit timings inside an individual event [1]. The likelihood cut only utilises spatial aspects of the PE distribution within individual events.

The fundamental idea behind my PDF classifier is to correlate both the spatial position and time information of all individual hits within an event. The reason for this is that there is likely correlation between these two sources of information and in treating them in unison useful information may be gleamed. For example an event originating at the centre of the detector would likely induce signals in all PMTs with equal likelihood and the timing profile solely dictated by scintillation emission. However the further from the centre the event originates, the more clustered the PMTs that register signals will be and the timing information will become skewed, shorter for PMTs located closer to the events origin and longer for those further away. This will become maximal for the BG events originating at the inner surface of the ID: the clustering will be extreme and the odd PMTs that do register signals away from the events origin will be skewed much later in time. Therefore differences are to be expected between MC signal events simulated throughout the LXe within the ID and BGMC events originating from multiple detector components (types 0-23 listed

[1]The flasher cut, only applied to 3 hit events, was the only old cut that correlated time and distance directly after it was understood that UV emission from one PMT's signal amplification can cause a hit in another PMT.

in section 3.4.2). These are used to fill a group of PDFs that attempt to fully capture the phase space of the ID and illustrate the event geometries.

All the MC events have all the StdCuts applied excluding the Cherenkov cut. This is because the Cherenkov cut is singular within the StdCuts that it looks specifically at BG events simulated within the internal XMASS BGMC. Therefore the performance of my PDF classifier will be compared against the Cherenkov cut + likelihood cut.

5.2.1 MC datasets

- **BG PDF events:** At the time this study was performed the BGMC was only generated and readily available for runs occurring before April 2016. As demonstrated in figure 3.6, the observed LY, l_A and l_S where stable from July 2015 - April 2016. Therefore the BGMC available for these runs was used to produce the BG PDFs. For each individual detector component BG (types 0-23), 2 PDFs where produced, events with $N_{Hits} \leq 40$ and events with $N_{Hits} > 40$, this encapsulates the observed short and long time structure of events respectively, depicted in figure 5.2.

- **BG test events:** BGMC generated for runs occurring before July 2015 (not used to construct the PDFs) was used to test my PDF classifier, BG types 0-29.

- **Signal PDF events:** To fully encapsulate the pentakis-dodecahedron structure of the ID, there are 2 main types of signal PDFs: radial and PMT distance. The detector can be considered essentially spherical away from the inner surface. Electrons were simulated on 15 distinct spherical shells from 0 cm to 35 cm with 2.5 cm intervals ([0,35,2.5] cm). The ID's inner surface is made up of flat PMT photocathodes and OFHC Cu plates and can't be considered spherical. Instead of radial distance, the perpendicular distance to the closest PMT's photocathode plane (l_{PMT}) is used. Electrons where simulated in a 30 - 42.5 cm radial shell, if $l_{PMT} < 7$ cm the event is associated with 1 of 7 PDFs (1 cm wide); depending on the specific l_{PMT}. Events simulated in the vicinity of

the operational PMTs and the bad PMTs that have been disabled are treated separately by further subdividing the l_{PMT} PDFs. In total 15 radial PDFs and 14 PMT PDFs (7 normal and 7 bad) were generated, although there is phase space overlap between them, this is permissible as the classification technique developed looks for the singular best fit PDF. The electron energies used for the MC simulation were uniformly distributed between 0 and 5 keV_{ee} and the optical parameters used in the simulation correspond to those measured during the runs used for the BGMC PDFs (l_A = 2000 cm and l_S = 52 cm).

- **Signal test events:** Electrons and ^{132}Xe atoms where simulated uniformly throughout the LXe with energies uniformly distributed 0-30 keV_{ee} and 0-125 $\mathrm{keV}_{\mathrm{nr}}$ respectively. To mirror the BGMC optical parameters pre July 2015, 3 sets of optical parameters where used in equal proportions: 1. l_A = 2000 cm, l_S = 52 cm, 2. l_A = 1000 cm, l_S = 52.5 cm, 3. l_A = 500 cm, l_S = 53 cm.

5.2.2 Event hit information

The peak searching algorithm discussed in section 3.2.4 determines the time of individual hits within an event. At low energy $\mathrm{N}_{\mathrm{Hits}}$ is small and the likelihood of multiple hits overlapping one another in the same PMT is negligible. The uncertainty of individual hit times is ~3 ns and is dominated by the PMTs' transit time uncertainty. The conditions necessary for an ID event to be triggered is discussed in section 3.2.4, there will always be a minimum of 3 hits. As the time between successive hits varies with energy the event time (t_{e}) was defined as the time the first hit occurred. Therefore, with respect to t_{e} the first hit time is 0 with all subsequent hit times relative to this. The PDF classifier is trained using the MC events outlined above, the hits that occur in PMTs that were disabled at the end of XMASS data taking where ignored entirely, when both filling the PDFs and testing their classification potential.

- **Absolute spatial positions:** Events can be considered a sequence of hits comprised of 2 pieces of information, the time (relative to the first hit) and the

spatial position - the hit PMT's identification number (PMTid). As discussed previously the detector is close to spherical with the PMTs' radial distance from the centre ranging from 38 - 42 cm. As such the PMTs' radial information is irrelevant and the spatial position of the PMTs are best represented by the angular components of their spherical polar coordinates (θ, ϕ), polar angle ($\frac{-\pi}{2} \rightarrow \frac{\pi}{2}$) and azimuthal angle ($0 \rightarrow 2\pi$) respectively. θ is relative to the detectors equator and ϕ is relative to an azimuth of no consequence. The first 2 lines in figure 5.5 demonstrate (t, PMTid) $\rightarrow$ (t, θ, ϕ) for an event with 8 hits.

- **Relative central angle:** As (θ, ϕ) are defined by the detector and not dictated by the events themselves, any structure or clustering observed would be averaged out in a PDF comprised of many superimposed randomly orientated events. If one considers 2 points on the surface of a sphere - i.e. 2 PMTs that observe hits within an event - the exact orientation of the sphere / coordinate system is unimportant, the only information that relates these 2 points is the spherical distance. Ignoring the radial factor this corresponds to the central angle ($0 \rightarrow \pi$) between the two points, calculated using equation 5.4:

$$\Delta\sigma = \arccos(\sin(\theta_1)\sin(\theta_2) + \cos(\theta_1)\cos(\theta_2)\cos(\phi_2 - \phi_1)). \tag{5.4}$$

This condenses 2 absolute angular variables into 1 relative measure and allows for the effective superposition of multiple events' when constructing PDFs - reflecting their hit geometries. The absolute detector characteristics are removed and the reduction in parameters means fewer MC simulations are required to obtain enough hits to fill the PDFs for the purposes of statistics. If you consider one particular hit within an event, it can be compared to any other hit or combination of hits. However 3 specific points of reference were chosen, the previous hit ($\Delta\sigma_{\mathrm{P}}$), the first hit ($\Delta\sigma_{\mathrm{F}}$) and the average θ and ϕ of all hits ($\Delta\sigma_{\mathrm{A}}$). The last 2 lines in figure 5.5 demonstrate (t, θ, ϕ) $\rightarrow$ (t, $\Delta\sigma_{\mathrm{P}}$, $\Delta\sigma_{\mathrm{F}}$, $\Delta\sigma_{\mathrm{A}}$) for an event with 8 hits.

$$\begin{pmatrix} t\ (\text{ns}) \\ \text{PMTid} \end{pmatrix}: \begin{pmatrix} 0 \\ 27 \end{pmatrix} \begin{pmatrix} 4 \\ 532 \end{pmatrix} \begin{pmatrix} 10 \\ 2 \end{pmatrix} \begin{pmatrix} 17 \\ 86 \end{pmatrix} \begin{pmatrix} 23 \\ 94 \end{pmatrix} \begin{pmatrix} 35 \\ 157 \end{pmatrix} \begin{pmatrix} 47 \\ 429 \end{pmatrix} \begin{pmatrix} 65 \\ 364 \end{pmatrix}$$

$$\begin{pmatrix} t\ (\text{ns}) \\ \theta\ (\text{rad}) \\ \phi\ (\text{rad}) \end{pmatrix}: \begin{pmatrix} 0 \\ 1.07 \\ 2.55 \end{pmatrix} \begin{pmatrix} 4 \\ -0.82 \\ 6.26 \end{pmatrix} \begin{pmatrix} 10 \\ 1.31 \\ 6.04 \end{pmatrix} \begin{pmatrix} 17 \\ 0.26 \\ 5.10 \end{pmatrix} \begin{pmatrix} 23 \\ 0.41 \\ 5.17 \end{pmatrix} \begin{pmatrix} 35 \\ 0.93 \\ 2.05 \end{pmatrix} \begin{pmatrix} 47 \\ -0.53 \\ 3.86 \end{pmatrix} \begin{pmatrix} 65 \\ 0.01 \\ 2.73 \end{pmatrix}$$

$$\begin{pmatrix} t\ (\text{ns}) \\ \Delta\sigma_{\text{P}}\ (\text{rad}) \\ \Delta\sigma_{\text{F}}\ (\text{rad}) \\ \Delta\sigma_{\text{A}}\ (\text{rad}) \end{pmatrix}: \begin{pmatrix} 0 \\ \text{N.A.} \\ \text{N.A.} \\ \text{N.A.} \end{pmatrix} \begin{pmatrix} 4 \\ 2.73 \\ 2.73 \\ 2.13 \end{pmatrix} \begin{pmatrix} 10 \\ 2.13 \\ 0.75 \\ 1.32 \end{pmatrix} \begin{pmatrix} 17 \\ 1.17 \\ 1.73 \\ 0.84 \end{pmatrix} \begin{pmatrix} 23 \\ 0.17 \\ 1.60 \\ 0.89 \end{pmatrix} \begin{pmatrix} 35 \\ 1.80 \\ 0.30 \\ 1.63 \end{pmatrix} \begin{pmatrix} 47 \\ 2.13 \\ 1.92 \\ 0.92 \end{pmatrix} \begin{pmatrix} 65 \\ 1.20 \\ 1.07 \\ 1.49 \end{pmatrix}$$

Figure 5.5: Example of absolute and relative information of individual hits within an event.

5.2.3 PDF generation

Three 2 dimensional PDFs (t, $\Delta\sigma$) are constructed by combining time with each of the 3 relative central angles presented above. For these PDFs the time is limited to 100 ns with 1 ns bins and the relative central angle spans $0 \rightarrow \pi$ segmented into 36 bins (5 deg). The relative central angle measured between all possible PMT pair combinations is demonstrated in figure 5.6 as a probability density. PMTs paired with themselves or the PMT located exactly opposite on the far side of the detector are in their own solitary bins at 0 and π respectively. This distribution is never used when classifying, it is used solely to smooth out the $\Delta\sigma_{\text{P}}$ and $\Delta\sigma_{\text{F}}$ PDFs by removing the detector's PMT distribution so one can more easily discern the geometry of events underpinning the PDF's profile. This is demonstrated in figure 5.7 for the PDF (t, $\Delta\sigma_{\text{P}}$) filled with events simulated on the 25 cm spherical shell. All future $\Delta\sigma_{\text{P}}$ and $\Delta\sigma_{\text{F}}$ PDF plots shown are scaled in this way. The $\Delta\sigma_{\text{A}}$ PDF plots are not scaled as the resultant profiles are already smooth. This is because the reference positions are not fixed to any specific PMT, each PMT can be paired with any point on the spherical surface hence present within the $\Delta\sigma_{\text{A}}$ PDFs is the continuous limit equivalent of the probability distribution outlined in figure 5.6.

Within each event there are $\text{N}_{\text{Hits}} - 1$ pieces of information used to fill the 3 separate PDFs with 1 caveat. The MC simulation of the recorded FADC waveforms are simpler than what is observed within the data, the noise is absent and the size

of the pulses are fixed to 1PE. Hence there is likely to be a difference in the MC and data performance when extracting the time of hits within a single PMT that occur close to one another in time. Therefore if the PMTid corresponding to the previous hit is the same as the current hit then the current hit is skipped to reduce the likelihood of overlapping hit interference when classifying and reduce the impact of this performance differential. After the PDFs have been filled with many events' hits they are normalised to a probability density, scaling by N_{Bins}/(total N_{Hits} used to construct the PDFs). This is applied consistently across all PDFs and helps stop the extracted PDF likelihood values - outlined in section 5.2.4 - from increasing rapidly.

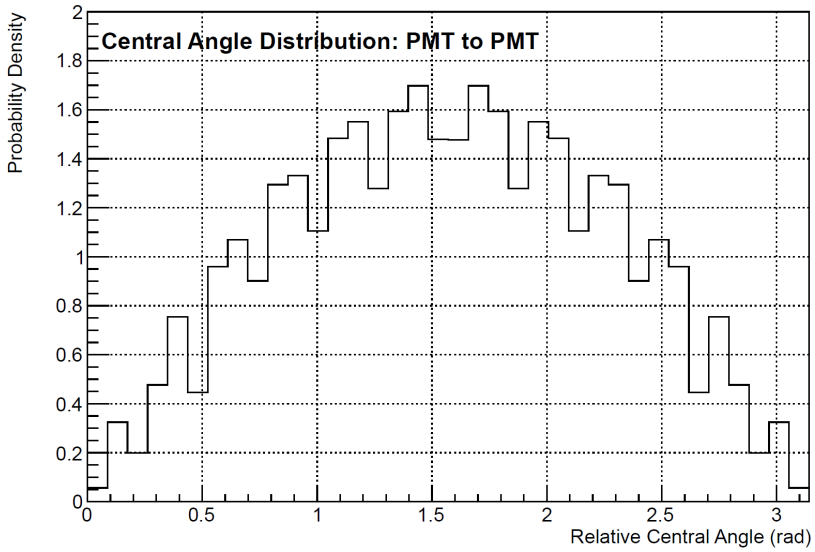


Figure 5.6: Relative central angle ($\Delta\sigma$) probability density distribution of every PMT pair combination. Minimal at 0 and π and maximal at $\pi/2$ due to relative PMT locations.

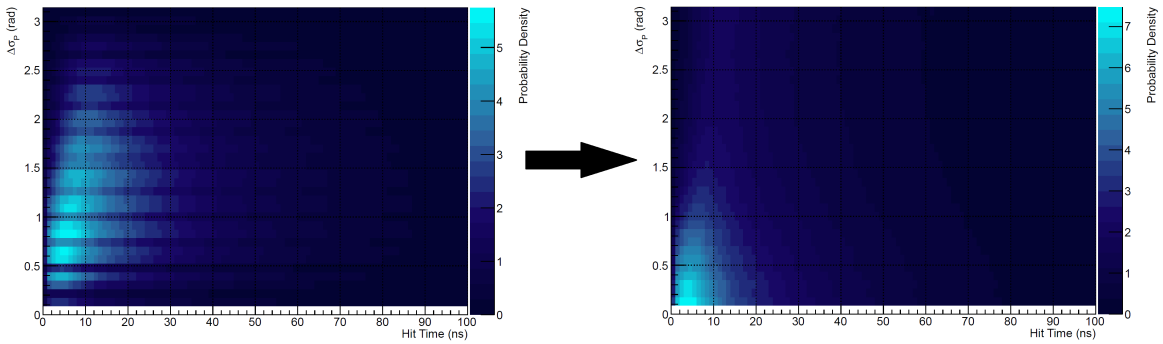


Figure 5.7: Events' Hits: t Vs $\Delta\sigma_{\text{P}}$ (Radius = 25 cm). Left: PDF, Right: PDF scaled by PMT relative central angle distribution. Removes relative PMT positions banding.

The line of smallest relative central angle bins (0-5 deg) in the $\Delta\sigma_{\mathrm{P}}$ PDFs is empty due to consecutive hits in the same PMT being skipped. The $\Delta\sigma_{\mathrm{F}}$ PDFs do have entries in this line of bins, however due to the first hit PMT and the previous hit PMT being identical for the 2^{nd} hit, a 2^{nd} hit recorded in the same PMT as the first hit is skipped. Therefore the first few ns in this line of bins is predominantly empty. Only hits that have intermediary hits recorded in other PMTs fill this line.

Section 5.2.1 outlines the MC events underpinning the multitude of signal PDFs (radial and PMT) and BG PDFs (type). Figures 5.8 - 5.15 show the radial PDFs for radii 0-35 cm in 5 cm steps. $\Delta\sigma_{\mathrm{P}}$ and $\Delta\sigma_{\mathrm{F}}$ smoothly progress from being uniformly distributed at the centre of the detector to highly peaked closer to the inner surface, additionally the average time of the hits at large $\Delta\sigma$ increases as the radial position increases. This is expected due to increased clustering and the transit time for scintillation photons to cross the detector. The large radius PDFs are similar in profile to the normal PMT and bad PMT 6-7cm PDFs, figures 5.17 and 5.19 respectively, the events used to generate these PDFs are located at similar spatial positions. At the detector's inner surface displayed in figure 5.16 for the normal PMT 0-1cm PDFs, the peak becomes even more extreme as scintillation light struggles to reach PMTs that aren't located directly next to the event's origin. The bad PMT 0-1cm PDFs shown in figure 5.18 are broader due to the events occurring directly in front of a disabled PMT. This is expected as the PMT that would receive the largest portion of light isn't active and thus the surrounding PMTs play a proportionally larger role. The fact that the bad PMT PDFs are different highlights their necessity, previous XMASS analyses have struggled to account for bad PMTs and deal with such events. Figures 5.20 and 5.21 show the BGType 2 $\mathrm{N_{Hits}} \leq 40$ and $\mathrm{N_{Hits}} > 40$ PDFs respectively, figures 5.22 and 5.23 show the corresponding BGType 15 PDFs. The $\Delta\sigma$ distributions vary between BGType but are primarily peaked at small $\Delta\sigma$ as expected as the events occur at the ID's inner surface. The average hit time increases with energy - previously demonstrated in figure 5.2. The random nature of whether a photon leads to a recorded signal (hit) - particularly the first hit which fixes the timing - shortens the

time span over which hits occur at low energy. Other BGType PDFs are similar.

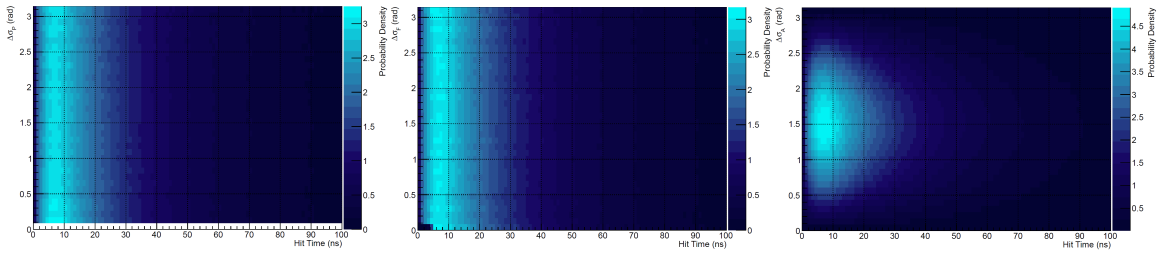


Figure 5.8: Electron 0 - 5 keV$_{ee}$ signal (radius = 0 cm) events' hits PDFs (t Vs $\Delta\sigma$). Left: $\Delta\sigma_{\mathrm{P}}$ (scaled), Middle: $\Delta\sigma_{\mathrm{F}}$ (scaled), Right: $\Delta\sigma_{\mathrm{A}}$. Exponential time decay with a uniform $\Delta\sigma$ distribution at the centre of the ID.

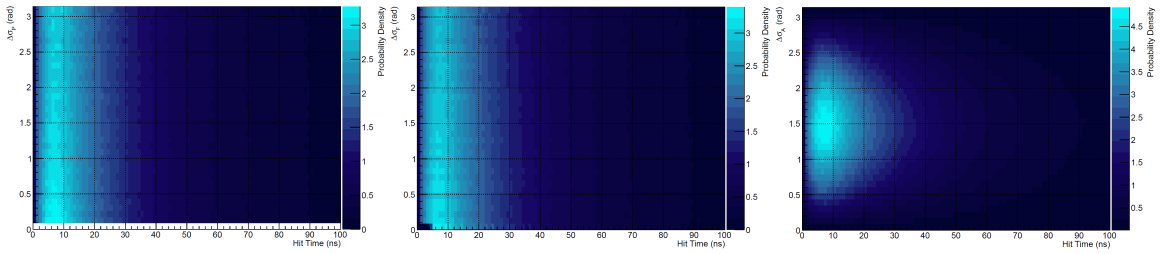


Figure 5.9: Electron 0 - 5 keV$_{ee}$ signal (radius = 5 cm) events' hits PDFs (t Vs $\Delta\sigma$). Left: $\Delta\sigma_{\mathrm{P}}$ (scaled), Middle: $\Delta\sigma_{\mathrm{F}}$ (scaled), Right: $\Delta\sigma_{\mathrm{A}}$.

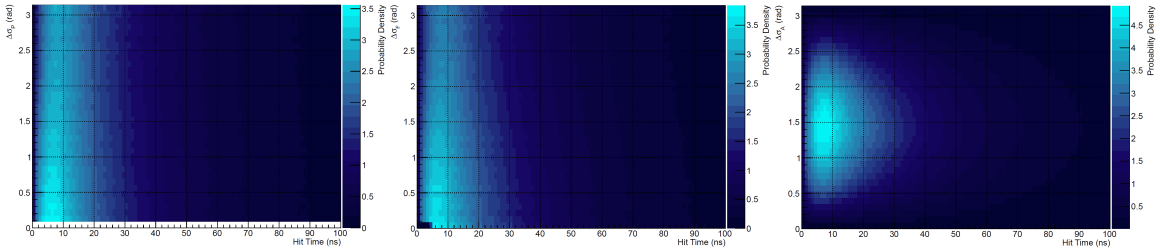


Figure 5.10: Electron 0 - 5 keV$_{ee}$ signal (radius = 10 cm) events' hits PDFs (t Vs $\Delta\sigma$). Left: $\Delta\sigma_{\mathrm{P}}$ (scaled), Middle: $\Delta\sigma_{\mathrm{F}}$ (scaled), Right: $\Delta\sigma_{\mathrm{A}}$.

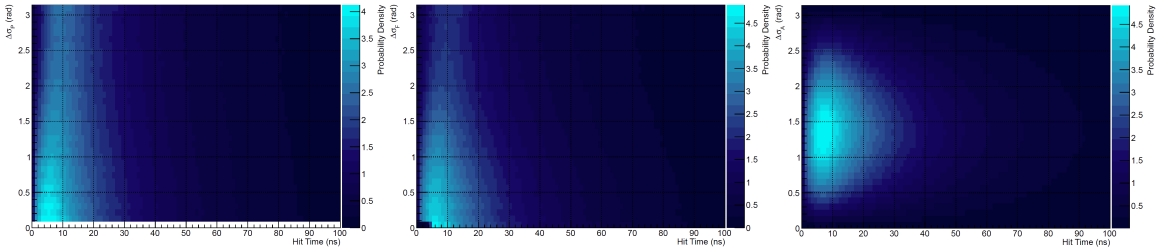


Figure 5.11: Electron 0 - 5 keV$_{ee}$ signal (radius = 15 cm) events' hits PDFs (t Vs $\Delta\sigma$). Left: $\Delta\sigma_{\mathrm{P}}$ (scaled), Middle: $\Delta\sigma_{\mathrm{F}}$ (scaled), Right: $\Delta\sigma_{\mathrm{A}}$.

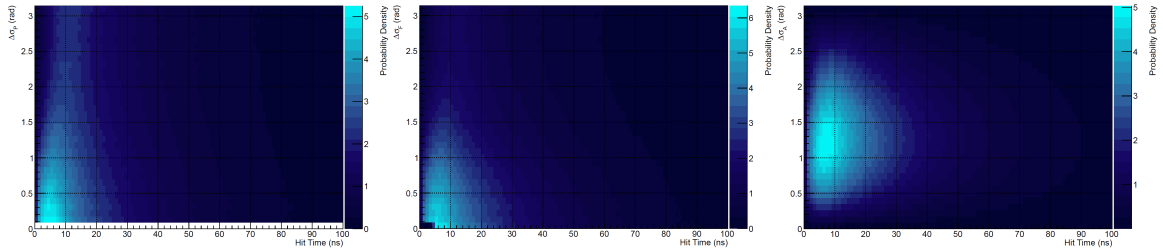


Figure 5.12: Electron 0 - 5 keV$_{ee}$ signal (radius = 20 cm) events' hits PDFs (t Vs $\Delta\sigma$). Left: $\Delta\sigma_{\mathrm{P}}$ (scaled), Middle: $\Delta\sigma_{\mathrm{F}}$ (scaled), Right: $\Delta\sigma_{\mathrm{A}}$. Exponential time decay with the distribution skewed towards small $\Delta\sigma$ the closer to the ID's inner surface the events occur.

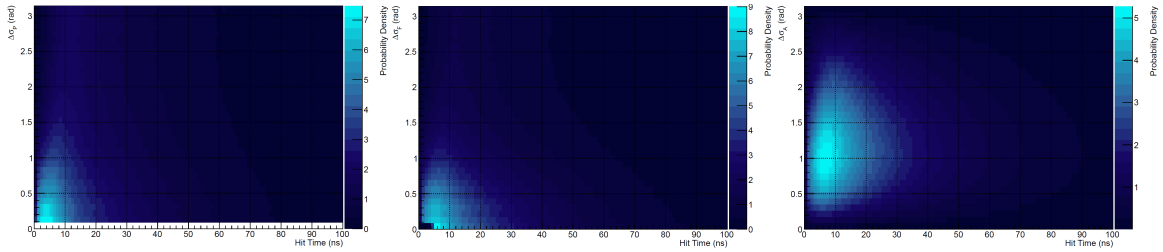


Figure 5.13: Electron 0 - 5 keV$_{ee}$ signal (radius = 25 cm) events' hits PDFs (t Vs $\Delta\sigma$). Left: $\Delta\sigma_{\mathrm{P}}$ (scaled), Middle: $\Delta\sigma_{\mathrm{F}}$ (scaled), Right: $\Delta\sigma_{\mathrm{A}}$.

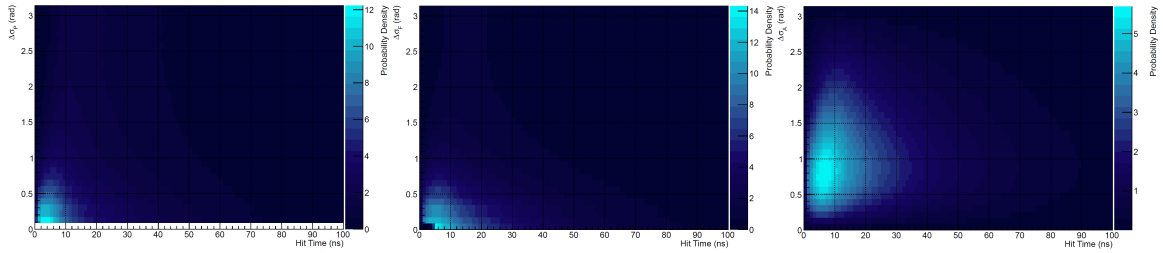


Figure 5.14: Electron 0 - 5 keV$_{ee}$ signal (radius = 30 cm) events' hits PDFs (t Vs $\Delta\sigma$). Left: $\Delta\sigma_{\mathrm{P}}$ (scaled), Middle: $\Delta\sigma_{\mathrm{F}}$ (scaled), Right: $\Delta\sigma_{\mathrm{A}}$.

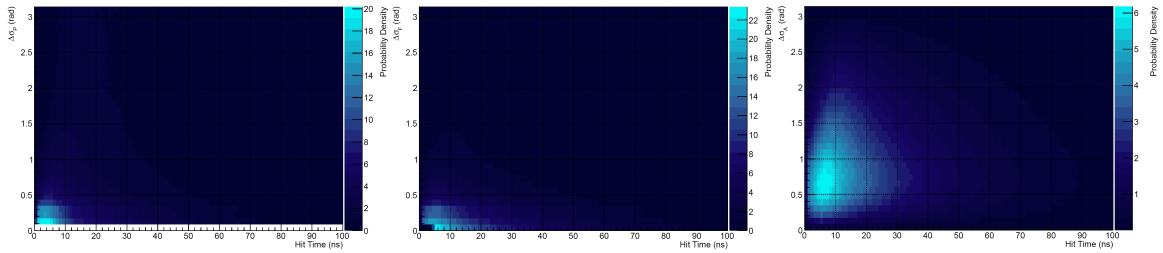


Figure 5.15: Electron 0 - 5 keV$_{ee}$ signal (radius = 35 cm) events' hits PDFs (t Vs $\Delta\sigma$). Left: $\Delta\sigma_{\mathrm{P}}$ (scaled), Middle: $\Delta\sigma_{\mathrm{F}}$ (scaled), Right: $\Delta\sigma_{\mathrm{A}}$.

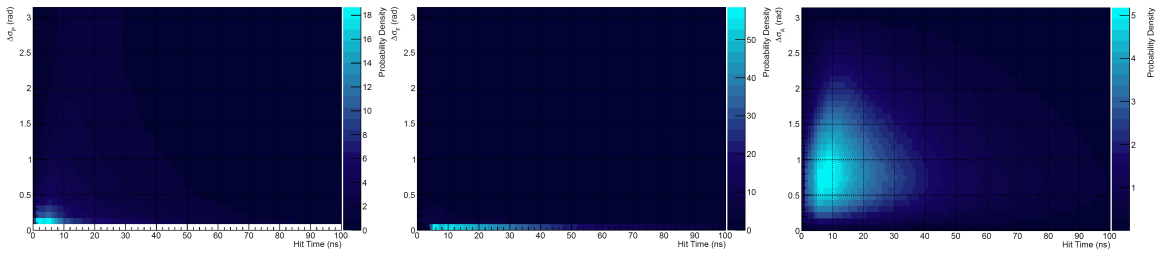


Figure 5.16: Electron 0 - 5 keV$_{ee}$ signal (normal PMTs 0-1 cm) events' hits PDFs (t Vs $\Delta\sigma$). Left: $\Delta\sigma_{\mathrm{P}}$ (scaled), Middle: $\Delta\sigma_{\mathrm{F}}$ (scaled), Right: $\Delta\sigma_{\mathrm{A}}$. Exponential time decay with the distribution skewed heavily towards small $\Delta\sigma$ for events occurring on the ID's inner surface.

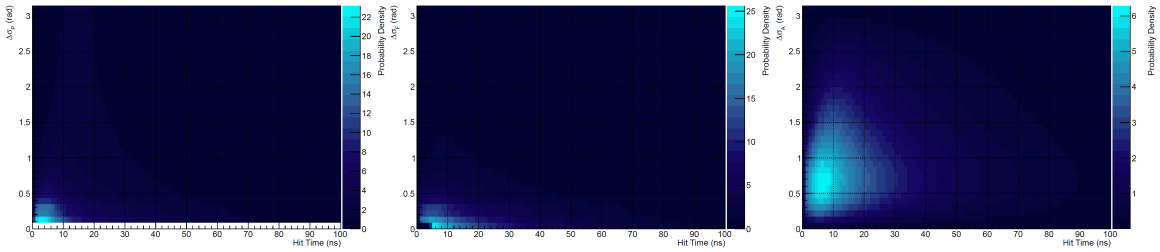


Figure 5.17: Electron 0 - 5 keV$_{ee}$ signal (normal PMTs 6-7 cm) events' hits PDFs (t Vs $\Delta\sigma$). Left: $\Delta\sigma_{\mathrm{P}}$ (scaled), Middle: $\Delta\sigma_{\mathrm{F}}$ (scaled), Right: $\Delta\sigma_{\mathrm{A}}$.

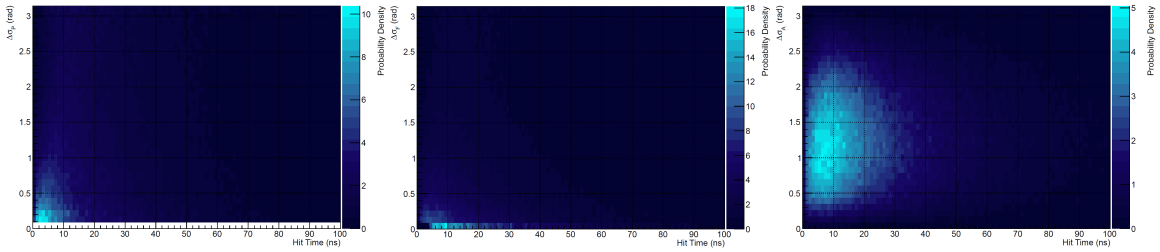


Figure 5.18: Electron 0 - 5 keV$_{ee}$ signal (bad PMTs 0-1 cm) events' hits PDFs (t Vs $\Delta\sigma$). Left: $\Delta\sigma_{\mathrm{P}}$ (scaled), Middle: $\Delta\sigma_{\mathrm{F}}$ (scaled), Right: $\Delta\sigma_{\mathrm{A}}$.

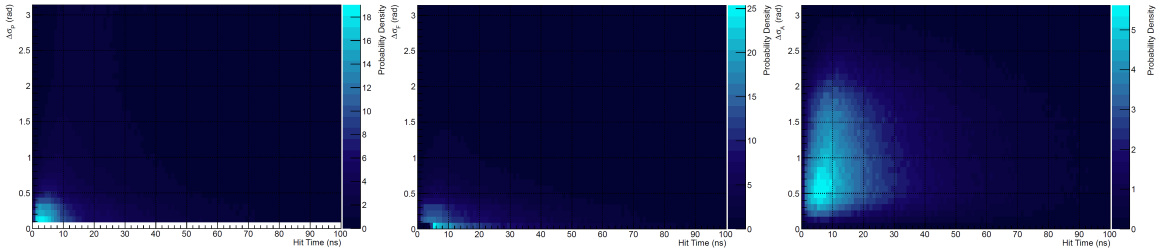


Figure 5.19: Electron 0 - 5 keV$_{ee}$ signal (bad PMTs 6-7 cm) events' hits PDFs (t Vs $\Delta\sigma$). Left: $\Delta\sigma_{\mathrm{P}}$ (scaled), Middle: $\Delta\sigma_{\mathrm{F}}$ (scaled), Right: $\Delta\sigma_{\mathrm{A}}$.

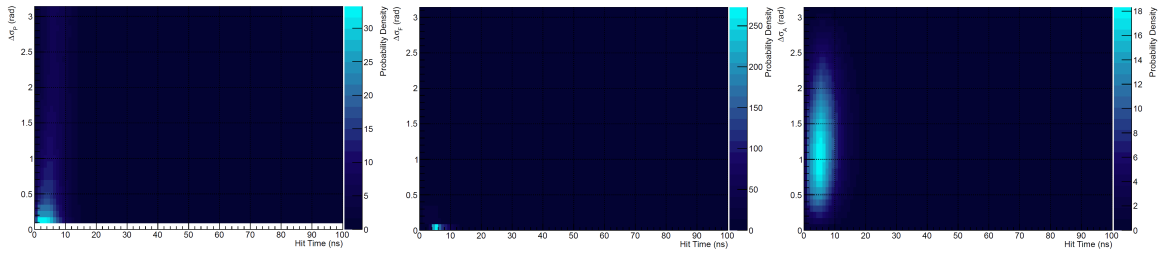


Figure 5.20: BGType 2 ($N_{Hits} \leq 40$) events' hits PDFs (t Vs $\Delta\sigma$). Left: $\Delta\sigma_P$ (scaled), Middle: $\Delta\sigma_F$ (scaled), Right: $\Delta\sigma_A$. Short Exponential time decay for low energy BG events and skewed heavily towards small $\Delta\sigma$.

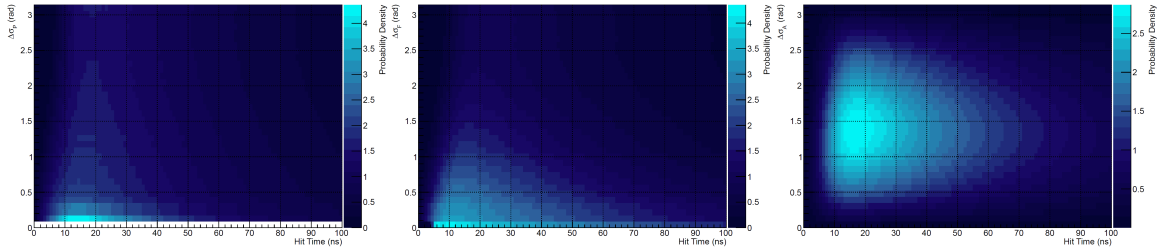


Figure 5.21: BGType 2 ($N_{Hits} > 40$) events' hits PDFs (t Vs $\Delta\sigma$). Left: $\Delta\sigma_P$ (scaled), Middle: $\Delta\sigma_F$ (scaled), Right: $\Delta\sigma_A$. Longer Exponential time decay for higher energy BG events and skewed heavily towards small $\Delta\sigma$.

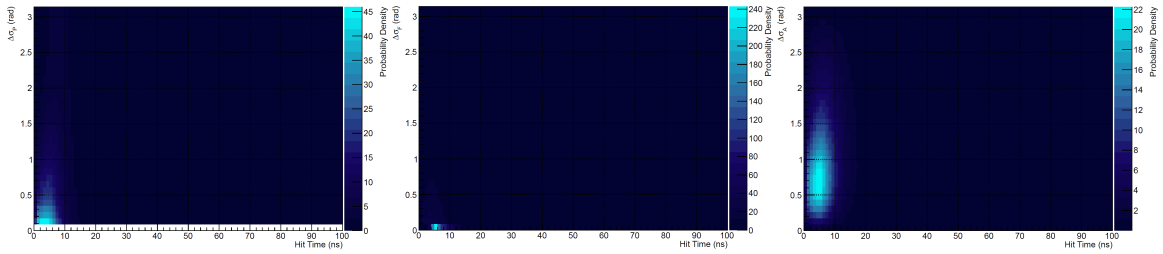


Figure 5.22: BGType 15 ($N_{Hits} \leq 40$) events' hits PDFs (t Vs $\Delta\sigma$). Left: $\Delta\sigma_P$ (scaled), Middle: $\Delta\sigma_F$ (scaled), Right: $\Delta\sigma_A$.

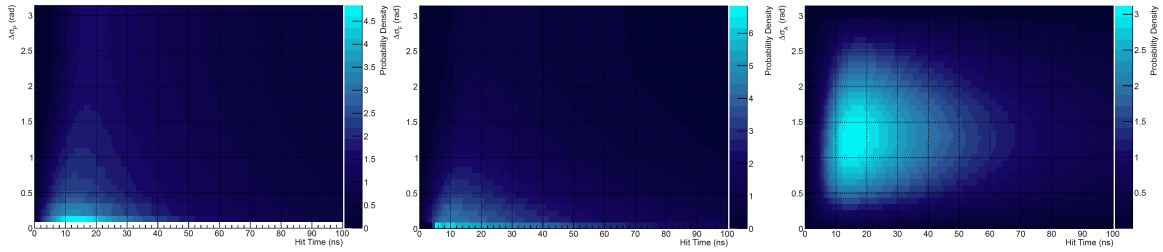


Figure 5.23: BGType 15 ($N_{Hits} > 40$) events' hits PDFs (t Vs $\Delta\sigma$). Left: $\Delta\sigma_P$ (scaled), Middle: $\Delta\sigma_F$ (scaled), Right: $\Delta\sigma_A$.

5.2.4 Classification parameter

These electron recoil (ER) signal radii and PMT distance PDFs along with the BG PDFs can now be used to classify BG events, nuclear recoil (NR) signal events and ER signal events. Any given event can be reformatted in terms of the hit times and 3 relative central angles (t, $\Delta\sigma_{\mathrm{P}}$, $\Delta\sigma_{\mathrm{F}}$, $\Delta\sigma_{\mathrm{A}}$) for each hit exactly as before. The likelihood (L) for all the different PDFs is calculated as follows. The probability density extracted from the 3 PDFs' bins defined by (t, $\Delta\sigma_{\mathrm{P}}$, $\Delta\sigma_{\mathrm{F}}$, $\Delta\sigma_{\mathrm{A}}$) are multiplied together - unweighted[2] - and this is done cumulatively for all hits within the event:

$$L = \prod_{\mathrm{hit}=2}^{N_{\mathrm{Hits}}} [\mathrm{PDF_P}(t^{\mathrm{hit}}, \Delta\sigma_{\mathrm{P}}^{\mathrm{hit}}) \times \mathrm{PDF_F}(t^{\mathrm{hit}}, \Delta\sigma_{\mathrm{F}}^{\mathrm{hit}}) \times \mathrm{PDF_A}(t^{\mathrm{hit}}, \Delta\sigma_{\mathrm{A}}^{\mathrm{hit}})]. \tag{5.5}$$

Although the signal PDFs encompass the entire phase space of the detector there is overlap between the large radial and outer PMT PDFs. However we are not performing a positional cut and we do not need to know which ER signal PDF best represents the event we only need its likelihood (L_{Signal}). The maximal BG likelihood (L_{BG}) is similarly obtained. The PDF classification parameter is then calculated by taking the natural log of their ratio and normalising via the event's energy:

$$C = \frac{\mathrm{Ln}(\frac{P_{\mathrm{BG}}}{P_{\mathrm{Signal}}})}{E/\mathrm{keV}_{ee}}. \tag{5.6}$$

The natural log induces an effective signal BG divide at 0 and makes the maximal L values more manageable. Normalising via energy helps fix the signal and BG classification parameter peak positions; this helps flatten the resultant cut position especially at higher energies. Figure 5.24 and 5.25 show the normalised classification parameter distributions in the 8 lowest energy bins 0.5 - 4.5 keV_{ee} (0.5 keV_{ee} bins). The ER (red) and NR (blue) MC signals are compared to the total cumulative MC BG (black) in figure 5.24 and figure 5.25 displays the 3 most prominent BG Types: 2 (orange, PMT Body ^{40}K), 15 (cyan, Al-seal ^{238}U) and 16 (green, Al-seal ^{210}Pb).

[2]Only utilising subsets of these 3 PDFs resulted in worse classification power than using all 3. Non-binary scaling factors where not tested due to limited computation time.

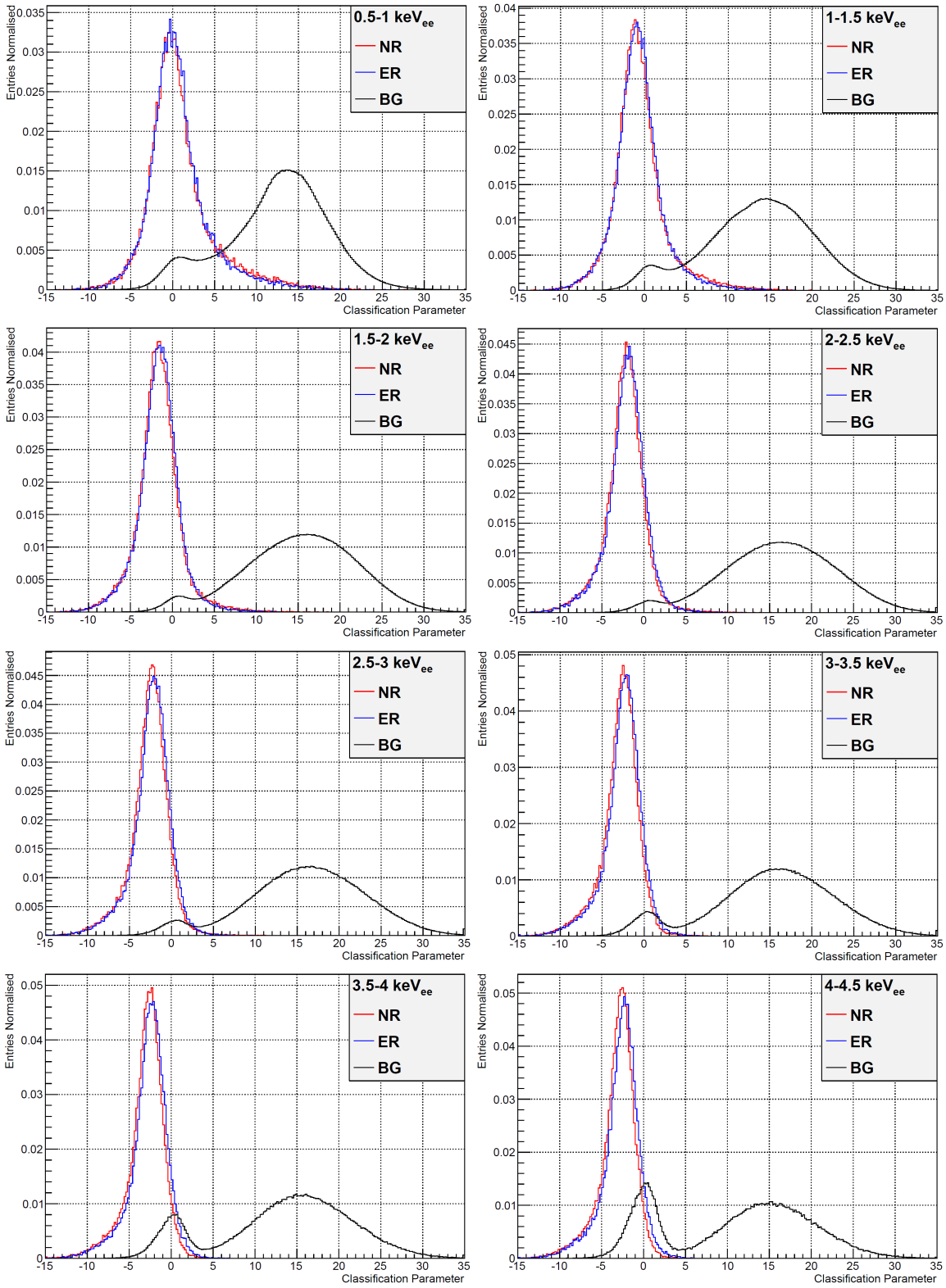


Figure 5.24: Classification parameter distributions of the NR (red) and ER (blue) signal and total BG (black). 8 lowest energy bins: 0.5 - 4.5 keV$_{ee}$ (0.5 keV$_{ee}$ bins). BG events with a short time structure easily distinguishable from signal and form the large peak located away from 0. BG events with a longer time structure similar to signal and peaked at 0. NR and ER signal peaks similar with NR located slightly further away from 0.

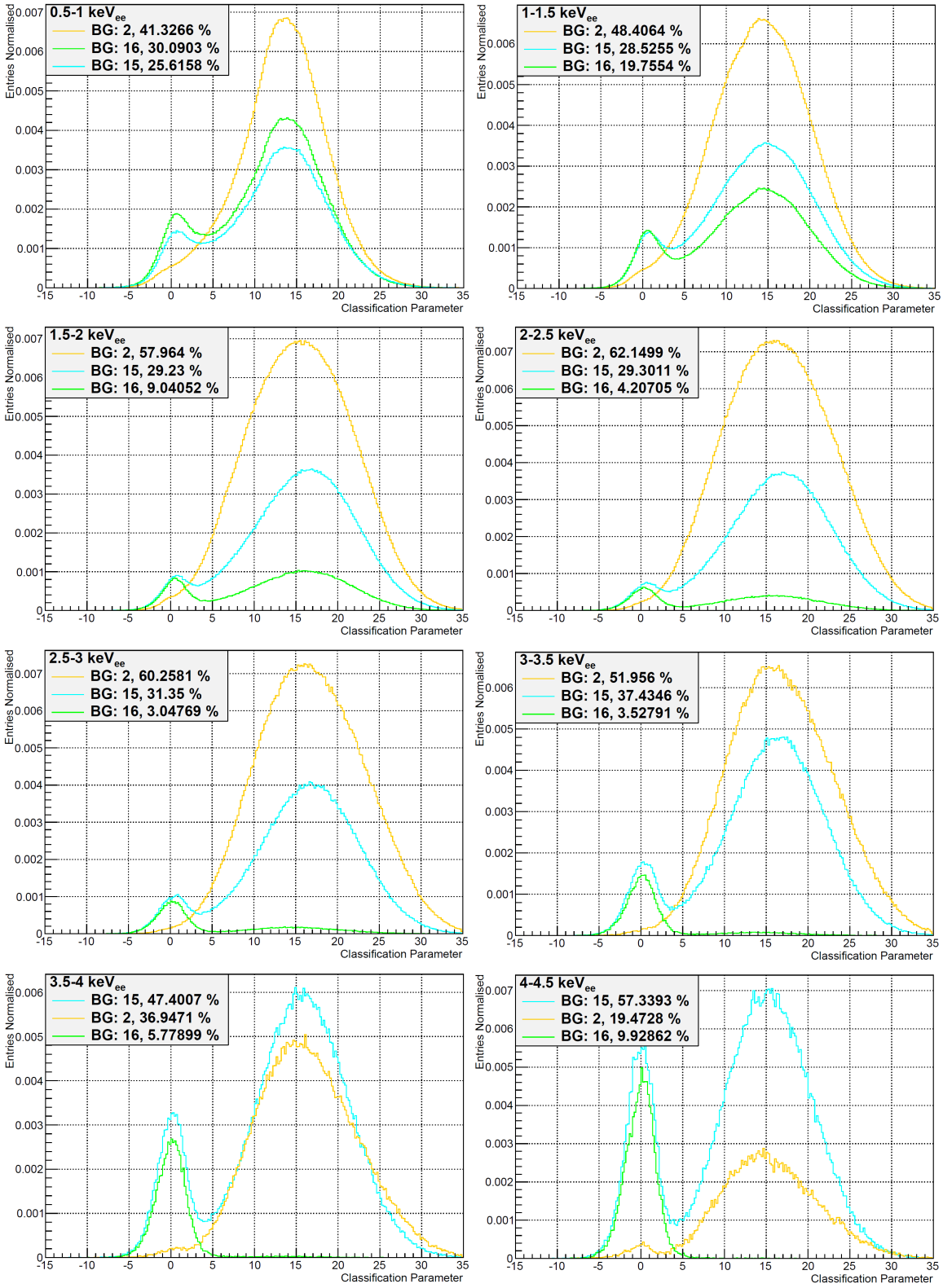


Figure 5.25: Classification parameter distributions of the 3 most prominent BG Types: 2 (orange, PMT Body ^{40}K), 15 (cyan, Al-seal ^{238}U) and 16 (green, Al-seal ^{210}Pb). 8 lowest energy bins: 0.5 - 4.5 keV$_{ee}$ (0.5 keV$_{ee}$ bins). BG Type 2 Cherenkov events form the majority of the BG classification peak located away from 0. The other BG longer time structure events form the peak at 0.

Cherenkov like events (short time frame) are easily identifiable as BG and form the BG peak located at large positive classification values. The BG events making up the peak located close to zero have a longer time structure, similar to those observed in the signal events, and since there are signal PDFs located at the ID's inner surface these BG events in general appear equally similar to both signal and BG. As energy increases the BG peak close to zero grows in prominence while the other diminishes to a negligible level at ~ 8 keV_{ee}, this inevitably reduces the classification power. Figure 5.26 demonstrates this at 4.5 - 5.0 keV_{ee}, 9.5 - 10.0 keV_{ee}, 14.5 - 15.0 keV_{ee} and 19.5 - 20.0 keV_{ee}. As energy increases the width of the BG peak reduces ever so slightly.

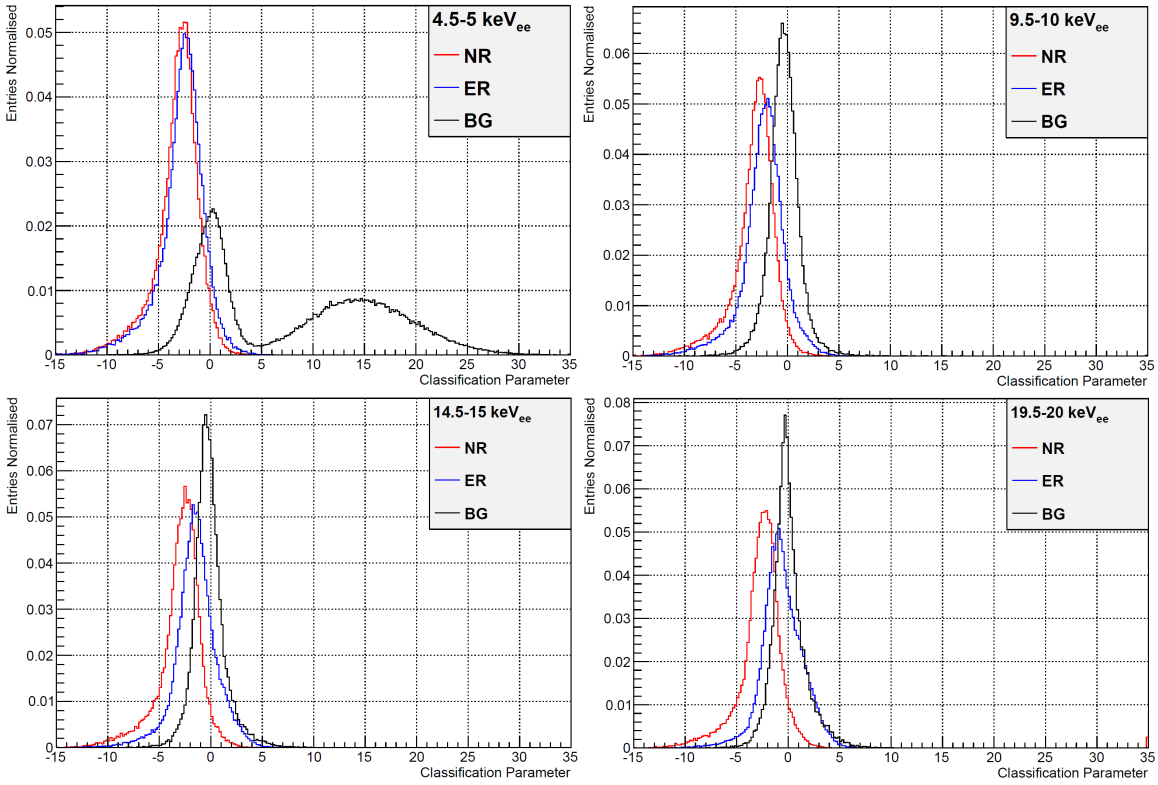


Figure 5.26: Classification parameter distributions of the NR (red) and ER (blue) signal and total BG (black). 8 lowest energy bins: 4.5 - 5.0 keV_{ee}, 9.5 - 10.0 keV_{ee}, 14.5 - 15.0 keV_{ee} and 19.5 - 20.0 keV_{ee}. At higher energy the BG peak away from 0 diminishes and all peaks are thinner/closer to 0.

The big difference between the NR signal events and ER signal events is the time profile of the scintillation emission used in the MC. Although only ER signal MC events are used to construct the signal PDFs - as discussed in section 5.2.1 - the NR

events differ from the BG PDFs to a greater extent than the ER signal PDFs, which results in a more negative classification position. As energy increases both the NR and ER signal peaks shift closer to zero, however the ER peak does so to a greater extent, the reason for this is likely due to the similarity in the ER and BG timing profile which becomes more evident with greater statistics (more hits). The mutually opposing trends of the signal peaks shifting closer to zero and the reducing BG peak width defines the shape of the signal/$\sqrt{\text{BG}}$ Vs Energy (keV$_{ee}$) curve in section 5.2.6.

5.2.5 MC classification: CDFs, ROC curves and signal/$\sqrt{\text{BG}}$

To perceive how any given classification parameter performs one must look at the cumulative distribution functions (CDFs). These are shown in figure 5.27 for the NR (red) and ER (blue) MC signal and total MC BG (black) in the 8 lowest energy bins 0.5 - 4.5 keV$_{ee}$ (0.5 keV$_{ee}$ bins) and are simply the normalised integral of the distributions shown in figure 5.24. These outline the proportion of signal or BG remaining after a cut at any given classification parameter position.

To demonstrate how the signal and BG compare it is best to plot the respective CDFs against one another: a receiver operating characteristic (ROC) curve. These are shown in figure 5.28 for the NR (red) and ER (blue) signal CDFs Vs the total BG CDF in the 8 lowest energy bins 0.5 - 4.5 keV$_{ee}$ (0.5 keV$_{ee}$ bins). These demonstrate the resultant amount of BG retained for a given signal retention. The theoretical best position (1, 0) means all BG has been removed and all signal retained.

For analyses where one is trying to detect a small signal residing within a large BG, the power of a classification parameter is rooted in the statistics of the remaining BG. As such the classification power = signal/$\sqrt{\text{BG}}$. This is displayed in figure 5.29 for the NR (red) and ER (blue) signal with the BG limited to a minimum of 0.02% to exclude statistical fluctuations. There are clear peak positions as expected which initially become more negative and increase in value as energy increases - more hits means more information which increases the classification power. Then, the BG peak at large positive classification values reduces, which reduces the classification power.

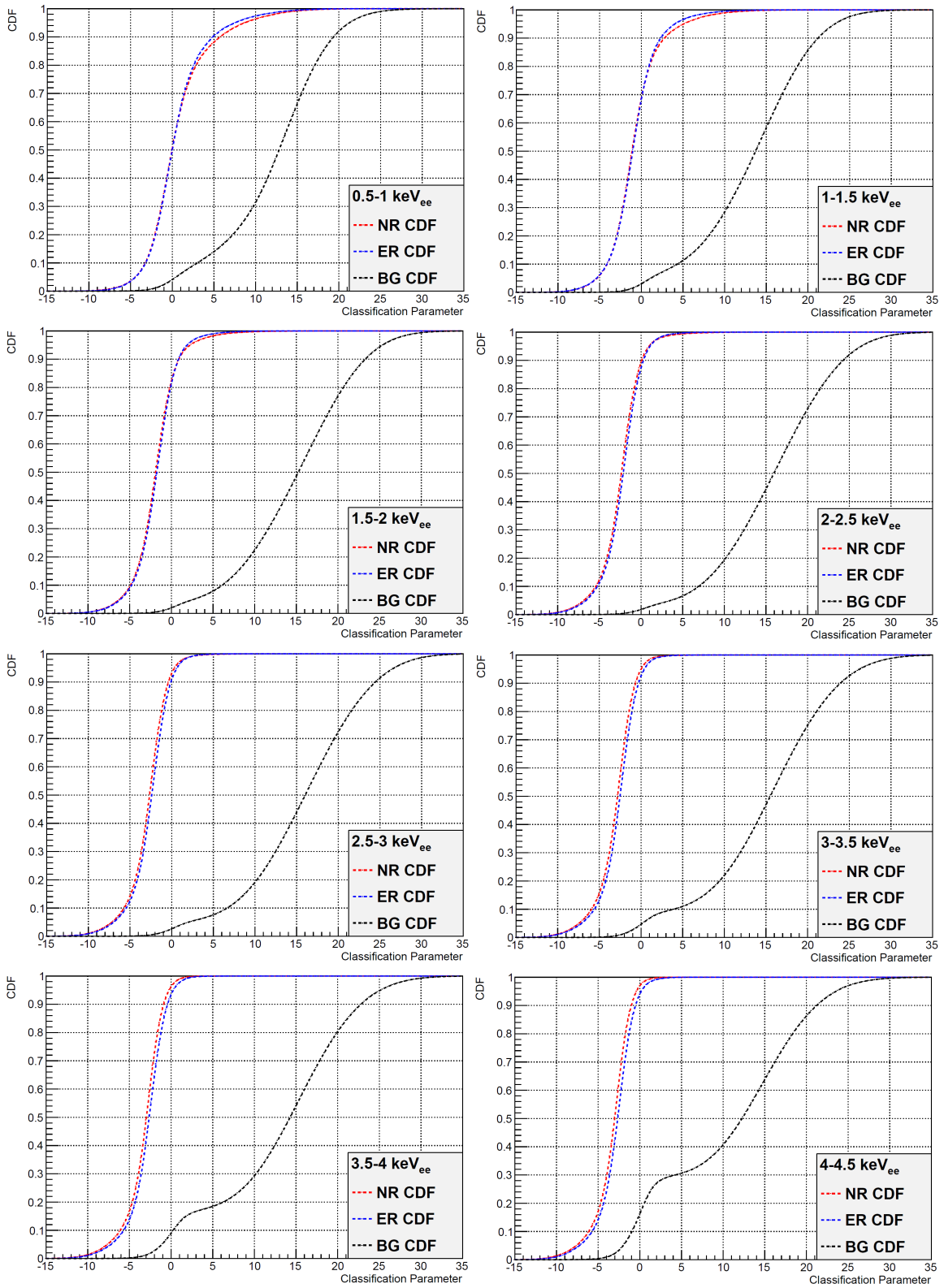


Figure 5.27: CDFs of the NR (red) and ER (blue) MC signal and total MC BG (black). 8 lowest energy bins: 0.5 - 4.5 keV$_{ee}$ (0.5 keV$_{ee}$ bins). Curves according to the peak locations.

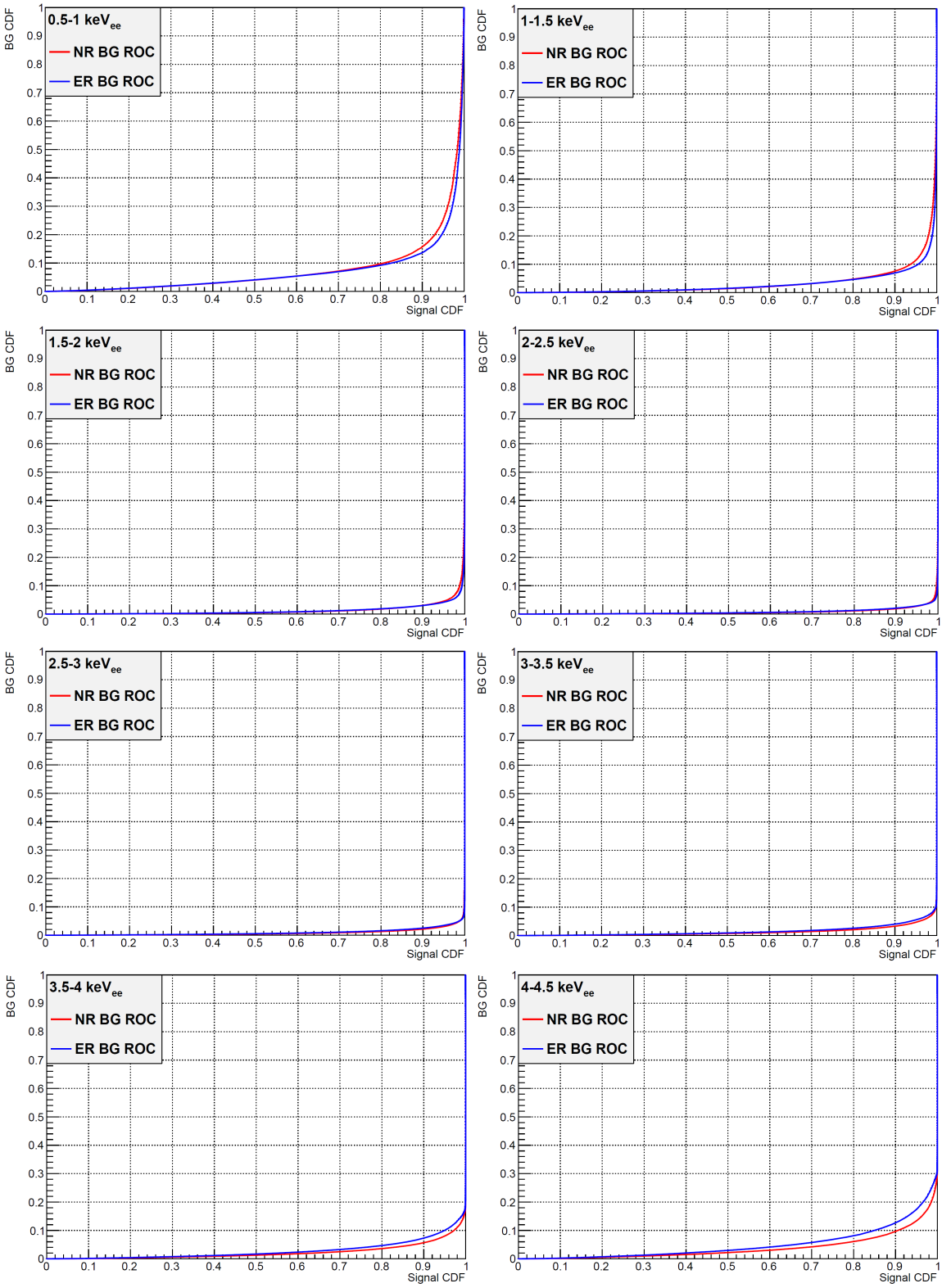


Figure 5.28: ROC curves of the NR (red) and ER (blue) MC signal CDFs Vs the total MC BG CDF. 8 lowest energy bins: 0.5 - 4.5 keV$_{ee}$ (0.5 keV$_{ee}$ bins). Close to the theoretical best position (1, 0), initially improves with energy.

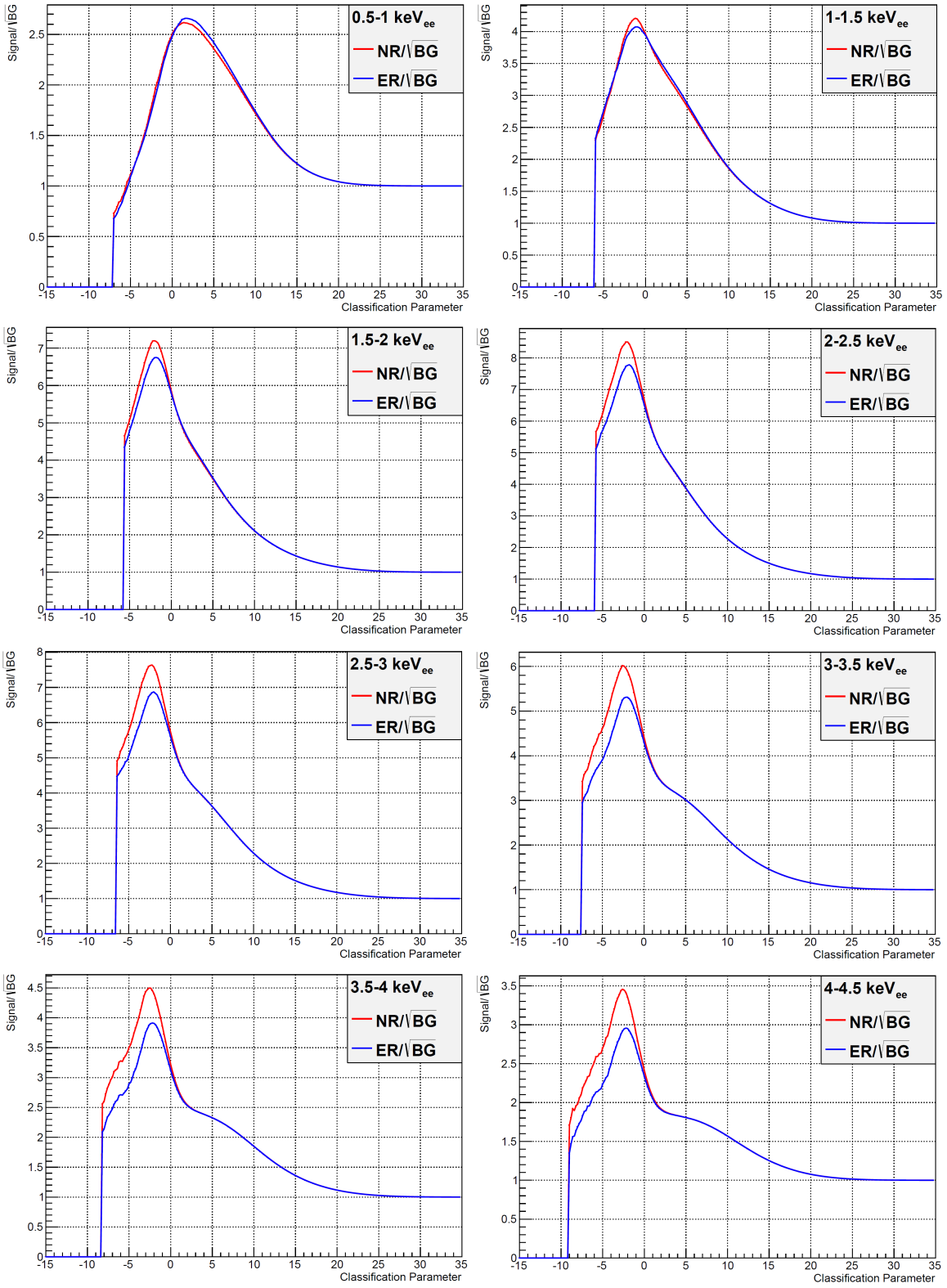


Figure 5.29: Signal/$\sqrt{\text{BG}}$ for the NR (red) and ER (blue) MC signals, MC BG limited to 0.02%. 8 lowest energy bins: 0.5 - 4.5 keV$_{ee}$ (0.5 keV$_{ee}$ bins). Maximal positions indicate the best cut positions to maximise classification power.

5.2.6 Classification power

As stated at the beginning of this section, the PDF classifier's performance should be compared directly to the Cherenkov cut and the additional likelihood cut used in the previous modulation analysis [49, 50]. Figures 5.30, 5.31 and 5.32 show the result of applying the Cherenkov cut, Cherenkov cut + likelihood cut and the standalone PDF cut respectively. The left hand plots show the NR (red) and ER (blue) MC signal and total MC BG (black) retention, the right hand plots display the resulting NR (red) and ER (blue) signal/$\sqrt{\text{BG}}$ classification power of the respective cuts. All 3 set of cuts are applied to the same signal and BG MC data; and by comparing figures 5.31 and 5.32 one can evaluate the different analyses' classifier's relative merits.

The Cherenkov cut was designed by comparing data with electron MC events and clearly favours ER events. The effect of applying the Cherenkov cut has a negative effect on the search for NR signals above 6 keV$_{ee}$, where NR retention flattens out at 60% while BG retention keeps on rising. The Cherenkov cut is applied for $\text{N}_{\text{HitPMTs}} <$ 200 and as such a step is observed $\sim$ 14 keV$_{ee}$ in both figures 5.30 and 5.31.

The maximal NR signal/$\sqrt{\text{BG}}$ for the PDF classifier varies between 40 - 60% NR retention. The distribution of the ER signal classification parameter is centred closer to 0 and hence fewer ER events are retained compared to NR. Therefore a larger NR retention of 60% was opted for because while it is close to maximal it retains more ER events, additionally it is similar to what the Cherenkov cut achieved. Figure 5.33 shows the PDF classification parameter cut position retaining 60% of the NR signal.

The shape of the PDF NR classification power curve in figure 5.32 is comprised of 3 components. The initial rise corresponds to higher energy which implies more hits, this extra information shifts the signal and BG peaks away from 0. The downturn at $\sim$ 3 keV$_{ee}$ is caused by the BG peak located closer to 0 growing in prominence. And the slow rise at higher energies is due to the signal and BG peaks' widths getting thinner. This slow rise is not replicated for the ER classification power. Figure 5.26 shows that the ER peak shifts closer to zero more quickly than the NR peak as energy

increases, therefore the 60% NR cut retains less ER signal.

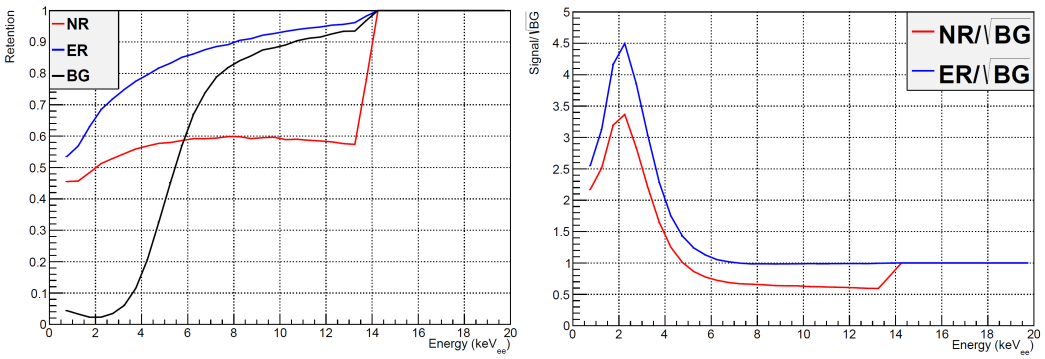


Figure 5.30: Cherenkov cut: $N_{HitPMTs} < 200 \rightarrow$ step at ~ 14 keV$_{ee}$. Left: NR (red) and ER (blue) signal and total BG (black) retention. Right: NR (red) and ER (blue) signal/$\sqrt{BG}$. Classification initially improves as information increases with energy and then reduces as easily identifiable BGs diminish.

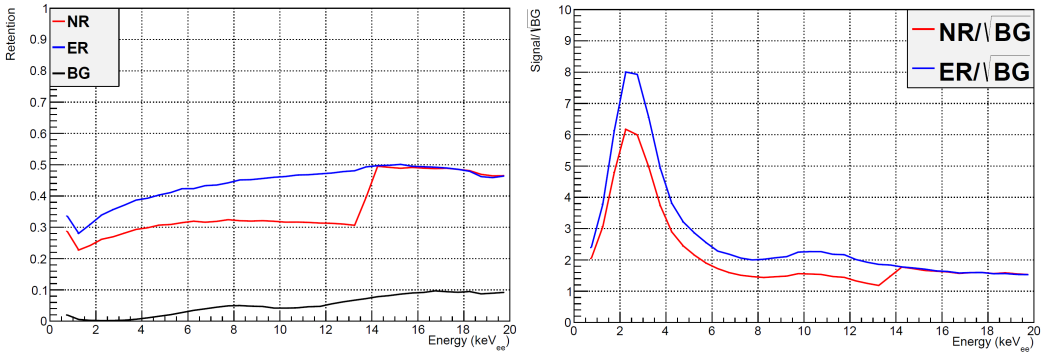


Figure 5.31: Likelihood cut (with Cherenkov cut: ~ 14 keV$_{ee}$ step). Left: NR (red) and ER (blue) signal and total BG (black) retention. Right: NR (red) and ER (blue) signal/$\sqrt{BG}$. Factor ~ 2 improvement over the Cherenkov cut.

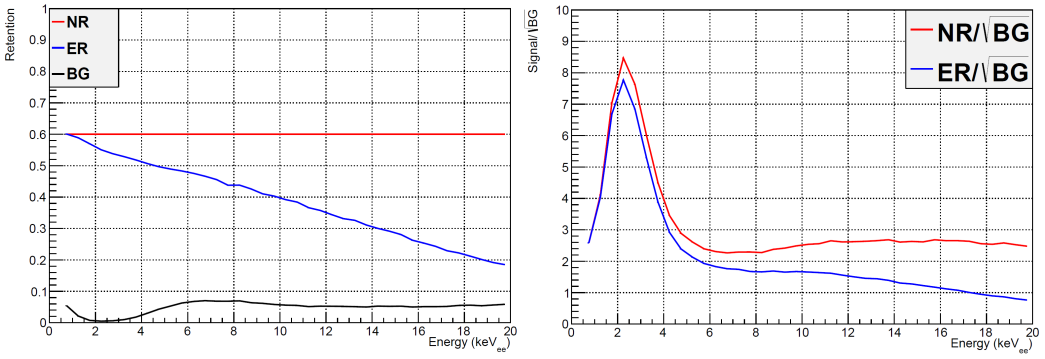


Figure 5.32: PDF cut (60% NR Retention). Left: NR (red) and ER (blue) signal and total BG (black) retention. Right: NR (red) and ER (blue) signal/$\sqrt{BG}$. Performs best for NR events but ER drops off considerably at higher energy as the ER retention reduces.

Figure 5.34 compares the PDF cut directly to the likelihood cut. The relative increase in BG retention is outlined in the left plot, while the relative increase in classification power NR (red) and ER (blue) is shown in the right plot. The NR performance is the primary concern as we are looking for a WIMP induced modulation signal. Hence the PDFs are optimised for NR, yet they still outperform for ER at the highly relevant lowest energies. Below 2 keV$_{ee}$ the PDF cut performs 10% and 30 - 50% better for ER and NR signal events respectively. The relative ER classification power reduces to below 1 above 2 keV$_{ee}$, while the relative NR classification power stays above 1 and rises to 2.25 at 13 keV$_{ee}$; just below the Cherenkov N$_{\mathrm{HitPMTs}}$ cut-off.

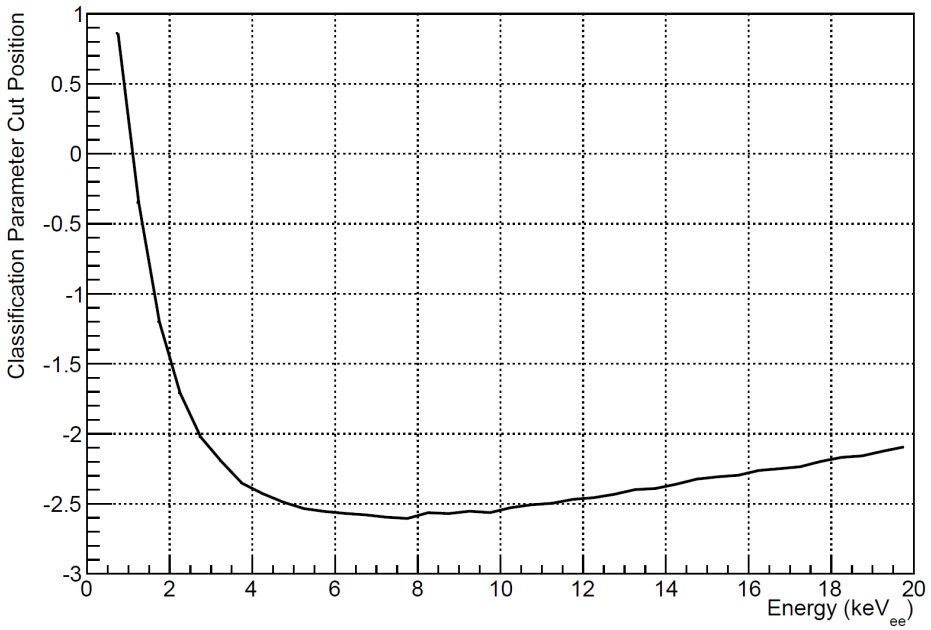


Figure 5.33: Classification parameter cut value for 60% NR retention as a function of energy. Reduces fast to begin with as the NR peak shifts away from 0 with increased information. Then it very slowly shifts closer to 0 as the peaks become thinner and move slightly closer to 0.

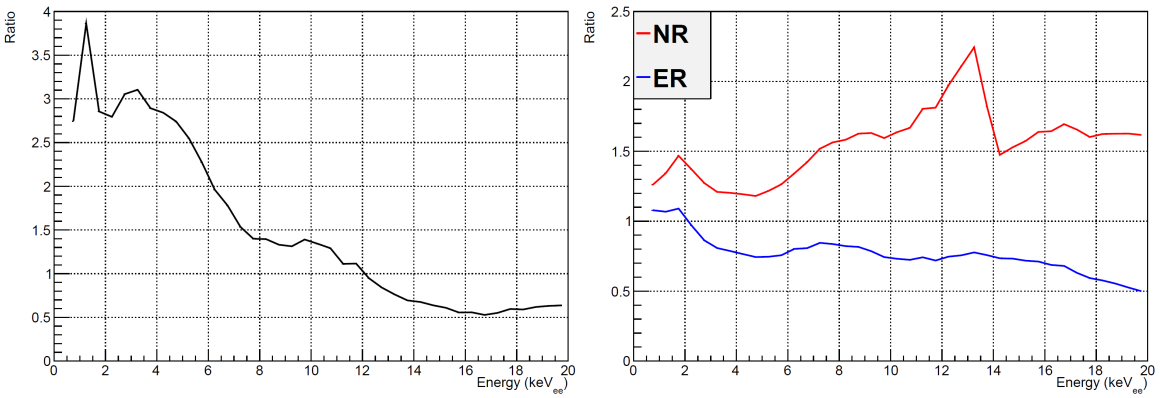


Figure 5.34: Relative increase: Likelihood cut (with Cherenkov cut: ~ 14 keV$_{ee}$ step) → PDF cut. Left: BG (black) retention. Right: NR (red) and ER (blue) signal/$\sqrt{\text{BG}}$. The PDF cut retains more BG but also retains much more NR signal. This is why the classification power is improved (¿ 1). The ER is not as fortunate as ER retention reduces with energy.

5.3 ^{55}Fe low energy calibration crosscheck

The PDFs constructed in this chapter are produced using MC and tested by comparing signal MC with BG MC. As demonstrated previously in figure 3.23 there are discrepancies between data and BG MC at low energies (< 7 keV$_{ee}$), casting doubt on the exact proportions of different BG sources. This would not change how the PDFs are constructed or how the classification parameter is calculated, however it may vary the max(signal/$\sqrt{\text{BG}}$) positions and hence the chosen cut positions. Therefore the resultant classification power obtained via my PDF classifier in the previous section may not be wholly accurate and there is the need for a comparison with real data.

In chapter 7 the event rate energy spectra for a range of WIMP masses are produced, by comparing these against the recorded data's energy spectra displayed in section 6.3 the true relative increase in classification power is obtained. As an interim measure, this new PDF classification technique can be tested by performing a direct comparison between calibration data and MC. ^{55}Fe was chosen specifically because it produces events at 2 distinct low energies. The energy ranges probed were 1 - 2 keV$_{ee}$ and 3 - 4 keV$_{ee}$ for all 9 internal calibration positions: Z = -40 cm to 40cm (10 cm steps). The ^{55}Fe calibration data utilised was taken on 2015/03/30, the first after the introduction of the low threshold trigger. ^{55}Fe MC was generated using the same

optical parameters as those measured at the time: $l_A \sim 1000$ cm and $l_S \sim 52.5$ cm.

After applying the XMASS StdCut the PDF classification parameter was calculated for the ^{55}Fe MC and the ^{55}Fe calibration data. To conduct a fair comparison, the BG present within the ^{55}Fe calibration data needed to be removed. This was achieved by calculating the classification parameter for normal data recorded in the following 5 days after calibration data taking. The classification parameter distributions for the normal data and ^{55}Fe calibration data was livetime normalised and the difference taken. A direct comparison between the ^{55}Fe MC and ^{55}Fe calibration-normal data was then possible by normalising both to unity. Figure 5.35 compares the ^{55}Fe MC and the ^{55}Fe calibration-normal data NPEs distribution. This is displayed in terms of NPEs so it can be directly compared with the ^{55}Fe distribution shown previously in figure 3.15 produced for the previous modulation analysis [49]. Small discrepancies are to be expected as this was a quick check and the optical parameters used weren't fine-tuned for an exact match. Figure 5.36 compares the ^{55}Fe MC and the ^{55}Fe calibration-normal data classification parameter distributions for all 9 internal calibration positions in the 3 - 4 keV$_{ee}$ energy range, figure 5.37 shows the equivalent 1 - 2 keV$_{ee}$ comparison.

It is directly apparent that the classification parameter distribution of the ^{55}Fe MC and the ^{55}Fe calibration-normal data are in good agreement with one another. Even though the distributions vary quite significantly over internal calibration position the difference between MC and data remains minimal, even for the 1 - 2 keV$_{ee}$ region with its poorer statistics. This is a good indication that the classification parameter performs well in this low enery region on both internal events: those originating from the ^{55}Fe source and BG events: those present in the normal data that have been subtracted.

This is indirect evidence that the PDF classifier developed in this chapter should perform as intended on both the data and NR signal MC that underpins the modulation analysis written about in this thesis.

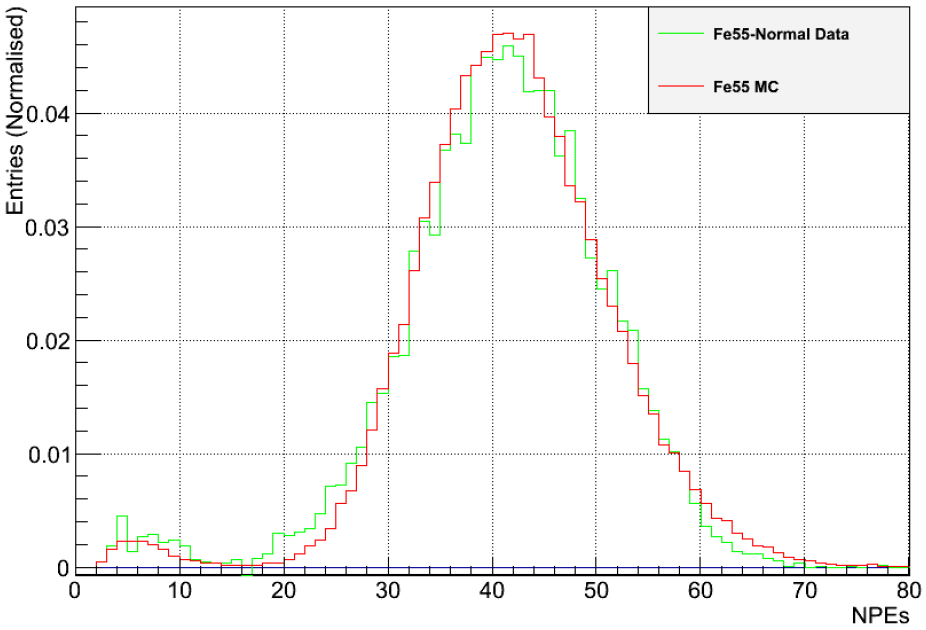


Figure 5.35: Comparison of the ^{55}Fe MC (red) and ^{55}Fe-normal data (green) NPEs distribution at the Z = 0 cm internal calibration position. There is a large peak at 5.9 keV and a small peak at 1.65 keV.

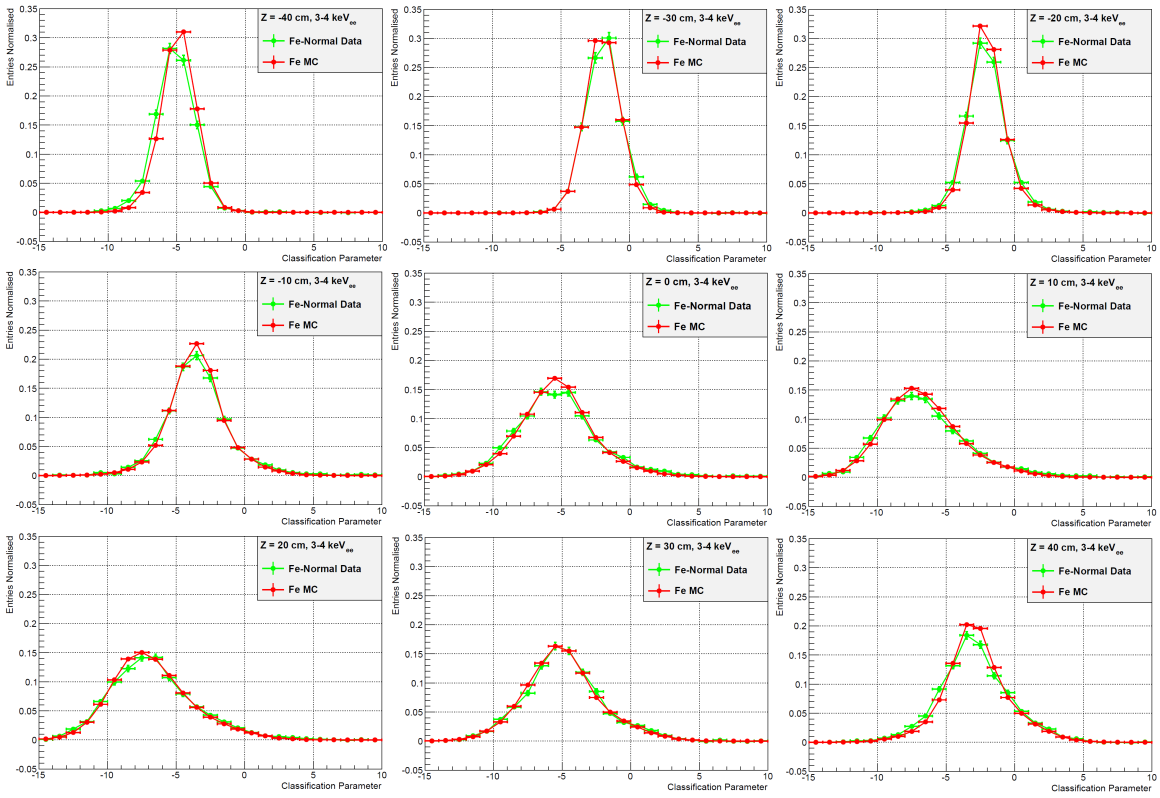


Figure 5.36: Comparison of ^{55}Fe 3 - 4 keV$_{ee}$ classification parameter distributions for ^{55}Fe MC (red) and ^{55}Fe-normal data (green) for all 9 internal calibration positions Z = -40 to 40 cm (10 cm steps).

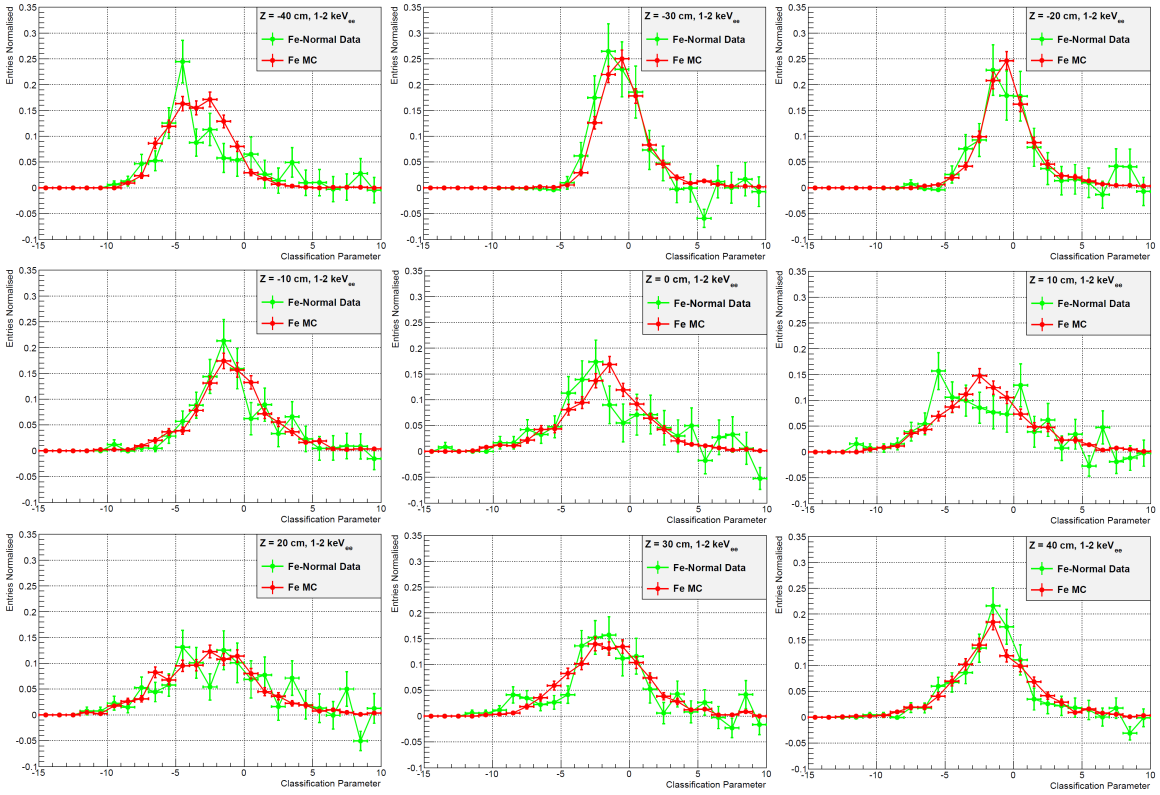


Figure 5.37: Comparison of ^{55}Fe 1 - 2 keV$_{ee}$ classification parameter distributions for ^{55}Fe MC (red) and ^{55}Fe-normal data (green) for all 9 internal calibration positions Z = -40 to 40 cm (10 cm steps).

5.4 Outlook

Although the PDF approach to classification is well founded and rooted in statistics, it is somewhat limited. It only captures the average distribution of any particular sample of events; if the events underpinning it have multiple distinct characteristics/distributions these distinctions will not only be completely averaged out but can seriously compromise classifier performance, with event subsets completely overlooked. A modern approach rooted in machine learning where there are no preconceived classes or categories can highlight such possible previously unknown subsets and allow for a more fine-tuned event selection where these nuances come to the fore.

Events recorded in XMASS are best described as a sequence of hits as outlined previously in figure 5.5. The relative spatial reference highlights the spherical sym-

metry of the detector and removes any information related to individual PMTs. This is the ideal input for a recurrent neural network (RNN) which looks to find patterns in sequences. It is predominantly used when analysing text and for the purposes of translation, however its structure could be altered to suit the purposes of a time based physics analysis.

Chapter 6

Data Selection, Time Periods, LY and Event Rates

A modulation analysis searches for the tell-tale sinusoidal modulation signal that is not BG related in an experiment's data. To observe periodic time variation effects within the data, it needs to be prepared by separating it into distinct time periods. Analyses that simply compare an expected signal spectra with the recorded data may have increased sensitivity by not time binning, however they require an exceedingly accurate understanding of the experimental BG and hence the results are debateable.

Two dark matter annual modulation analyses are reported in this thesis. One follows the method previously in [49,50] applied to the complete dataset at the behest of the XMASS collaboration, modified only where the previously used dataset led to selection criteria that, if left unchanged, would have severely limited the analysis. The other newly developed here, utilises the PDF classification technique outlined in chapter 5 and limits the dataset to the final 4 years where the LY is most stable. This allows for a new approach to the analysis which doesn't rely on MC generated BG LY relative efficiency curves.

Section 6.1 outlines which runs are selected for each analysis and how they are combined into periods, additional run selection cuts are required for the lowest energies affected by the introduction of the low threshold trigger. Section 6.2 consolidates the inner calibration LY with an effective hose LY to obtain the LY throughout the detector's entire operational history. The LY and recorded data's event rates are

intrinsically linked and section 6.3 demonstrates the use of MC generated BG LY relative efficiency curves on the likelihood cut event rates for the complete dataset and explains why a new approach is necessary for the PDF cut event rates.

6.1 Run selection and period structure

The previous XMASS modulation analyses [49, 50] amalgamated data into 2 periods per month and measured the time in days from 2014/01/01, for consistency the analyses presented in this thesis continues with this arrangement. This period length was chosen as it reflected the calibration schedule at the experiment, internal calibration measurements initially occurred fortnightly; eventually became monthly and finally ceased measurements at the end of 2017.

Only normal physics runs are used in the analysis, all runs dedicated to calibration measurements were excluded. Additionally, specific runs were precluded from the analysis if the detector was undergoing an operational change, these include but are not limited to: cooling tower (CT) exchange, LXe refilling, Xe gas flow change, etc. Periods should ideally contain an uninterrupted series of runs so their total combined run time is equal to the time over which they span. The half-month period structure is varied on occasion to account for these omitted runs, see appendix A.1.

The analysis that employs the likelihood cut utilises the complete dataset and the other that employs the new PDF cut utilises a subset of the complete dataset: the stable LY dataset which is limited to runs occurring after day 397 due to the extended period of light yield stability that the experiment eventually settled into.

6.1.1 Normal threshold periods

In total there are 125 normal threshold periods in the complete dataset and 96 normal threshold periods in the stable LY dataset. The livetime of each individual period is shown in figure 6.1, this amounts to a total of 1549.32 days and 1203.72 days for the complete dataset and stable LY dataset respectively.

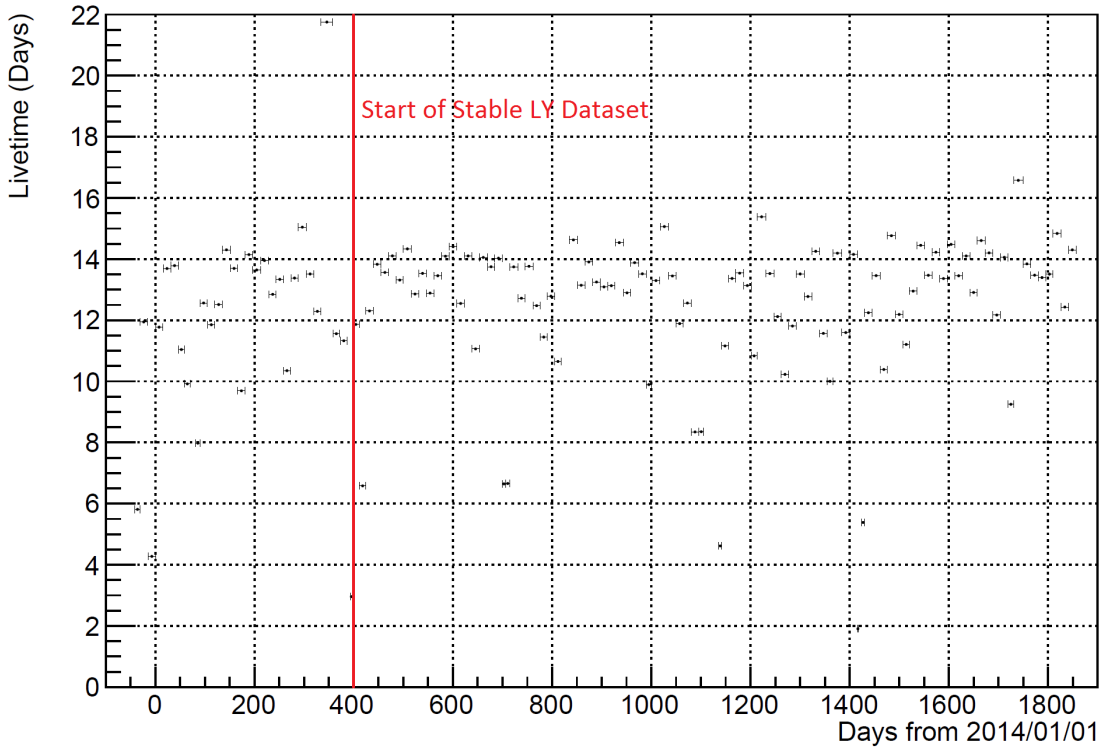


Figure 6.1: Livetime for each of the normal threshold periods.

6.1.2 Additional run selection criteria for low threshold data

The lowering of the trigger threshold allows one to probe lower energies, which is vitality important in DM direct detection as the deposited kinetic energy is predicted to be relatively small as outlined in section 2.2.2. However this introduces certain challenges associated with additional sources of BG and stricter requirements on the stability of each individual PMT in the detector.

- **Dark rate (R_{Dark}):** LED calibration as described in section 3.3.1 triggers 8 blue LEDs to flash once every second. The LEDs take ~40 ns to flash, and the forced detector readout includes the recorded response from 1 μs prior to the trigger. PMT dark rates are measured in this 1 μs prior to the LED flash throughout all of data taking. At low threshold accidental ~ PE level signal coincidences of dark hits contribute, constituting an additional source of BG. A R_{Dark} ~ 3000 Hz corresponds to a ~ 0.015 Hz 3hit event rate measured within the data after applying the StdCuts (excluding the flasher cut) [50].

To calculate the dark rate, runs are combined until their total time ~ 2 days. The number of LED calibration events (N_{LED}) and the total number of dark hits registered within those events (N_{Dark}) is tallied. As LED triggered events occur every 1 s and dark hits are measured in a 1 μs window, the dark rate is:

$$R_{Dark} = \frac{N_{Dark}}{N_{LED}} \times 10^6. \tag{6.1}$$

The total dark rate from all PMTs (R_{Dark}) is demonstrated over time in the left hand plot in figure 6.2, each point represents one continuous ~2 day time period since the start of low threshold data taking. These dark hits occur at different rates in different PMTs and the maximum dark rate observed in an individual PMT as a proportion of the total dark rate ($R_{Dark}^{\frac{MaxPMT}{Total}}$) is shown in the right hand plot in the same figure. The long period of increased R_{Dark} followed the Xe recovery and distillation which occurred 2017/01/10 - 2017/02/08. You don't see a rise in the $R_{Dark}^{\frac{MaxPMT}{Total}}$ because many PMTs are observing above average rates. Additionally, there are times where both metrics increase simultaneously, such as the clusters of periods around 770 days, 970 days, 1080 days and 1830 days, this is predominantly down to an event rate spike in an individual PMT which is subsequently disabled. All of these outlier periods are coloured red and runs associated with these periods are excluded from the low threshold dataset.

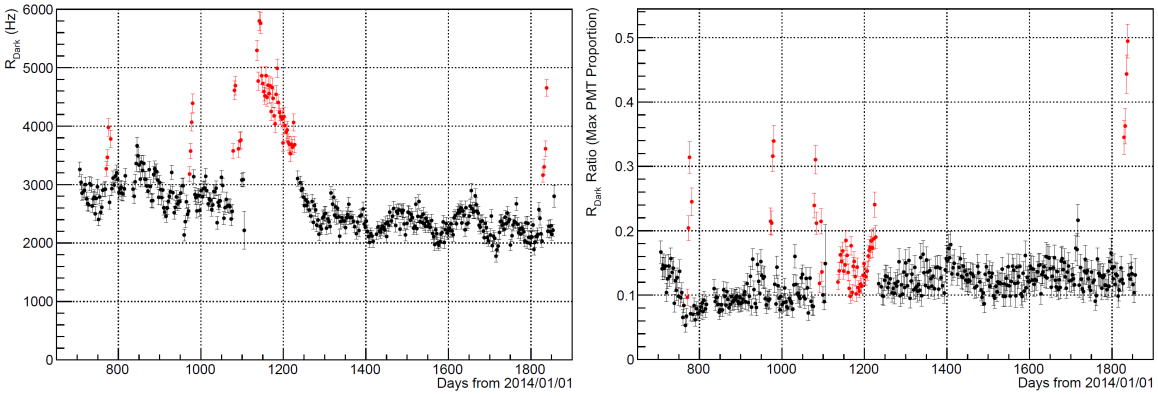


Figure 6.2: R_{Dark} (left) and $R_{Dark}^{\frac{MaxPMT}{Total}}$ (right). Rejected periods with large R_{Dark} or $R_{Dark}^{\frac{MaxPMT}{Total}}$ are highlighted red.

- **LED events' waveform gain and PE stability:** While the accidental coincidence contribution to the BG is measured using the LED events by investigating dark hits extracted from the 1 μs prior to the LED flash, the LED related pulses themselves are utilised to evaluate PMT stability. For each pulse recorded in each individual PMT the waveform gain (G) and the PE are extracted. G is related to the magnitude of the FADC response and varies between PMTs, the PE is related to the integral of these recorded waveforms and is corrected so on average 1 LED photon arriving at any given PMT results in 1 PE being measured. The average PE observed in any PMT is $\gtrapprox 1$ as there is a small probability of multiple LED photons arriving at a PMT simultaneously. The average G and PE within each ~ 2 day time period is extracted for each individual PMT. Both of these measures vary linearly over time. However, while a single linear fit is sufficient to capture the time variation of the PE within individual PMTs, an abrupt change in G is observed in most PMTs after Xe distillation occurred. Therefore 2 linear fits - one before and one after Xe distillation - are required to adequately capture the time variation of the G within individual PMTs. Figure 6.3 shows the recorded PE (left) and G (right) over time for an individual PMT with the resultant linear fits. Each measurement can then be compared to its respective linear fit and represented in terms of sigma (σ_{PE} and σ_{G}) as demonstrated in figure 6.4. For each individual time period the σ_{PE} and σ_{G} distributions of all PMTs can be obtained as depicted in figure 6.5 for the first time period. The mean of these distributions ($\langle\sigma_{\mathrm{PE}}\rangle$ and $\langle\sigma_{\mathrm{G}}\rangle$) can be obtained and plotted for each time period as outlined in figure 6.6. These mean values can be converted into sigma variations from 0 ($\sigma_{\langle\sigma_{\mathrm{PE}}\rangle}$ and $\sigma_{\langle\sigma_{\mathrm{G}}\rangle}$) as depicted in figure 6.7. Both $\sigma_{\langle\sigma_{\mathrm{PE}}\rangle}$ and $\sigma_{\langle\sigma_{\mathrm{G}}\rangle}$ display 2 prominent deviations at later time. All time periods exceeding ± 5 sigma bounds for either $\sigma_{\langle\sigma_{\mathrm{PE}}\rangle}$ and $\sigma_{\langle\sigma_{\mathrm{G}}\rangle}$ are coloured red. All runs associated with these time periods are rejected from the low threshold dataset as a majority of PMTs were deviating from their normal operation characteristics in unison.

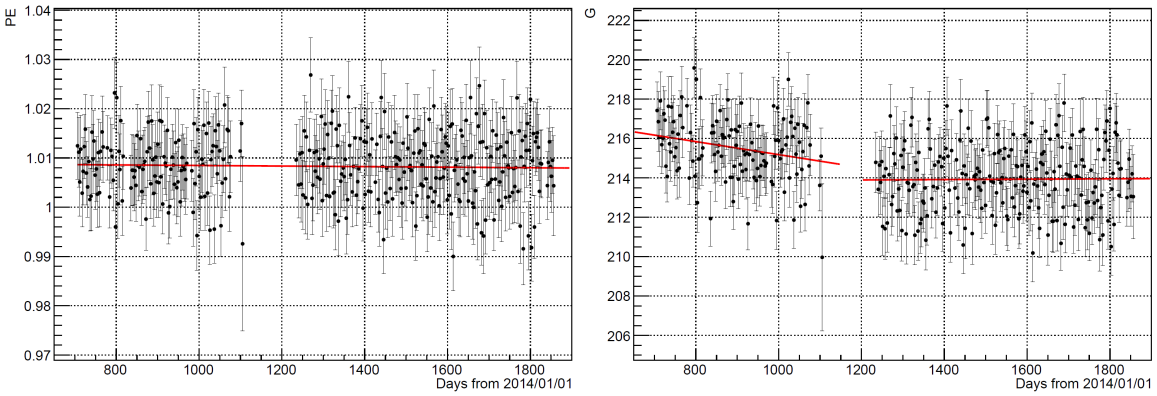


Figure 6.3: PE (left) and G (right) linearly fit over time (PMTid = 4). PE linearly reduces by a very small amount over time. The G varies linearly in two separate time windows, before and after distillation.

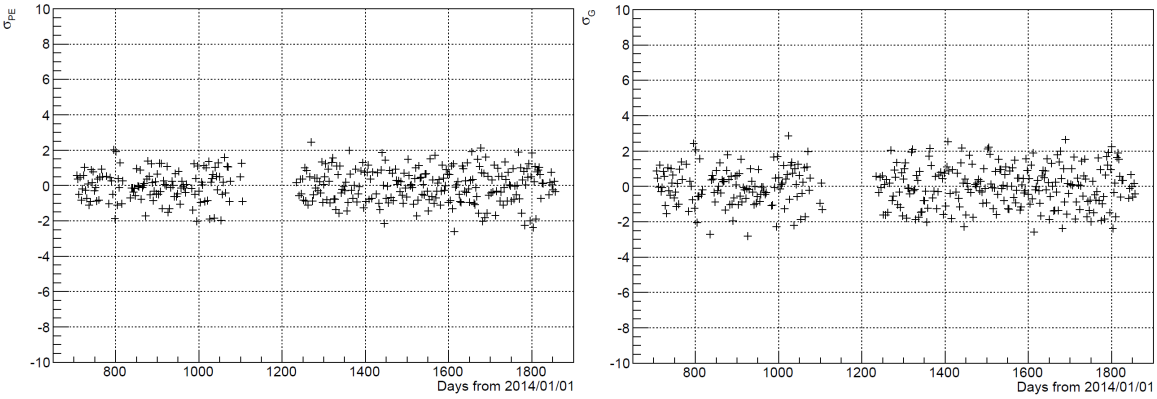


Figure 6.4: σ_{PE} (left) and σ_{G} (right) over time (PMTid = 4).

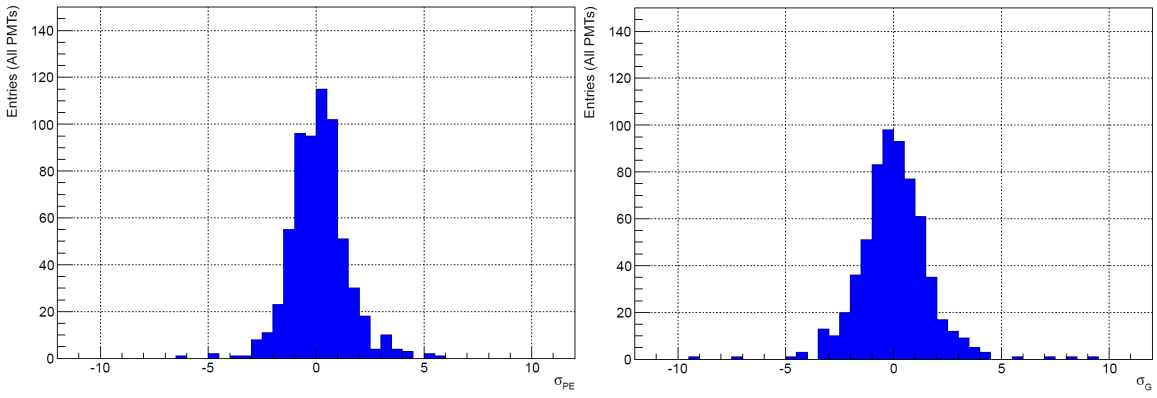


Figure 6.5: Distributions of σ_{PE} (left) and σ_{G} (right) for all PMTs (first time period). Expect it to be close to 0 however a deviation away from 0 will indicate multiple PMTs misbehaving.

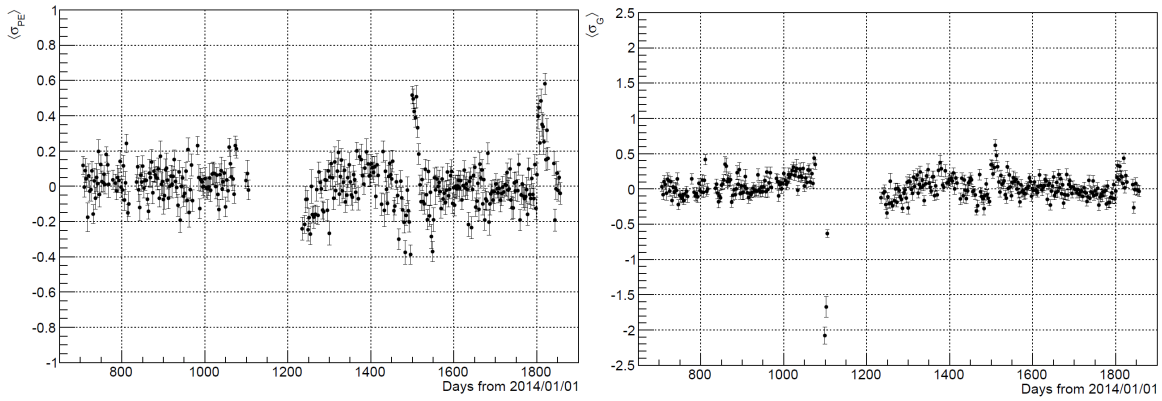


Figure 6.6: $\langle\sigma_{\mathrm{PE}}\rangle$ (left) and $\langle\sigma_{\mathrm{G}}\rangle$ (right) over time (all PMTs averaged). There are specific periods of time where multiple PMTs are misbehaving in tandem and causing $\langle\sigma_{\mathrm{PE}}\rangle$ or $\langle\sigma_{\mathrm{G}}\rangle$ to shift away form 0 by a statistically large amount.

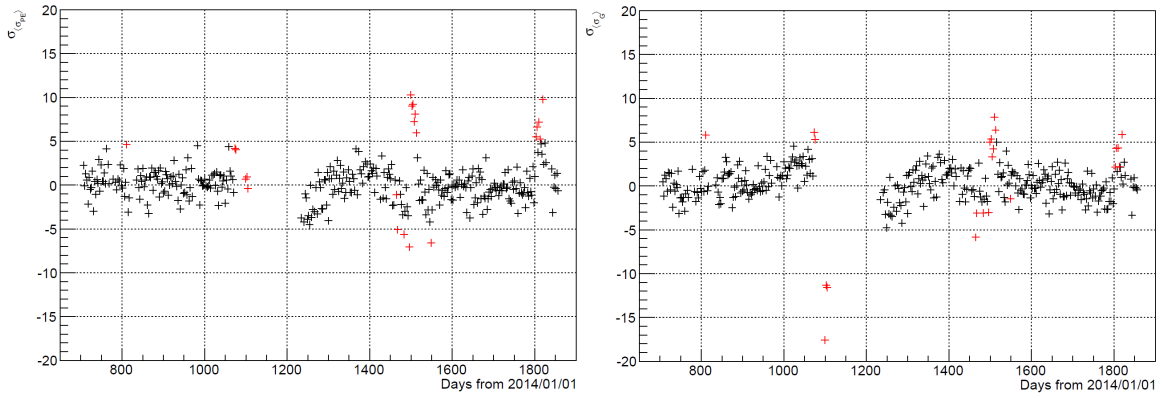


Figure 6.7: $\sigma_{\langle\sigma_{\mathrm{PE}}\rangle}$ (left) and $\sigma_{\langle\sigma_{\mathrm{G}}\rangle}$ (right) over time (all PMTs averaged). The statistically significant deviations away from 0 (¿5σ) are rejected periods and are highlighted red.

- **Low threshold periods, livetime and R_{Dark}:** The additional runs rejected when considering the dark rate (R_{Dark}) and PMT stability ($\sigma_{\langle\sigma_{PE}\rangle}$ and $\sigma_{\langle\sigma_G\rangle}$) reduces the total low threshold livetime by ~ 18.1% from 930.66 to 761.96 days. The low threshold periods are arranged similarly to the normal threshold periods; taking into account detector operational changes. The livetime for each individual period is plotted in figure 6.8, there are 67 periods in total.

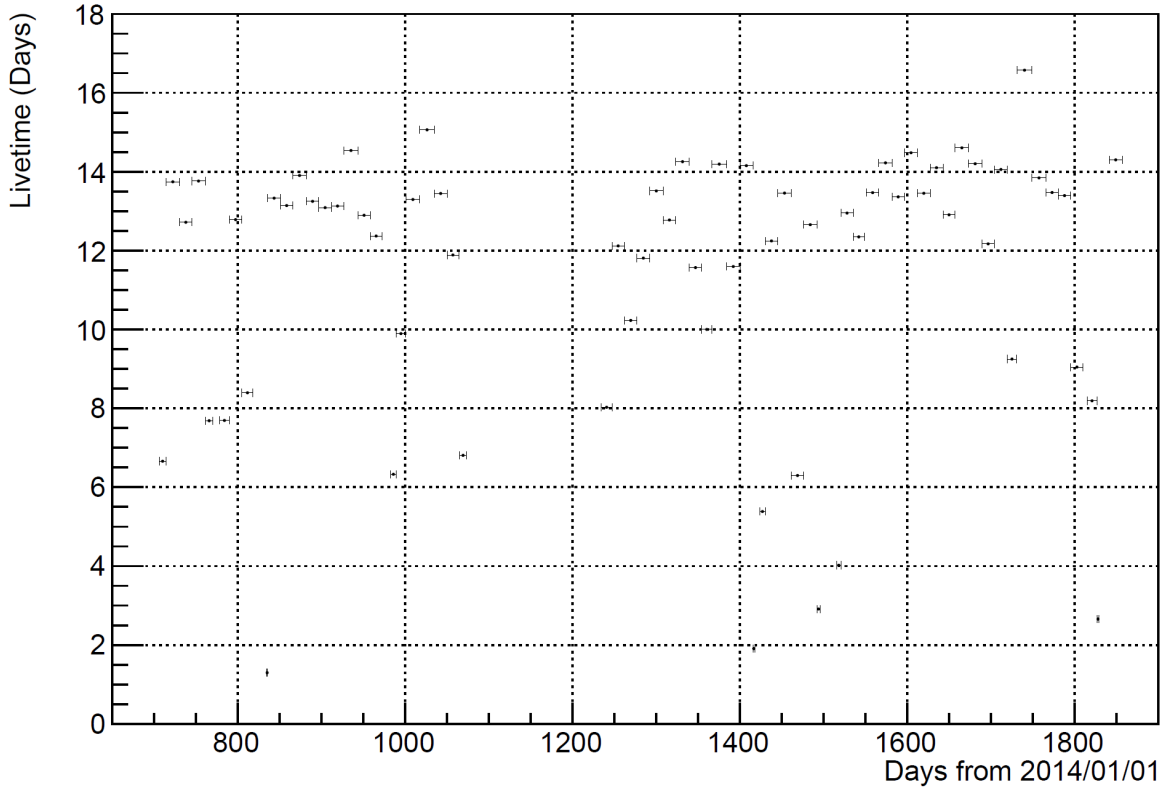


Figure 6.8: Livetime for all of the low threshold periods.

The complete dataset likelihood cut analysis - based on the previous modulation analysis [49,50] - utilises MC generated BG LY relative efficiency curves, section 6.3 outlines how these are implemented. R_{Dark} is considered a new source of BG and as such is not simulated within the 30 internal BG MC types and therefore is treated separately within this analysis. The previous analysis [49,50] examined the relation between the $N_{Hits} = 3$ event rate ($R_{N_{Hits}=3}$) and the measured R_{Dark} within normal physics runs. The relative difference of these measures (ΔR_{Dark} and $\Delta R_{N_{Hits}=3}$) was obtained by looking at periods of time where R_{Dark} was

large and where it was small and comparing the respective event rates. This was repeated multiple times and the resulting data points (ΔR_{Dark}, $\Delta R_{N_{Hits}=3}$) where fit with a single gradient term: $G^D = 0.16 \pm 0.09$. R_{Dark} measured within each low threshold period is displayed in figure 6.9. The decline in R_{Dark} present in figure 6.2 is relatively linear with additional variation on top. If this decline were solely due to PMTs being disabled - after their dark rate vastly increases - one would expect to observe multiple clear step reductions in R_{Dark}. Why R_{Dark} generally decreases over time is unknown and no additional corrections for PMTs being disabled are applied. The effect of R_{Dark} on $R_{N_{Hits}=3}$ was incorporated into χ^2 minimisation by obtaining the dark rate relative to the minimal period dark rate ΔR^{Min}_{Dark} and scaling. The central scaling value is G^D however this was allowed to vary to obtain an optimal fit. A pull term of the variation as a proportion of the uncertainty on G^D is added to the total χ^2 to restrict unlimited variation. The dark rate systematic effect on the event rate in the lowest energy bin is shown in figure 6.10 for the central G^D and $\pm 1\sigma$ values.

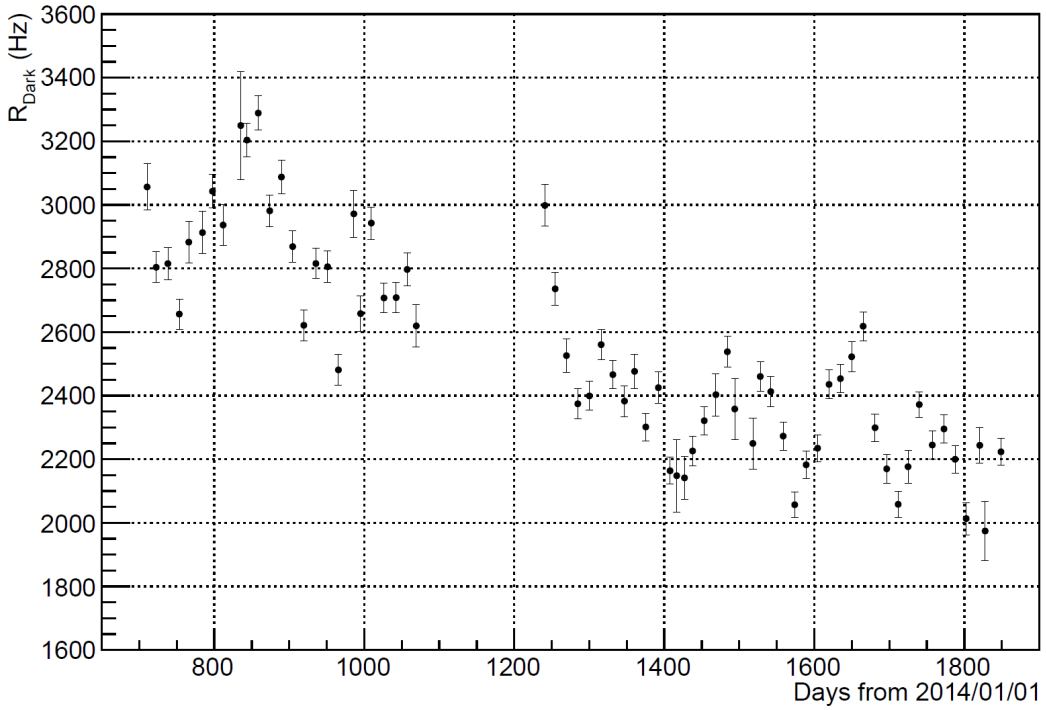


Figure 6.9: Dark rate measured within each low threshold period. Reduction over time likely due to large dark rate PMTs being disabled.

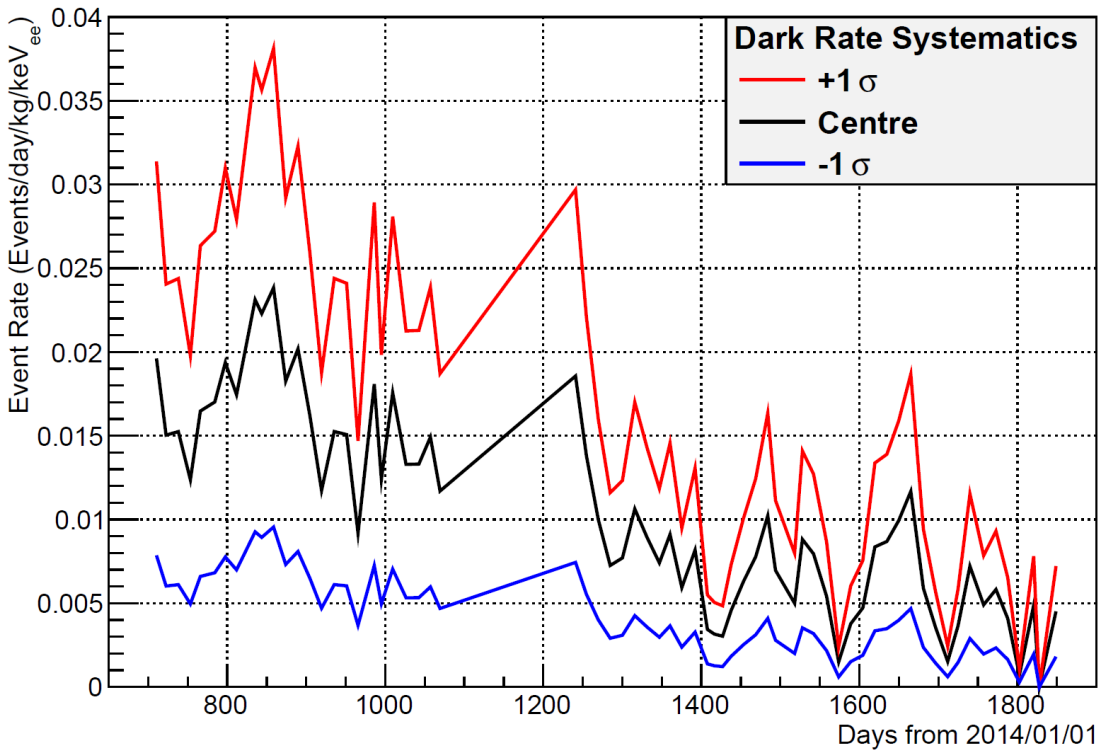


Figure 6.10: Dark rate systematic effect on the low threshold event rate for the complete dataset likelihood cut analysis. Reduction over time reflects the reduction in dark rate.

6.2 Light yield history

Now that the data is both selected and collated into periods for both the normal threshold energies and those affected by the addition of the low threshold trigger, the only remaining piece of information necessary to fully comprehend the recorded event rates is to obtain the LY over time and for each specific period.

As detailed in section 3.3.2, the internal ^{57}Co calibration data is used to obtain the LXe's optical parameters governing scintillation light propagation and the observed LY at any internal position along the z-axis. Most XMASS analyses use the ^{57}Co 0 cm LY as they additionally apply a fiducial volume (FV) cut to reduce the ID surface's BG events' contribution; only events reconstructed within 20cm of the ID's centre are analysed. The detector has a ~ 40 cm radius, so restricting the FV to a 20 cm radius reduces the total usable LXe to $\frac{1}{8}$ of the total 832kg contained within the ID. The FV Cut does not probe the lowest energies as it fails to reconstruct the

event radius. However, the annual modulation analysis outlined in this thesis and the annual modulation analyses conducted previously do not use a FV cut as they use low hit events for which the position reconstruction is not precise enough. Both the Cherenkov Cut + Likelihood cut and PDF cut exploit the entire active volume of the ID. The previous analysis [49,50] utilised the ^{57}Co -30 cm LY as $\frac{7}{8}$ of the entire active volume lies within the 20 - 40 cm radial shell. The ^{57}Co -30 cm LY is demonstrated over time in the bottom right plot in figure 3.6. At the end of 2017 the detector was considered stable and XMASS ceased inner calibration data taking with the proviso that the hose data remained consistent. This held up and only one final ^{57}Co inner calibration was performed at the very end of normal data taking.

At the end of 2017 the detector was considered stable and XMASS ceased inner calibration data taking with the proviso that the hose data remained consistent. This held up and only one final ^{57}Co inner calibration was performed at the very end of normal data taking.

The previous modulation analysis [49,50] used data from the end of 2013 up until June 2017 and the ^{57}Co inner calibration data was available throughout this entire period. The analyses presented in this thesis incorporate the final year and a half of data taking - up until February 2019 - and are the first to use data recorded after inner calibration data taking ceased. This section outlines how the external hose ^{60}Co calibration data is used to quantify the LY throughout the whole analysis period.

6.2.1 Hose data LY ratio

Figure 6.11 demonstrates the PE spectrum of 2 sets of hose data, that taken on 2016/06/23 on the left in blue and 2014/02/06 on the right in red. As ^{60}Co events occur throughout the detector volume - falling off according to the distance from the source - and the high energy of the ^{60}Co gammas often leads to saturation in the PMTs for gamma events originating close to the PMT surface the peak observed is broad and non-Gaussian. Therefore one cannot simply peak fit to obtain the LY and it's corresponding error; unlike that of the ^{57}Co data. Instead a LY ratio is obtained

by directly comparing a given hose dataset with a specific reference hose dataset. The Hose data recorded on 2016/06/23 was chosen as the reference for 2 main reasons: The detector conditions were particularly stable during this period and it has one of the largest statistics available.

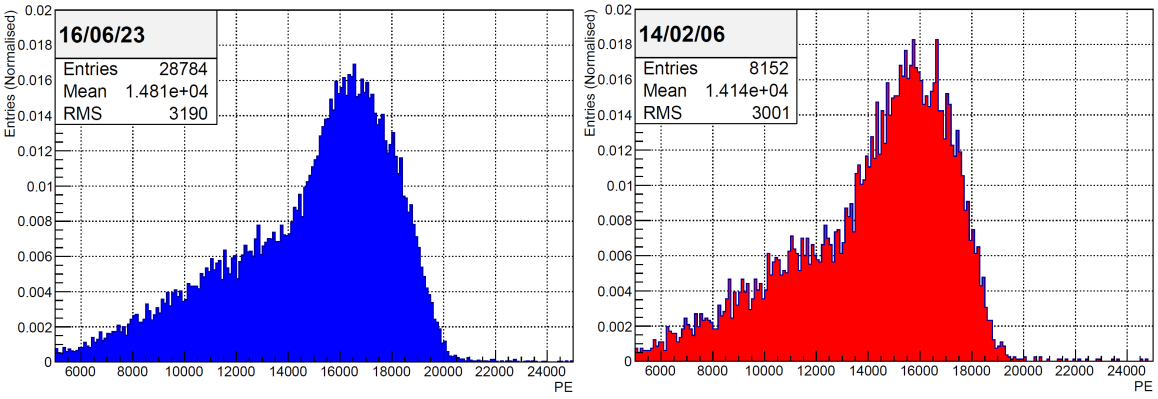


Figure 6.11: Hose data energy spectrums: 2016/06/23 (left) and 2014/02/06 (right).

Two datasets are compared by performing a Kolmogorov Smirnov (KS) test: both PE spectra are integrated into their respective CDFs and the maximum distance (D) between them is obtained; this is limited to the 5000 - 25000 PE range. This same test is carried out for a range of scaling factors where every PE entry in the reference hose dataset is multiplied by said scaling factor. Figure 6.12 demonstrates 2 different scaling factor CDF comparison examples using the previously displayed hose PE spectra (same colours as before). The plot on the left has had no scaling applied, whereas the right hand plot has seen the reference dataset scaled by 0.954; the best fit for this particular dataset comparison. The relation between the scaling factor and D is outlined in figure 6.13. The best fit scaling factor with the minimum D is termed the LY Ratio for that particular hose dataset.

To demonstrate the relation between the inner calibration data and the hose data one needs not only the LY and LY Ratio respectively but also their corresponding statistical errors. For the ^{57}Co -30cm LY (LY^{Inner}_{-30cm}) the statistical error ($\sigma_{LY^{Inner}_{-30cm}}$) is ~ 0.008 PE/keV and is obtained alongside the LY when fitting the 122keV peak, p1 in figure 3.18.

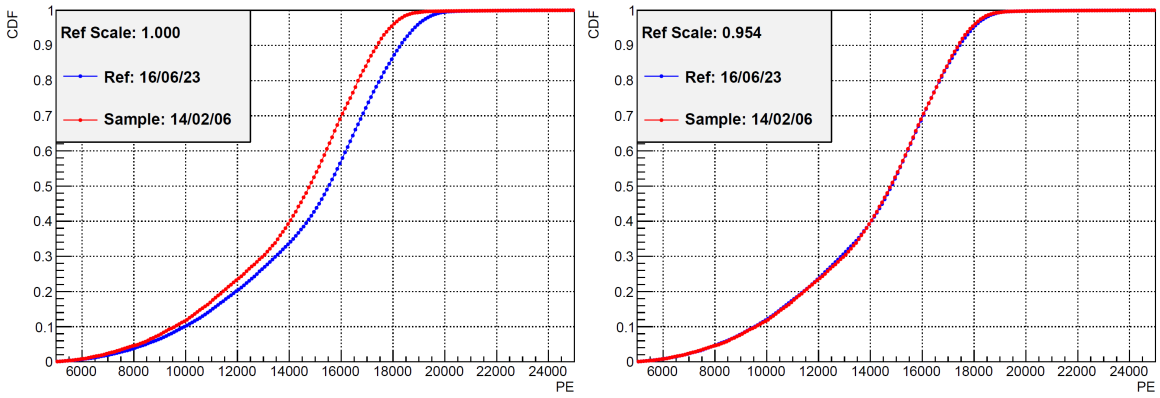


Figure 6.12: CDFs of hose data energy spectrums: 2016/06/23 (blue) and 2014/02/06 (red). The reference is scaled by 0.954 in the right hand plot, no scaling in the left hand plot.

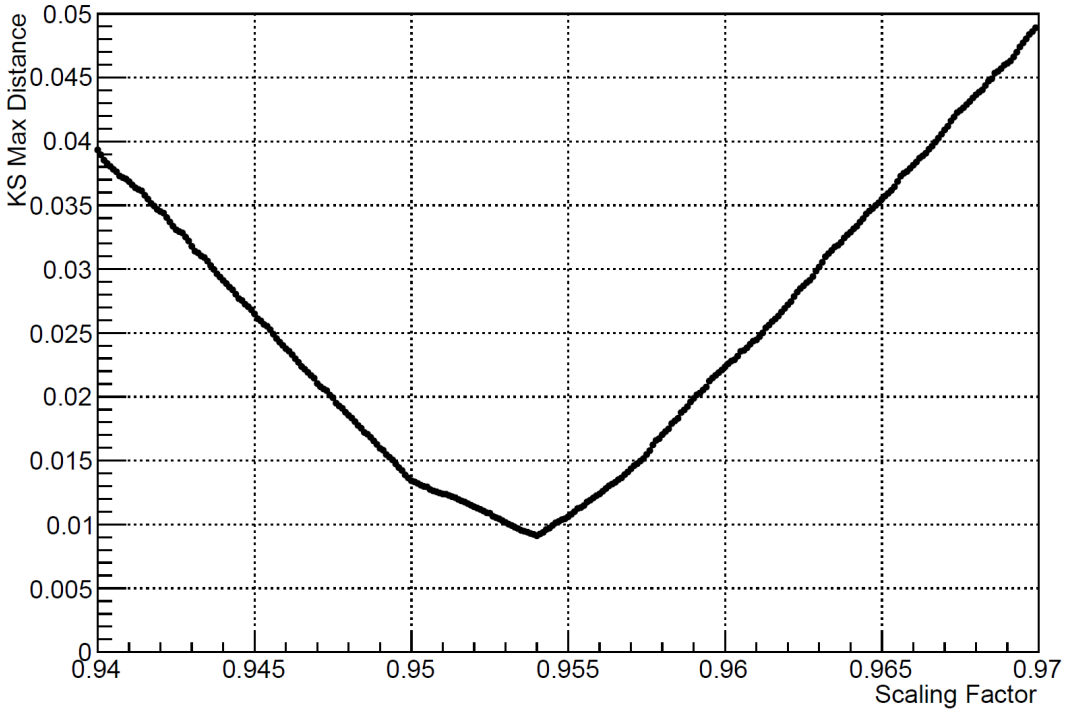


Figure 6.13: KS max distance distribution between hose data taken on 2014/02/06 and the reference hose data (2016/06/23). Best scaling factor obtained at minimum.

The statistical error for the hose data's LY Ratios is obtained as follows. The total PE of each event within a given hose dataset follows Poisson statistics and each can be randomly varied to produce a statistically randomised PE spectrum. Multiple randomised dummy PE spectra are generated and the LY Ratio of each can be calculated using the same technique outlined previously. The standard deviation of the dummy datasets LY Ratio distribution is then taken as the statistical error on

the true LY ratio. This is repeated for all hose datasets.

These errors are ~4 times smaller than the errors for the inner calibration data LY values; this is expected seeing as there is roughly twice the statistics and the average PE is ~8 times larger. The resultant LY Ratio (LY^{Hose}_{Ratio}) and it's error ($\sigma_{LY^{Hose}_{Ratio}}$) is obtained for each hose calibration dataset and plotted over time in figure 6.14.

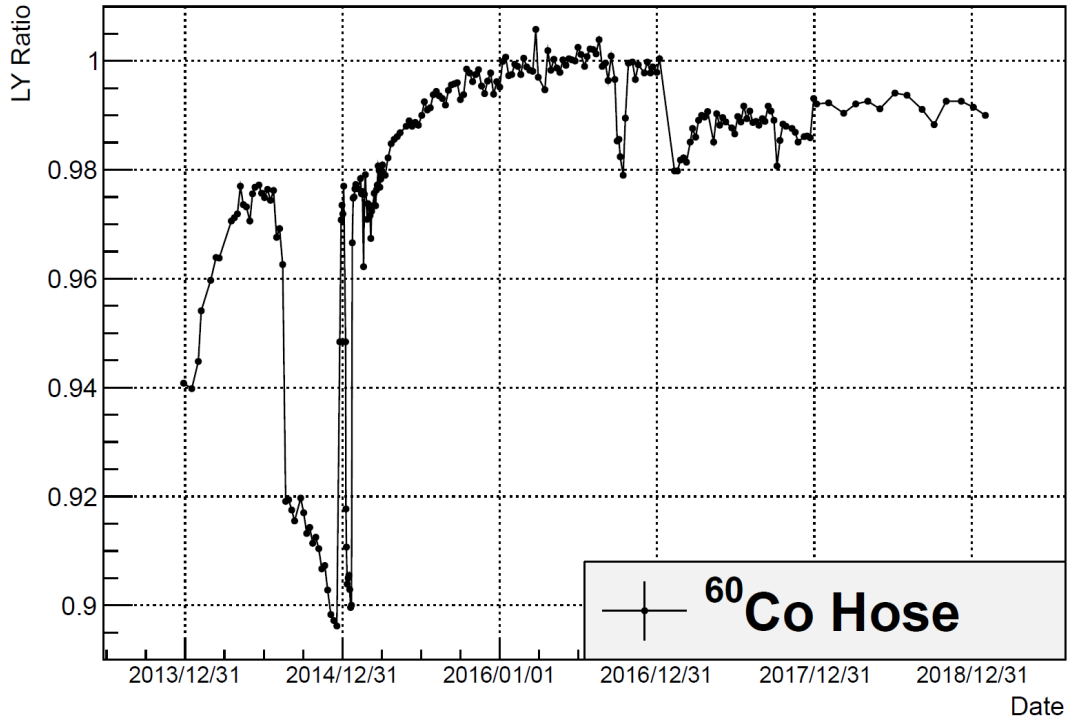


Figure 6.14: The hose calibration datasets LY ratio with errors over time with respect to the reference hose dataset (2016/06/23). Variation over time reflects detector conditions.

6.2.2 Hose LY ratio Vs Inner ^{57}Co -30 cm LY

To linearly transform LY^{Hose}_{Ratio} into an effective -30cm LY ($LY^{Hose}_{Eff\ -30cm}$) the LY^{Hose}_{Ratio} must first be compared directly with LY^{Inner}_{-30cm}. The points selected for comparison where chosen with 2 key criteria, stability and reliability. Stability, in that the detector must be acting under normal operational circumstances, i.e. not during initial detector stabilisation - where the two LY measures are inconsistent with one another - and not during the periods of sizeable LY variation. This was achieved by using only hose calibration data points occurring after August 2014 and requiring that the LY^{Hose}_{Ratio} of

the hose data points preceding and following any given data point deviate from said data point by $< 0.5\%$. Reliability embodies a fair comparison of equivalent data, the LY clearly varies between measurements so this is only achieved by comparing hose and inner calibration data taken in close proximity: within 1 day of each other. The hose data points and their corresponding inner calibration data points that satisfy these criteria are plotted against one another in figure 6.15.

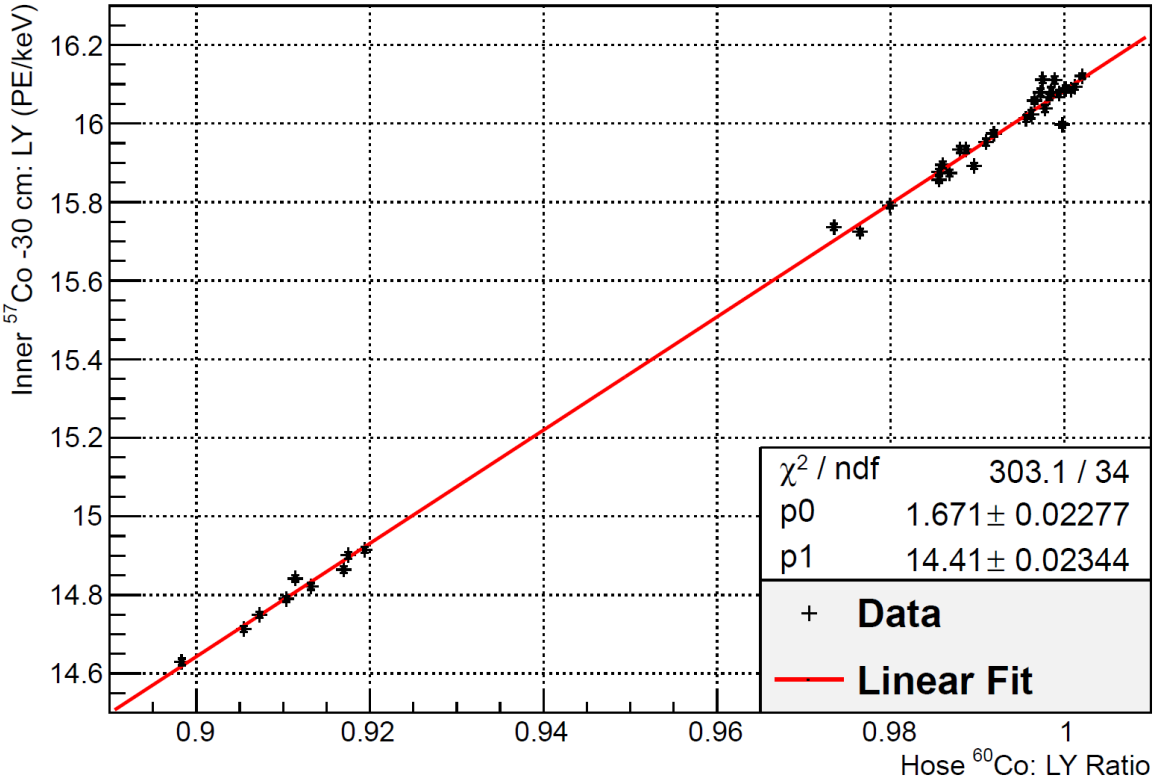


Figure 6.15: Hose Data: LY^{Inner}_{-30cm} Vs LY^{Hose}_{Ratio} linear fit.

The data points in this figure are linearly fit and the resultant function can be used to transform the hose data into an effective -30cm LY:

$$LY^{Hose}_{Eff\ -30cm} = 1.671 + 14.41 \times LY^{Hose}_{Ratio}. \tag{6.2}$$

The systematic error for the hose data's effective -30cm LY is obtained using the standard deviation of the points distributed around the linear fit. This is then

combined in quadrature with the scaled statistical error to obtain the total error:

$$\sigma^{Sys}_{\mathrm{LY}^{\mathrm{Hose}}_{\mathrm{Eff\ -30cm}}} = \sqrt{\frac{\sum^{N}\left(\mathrm{LY}^{\mathrm{Hose}}_{\mathrm{Eff\ -30cm}} - \mathrm{LY}^{\mathrm{Inner}}_{\mathrm{-30cm}}\right)^2}{N-1}} \quad \text{with}$$
$$\sigma_{\mathrm{LY}^{\mathrm{Hose}}_{\mathrm{Eff\ -30cm}}} = \sqrt{\left(\sigma^{Sys}_{\mathrm{LY}^{\mathrm{Hose}}_{\mathrm{Eff\ -30cm}}}\right)^2 + \left(14.41 \times \sigma_{\mathrm{LY}^{\mathrm{Hose}}_{\mathrm{Ratio}}}\right)^2} \sim 0.025\ \mathrm{PE/keV}. \tag{6.3}$$

Figure 6.16 shows the inner calibration $\mathrm{LY}^{\mathrm{Inner}}_{\mathrm{-30cm}}$ and the transformed hose calibration $\mathrm{LY}^{\mathrm{Hose}}_{\mathrm{Eff\ -30cm}}$ data points with error bars over the entire operational lifetime of the detector. After initial detector stabilisation they overlap one another throughout and can therefore be used as interim LY measures during the year long period without inner calibration data taking.

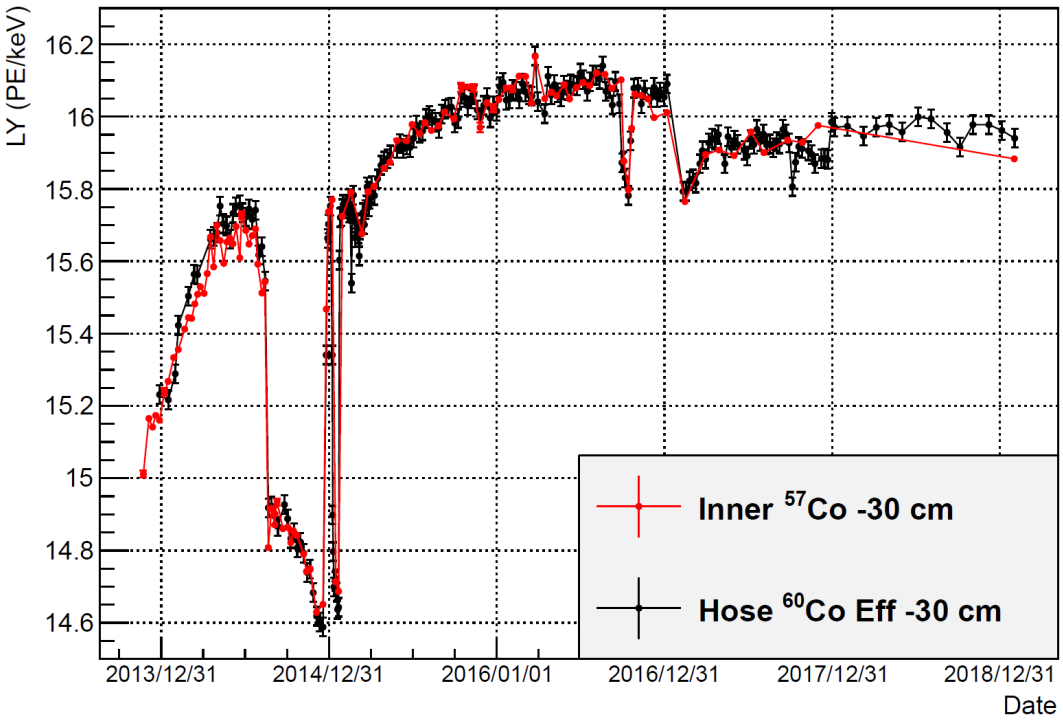


Figure 6.16: Inner calibration data $\mathrm{LY}^{\mathrm{Inner}}_{\mathrm{-30cm}}$ and hose calibration data $\mathrm{LY}^{\mathrm{Hose}}_{\mathrm{Eff\ -30cm}}$, with errors over time. Variation over time reflects detector conditions. There is a good match after the initial few months of detector stabilisation.

As mentioned at the start of section 6.2, inner calibration data taking ceased at the end of 2017 as the detector was considered stable. This would only remain the case with the proviso that the hose data remained consistent which it did. As

discussed in section 3.3.3 hose calibration moved from a U-shaped tube to a stainless steel vacuum tube which terminated on the wall of the OFHC Cu cryostat vessel at the level of the centre of the ID in December 2013. Therefore there is no comparable external hose data before this point in the first couple of months of XMASS being operational.

6.2.3 Normal threshold and low threshold LY

Unfortunately neither calibration technique spans the entire lifetime of the detector, the hose data is lacking in the first 2 months and the inner ^{57}Co data is lacking throughout 2018. Therefore the complete dataset requires both sets of calibration data to obtain the LY for each period. As the previous analyses solely used $\mathrm{LY}^{\mathrm{Inner}}_{\mathrm{-30cm}}$, this is utilised wherever possible and $\mathrm{LY}^{\mathrm{Hose}}_{\mathrm{Eff\ -30cm}}$ where the inner ^{57}Co data is lacking.

The stable LY PDF cut analysis however is not a simple extension of the previous analyses and the $\mathrm{LY}^{\mathrm{Hose}}_{\mathrm{Eff\ -30cm}}$ is available throughout the entirety of the dataset. Therefore 2 options are available, use the same mixed source LY as the complete dataset or use only the hose LY. Although the $\mathrm{LY}^{\mathrm{Hose}}_{\mathrm{Ratio}}$ data is obtained using an external source, they are transformed into $\mathrm{LY}^{\mathrm{Hose}}_{\mathrm{Eff\ -30cm}}$ using the $\mathrm{LY}^{\mathrm{Inner}}_{\mathrm{-30cm}}$ data. Therefore any advantage they would have by not disrupting the detector - inserting a rod inevitably varies the temperature and flow distribution of the LXe - is nullified. Consequently the same mixed source LY values are utilised for the stable LY dataset.

The light yield for each of the normal threshold and low threshold periods is demonstrated in figures 6.17 and 6.18 respectively. These values are obtained by evaluating the LY at the periods' central time.

The low threshold trigger was implemented in December 2015 and that's when the low threshold periods begin. That's why the low threshold LY plot in figure 6.18 only considers periods in time after 700 days - where the LY only varies between 15.85 - 16.15 PE/keV. As discussed in section 6.1.2 the low threshold has additional run selection criteria which means the low threshold and normal threshold normal run lists do differ slightly over the time both were taken. Some periods are completely removed

- like those occurring directly after Xe distillation - and in others the different run lists affect said period's central time and hence results in a slightly varied LY between the low threshold and normal threshold for a given period. The overall shape of the observed LY and reasons for occasional variations is outlined in section 3.2.3.

Attributing a LY error (σ_{LY}) to a period of 2 weeks' worth of amalgamated data is impractical. Instead LY error is considered with respect to individual events as these are measured at distinct time. As described in section 3.3.2 the LY is used when calculating the energy of an event and an error on the LY can skew this energy to be higher or lower. Event rate energy spectra are obtained for each period (j) and these are calculated using the central LY, the central LY + σ_{LY} and the central LY – σ_{LY}, the event rates recorded in each energy bin (i) are denoted R^{ij} $\mathrm{R}^{ij}_{\mathrm{LY+}}$ and $\mathrm{R}^{ij}_{\mathrm{LY-}}$ respectively. The systematic error on the event rate is:

$$\sigma^{\mathrm{LY}}_{\mathrm{R}^{ij}} = \frac{|\mathrm{R}^{ij}_{\mathrm{HLY}} - \mathrm{R}^{ij}_{\mathrm{LLY}}|}{2}. \tag{6.4}$$

The previous analysis [49, 50] used $\sigma^{\mathrm{LY}}_{\mathrm{R}^{ij}} = \frac{\mathrm{R}^{ij}_{\mathrm{LY+}} + \mathrm{R}^{ij}_{\mathrm{LY-}} - 2\mathrm{R}^{ij}}{2}$, however this reduces the size of the error by comparing the true rate to the mean of the high and low rates.

$\sigma_{\mathrm{LY}^{\mathrm{Inner}}_{\mathrm{-30cm}}}$ is purely statistical and is < than the observed level of fluctuation between consecutive measurements, whereas $\sigma_{\mathrm{LY}^{\mathrm{Hose}}_{\mathrm{Eff\ -30cm}}}$ is ≥ to the observed level of LY fluctuation. The previous analysis [49, 50] incorporated a 0.3% LY error between April 2015 and September 2015 (periods 9-20) only because of an FADC gain uncertainty that impacted the LY during this period [49, 50]. The FADC LY error is retained for these periods, however $\sigma_{\mathrm{LY}^{\mathrm{Inner}}_{\mathrm{-30cm}}}$ and $\sigma_{\mathrm{LY}^{\mathrm{Hose}}_{\mathrm{Eff\ -30cm}}}$ are additionally applied whenever their respective LY datasets are used. The FADC error does not feature in the stable LY dataset. The systematic errors (≤ 1% at low energy) are displayed in appendix A.2, figures A.1 and A.2 for the complete dataset likelihood cut analysis and stable LY dataset PDF cut analysis respectively.

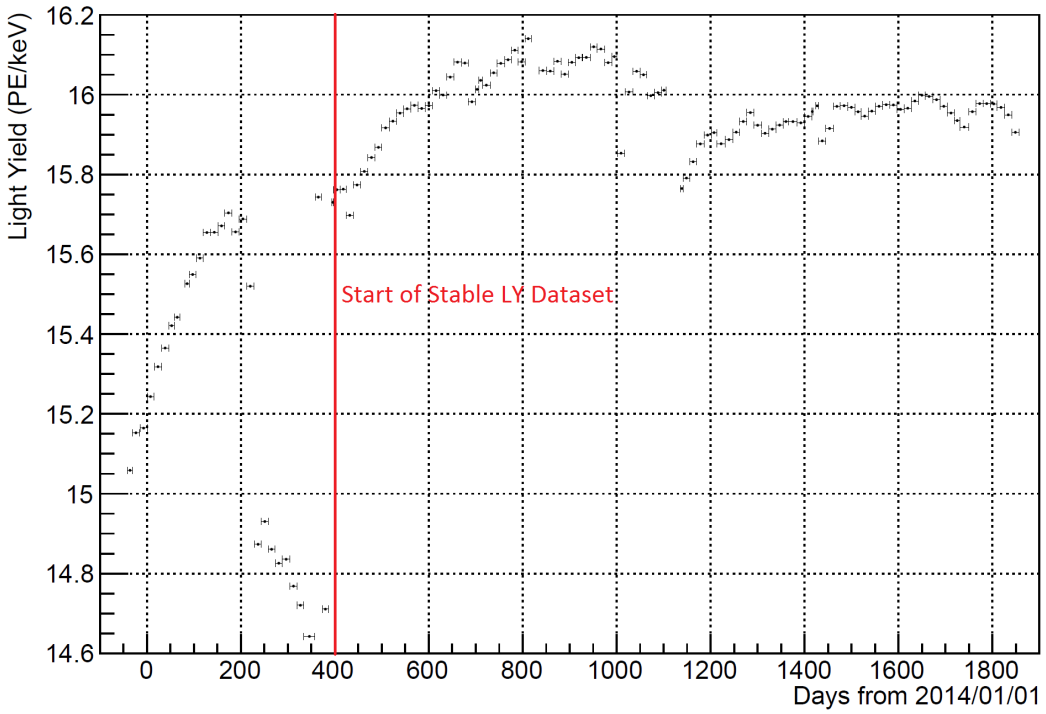


Figure 6.17: LY for all of the normal threshold periods.

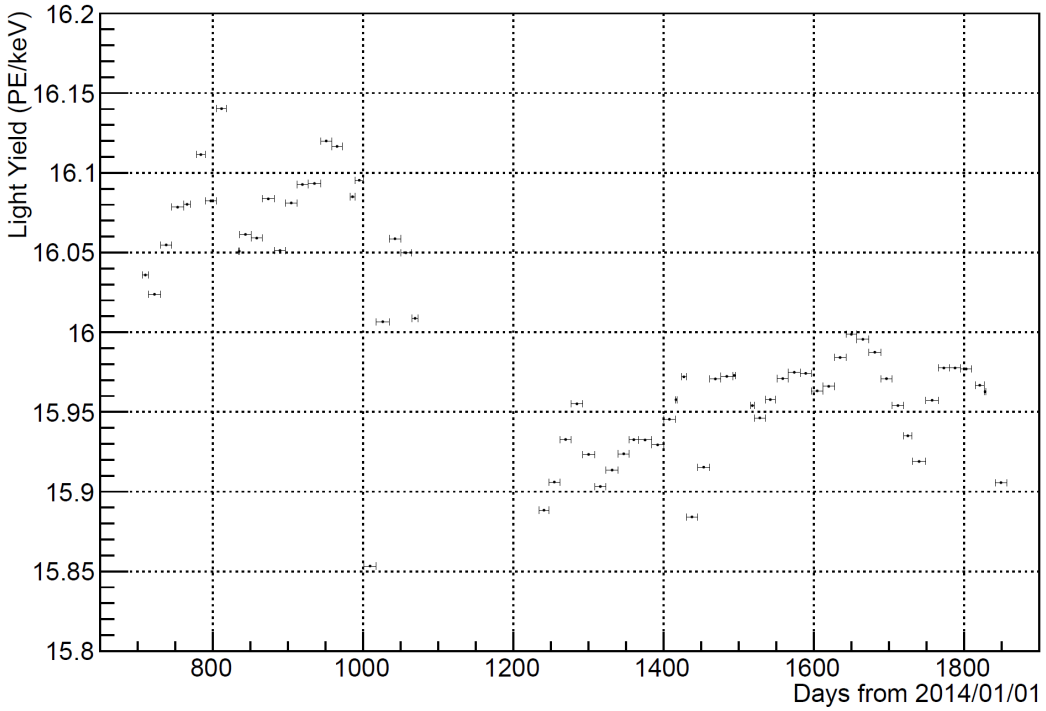


Figure 6.18: LY for all of the low threshold periods. These differ slightly from Normal threshold LY due to differing run selection and period central times.

6.3 Light yield dependence of observed event rate

The event rates after cuts for every half-month period within the complete dataset are displayed in figures 6.19 and 6.20 for the likelihood and PDF analyses, respectively. They demonstrate how the event rates vary across energy, time and LY in the 8 lowest energy bins (0.5-4.5 keV$_{ee}$). The previous analysis [49,50] only used the low threshold periods for the lowest energy bin (0.5-1.0 keV$_{ee}$), the same is implemented here.

The previous analysis [49, 50] utilised MC generated BG LY relative efficiency curves within 4 energy ranges: 0.5-1.0 keV$_{ee}$, 1.0-2.0 keV$_{ee}$, 2.0-6.0 keV$_{ee}$ and 6.0-20.0 keV$_{ee}$. These use the BG MC introduced in section 3.4.2 and utilised in chapter 5; all 30 BG types are generated for each run, simulated for the optical parameters measured in the detector at the time of the respective period. The runs are combined according to LY. Event rates are averaged within distinct LY ranges and then compared with LY = 15.46 PE/keV event rates (equates to l_A = 800 cm using equation 3.4) to estimate the dependence of detection efficiency on LY. The likelihood cut MC generated BG LY relative efficiency curves are demonstrated in the left hand plots in figure 6.21, the error bars represent systematic uncertainties and originate from varying the detector MC simulation's positioning and geometry of the OFHC Cu plates - used to suppress the BG emanating from the Al-seal as discussed in section 3.4.2. By using each period's central LY value, the right hand plots demonstrate the LY relative efficiencies cast over time for the 4 energy ranges. The application of the LY relative efficiencies to the data is discussed in chapter 8; they are shown to adequately remove the LY effects from the data's likelihood cut event rates. Equivalent PDF cut MC generated BG LY relative efficiency curves are displayed in figure 6.22. The LY relative efficiencies are similar between cuts for the lowest energy range, however for the 1.0-2.0 keV$_{ee}$ and 2.0-6.0 keV$_{ee}$ energy ranges the PDF cut MC generated BG relative efficiencies are particularly flat. Furthermore, this effect is not seen in the raw data event rates displayed in figure 6.20, these MC generated efficiencies do not sufficiently remove the LY effects observed in the data, therefore a new approach is necessary.

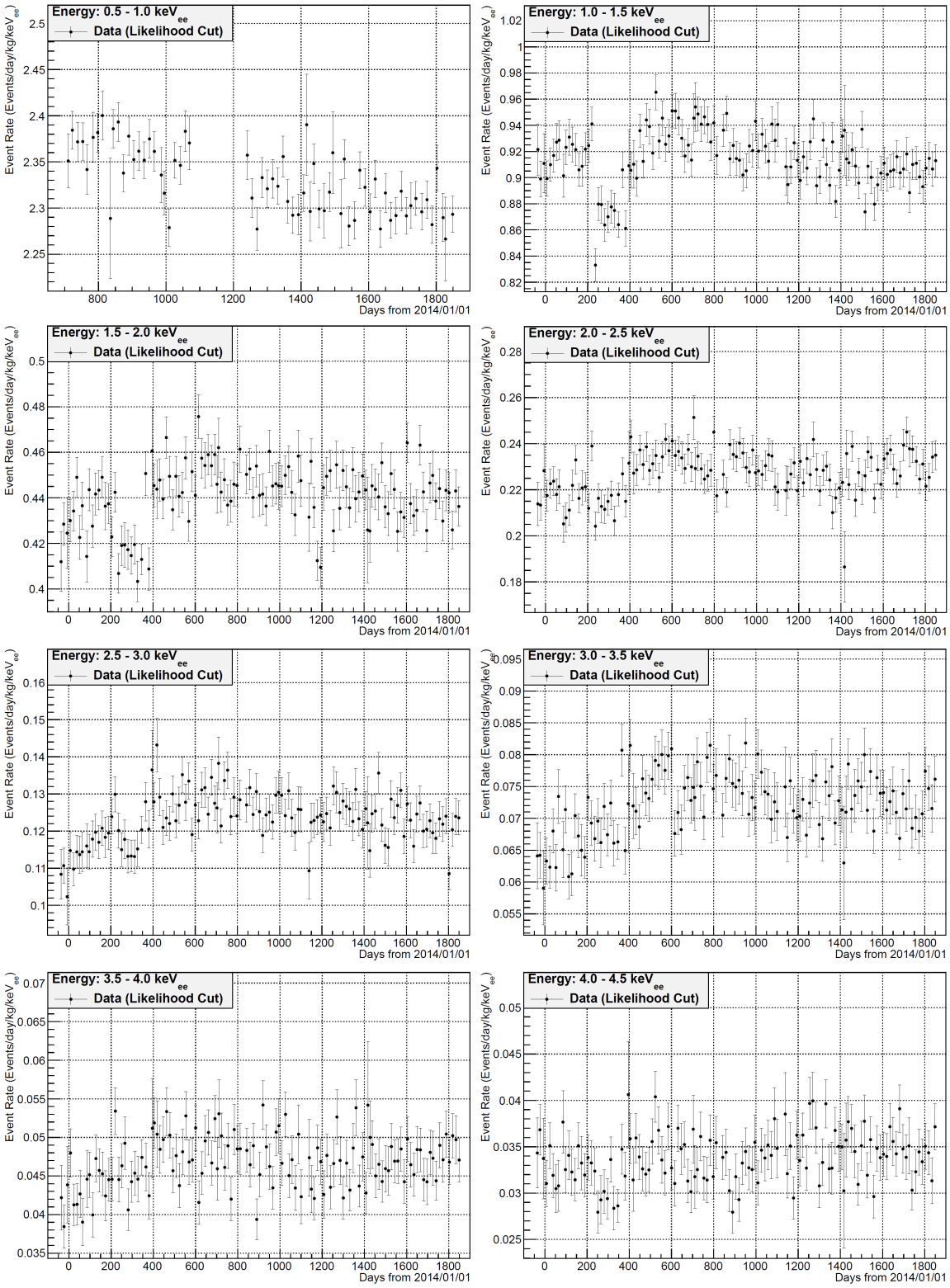


Figure 6.19: Likelihood cut event rates for the complete dataset, 8 lowest energy bins 0.5-4.5 keV$_{ee}$, only the lowest energy bin utilises low threshold periods. Variations in event rate over time due to linear BG and LY variations.

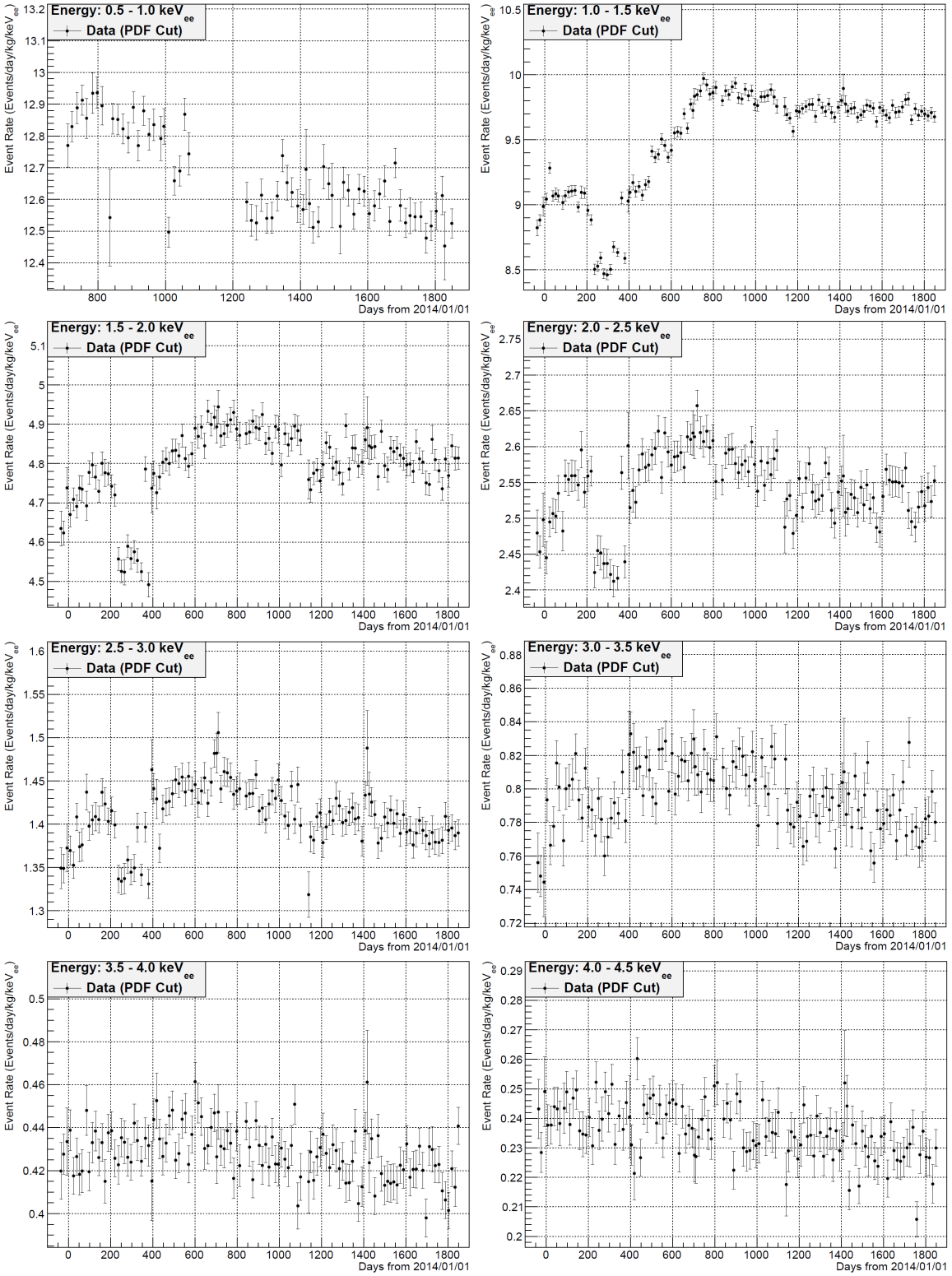


Figure 6.20: PDF cut event rates for the complete dataset, 8 lowest energy bins 0.5-4.5 keV$_{ee}$, only the lowest energy bin utilises low threshold periods. Variations in event rate over time due to linear BG and LY variations and the introduction of the low threshold trigger causing a step in the event rate at low energies.

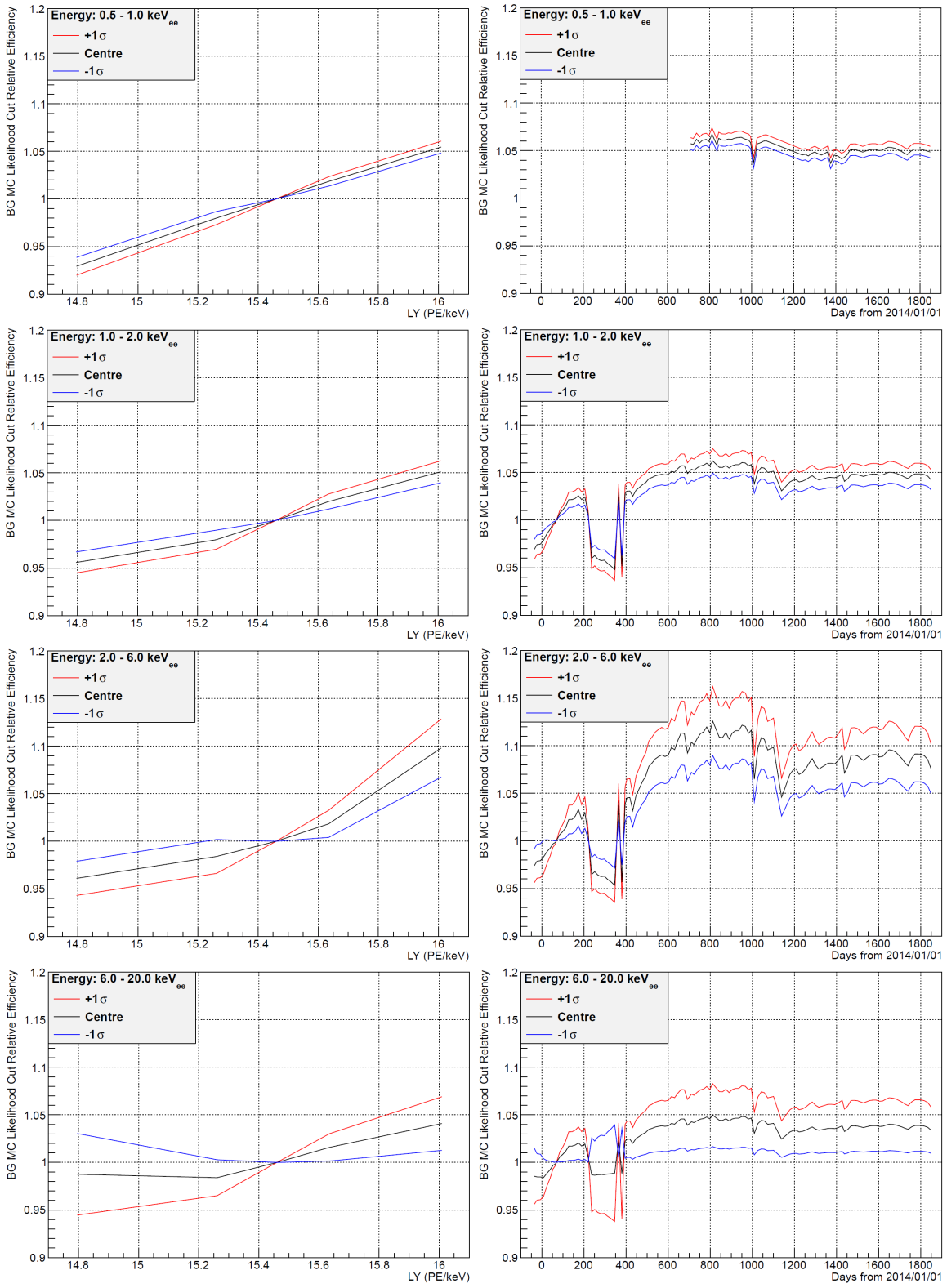


Figure 6.21: Likelihood cut MC generated BG LY relative efficiency curves as a function of LY (left) and for each distinct period over time (right). For 4 distinct energy ranges: 0.5-1.0 keV$_{ee}$, 1.0-2.0 keV$_{ee}$, 2.0-6.0 keV$_{ee}$ and 6.0-20.0 keV$_{ee}$. Likelihood cut MC generated BG LY relative efficiency curves predominantly increase with LY.

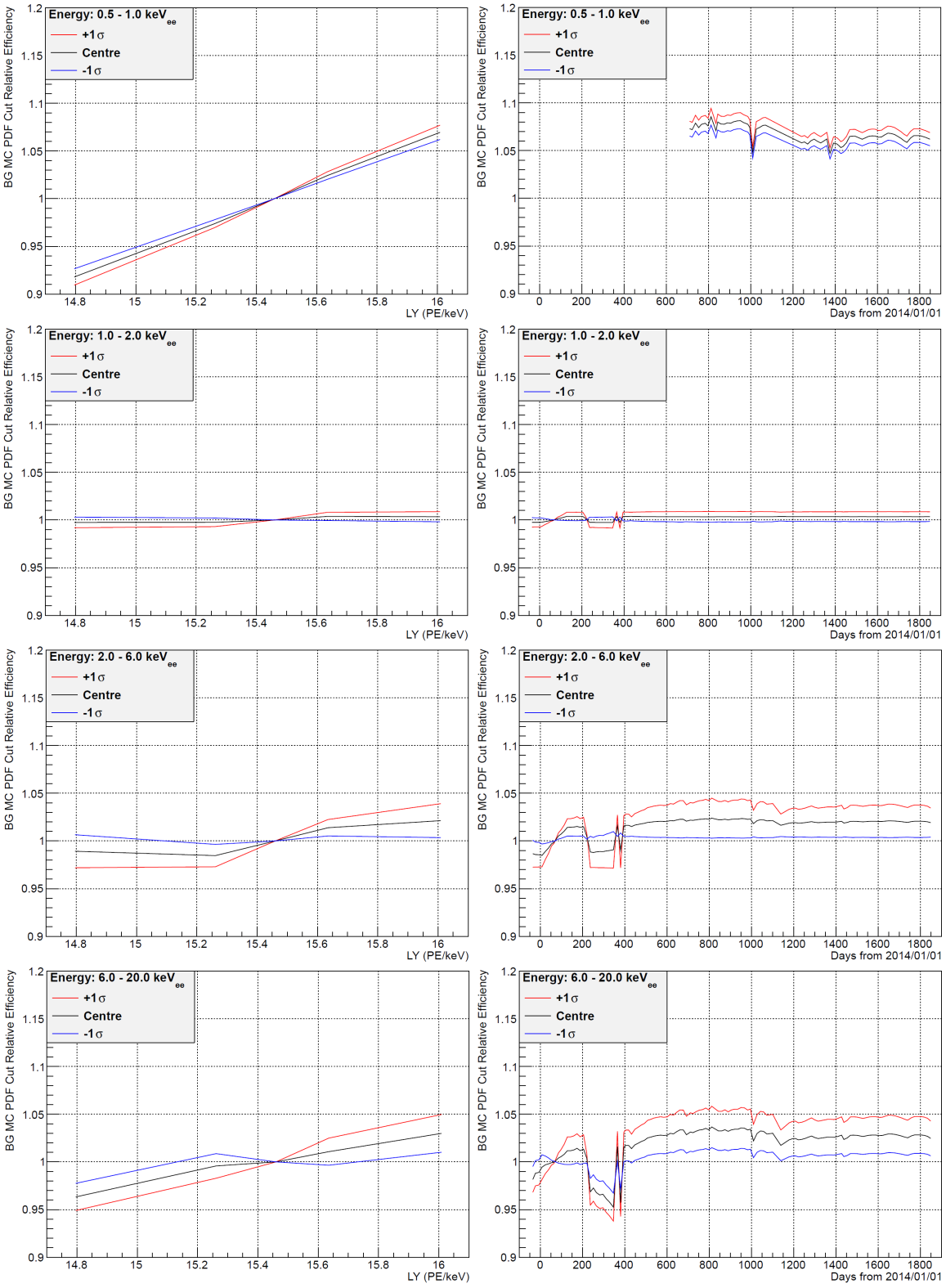


Figure 6.22: PDF cut MC generated BG LY relative efficiency curves as a function of LY (left) and for each distinct period over time (right). For 4 distinct energy ranges: 0.5-1.0 keV$_{ee}$, 1.0-2.0 keV$_{ee}$, 2.0-6.0 keV$_{ee}$ and 6.0-20.0 keV$_{ee}$. The PDF cut MC generated BG LY relative efficiency curves vary by a smaller amount than the Likelihood cut MC generated BG LY relative efficiency curves and don't fully account for the event rate variation.

Instead of relying on MC generated BG relative efficiency curves that contain large systematic uncertainties, the PDF cut event rates are fit directly. This is applied during χ^2 minimisation by incorporating a LY efficiency function whose parameters are free to vary. Coupled with a constant event rate and a linear reduction in event rate over time, the BG is fully described and the shape of the data's event rates is captured for each energy bin as we will see in chapter 8.

Figure 6.23 displays the data's PDF cut event rates (normalised) plotted against LY for the 8 lowest energy bins 0.5-4.5 keV_{ee}. A quadratic fit is applied for all energy bins besides the 1.0-1.5 keV_{ee} region, this uses a polynomial degree 5 fit because of an additional issue which will be acknowledged shortly. There are three main takeaways from this fitting procedure which directed us towards limiting the dataset. Firstly, the majority of the data's event rates occurring before July 2014 (LY: ~15 - 15.7) fall below the fitted LY curves for energies above 2.0 keV_{ee}. This behaviour is similar to that noted previously between the $\text{LY}^{\text{Hose}}_{\text{Eff -30cm}}$ and the $\text{LY}^{\text{Inner}}_{\text{-30cm}}$ - and results in skewed fitting. Secondly, to simplify the fitting so that it is purely linear - reducing the number of additional free parameters to only 1 per energy bin - the LY range had to be reduced. The orientation of the event rates at high LY (once the detector had stabilised) doesn't fit linearly with the data recorded at low LY. Thirdly, after applying these LY fitted corrections a step in the event rate occurring at the start of low threshold data taking is clearly evident in the 1.0-1.5 keV_{ee} energy bin and is also there but to a lesser extent in the 1.5-2.0 keV_{ee} energy bin. These corrected event rates are displayed in figure 6.24; a step at 700 days is prominent which has clearly impacted the fitting procedure - as previously mentioned with respect to requiring a polynomial degree 5 fit for the 1.0-1.5 keV_{ee} energy bin.

Considering these problems that we encounter when trying to include the early data taken when the detector was clearly not yet stable, the natural solution is to restrict the analysis to a time period of demonstrably stable data taking. Following the discussion in section 6.1 we thus limited the runs utilised to those occurring after day 397 - resulting in 29 fewer half-month periods. Additionally the lowest 3 energy

bins are considered low threshold and utilise only the low threshold periods. Figure 6.25 shows the stable LY dataset PDF cut event rates recorded in each period for the 8 lowest energy bins.

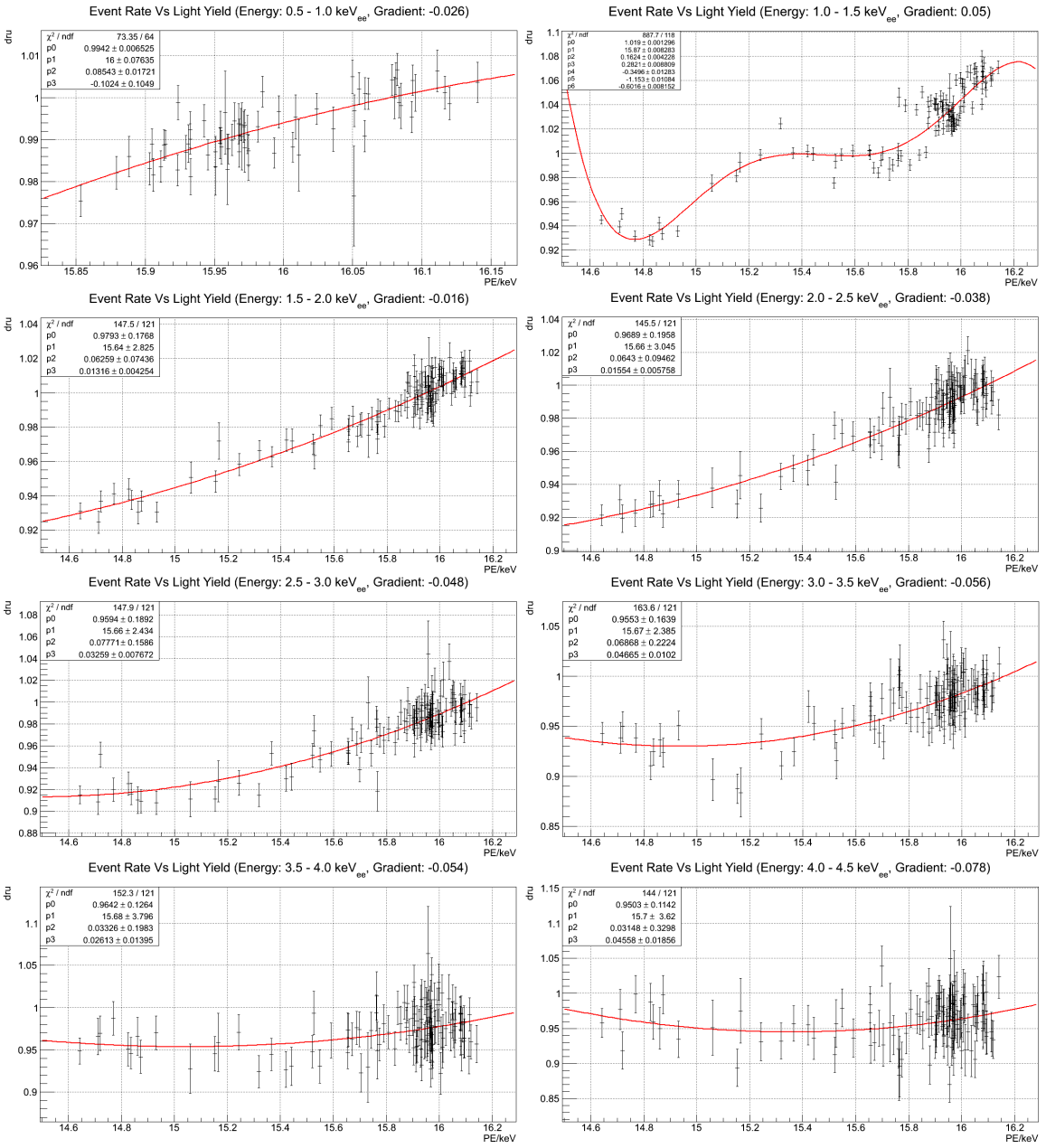


Figure 6.23: PDF cut event rates (normalised to 1) plotted against LY for the complete dataset in the 8 lowest energy bins 0.5-4.5 keV$_{ee}$, the lowest energy bin utilises the low threshold periods. The linear time gradients are listed in the plot titles are the event rates have been scaled to account for this. All energy bins are fit with a quadratic function except for the 1.0-1.5 keV$_{ee}$ energy bin which uses a polynomial degree 5 fit - a step in the event rate at the start of low threshold heavily affects this energy bin.

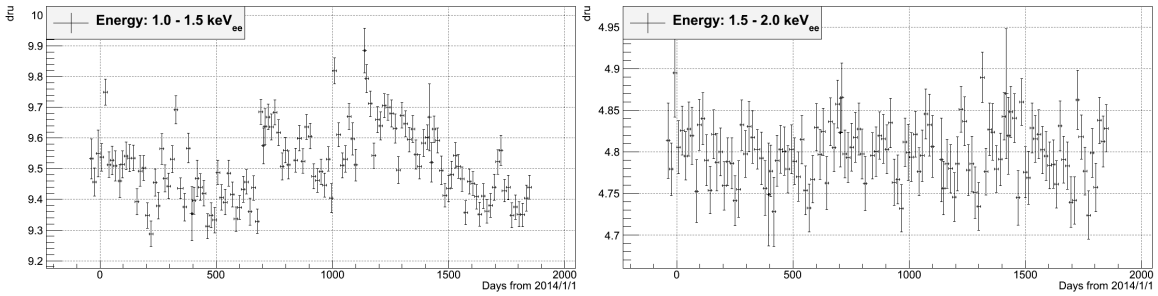


Figure 6.24: PDF cut event rates (Time and LY corrected) for the complete dataset, energy bins 1.0-1.5 keV$_{ee}$ and 1.5-2.0 keV$_{ee}$. A clear event rate step at 700 days is evident.

The average event rate at each stage in the event selection process is shown in figure 6.26, the ID trigger (only), XMASS StdCuts (includes Cherenkov cut), likelihood cut (includes Cherenkov cut) and PDF cut (excludes Cherenkov cut) are represented by black, yellow, red and blue lines respectively. Solid lines signify the complete dataset and dashed lines the stable LY dataset. These are similar as expected, firstly the stable LY dataset makes up $> \frac{3}{4}$ of the complete dataset and secondly the LY in the first 400 days of data taking is only $\sim 5\%$ less on average than the LY measured thereafter (stable LY dataset). The most notable variation is in the 1.0-1.5 keV$_{ee}$ and 1.5-2.0 keV$_{ee}$ energy bins as these are considered low threshold energies for the stable LY dataset. The solid red and dashed blue lines represent the energy spectra for the 2 analyses presented in this thesis, the complete dataset likelihood cut analysis and the stable LY PDF cut analysis respectively.

With this we have all the ingredients to analyse the data for modulation: we defined suitable time periods to bin the data by, know their respective livetimes, detector conditions and expected BG and observed data event rates. The next chapter details the generation of the WIMP and electron signal spectra, with the subsequent chapter outlining the expected event rate formulae, χ^2 minimisation process, dummy sample generation, and both the MI amplitude search and WIMP limit calculations.

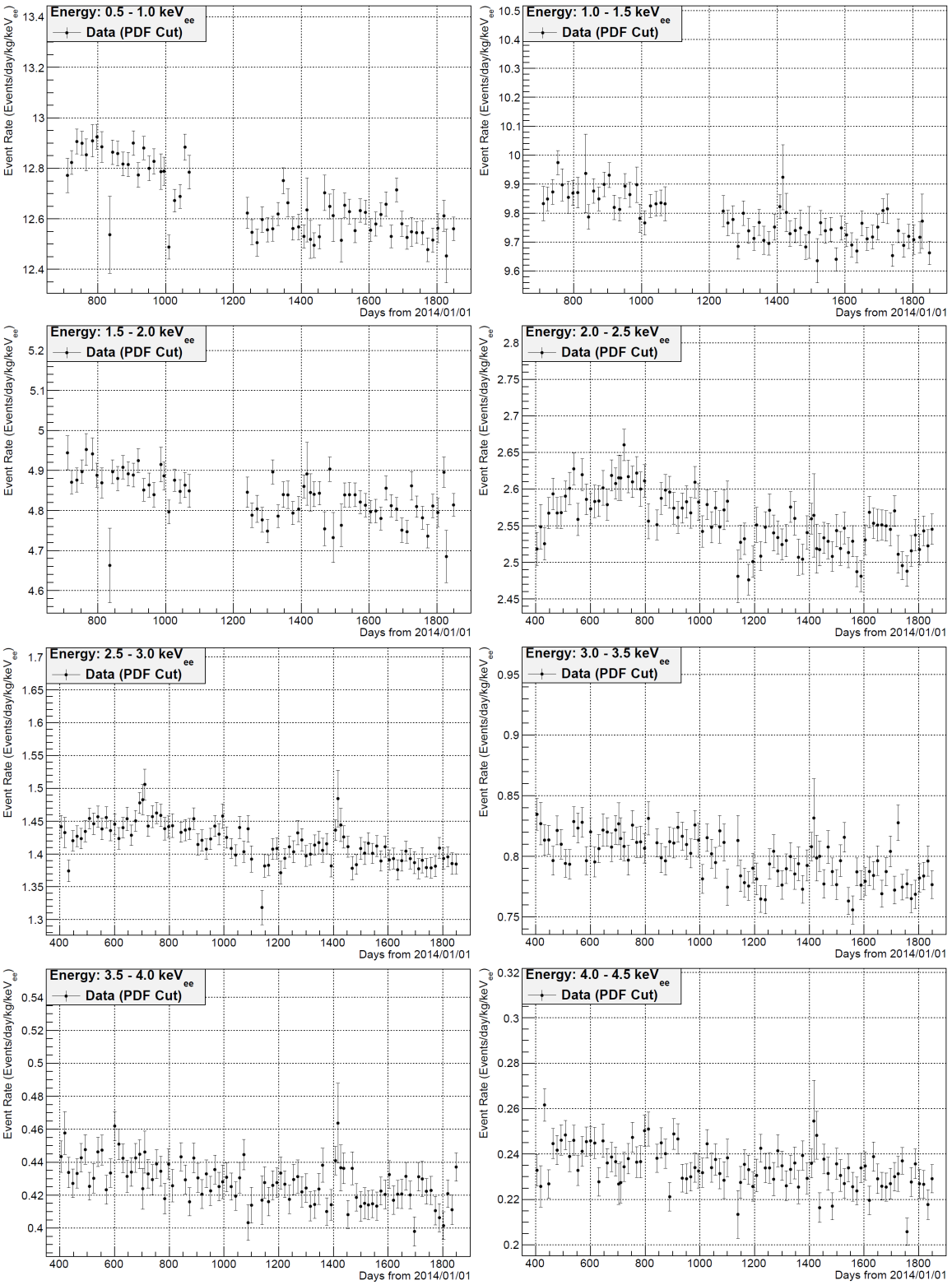


Figure 6.25: PDF cut event rates for the stable LY dataset, 8 lowest energy bins 0.5-4.5 keV$_{ee}$, the 3 lowest energy bins utilise the low threshold periods. Variations in event rate over time due to linear BG and LY variations.

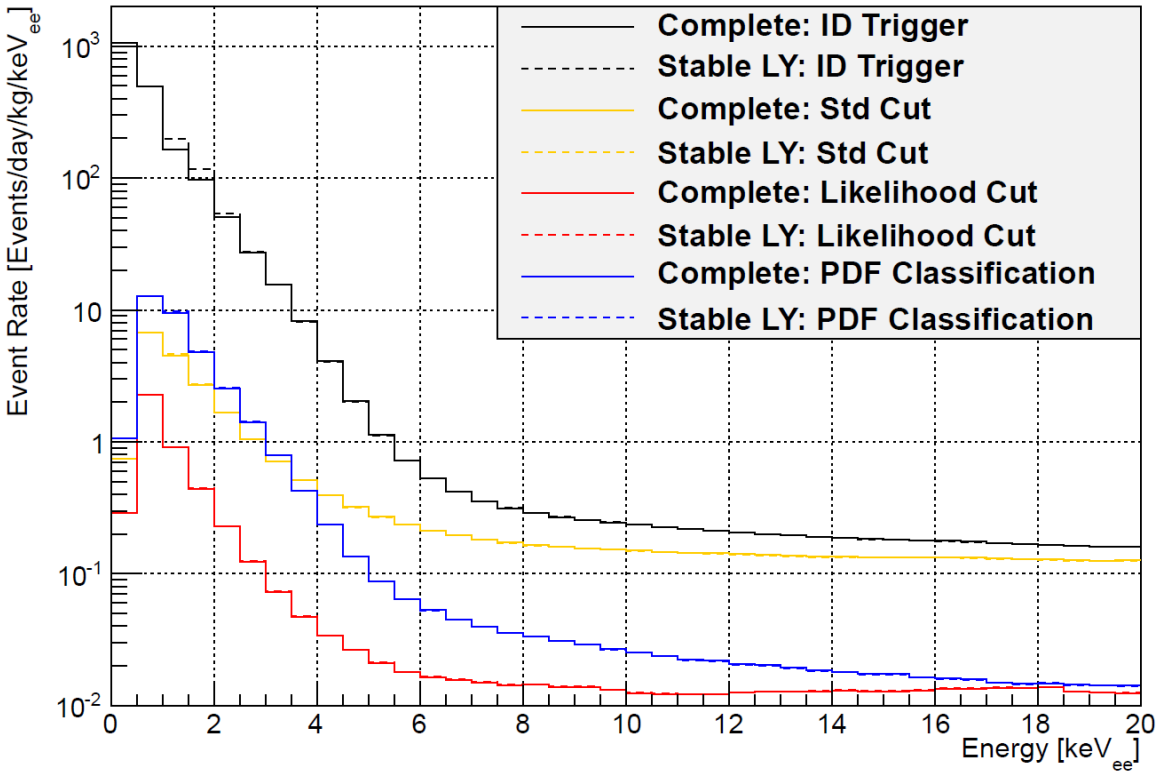


Figure 6.26: Event rate energy spectra of all the different cuts. The ID trigger (only), XMASS StdCuts (includes Cherenkov cut), likelihood cut (includes Cherenkov cut) and PDF cut (excludes Cherenkov cut) are represented by black, yellow, red and blue lines respectively. Solid lines signify the complete dataset and dashed lines the stable LY dataset, these are similar as there is only a ~ 25% dataset change.

Chapter 7

Signal Spectra

There are two analyses presented in this thesis, the complete dataset likelihood cut analysis and the stable LY dataset PDF cut analysis - both outlined in chapter 6. For each of these analyses two annual modulation searches are undertaken: A WIMP SI search and a model independent (MI) search. The former utilises nuclear recoil (NR) event rate energy spectra, simulated for both the constant term ($C_0(E_R)$) and the modulation amplitude term ($A_{\text{annual}}(E_R)$) in equation 2.20 - distinct for each WIMP mass. The latter disregards the constant term and simply searches for a modulation amplitude within each energy bin, this is designed to be agnostic of the specific type of recoil in the LXe that produced the event in question. Electron recoil (ER) events are used to ascertain the systematic effect of the LY dependence on the MI amplitudes and signal efficiency, this allows for a direct comparison with the DAMA/Libra observation of an annual modulation of their event rate [43–45], they cannot avoid this latter limit by pointing to the underlying signal hypothesis.

This chapter discusses the NR and ER simulations and the spectra that result from applying the PDF cut event selection - detailed in chapter 5 - to these simulated signal events. Section 7.1 details the NR spectra and the systematic uncertainties that arise from the LY, the NR long decay constant (DC) and the nuclear recoil scintillation efficiency L_{Eff}. Section 7.2 discusses the ER signal efficiency and the LY systematics. Section 7.3 briefly discusses the spectra that result from applying the Likelihood cut event selection, simulated for the previous analysis [49, 50].

7.1 WIMP SI energy spectra

As previously outlined in section 2.3 the deposited energy spectrum resulting from a WIMP SI interaction with a Xe nucleus depends on both the WIMP's mass and the relative velocity between the non-relativistic WIMPs and the detector. These spectra were calculated for a range of WIMP masses when the first XMASS modulation analysis was conducted [73, 74]. The annual average deposited nuclear recoil energy spectra expected within XMASS for a range of WIMP masses with a DM-nucleon interaction cross section $\sigma_{\mathrm{SI}} = 10^{-36}$ cm^2 (1 picobarn) is shown in figure 7.1. Figure 7.2 shows the corresponding annual residual spectra: the difference between spectra generated at the maximum and the minimum relative velocity of the detector hurtling through a stationary sea of WIMP dark matter present in the galactic halo.

Xe nuclear recoil MC simulation is required to generate the recoil energy spectra for each WIMP mass. As discussed before multiple absorption lengths (l_A), DC values and $\mathrm{L_{Eff}}$ functions are used to correct for variations in the detector response over time and incorporate their systematic uncertainties. The spectra produced in the previous analysis [49, 50] are re-used here to extend the previous likelihood cut analysis over the complete XMASS data set. This section focuses solely on the newly generated spectra for the stable LY PDF cut analysis.

7.1.1 Xe NR MC energy spectra

As in the previous likelihood cut modulation analysis [49,50], Xe nuclear recoil events where simulated in 0.1 keV$_{nr}$ width energy bins from 1.0 - 200.0 keV$_{nr}$. For consistency with the previous analysis, the same number of events were simulated, this decreases with energy to reduce computation time according to the following formula: $\mathrm{floor}\left(\frac{100000}{1+\mathrm{floor}\left(\frac{\mathrm{Energy/keV_{nr}}}{10}\right)}\right)$.

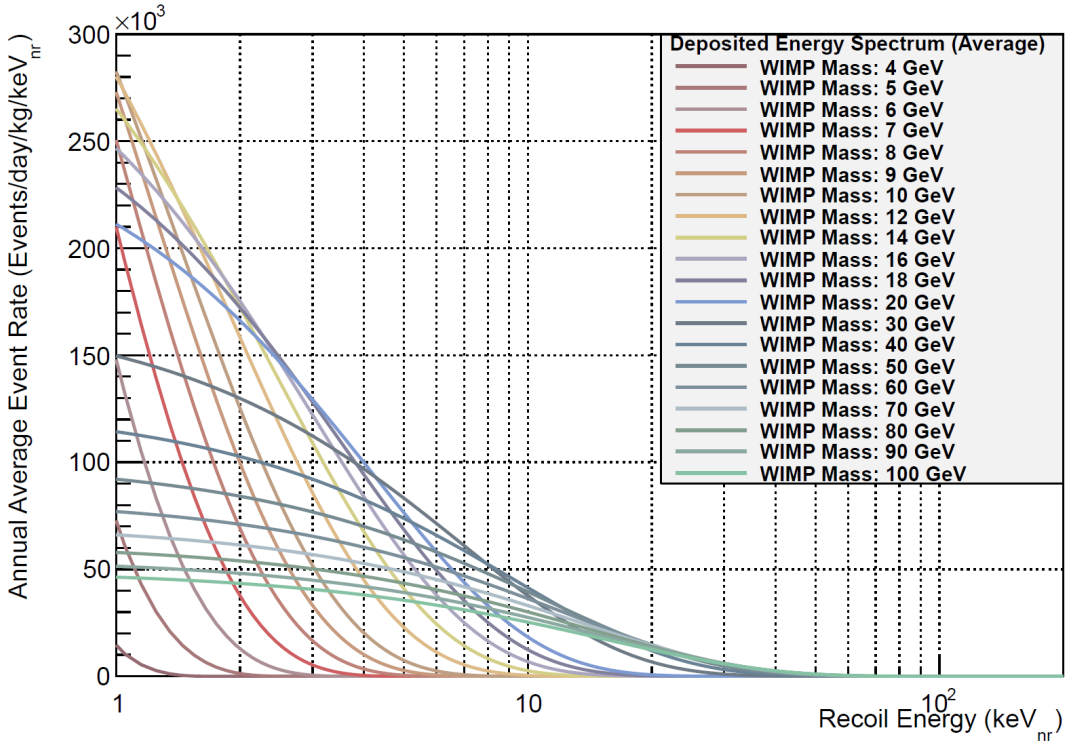


Figure 7.1: Annual average Xe nuclear recoil energy spectra deposited by WIMPs for a range of masses.

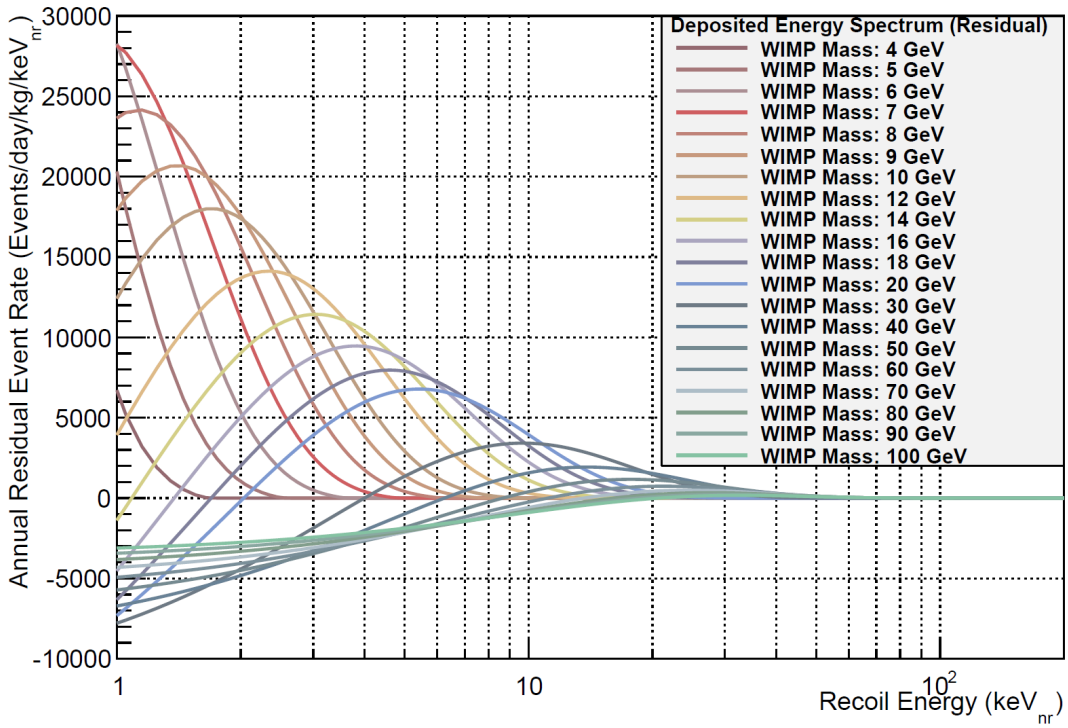


Figure 7.2: Annual residual (Maximum relative velocity - Minimum relative velocity) Xe nuclear recoil energy spectra deposited by WIMPs for a range of masses. Positive for low mass WIMPs but negative at low energy for high mass WIMPs.

Events were simulated using four distinct l_A values: 1000 cm, 1500 cm, 2000 cm and 3000 cm. The base LY chosen for the stable LY PDF cut analysis is l_A = 2000 cm. Figure 7.3 shows the spectra (keV$_{ee}$) of visible energy in the detector for recoiling Xe nuclei, simulated using l_A = 2000 cm in 5 distinct nuclear recoil energy bins, 1.0-1.1 keV$_{nr}$, 5.0-5.1 keV$_{nr}$, 10.0-10.1 keV$_{nr}$, 20.0-20.1 keV$_{nr}$ and 50.0-50.1 keV$_{nr}$ coloured black, blue, red, orange and green respectively. The PDF cut has been applied to said spectra and they are normalised by the number of simulated events.

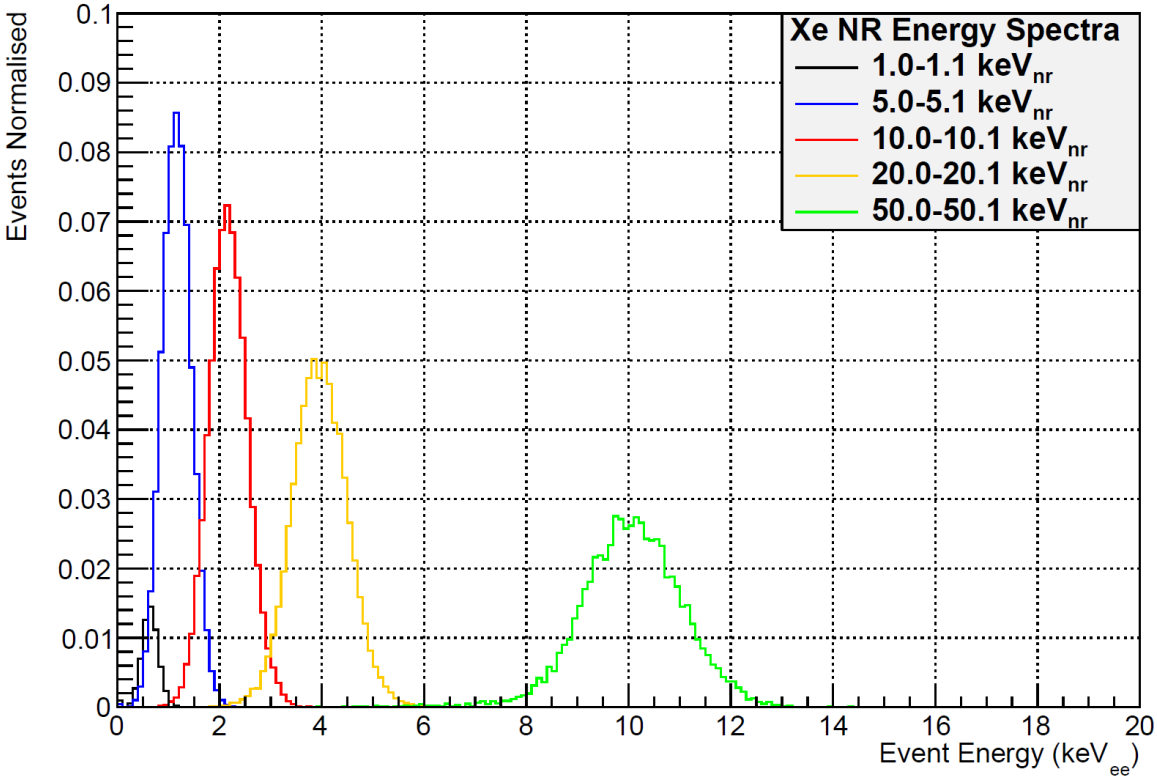


Figure 7.3: Visible event energy spectra of Xe NR events that survive the PDF cut simulated at 5 distinct Xe NR energies. Broader distributions at higher energies and only a limited number of events pass the cuts at the lowest energies.

All 1990 (1.0 - 200.0 keV$_{nr}$, 0.1 keV$_{nr}$ bins) distinct Xe NR event energy spectra (keV$_{ee}$) simulated at l_A = 2000 cm are superimposed and scaled according to the Xe NR deposited energy spectra in figures 7.1 and 7.2. The resultant annual average and residual event rate energy spectra are shown in figures 7.4 and 7.5 respectively for each WIMP mass using the same WIMP colour denotation used in those previous figures.

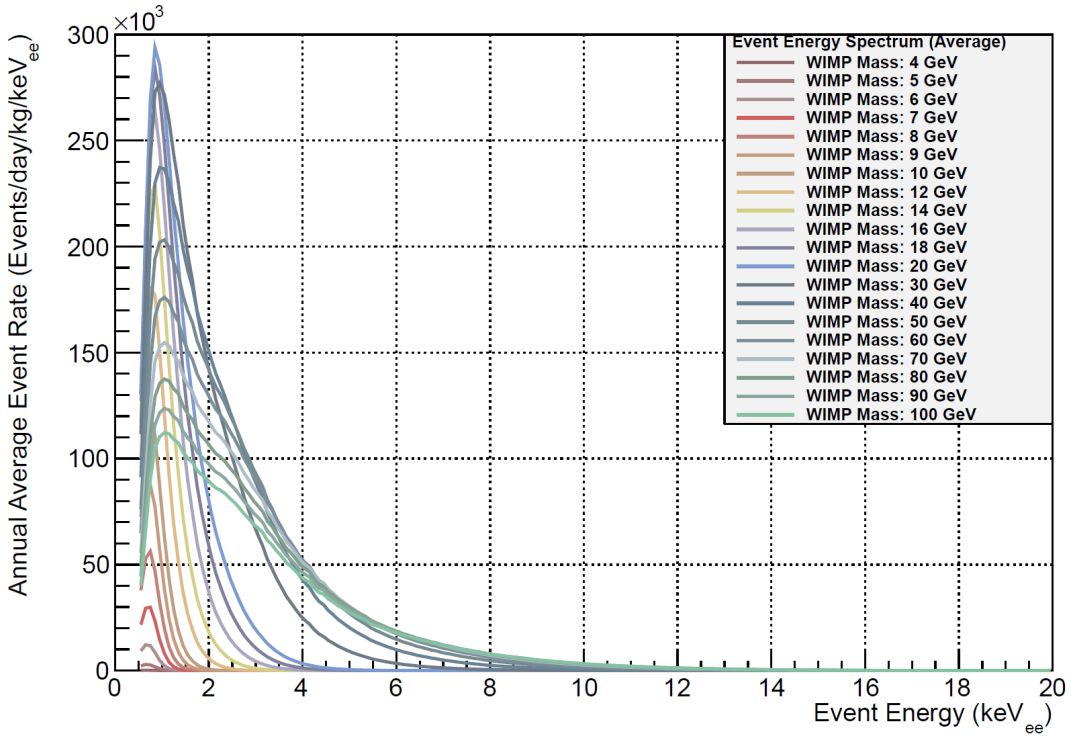


Figure 7.4: Annual average WIMP Xe spin independent interaction event rate energy (visible event energy) spectra for a range of WIMP masses. Reduces quickly with energy.

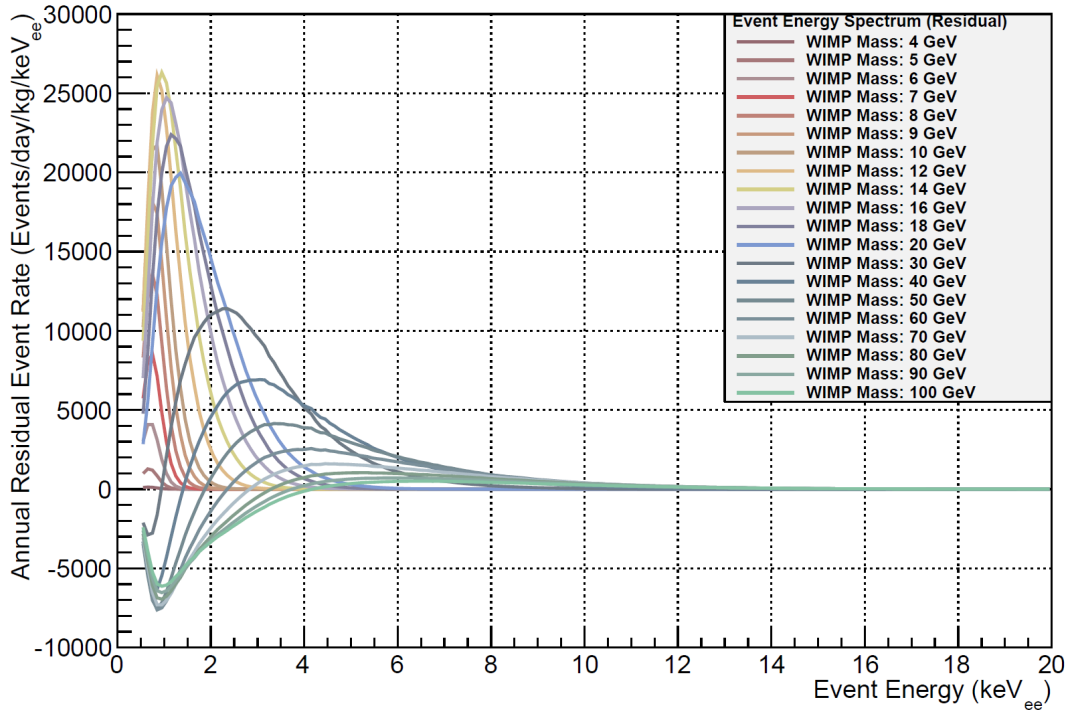


Figure 7.5: Annual residual (Maximum relative velocity - Minimum relative velocity) WIMP Xe spin independent interaction event rate energy (visible event energy) spectra for a range of WIMP masses. Reduces quickly with energy and sign flips according to figure 7.2.

The same procedure is carried out using the remaining three l_A values. Collectively these will be used to obtain the signal spectra's LY relative efficiencies.

As stated in section 3.1.3 DC= 27.5 ns with a conservative error of ±2 ns and L_{Eff} with its $\pm1\sigma$ and $\pm2\sigma$ bands from 1 - 200 keV_{nr} are displayed in figures 3.4 and 3.5. DC= 27.5 ns and the central L_{Eff} function were used to generate the WIMP spectra at all four l_A values. Additional spectra were obtained fixing l_A = 2000 cm but independently varying DC by $\pm1\sigma$ and applying the -1σ and -2σ L_{Eff} functions. The spectra's relative variation from the central values are fitted in section 7.1.2.

The true classification power $\frac{signal}{\sqrt{BG}}$ for both the PDF cut and likelihood cut is unknowable. MC simulations have been used to calculate them in chapter 5, however there are some major discrepancies with the BG simulation especially at low energy (< 7 keV_{ee}), these are discussed in section 3.4.2. Therefore one would expect the true likelihood cut and PDF cut classification powers to differ from those predicted in figures 5.31 and 5.32 respectively. As the classification power is not a parameter that is applied to the analyses and is simply a gauge of the classifiers performance, a more robust comparison between the two cuts can be achieved by using the recorded data as a proxy for the BG - this assumption may not be perfect but it is better than using the MC simulated BG with its large uncertainties and remaining discrepancies. The stable LY dataset energy spectra for both the likelihood cut (dashed red line) and the PDF cut (dashed blue line) in figure 6.26 can be utilised to perform a fair comparison. The signal used is the WIMP NR spectrum after the respective cuts were applied. As outlined the WIMP energy spectra displayed in figure 7.4 were generated by applying the PDF cut to the simulated nuclear recoils in LXe, equivalent WIMP energy spectra were generated by applying the likelihood cut to the same MC. The classification power is calculated and the ratio (PDF/likelihood) is demonstrated in figure 7.6 for each WIMP mass using the same colour denotation as before. The ratio goes to 1 when the WIMP spectra's remaining statistics in the distribution's tail becomes < 0.1% of the total statistics for either the likelihood cut or PDF cut.

The PDF cut developed in this thesis is superior for the low-mass WIMPs as

their spectra are non-zero only in the lowest energy bins and for the high-mass WIMPs whose spectra stretch out to larger energies. The likelihood cut is better for intermediate-mass WIMPs with masses of ~ 10 – 40 GeV. The general shape of the curve is similar to that observed in figure 5.34 (red line), however it is reduced somewhat and the decrease between 1.0-6.0 keV_{ee} is larger than in figure 5.34. The Likelihood cut simply compares electron events simulated on the ID's inner surface and those generated uniformly throughout the bulk of the ID. It doesn't rely on the BG MC simulation. However the PDF cut does. The true BG classification parameter distributions likely differ from those shown in figures 5.24 due to discrepancies between the true BG and the BG MC simulation. If the NR and BG PDF classification parameter peaks' central positions or widths vary, then the BG tails where the cut occurs could vary slightly. Therefore seeing discrepancies between figure 5.34 and 7.6 at low energy where the BG discrepancy is known to be at its worst is understandable.

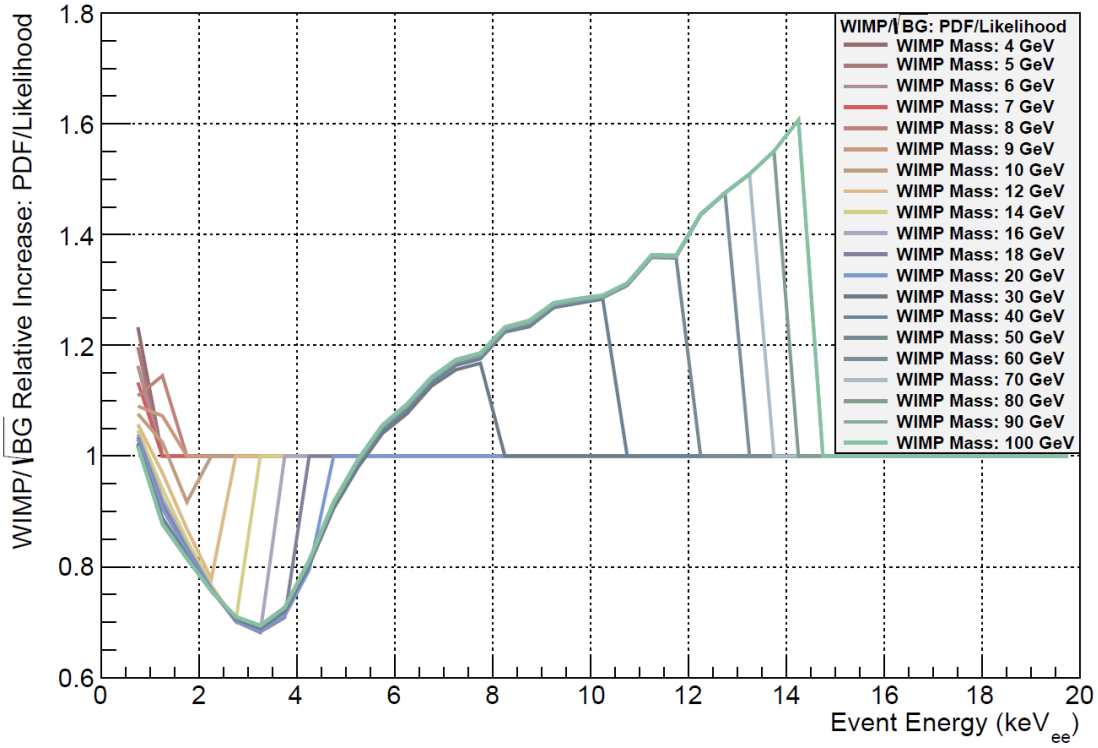


Figure 7.6: Ratio(PDF cut/likelihood cut) in the classification power Signal/$\sqrt{BG}$ where the BG is the recorded data and the signals are the respective MC generated WIMP spectra. This shows a similar trend to figure 5.34 however it is reduced and dips below 1 between 1.0 - 5.5 keV_{ee}.

7.1.2 Xe NR energy spectra relative efficiencies

The relative LY efficiency of the annual average event rate spectra is obtained by directly comparing the spectra simulated using l_A = 1000 cm, l_A = 1500 cm and l_A = 3000 cm with those of l_A = 2000 cm (equates to LY = 16.04 according to equation 3.4). l_A is converted to LY using formula 3.4 and the relative efficiency is obtained by directly comparing the event rates within 4 specific energy ranges: 0.5-1.0 keV$_{ee}$, 1.0-2.0 keV$_{ee}$, 2.0-6.0 keV$_{ee}$ and 6.0-20.0 keV$_{ee}$. The same procedure was implemented previously in the previous analysis [49,50] for both the signal spectra and the BG spectra (outlined in section 6.3). These energy ranges were chosen to save on MC simulation yet still have granularity at the lowest energies which are the most important. Figure 7.7 demonstrates the relative efficiencies in each energy range for each distinct WIMP mass, using the same colour denotation as before. The lower WIMP masses induce smaller recoil energies and as such their energy spectra are confined to smaller visible energies. Therefore some WIMP masses are absent from the higher energy range's relative efficiency curves.

The relative efficiency that results from independently varying the DC ($\pm 1\sigma$) and L_{Eff} (-1σ and -2σ) is similarly obtained by directly comparing these spectra's event rates with those simulated using the central values/functions, all at a fixed l_A = 2000 cm. The relative efficiencies of both the average and residual spectra for each WIMP mass were calculated for each 0.5 keV$_{ee}$ energy bin. Figures 7.8 and 7.9 demonstrate this for the 20 GeV WIMP annual average spectra's relative efficiencies plotted as we explore the DC and L_{Eff} at the stated sigma levels (σ_{DC} and $\sigma_{L_{Eff}}$) respectively in the 8 lowest energy bins form 0.5 keV$_{ee}$ to 4.5 keV$_{ee}$. The DC and L_{Eff} relative efficiencies are then fit linearly ($1 + DC^{G} \times \sigma_{DC}$) and exponentially ($e^{\frac{\sigma_{L_{Eff}}}{L^{G}_{Eff}}}$) respectively with parameters DC^{G} and L^{G}_{Eff} noted in the plots' legends alongside their errors obtained via fitting. DC^{G} and L^{G}_{Eff} are obtained for all WIMP masses' annual average and residual spectra's relative efficiencies.

The relative efficiencies demonstrated in figure 7.7 are applied directly to the

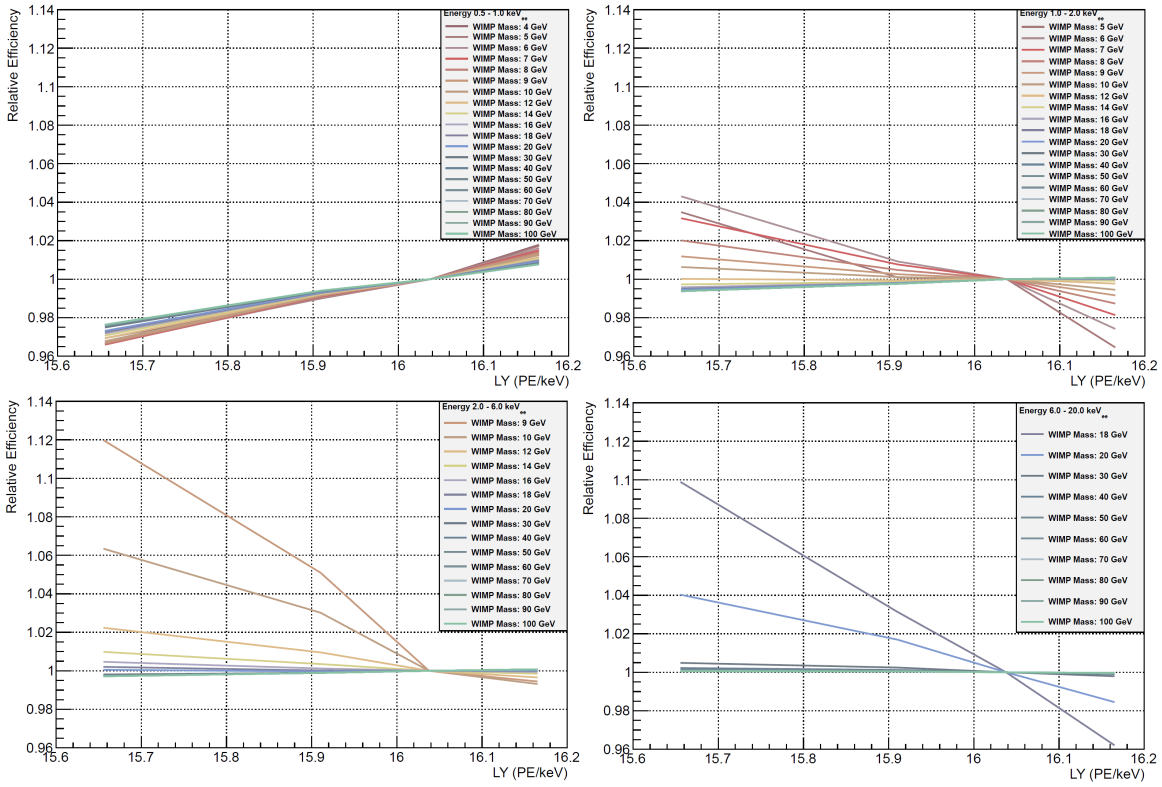


Figure 7.7: Relative Efficiency Vs LY for a range of WIMP masses in all 4 energy ranges: 0.5-1.0 keV$_{ee}$ (top left), 1.0-2.0 keV$_{ee}$ (top right), 2.0-6.0 keV$_{ee}$ (bottom left) and 6.0-20.0 keV$_{ee}$ (bottom right). Annual average WIMP Xe SI interaction event rate energy spectra. These efficiency curves are close to linear and for the higher energy ranges only the larger WIMP masses are present as the low mass WIMPs don't induce events within these energy regions.

WIMP signal spectra in figures 7.4 and 7.5, scaling the expected event rate for each period according to its respective LY.

In chapter 8 the recorded data event rates for each period are scaled according to LY and a linearly reducing BG function before being fit with an annually modulating signal component composed from both constant and amplitude terms which vary as a function of energy according to the annual average and residual WIMP energy spectra respectively - displayed in figures 7.4 and 7.5. χ^2 minimisation is conducted separately for each WIMP mass and over a range of σ_{SI} values which allows a 90% confidence limit to be calculated.

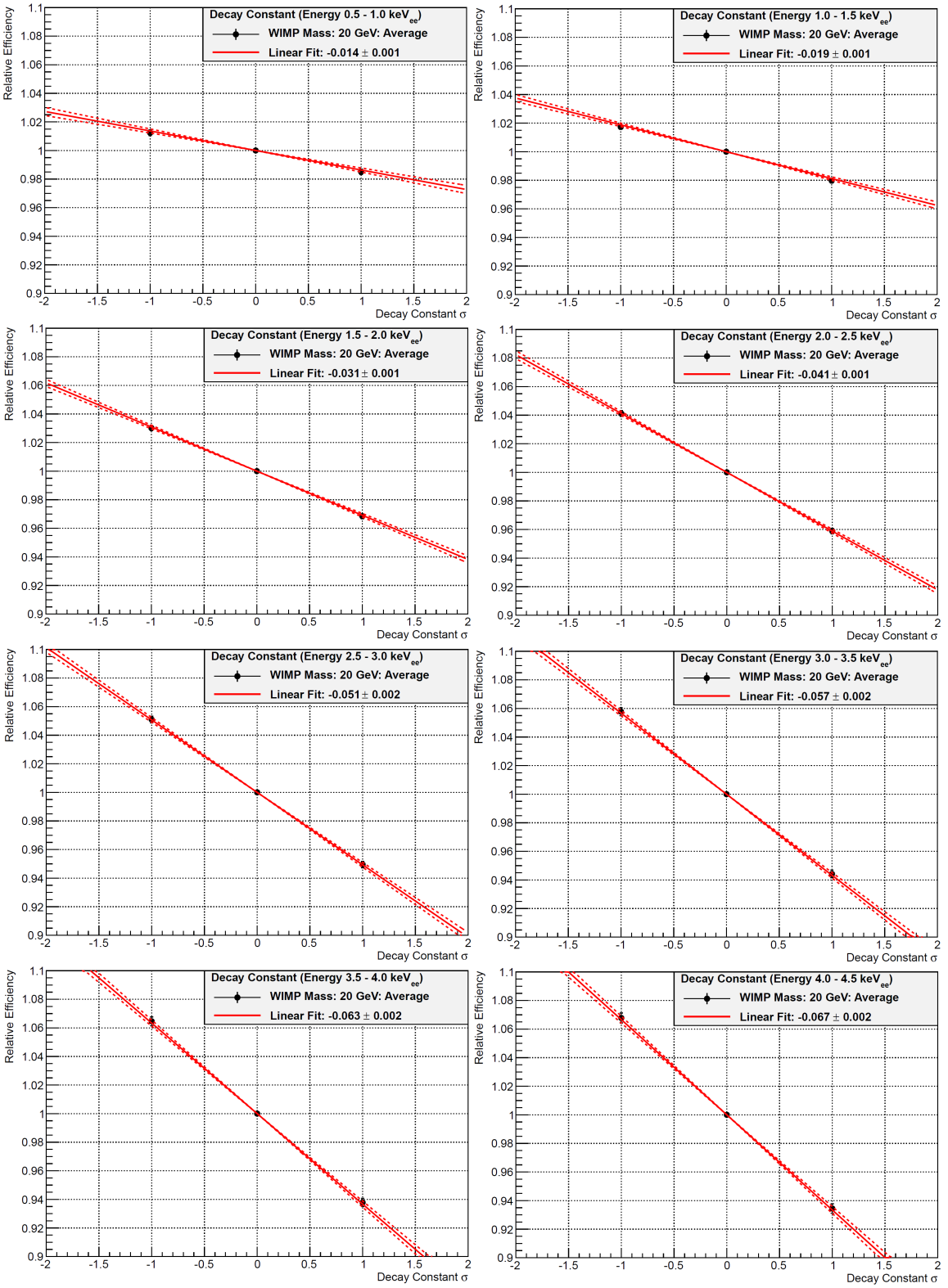


Figure 7.8: Annual average 20 GeV WIMP Xe spin independent interaction event rate energy spectra: Relative Efficiency Vs Decay Constant σ. Linear Fits for the 8 lowest energy bins 0.5-4.5 keV$_{ee}$ with the fit parameters listed in the legends.

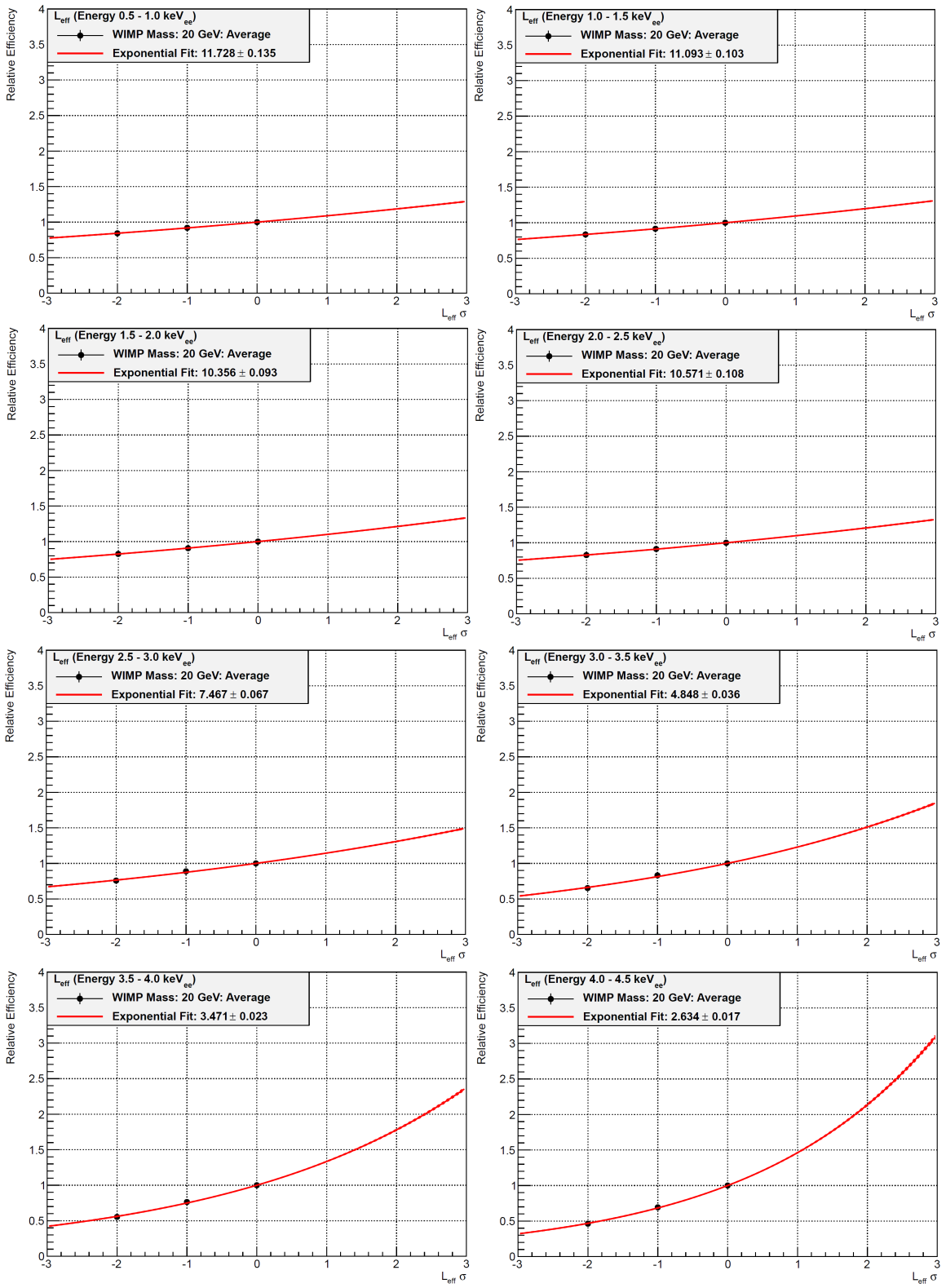


Figure 7.9: Annual average 20 GeV WIMP Xe spin independent interaction event rate energy spectra: Relative Efficiency Vs L_{Eff} σ. Exponential Fits for the 8 lowest energy bins 0.5-4.5 keV_{ee} with the fit parameters listed in the legends.

During χ^2 minimisation the average and residual event rates expected in each 0.5 keV_{ee} energy bin are scaled according to said WIMP's DC and L_{Eff} relative efficiency fits - demonstrated above for a 20 GeV WIMP. Each fit in each energy bin is evaluated using χ^2 minimisation pull terms β_{DC} and $\beta_{\text{L}_{\text{Eff}}}$ measured in the respective standard deviations σ_{DC} and $\sigma_{\text{L}_{\text{Eff}}}$. β_{DC} and $\beta_{\text{L}_{\text{Eff}}}$ are free parameters and common to all energy bins, therefore the extracted and utilised DC and L_{Eff} relative efficiencies are consistent for all energy bins. The pull terms β_{DC} and $\beta_{\text{L}_{\text{Eff}}}$ are added in quadrature to the total χ^2 formula to incorporate their respective systematic uncertainties.

7.2 Electron signal spectra for the model independent search

Alongside the WIMP SI annual modulation search a model independent (MI) annual modulation search is also conducted. This treats each 0.5 keV_{ee} energy bin independently and simply looks for the annual modulation best fit amplitude within each bin. This essentially ignores the signal's contribution to the total event rate and is equivalent to looking for a modulation signal in BG event rate after applying cuts, ignoring the WIMP specific spectral information. Electron recoil events are used to simulate the MI signal. As we are only searching for modulation amplitudes and each energy bin is fitted independently the actual event rate energy spectra are of no consequence. The only relevant information is the relative efficiency as a function of LY and the electron signal efficiency which is used to scale the best fit amplitudes so the results can be directly compared with other experiments. Figure 7.10 displays the electron signal efficiencies for the two analyses: the complete dataset likelihood cut analysis which uses electron MC simulated at l_A = 800 cm and the stable LY dataset PDF cut analysis which uses electron MC simulated at l_A = 2000 in red and blue respectively.

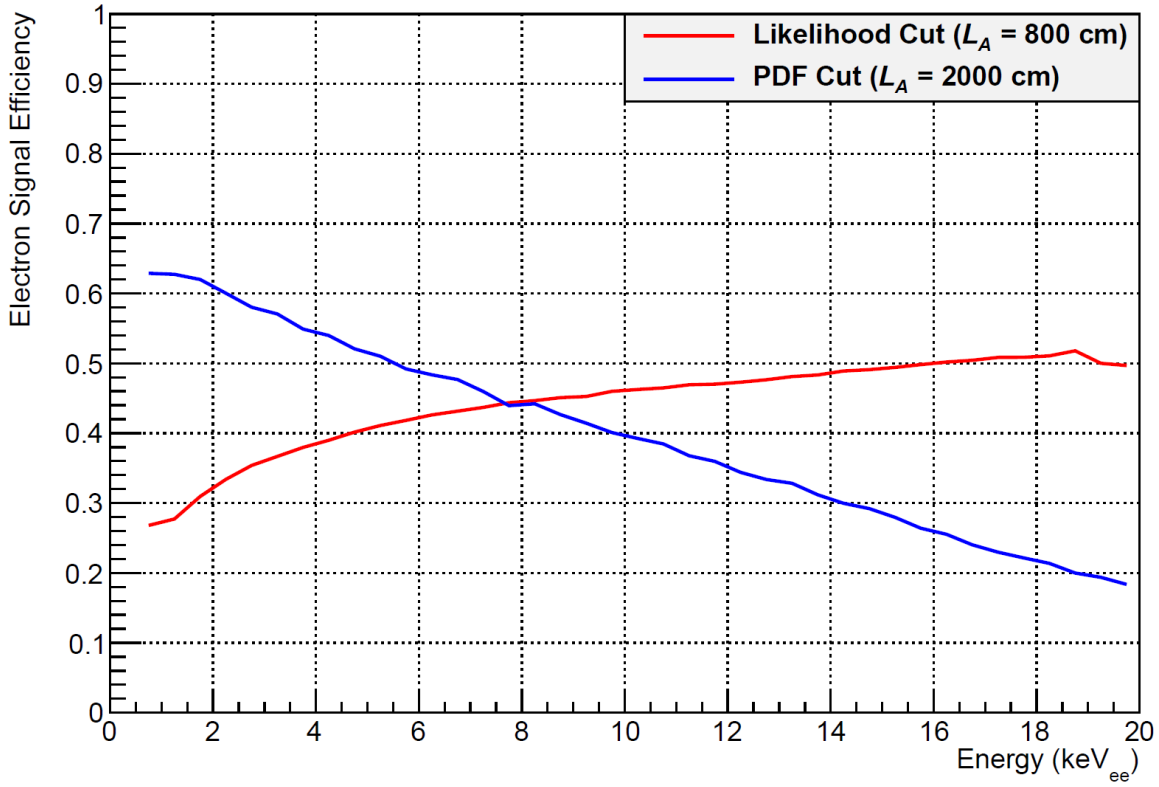


Figure 7.10: Electron signal efficiency for the likelihood cut (red line) and PDF cut (blue line). Electron MC generated at the analyses L_{Base}: l_A = 800 cm and l_A = 2000 cm respectively. PDF cut ER signal efficiency reduces linearly over time and affects the ER classification power.

7.2.1 Electron signal relative efficiencies

The effect of the LY on event rates has been clearly demonstrated for both the BG and the WIMP NR spectra. The electron MC was simulated using the same four l_A values as the WIMPs with l_A = 2000 as the base value. These l_A values are converted to LY using formula 3.4 and the respective relative efficiencies found in the four energy ranges: 0.5-1.0 keV$_{ee}$, 1.0-2.0 keV$_{ee}$, 2.0-6.0 keV$_{ee}$ and 6.0-20.0 keV$_{ee}$. Figure 7.11 demonstrates the relative efficiency of the electron signal events as a function of LY in these 4 energy ranges. A dip in the relative efficiency at low LY in the lowest energy range was similarly observed with the WIMP spectra in figure 7.7. The electron modulation signal event rate is scaled for each period according to its respective LY.

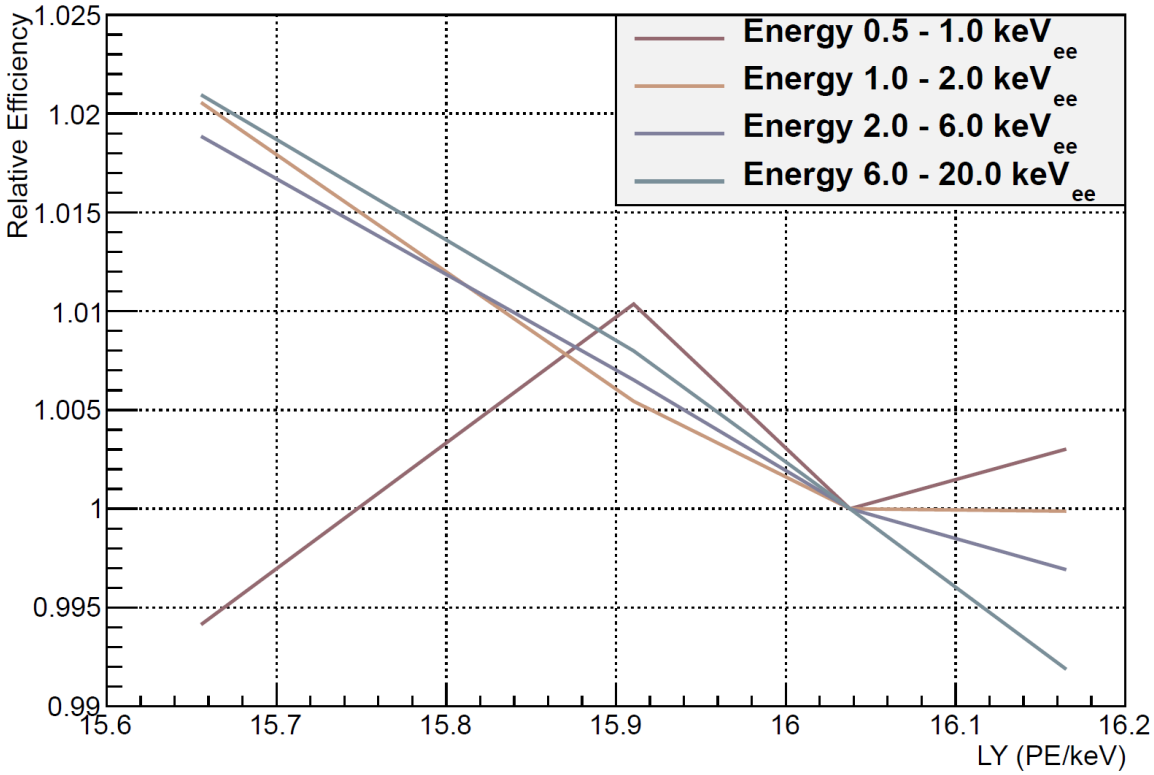


Figure 7.11: Electron MC: Relative Efficiency Vs LY for a range of Energies. Mostly linear however there is a reduction in efficiency at low LY for the lowest energies.

7.3 Previous analysis spectra and relative efficiencies

The complete dataset likelihood cut analysis uses the previously generated signal spectra and relative efficiencies for both the WIMP SI annual modulation search and the MI annual modulation search [49, 50]. As previously stated the base LY for this analysis corresponds to l_A = 800. The other l_A values used to construct the LY relative efficiency curves are 400 cm, 1100 cm and 2000 cm. The DC (-1σ) and L_{Eff} (-1σ and -2σ) uncertainty variations are probed and are fitted in the same manner. This wasn't varied for the Likelihood cut analysis for consistency with the previous analysis [49, 50]. Only WIMP Masses $\leq$ 20 GeV are utilised.

How all of these signal spectra and relative efficiency curves and functions are utilised is outlined explicitly in chapter 8.

Chapter 8

χ^2 Minimisation, Cross Section Scans and Dummy Samples

This chapter outlines the WIMP spin independent (SI) and model independent (MI) searches undertaken for both the complete dataset likelihood cut analysis and the stable LY dataset PDF cut analysis. Section 8.1 details the formulae that govern the total χ^2 and expected event rates (R_{Exp}) for each particular search. Section 8.2 displays the null signal best fits and their respective parameters obtained through χ^2 minimisation. Section 8.3 outlines how these parameters are varied randomly within errors and used to construct dummy expected event rates for each energy bin and period. This process is repeated 1000 times to create 1000 dummy samples that are used to obtain expected ranges of sensitivity for the given searches. Section 8.4 explains how the MI best fit amplitudes are scaled by signal efficiency so as to be compared directly with the annually modulated event rates observed by DAMA. Section 8.5 explains how a cross section scan is performed for the WIMP SI searches and how this translates into a 90% confidence level upper limit on the cross section.

8.1 Expected event rate and χ^2 formulae

The previous chapters outlined event classification, run selection, period and energy bins, observed LY, signal energy spectra, relative efficiency curves and systematic effects that need to be accounted for. This section integrates all of this information in an attempt to perform a DM search with XMASS data by means of χ^2 minimisation.

Multiple searches are performed. Section 8.1.1 outlines the set of parameters that are common to all analyses and searches. Section 8.1.2 details the formulas used to model the expected event rates originating from all the different fit components: The BG component which includes a linear time fit and accounts for the LY - differently in the PDF cut and likelihood cut analyses. The MI component which searches for an annually modulating signal in each energy bin independently. And the WIMP SI component which searches for both a constant and annually modulating signal across all energy bins simultaneously according to the WIMP energy spectra. Section 8.1.3 outlines the χ^2 formulae that govern the χ^2 minimisation fitting procedure for the null signal fit and MI search for both analyses separately. Finally section 8.1.4 outlines equivalent formulae for the WIMP SI search.

8.1.1 General χ^2 variables

As outlined in section 6.1 the data has been segmented into time periods ($\mathrm{T_{Period}}$): 67 low threshold periods and 125 (96) normal threshold periods for the complete (stable LY) dataset. The data is further divided into 39 energy bins ($\mathrm{E_{Bin}}$) of width 0.5 keV_{ee} covering the 0.5 - 20.0 keV_{ee} energy range. The recorded data and theoretically expected event rates in each energy bin (i) and time period (j) are $R^{i,j}_{\mathrm{Data}}$ and $R^{i,j}_{\mathrm{Exp}}$ respectively. This parameterisation is used irrespective of the particular cuts applied.

The theoretically expected event rates $R^{i,j}_{\mathrm{Exp}}$ for all of the BG, MI signal and WIMP SI signal components are detailed explicitly in section 8.1.2, before being compared to the recorded data event rates $R^{i,j}_{\mathrm{Data}}$ using χ^2 formulae in sections 8.1.3 and 8.1.4. The complete dataset and stable LY dataset analyses calculate the BG components differently. The former ($R^{i,j}_{\mathrm{BG_C}}(\alpha)$) uses LY BG relative efficiency curves discussed in section 6.3 and displayed in figure 6.21, while the latter ($R^{i,j}_{\mathrm{BG_S}}$) applies a linear LY correction factor distinct for each energy bin. α is a pull term that allows the BG relative efficiency curves to vary proportional to their uncertainty, aiding χ^2 minimisation. The expected event rates for the MI signal and WIMP SI signal are $R^{i,j}_{\mathrm{Sig_{MI}}}$ and $R^{i,j}_{\mathrm{Sig_W}}(\beta)$ respectively. The latter is constructed using the energy spectra

detailed in section 7.1.1 and displayed in figures 7.4 and 7.5 for the constant and annually modulating signal components respectively. The systematic effects regarding the long decay constant (DC) and the nuclear recoil scintillation efficiency (L_{Eff}) in generating these energy spectra is handled with a linear and exponential fit respectively detailed in section 7.1.2. Pull term β is shorthand for both β_{DC} and $\beta_{L_{Eff}}$, these allow both WIMP systematic relative efficiency functions to vary proportional to their uncertainty, aiding χ^2 minimisation.

The systematic effect of the dark rate on the complete dataset analysis' lowest energy bin's event rate is demonstrated in figure 6.10 for each period with its uncertainty. The dark rate's central value and uncertainty are combined using the pull term γ: $R^{i=0,j}_{DR}(\gamma) = R^{j}_{DR}(0) + \gamma \cdot \Delta R^{j}_{DR}$ and subtracted from $R^{i=0,j}_{Data}$ during χ^2 minimisation. The dark rate is not incorporated in the BG MC relative efficiency curves that are applied to the complete dataset analysis. Therefore this effect is treated separately and for the lowest energy bin only. No such relative efficiency curves are utilised in the stable LY dataset analysis and hence the additional effects of the dark rate are not considered separately; the event rate in the lowest energy bins are fit with a linear LY gradient term like all the others.

The statistical uncertainty of the expected event rate is $\sigma^{i,j}_{Exp} = \sqrt{\frac{R^{i,j}_{Exp}}{T^j M w}}$ where T^j is the livetime in days of period j, M is the mass of LXe within the ID's active region (832 kg) and w the energy bin width (0.5 keV_{ee}).

$\sigma^{i,j}_{Sys}$ is the systematic uncertainty on the data's event rate for each energy and time bin that result from uncertainties on the LY. As outlined in section 6.2.3 both analyses utilise $\sigma_{LY^{Inner}_{-30cm}}$ and $\sigma_{LY^{Hose}_{Eff\ -30cm}}$ with the complete dataset likelihood cut analysis incorporating an additional LY systematic error of 0.3% between April 2015 - September 2015. $\sigma^{i,j}_{Sys}$ is calculated using equation 6.4 and demonstrated for the 8 lowest energy bins in figures A.1 and A.2 for the complete dataset likelihood cut and stable LY dataset PDF cut analyses respectively.

8.1.2 Formulae and variables for the expected event rate

The $R^{i,j}_{\mathrm{Exp}}$ components discussed above: $R^{i,j}_{\mathrm{BG_C}}(\alpha)$, $R^{i,j}_{\mathrm{BG_S}}$, $R^{i,j}_{\mathrm{Sig_{MI}}}$ and $R^{i,j}_{\mathrm{Sig_W}}(\beta)$ are calculated using the formulae in equation 8.1. The expected event rates for a given period are obtained by integrating over time (t: days from 2014/01/01) between the time of the first run and the last run in said period: t^j_F and t^j_L respectively. For modulation signals: $T_{\mathrm{Year}} = 365.24$ days is a period of one year and $t_0 = 152.5$ days is the phase of maximal amplitude for the theorised DM interaction.

$$\begin{aligned}
R^{i,j}_{\mathrm{BG_C}}(\alpha) &= \int_{t^j_F}^{t^j_L} \left[E^{ij}_{\mathrm{BG}}(\alpha)\cdot\left(C^i_{\mathrm{BG}} + S^i_{\mathrm{BG}}\cdot t\right)\right] dt. \\
R^{i,j}_{\mathrm{BG_S}} &= \int_{t^j_F}^{t^j_L} \left[\left(1 + G^i_{\mathrm{BG}}\cdot(L^j - L_{\mathrm{Base}})\right)\cdot\left(C^i_{\mathrm{BG}} + S^i_{\mathrm{BG}}\cdot t\right)\right] dt. \\
R^{i,j}_{\mathrm{Sig_{MI}}} &= \int_{t^j_F}^{t^j_L} \left[E^i_{\mathrm{MI}}(L^j)\cdot A^i_{\mathrm{MI}}\cdot\cos\left(2\pi\frac{t-t_0}{T_{\mathrm{Year}}}\right)\right] dt. \\
R^{i,j}_{\mathrm{Sig_W}}(\beta) &= \int_{t^j_F}^{t^j_L} \left[E^i_{\mathrm{W}}(L^j)\cdot\left(C^i_{\mathrm{W}}(\beta) + A^i_{\mathrm{W}}(\beta)\cdot\cos\left(2\pi\frac{t-t_0}{T_{\mathrm{Year}}}\right)\right)\right] dt.
\end{aligned} \tag{8.1}$$

C^i corresponds to a constant event rate within a given energy bin. When describing the BG (C^i_{BG}) it is paired with a linear time slope S^i_{BG} distinct for each energy bin and both are free variables under χ^2 minimisation. The first XMASS modulation analysis [73, 74] treated the BG as constant, however the previous modulation analysis [49, 50] introduced said time slope to capture the natural decay of the BG radioactivity - a major component of which is a daughter from the ^{238}U chain: ^{210}Pb which decays with a half-life of 22 years. When describing the WIMP signal ($C^i_{\mathrm{W}}(\beta)$) it's central value $C^i_{\mathrm{W}}(0)$ is fixed for each energy bin, obtained directly from the annual average WIMP SI energy spectra, displayed in figure 7.4 for each specific WIMP mass. However 2 free parameters - common to all energy bins - incorporating the DC (β_{DC}) and $\mathrm{L_{Eff}}$ ($\beta_{\mathrm{L_{Eff}}}$) systematics allows $C^i_{\mathrm{W}}(0)$ to be scaled by both relative efficiency fitted functions $E^i_{C_{\mathrm{DC}}}$ and $E^i_{C_{\mathrm{L_{Eff}}}}$. $E^i_{C_{\mathrm{DC}}}$ and $E^i_{C_{\mathrm{L_{Eff}}}}$ are linear and exponential respectively, outlined in section 7.1.2 and demonstrated for a WIMP of mass 20 GeV in figures 7.8 and 7.9 respectively. By evaluating $E^i_{C_{\mathrm{DC}}}$ and $E^i_{C_{\mathrm{L_{Eff}}}}$ at their respective free parame-

ters $E^i_{C_{\mathrm{DC}}}(\beta_{\mathrm{DC}})$ and $E^i_{C_{\mathrm{L_{Eff}}}}(\beta_{\mathrm{L_{Eff}}})$: $C^i_{\mathrm{W}}(\beta) = C^i_{\mathrm{W}}(0) \cdot E^i_{C_{\mathrm{DC}}}(\beta_{\mathrm{DC}}) \cdot E^i_{C_{\mathrm{L_{Eff}}}}(\beta_{\mathrm{L_{Eff}}})$.

The WIMP signal amplitudes ($A^i_{\mathrm{W}}(\beta)$) similarly have fixed central values ($A^i_{\mathrm{W}}(0)$), obtained directly from the annual residual WIMP SI energy spectra, displayed in figure 7.5 for each specific WIMP mass. The June - December residual values are halved to obtain the amplitude. The same scaling procedure is implemented with the residual DC and $\mathrm{L_{Eff}}$ relative efficiency fitted functions - linear $E^i_{A_{\mathrm{DC}}}$ and exponential $E^i_{A_{\mathrm{L_{Eff}}}}$ respectively - evaluated at the same 2 free parameters (β_{DC} and $\beta_{\mathrm{L_{Eff}}}$): $A^i_{\mathrm{W}}(\beta) = A^i_{\mathrm{W}}(0) \cdot E^i_{A_{\mathrm{DC}}}(\beta_{\mathrm{DC}}) \cdot E^i_{A_{\mathrm{L_{Eff}}}}(\beta_{\mathrm{L_{Eff}}})$. The MI search finds the best fit signal amplitudes: A^i_{MI}, a free parameter in each energy bin.

The WIMP and MI signal functions are scaled by their respective LY relative efficiency functions $E^i_{\mathrm{MI}}(L^j)$ and $E^i_{\mathrm{W}}(L^j)$ evaluated at the LY for that specific period (L^j). The figures 7.7 and 7.11 display E^i_{MI} and E^i_{W} respectively for the 4 distinct energy ranges that combined span the entire analysed energy range.

The BG LY relative efficiency curves for the complete dataset likelihood cut analysis evaluated at each period's LY are displayed in figure 6.21 - for the same 4 energy ranges discussed above. As discussed in section 6.3 the errors are systematic and associated with variations of the geometry of the cupper plates covering the Al-seal in the MC simulation. As such the uncertainty on the event rate induced by scaling with said relative efficiencies is treated in the same way as the dark rate, a pull term α common to all energy bins allows the relative efficiency curves to vary according to: $E^{ij}_{\mathrm{BG}}(\alpha) = E^{ij}_{\mathrm{BG}} + \alpha \cdot \Delta E^{ij}_{\mathrm{BG}}$.

The stable LY dataset analysis removes the systematic effects of the dark rate ($R^{i=0,j}_{\mathrm{DR}}(\gamma)$) and the BG LY relative efficiency curves ($E^{ij}_{\mathrm{BG}}(\alpha)$) by incorporating a simple LY gradient parameter (G^i_{BG}) distinct for each energy bin and free under χ^2 minimisation. L_{Base} is the LY that equates to $l_A = 2000$ cm for this analysis.

8.1.3 Null signal fit and MI search

In this section the χ^2 formulae that govern the null signal fit and MI searches are outlined for both the stable LY dataset PDF cut analysis and the complete dataset

likelihood cut analysis.

- **Stable LY dataset PDF cut analysis:**

  Null signal fit expected event rate: $R^{i,j}_{\mathrm{Exp}} = R^{i,j}_{\mathrm{BG_S}}$.

  MI signal search expected event rate: $R^{i,j}_{\mathrm{Exp}} = R^{i,j}_{\mathrm{BG_S}} + R^{i,j}_{\mathrm{Sig_{MI}}}$.

  For the stable LY dataset PDF cut analysis neither incorporate any pull parameters. Therefore they both use the same basic χ^2 formula where the expected event rate - albeit different - is compared directly to the data's event rate summed over all energy bins and stable LY periods:

$$\chi^2 = \sum_{i}^{\mathrm{E_{Bin}}} \sum_{j}^{\mathrm{T_{Period}}} \frac{\left(R^{i,j}_{\mathrm{Data}} - R^{i,j}_{\mathrm{Exp}}\right)^2}{(\sigma^{i,j}_{\mathrm{Exp}})^2 + (\sigma^{i,j}_{\mathrm{Sys}})^2}. \tag{8.2}$$

  The null fit χ^2 minimisation best fit parameters C^i_{BG}, S^i_{BG} and G^i_{BG} are used to produce the dummy event rates for the stable LY dataset PDF cut analysis.

- **Complete dataset likelihood cut analysis:**

  Null signal fit expected event rate: $R^{i,j}_{\mathrm{Exp}}(\alpha) = R^{i,j}_{\mathrm{BG_C}}(\alpha)$.

  MI signal search expected event rate: $R^{i,j}_{\mathrm{Exp}}(\alpha) = R^{i,j}_{\mathrm{BG_C}}(\alpha) + R^{i,j}_{\mathrm{Sig_{MI}}}$.

  For the complete dataset likelihood cut analysis both of these incorporate 2 pull parameters: dark rate (γ) and BG LY relative efficiency (α). Therefore they both use the same χ^2 formula where the expected event rate - albeit different - is compared directly to the data's event rate and summed over all energy bins and complete dataset periods, with the systematics constrained by the pull term contributions:

$$\chi^2 = \sum_{i}^{\mathrm{E_{Bin}}} \sum_{j}^{\mathrm{T_{Period}}} \frac{\left(R^{i,j}_{\mathrm{Data}} - R^{i,j}_{\mathrm{Exp}}(\alpha) - R^{i=0,j}_{\mathrm{DR}}(\gamma)\right)^2}{(\sigma^{i,j}_{\mathrm{Exp}})^2 + (\sigma^{i,j}_{\mathrm{Sys}})^2} + \alpha^2 + \gamma^2. \tag{8.3}$$

  The null fit χ^2 minimisation best fit parameters C^i_{BG} and S^i_{BG} are used to produce the dummy event rates for the complete dataset likelihood cut analysis.

8.1.4 WIMP SI search

The following searches were conducted for distinct WIMP masses one by one. A cross section scaling parameter σ is initially free under χ^2 minimisation to find the best fit cross section and is then fixed and iteratively varied to perform a cross section χ^2 scan. This is used in section 8.5 to extract the 90% confidence limits. Here are the specific χ^2 formulae that govern the two analyses.

- **Stable LY dataset PDF cut analysis:**

  WIMP signal search expected event rate: $R^{i,j}_{\mathrm{Exp}}(\beta) = R^{i,j}_{\mathrm{BG_S}} + \sigma \cdot R^{i,j}_{\mathrm{Sig_W}}(\beta)$.

  For the stable LY dataset PDF cut analysis the only pull parameters incorporated belong to the DC and $\mathrm{L_{Eff}}$ relative efficiency fitted functions (β_{DC} and $\beta_{\mathrm{L_{Eff}}}$ respectively). The χ^2 formula compares directly the expected event rate to the data's event rate summed over all energy bins and stable LY dataset periods, with the systematics constrained by the pull term contributions:

$$\chi^2 = \sum_{i}^{\mathrm{E_{Bin}}} \sum_{j}^{\mathrm{T_{Period}}} \frac{\left(R^{i,j}_{\mathrm{Data}} - R^{i,j}_{\mathrm{Exp}}(\beta)\right)^2}{(\sigma^{i,j}_{\mathrm{Exp}})^2 + (\sigma^{i,j}_{\mathrm{Sys}})^2} + \beta^2_{\mathrm{DC}} + \beta^2_{\mathrm{L_{Eff}}}. \tag{8.4}$$

- **Complete dataset likelihood cut analysis:**

  WIMP signal search expected event rate: $R^{i,j}_{\mathrm{Exp}}(\alpha,\beta) = R^{i,j}_{\mathrm{BG_C}}(\alpha) + \sigma \cdot R^{i,j}_{\mathrm{Sig_W}}(\beta)$.

  For the complete dataset likelihood cut analysis all pull parameters are incorporated: dark rate (γ), BG LY relative efficiency (α) and the DC and $\mathrm{L_{Eff}}$ relative efficiency fitted functions (β_{DC} and $\beta_{\mathrm{L_{Eff}}}$ respectively). The χ^2 formula compares directly the expected event rate to the data's event rate, summed over all energy bins and complete dataset periods, systematics constrained by the pull term contributions:

$$\chi^2 = \sum_{i}^{\mathrm{E_{Bin}}} \sum_{j}^{\mathrm{T_{Period}}} \frac{\left(R^{i,j}_{\mathrm{Data}} - R^{i,j}_{\mathrm{Exp}}(\alpha,\beta) - R^{i=0,j}_{\mathrm{DR}}(\gamma)\right)^2}{(\sigma^{i,j}_{\mathrm{Exp}})^2 + (\sigma^{i,j}_{\mathrm{Sys}})^2} + \alpha^2 + \beta^2_{\mathrm{DC}} + \beta^2_{\mathrm{L_{Eff}}} + \gamma^2. \tag{8.5}$$

8.2 Null signal best fit parameters

The null fit χ^2 minimisation is conducted first for both analyses and the best fit parameters are obtained. For the stable LY dataset PDF cut analysis C^i_{BG}, S^i_{BG} and G^i_{BG} are obtained independently for each energy bin. For the complete dataset likelihood cut analysis C^i_{BG}, S^i_{BG} are obtained independently for each energy bin, along with α and γ, pull terms common to all energy bins in place of G^i_{BG}. These are then used to produce dummy sample event rates, discussed in section 8.3.

The data event rates for the complete dataset likelihood cut analysis and the stable LY dataset PDF cut analysis are displayed in figures 6.19 and 6.25 respectively for the 8 lowest energy bins 0.5-4.5 keV$_{ee}$.

Figure 8.1 demonstrates the PDF cut event rates (statistical error bars only), flattened by removing the linear time slope and linear LY gradient effects, for the 8 lowest energy bins 0.5-4.5 keV$_{ee}$. These variables - included in the plots' legends - adequately flatten the data, it is now ready to be fit with additional modulation variables to perform a MI and WIMP search outlined in section 8.4 and 8.5 respectively. Figure 8.2 similarly demonstrates the PDF cut event rates where only the linear LY gradient effects have been corrected for, the linear fits represent the time slopes. Figure 8.3 demonstrates the corollary where the linear time effects have been corrected for and the linear fits represent the LY relative efficiency gradients.

Figure 8.4 displays the likelihood cut event rates (statistical error bars only) for the 8 lowest energy bins 0.5-4.5 keV$_{ee}$, where the MC generated BG LY relative efficiency curves - discussed in section 6.3 - have been applied to remove the LY effects from the raw data. α is χ^2 minimised and the linear fits represent the time slopes. A discrepancy in the early time data is evident in the energy bins above 2.5 keV$_{ee}$, further supporting the removal of this portion of the dataset for the newly developed PDF cut stable LY dataset analysis. These deviations were also present in the previous modulation analysis [49, 50].

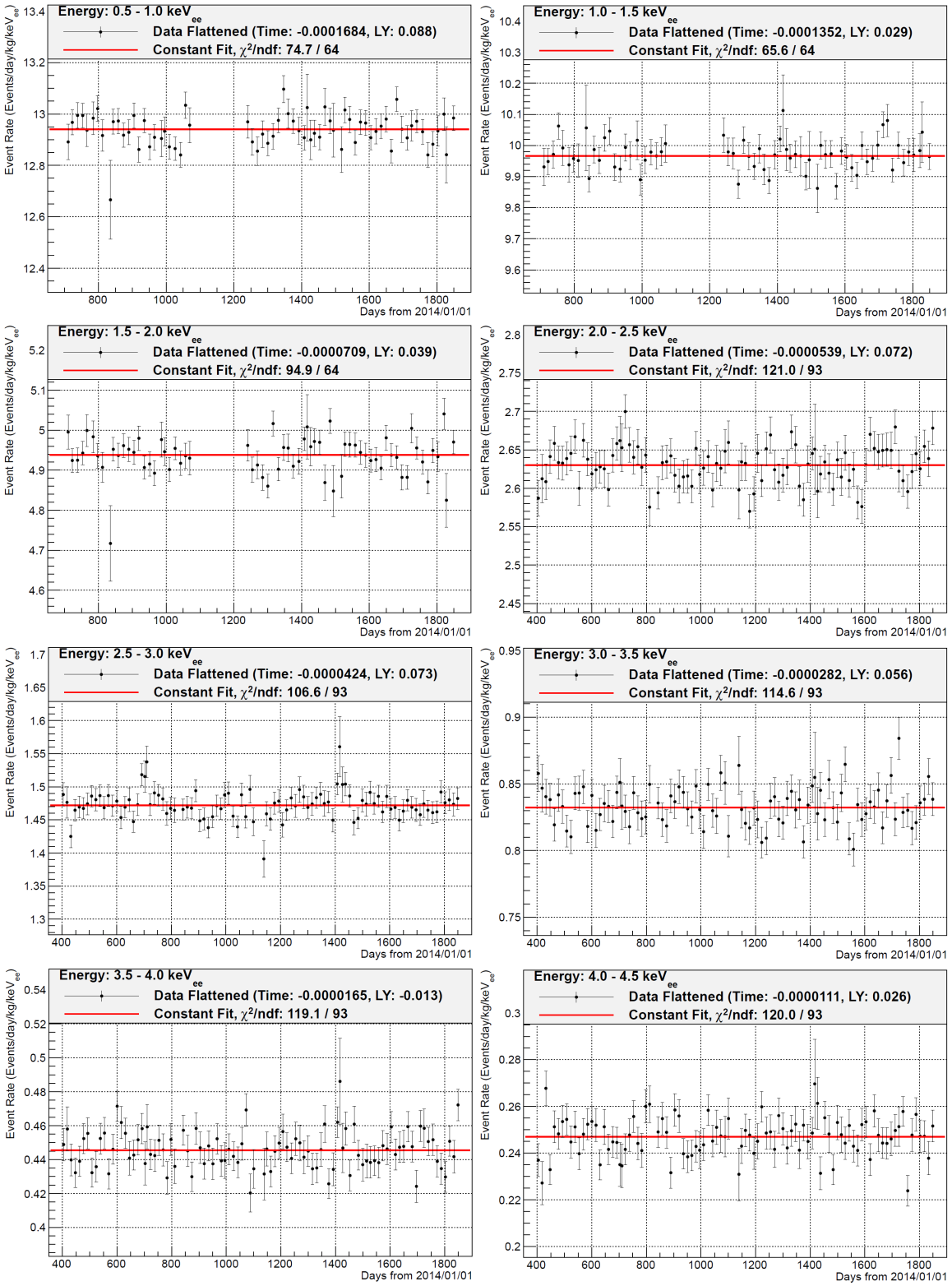


Figure 8.1: Event rates for the stable LY dataset PDF cut flattened (LY corrected and time corrected), 8 lowest energy bins 0.5-4.5 keV$_{ee}$.

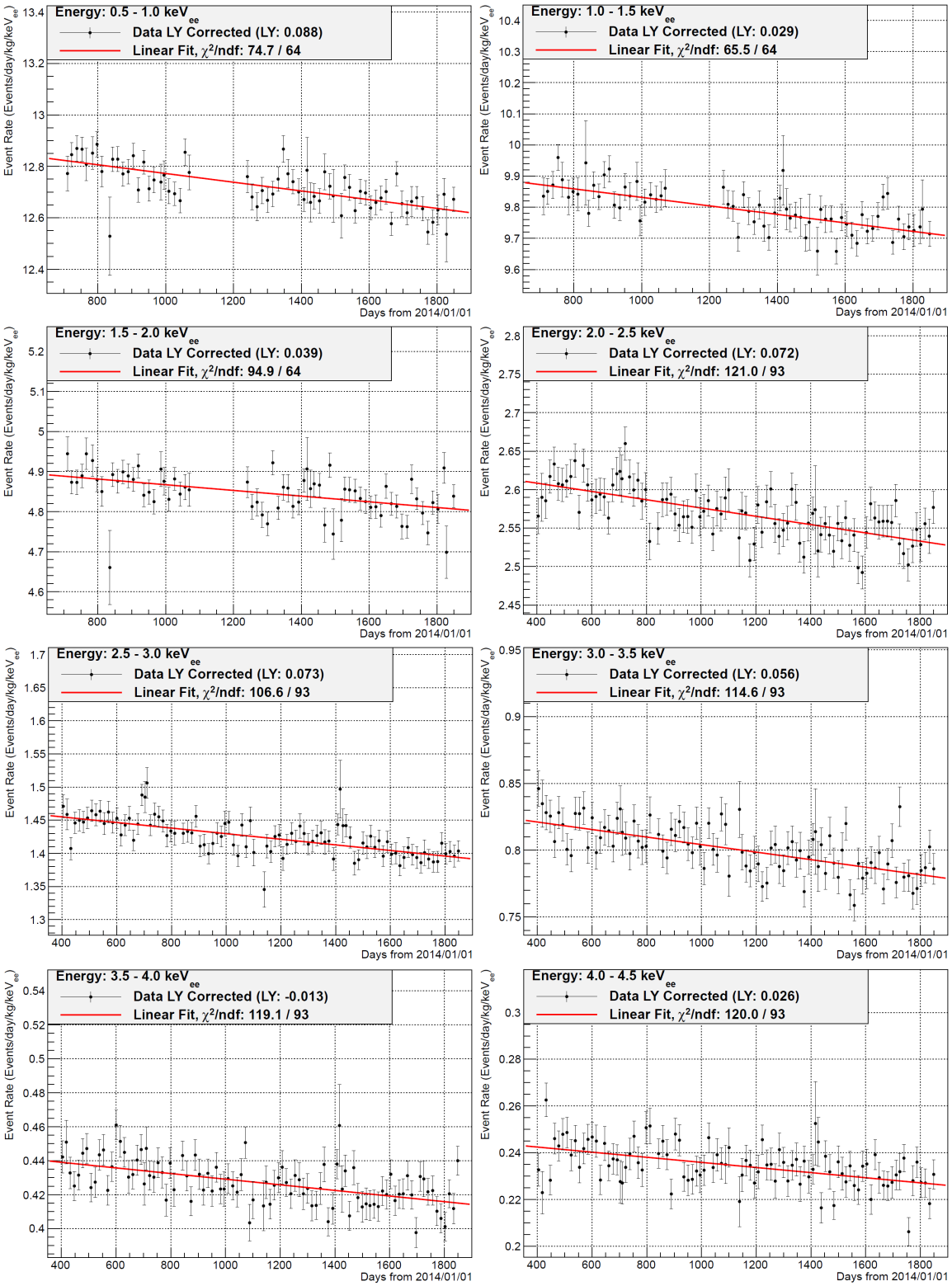


Figure 8.2: Event rates for the stable LY dataset PDF cut linear time fit (LY corrected), 8 lowest energy bins 0.5-4.5 keV_{ee}.

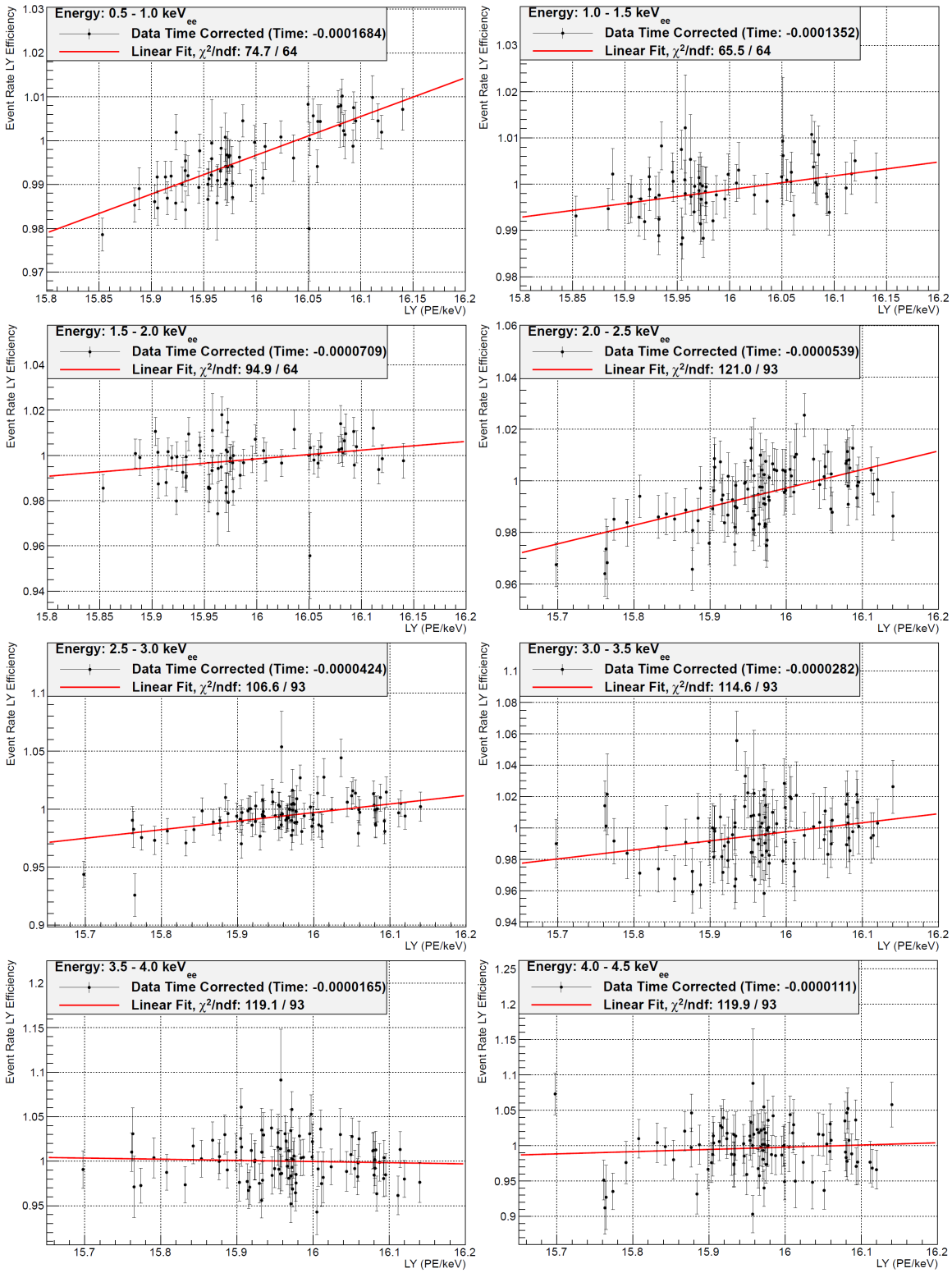


Figure 8.3: Event rates for the stable LY dataset PDF cut linear LY fit (time corrected), 8 lowest energy bins 0.5-4.5 keV$_{ee}$.

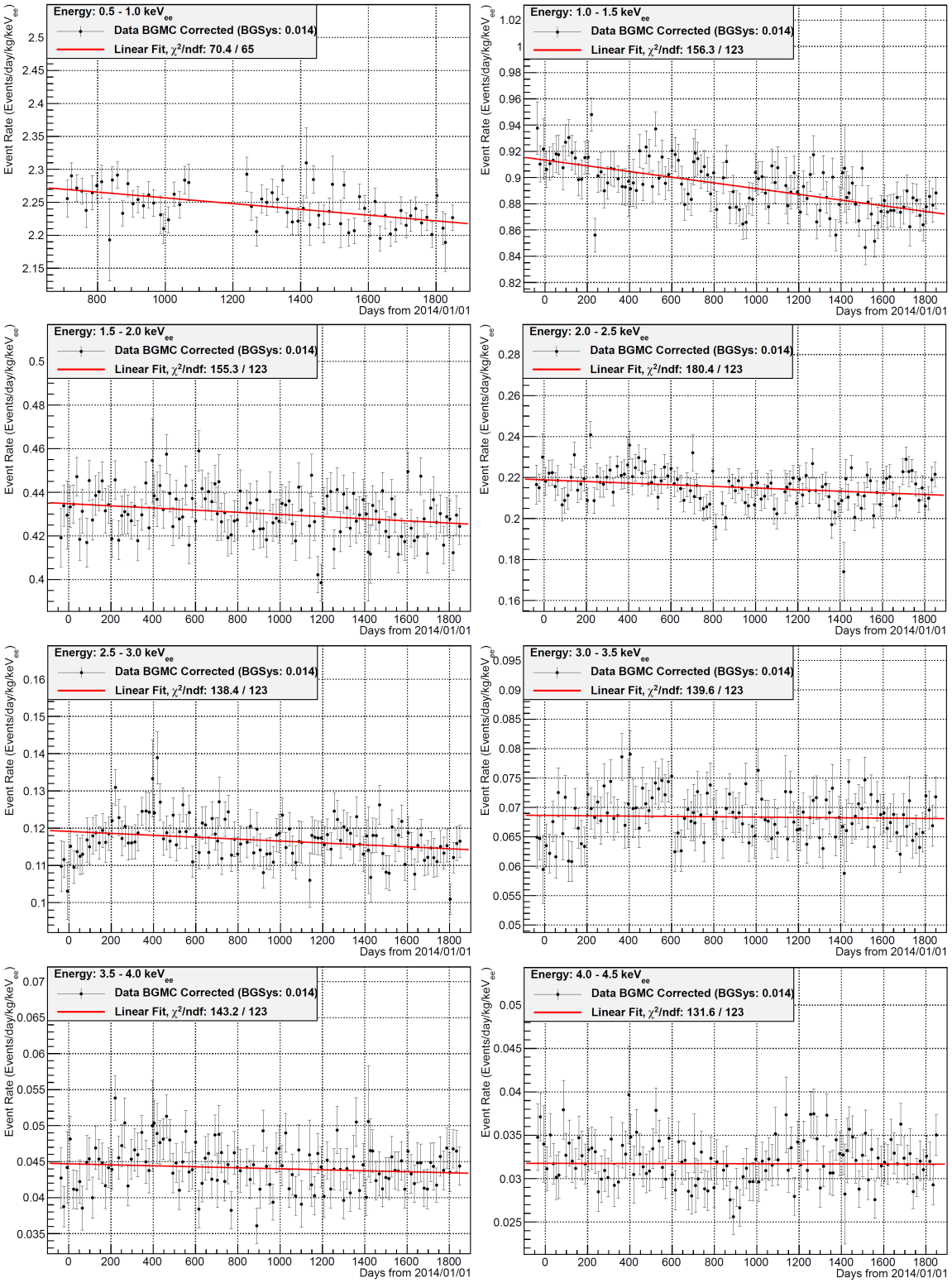


Figure 8.4: Event rates for the complete dataset likelihood cut after being corrected using the BGMC Relative efficiency curves (same as previous analysis), 8 lowest energy bins 0.5-4.5 keV$_{ee}$. Still the linear BG component present within the data so not completely flattened.

8.3 Dummy sample event rates

A dummy sample dataset comprises of simulated BG event rates for all energy bins in all time periods, equivalent to $R^{i,j}_{\mathrm{Data}}$. 1000 dummy sample datasets are generated for both analyses using their respective null signal best fit parameters and are void of any signal component. These are used to ascertain the expected uncertainties on the extracted modulation amplitudes and the inferred 90% cross section limits that arise from random statistical deviations of the event rates within these datasets. The complete dataset likelihood cut analysis dummy samples are generated in the same manner as for the previous analysis [49, 50].

- **Complete dataset likelihood cut analysis:** $C^{i}_{\mathrm{BG_{Best}}}$ and $S^{i}_{\mathrm{BG_{Best}}}$ (with error $\Delta S^{i}_{\mathrm{BG_{Best}}}$) are extracted from the null signal fit. Three Gaussian (μ = 0, σ = 1) randomised values are obtained, two of these correspond to random versions of the BG pull terms: α_{Rand} and γ_{Rand} and the other S_{Rand} is used to randomly vary the slope of each energy bin in the same manner $S^{i}_{\mathrm{BG_{Rand}}} = S^{i}_{\mathrm{BG_{Best}}} + S_{\mathrm{Rand}} \cdot \Delta S^{i}_{\mathrm{BG_{Best}}}$.

  An expected event rate $R^{i,j}_{\mathrm{BG_C}}(\alpha)$ for each energy bin and for each period is constructed using $C^{i}_{\mathrm{BG_{Best}}}$, $S^{i}_{\mathrm{BG_{Rand}}}$, $E^{ij}_{\mathrm{BG}}(\alpha_{\mathrm{Rand}})$ and adding a random dark rate to the lowest energy bin $R^{i=0,j}_{\mathrm{DR}}(\gamma_{\mathrm{Rand}})$. These are further Gaussian randomised with $\sigma^{i,j}_{\mathrm{Sys}}$ and finally the resultant number of events are Poisson randomised to produce purely random event rates for each energy bin and period.

- **Stable LY dataset PDF cut analysis:** $C^{i}_{\mathrm{BG_{Best}}}$ (with error $\Delta C^{i}_{\mathrm{BG_{Best}}}$), $S^{i}_{\mathrm{BG_{Best}}}$ (with error $\Delta S^{i}_{\mathrm{BG_{Best}}}$) and $G^{i}_{\mathrm{BG_{Best}}}$ (with error $\Delta G^{i}_{\mathrm{BG_{Best}}}$) are extracted from the null signal fit. Unlike the randomisation associated with the complete dataset likelihood cut analysis, three Gaussian (μ = 0, σ = 1) randomised values were generated for each energy bin (C^{i}_{Rand}, S^{i}_{Rand} and G^{i}_{Rand}) to vary each of these three best fit parameters for each energy bins separately: $C^{i}_{\mathrm{BG_{Rand}}} = C^{i}_{\mathrm{BG_{Best}}} + C^{i}_{\mathrm{Rand}} \cdot \Delta C^{i}_{\mathrm{BG_{Best}}}$, $S^{i}_{\mathrm{BG_{Rand}}} = S^{i}_{\mathrm{BG_{Best}}} + S^{i}_{\mathrm{Rand}} \cdot \Delta S^{i}_{\mathrm{BG_{Best}}}$ and $G^{i}_{\mathrm{BG_{Rand}}} = G^{i}_{\mathrm{BG_{Best}}} +$

$G^i_{\mathrm{Rand}} \cdot \Delta G^i_{\mathrm{BG_{Best}}}$.

An expected event rate $R^{i,j}_{\mathrm{BG_S}}$ for each energy bin and for each period is constructed using $C^i_{\mathrm{BG_{Rand}}}$, $S^i_{\mathrm{BG_{Rand}}}$, $G^i_{\mathrm{BG_{Rand}}}$. These are further Gaussian randomised with $\sigma^{i,j}_{\mathrm{Sys}}$ and finally the resultant number of events are Poisson randomised to produce purely random event rates for each energy bin and period.

8.4 MI best fit amplitudes

As stated previously the aim of the MI signal search is to find the best fit modulation amplitude for each energy bin separately and that is why A^i_{MI} is a free parameter in all energy bins. Figures 8.5 and 8.6 display the complete dataset likelihood cut analysis recorded data event rates (blue) overlaid with the Linear BG fit + MI amplitude signal best fit function (red) for the 0.5-5.5 keV$_{ee}$ and the 5.5-10.5 keV$_{ee}$ energy bins respectively. Figures 8.7 and 8.8 display equivalent plots for the stable LY PDF cut dataset analysis. The resultant amplitudes are scaled by the electron signal efficiency - displayed in figure 7.10 - and then compared directly to the modulated event rate DAMA observes [43–45].

For both the complete dataset likelihood cut and stable LY dataset PDF cut analyses, this MI annual modulation search is conducted on the recorded data and on the 1000 dummy samples to obtain 1σ and 2σ estimated sensitivity bands.

To check that there is no singular dominant phase t_0 across all energy bins an additional χ^2 minimisation search is conducted. A grid search is performed separately for each energy bin (i) over phase t_0: $0 \rightarrow T_{\mathrm{Year}}$ and amplitude A^i_{MI}: $-2\% \rightarrow +2\%$ proportion of that energy bin's BG constant C^i_{BG}. The χ^2 values are converted to a probability $e^{\frac{\chi^2_{\mathrm{min}}-\chi^2}{2}}$ and the resultant plots - displayed and discussed in section 9.5 - contain 2 peaks with said maxima located at a positive amplitude with the best fit phase and another at negative amplitude with the best fit phase $+\frac{1}{2} \cdot T_{\mathrm{Year}}$. Both positive and negative amplitudes where used to check the consistency with zero amplitude.

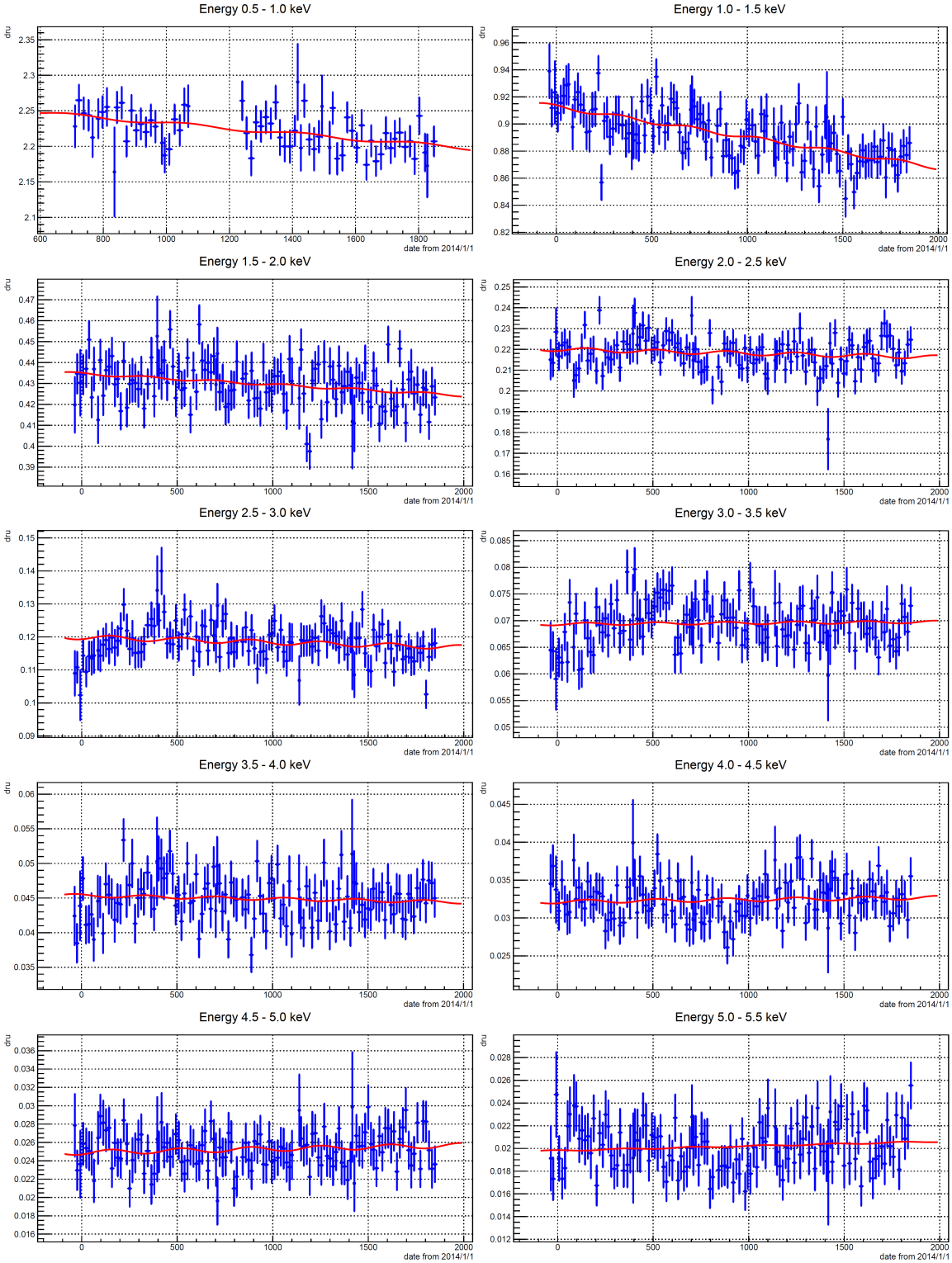


Figure 8.5: Complete dataset likelihood cut analysis event rates (blue) - LY effects corrected for - overlaid with the Linear BG + MI signal best fit (red) in energy bins 0.5-5.5 keV$_{ee}$, dru = events/day/keV$_{ee}$/kg.

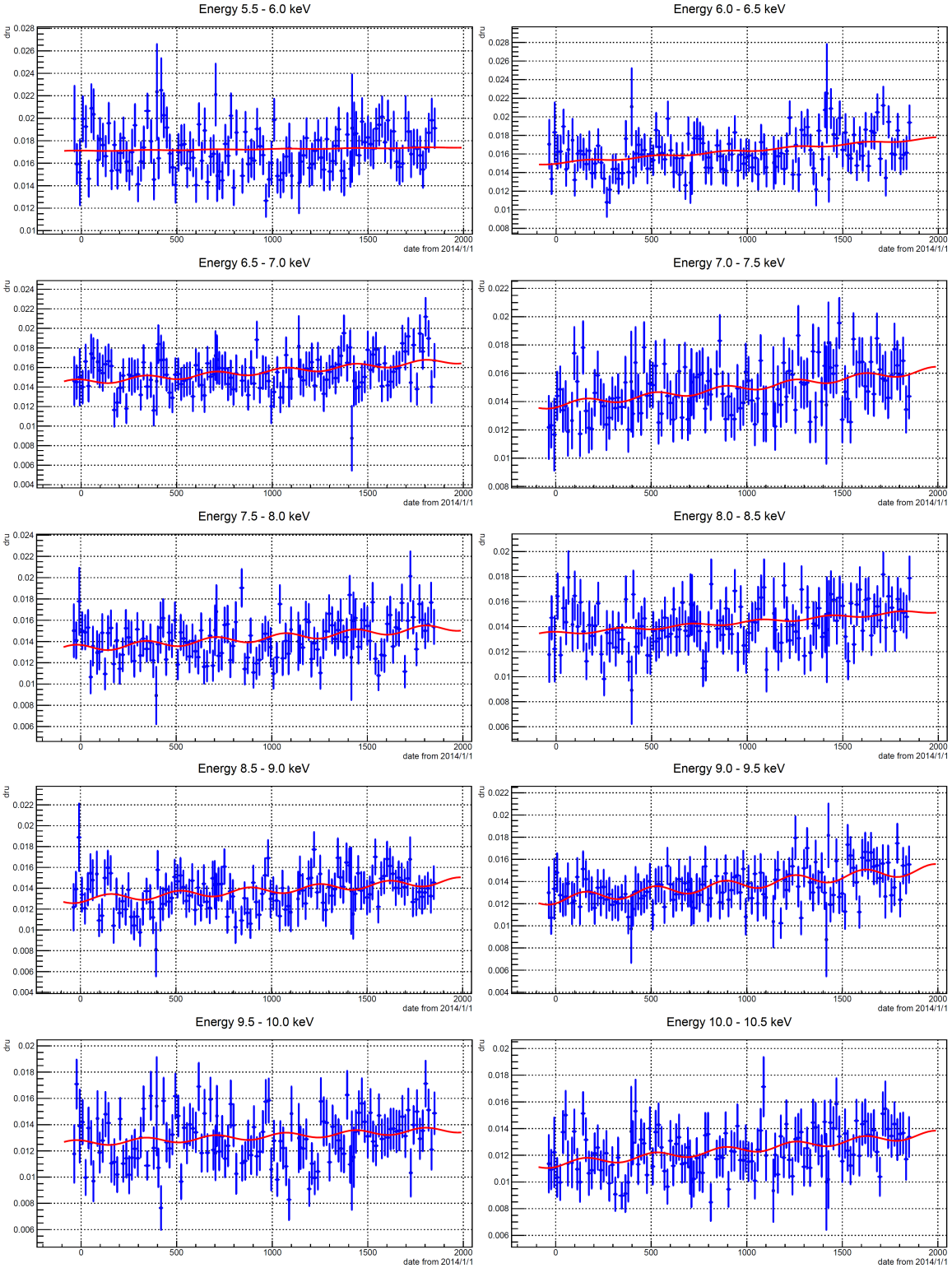


Figure 8.6: Complete dataset likelihood cut analysis event rates (blue) - LY effects corrected for - overlaid with the Linear BG + MI signal best fit (red) in energy bins 5.5-10.5 keV$_{ee}$, dru = events/day/keV$_{ee}$/kg.

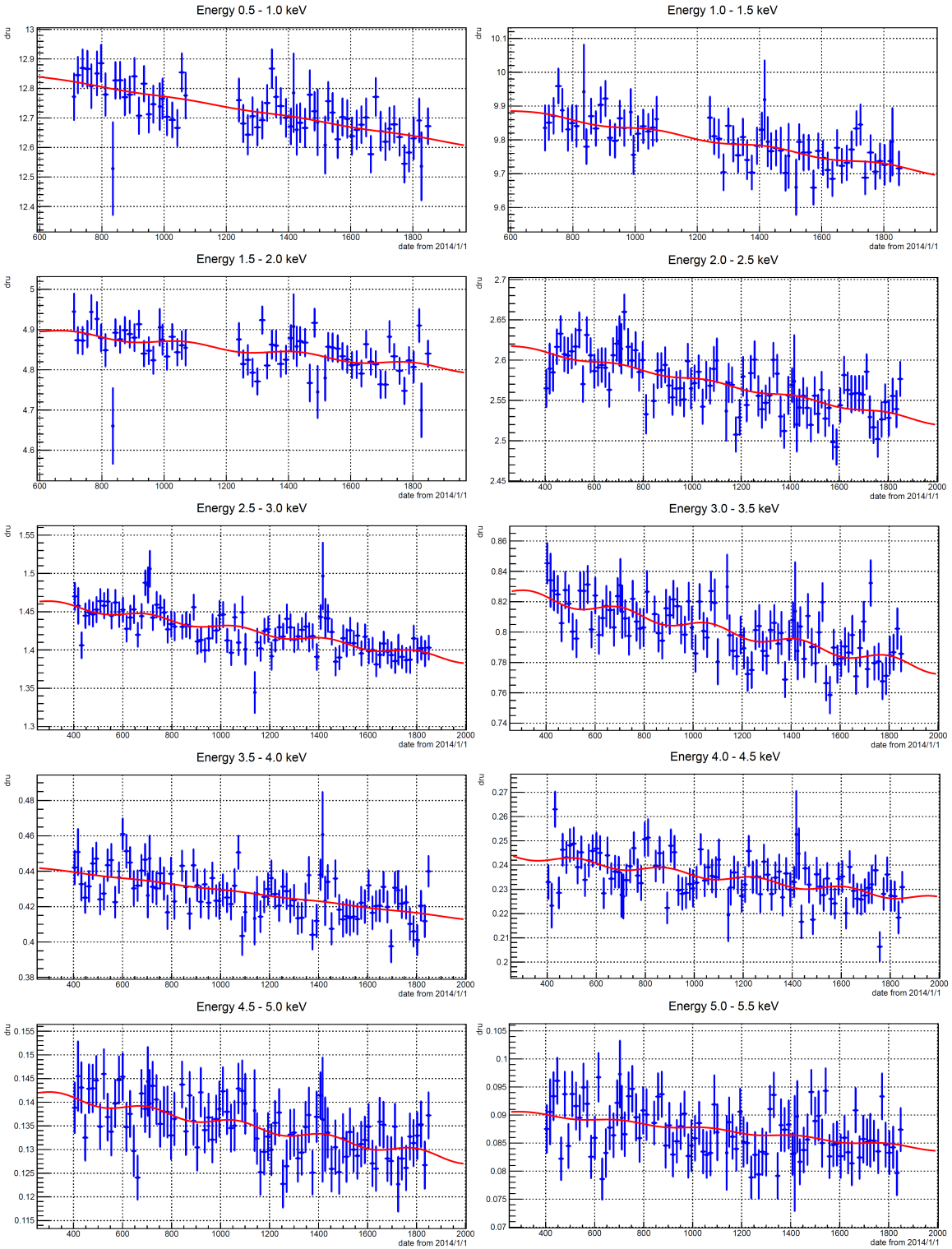


Figure 8.7: Stable LY dataset PDF cut analysis event rates (blue) - LY effects corrected for - overlaid with the Linear BG + MI signal best fit (red) in energy bins 0.5-5.5 keV$_{ee}$, dru = events/day/keV$_{ee}$/kg.

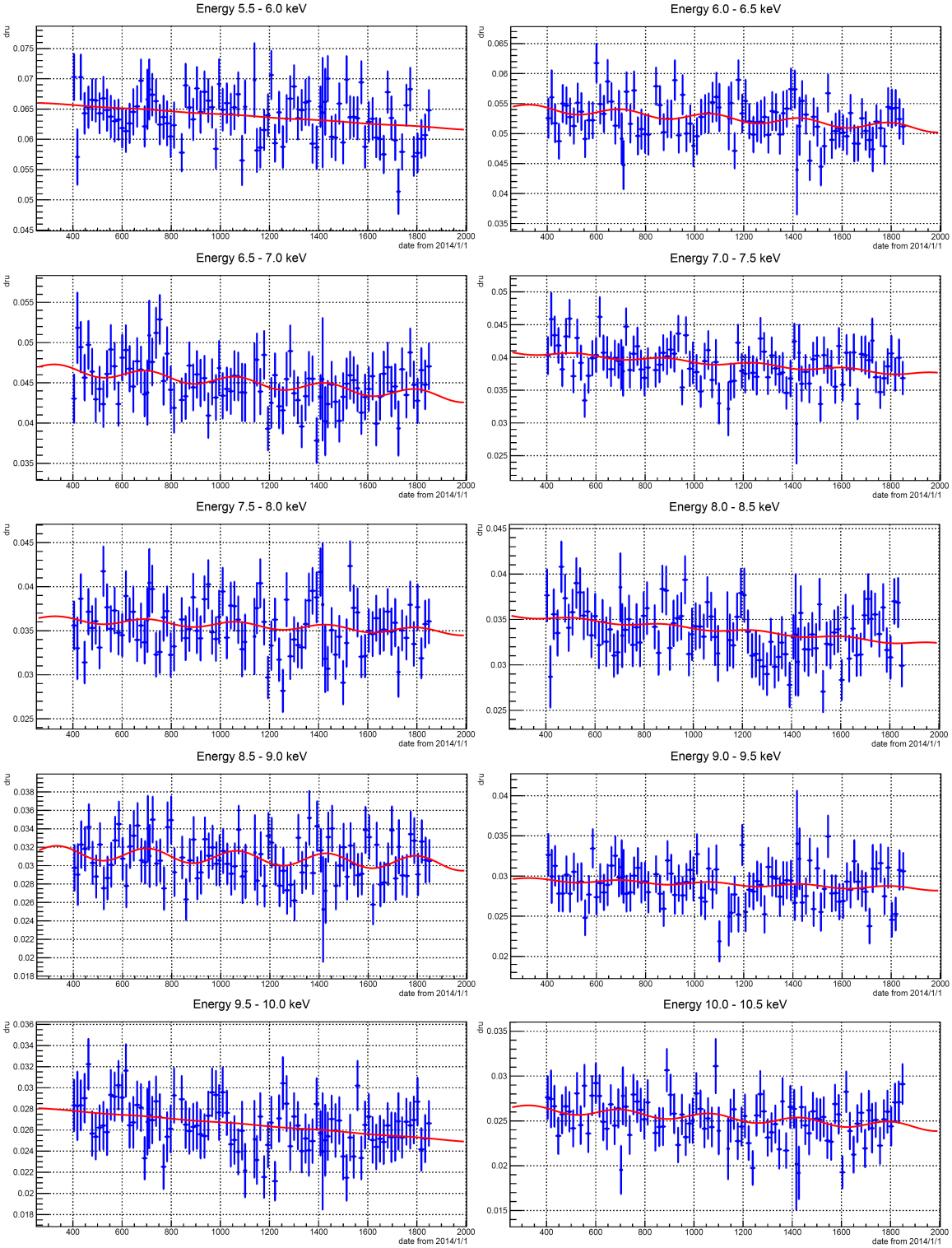


Figure 8.8: Stable LY dataset PDF cut analysis event rates (blue) - LY effects corrected for - overlaid with the Linear BG + MI signal best fit (red) in energy bins 5.5-10.5 keV$_{ee}$, dru = events/day/keV$_{ee}$/kg.

8.5 Cross section scan and 90% confidence limit

The central values of the constant and amplitude for the WIMP SI search are predefined for each energy bin and obtained directly from the energy spectra which were produced using an interaction cross section of 1 pb. There are no free parameters in $R^{i,j}_{\mathrm{Sig_W}}(\beta)$ besides the efficiency pull parameters. The cross section scaling parameter σ is initially free to obtain the best fit spin independent cross section $\sigma_{SI}^{\mathrm{BestFit}}$ and then iterated through fixed σ values to obtain a χ^2 cross section scan.

The cross section scan is performed in the same way as the previous analysis [49,50] with the same values. σ is set to 0 and is increased iteratively by $\delta\sigma \times \mathrm{M^N}$ where $\delta\sigma = \frac{\mathrm{Max}(|R_{\mathrm{Residual}}|)}{2\times \mathrm{F}\times 10^7}$ and N is a step parameter: if $\chi^2 - \chi^2_{\mathrm{prev}} < 1$ then N= floor$(\chi^2 - \chi^2_{\mathrm{min}})$, if $\chi^2 - \chi^2_{\mathrm{prev}} \geq 1$ then N gets iteratively larger by 1 each time. Max$(|R_{\mathrm{Residual}}|)$ is the absolute maximum event rate from the residual energy spectrum; it is halved (residual to amplitude), scaled by 10^{-7} (XMASS searches for $\sigma_{\mathrm{SI}} \sim 10^{-43}$ cm^2) and further scaled by F to match the ideal cross section for a given WIMP mass. M and F both scale the step size in the cross section scan; if the step size is too large then the extracted 90% confidence level upper limit will not be accurate and if the step size is too small the then the computation time is needlessly inflated. M and F vary with WIMP mass and the same values are used as in the previous analysis [49, 50] for WIMP masses ≤ 20 GeV. For WIMP masses > 20 GeV a new value was obtained for F by trial and error. The values for M are 1.5, 1.7, 1.5 and 1.2 for 4-7 GeV, 8-10 GeV, 12-14 GeV and 16-100 GeV respectively. The values for F are 40, 120, 250, 600 and 2000 for 4-7 GeV, 8-10 GeV, 12-14 GeV 16-20 GeV and 30-100 GeV respectively.

The cross section scan continues calculating the χ^2 values until $\chi^2 - \chi^2_{\mathrm{min}} > 32$. The calculations stop at this value because the probability $e^{\frac{\chi^2_{\mathrm{min}} - \chi^2}{2}}$ becomes vanishingly small. The 90% confidence level upper limit for the spin independent cross section $\sigma_{SI}^{90\%}$ is obtained by converting the χ^2 values into probabilities, integrating the probability distribution into a CDF and finding the cross section value that equates to

90%:

$$\frac{\int_0^{\sigma_{SI}^{90\%}} e^{\frac{\chi^2_{\min}-\chi^2}{2}}}{\int_0^{\infty} e^{\frac{\chi^2_{\min}-\chi^2}{2}}} = 0.9. \tag{8.6}$$

For both the complete dataset likelihood cut and stable LY dataset PDF cut analyses, $\sigma_{SI}^{\text{BestFit}}$ and $\sigma_{SI}^{90\%}$ are obtained for each evaluated WIMP mass, using the recorded data and the 1000 dummy samples to obtain 1σ and 2σ sensitivity bands.

Figure 8.9 displays the stable LY dataset PDF cut analysis' 1000 dummy samples' σ_{SI} calculations for WIMP masses: 4 GeV, 10 GeV, 40 GeV and 100 GeV. The left hand plots demonstrate the relation between each sample's $\sigma_{SI}^{\text{BestFit}}$ and resulting $\sigma_{SI}^{90\%}$. The right hand plots show the $\sigma_{SI}^{90\%}$ CDF for all 1000 dummy samples, the central value and the $\pm1\sigma$ and $\pm2\sigma$ bands are the blue, red and green lines respectively.

A $\sigma_{SI}^{90\%}$ result that is consistent with the null hypothesis has its $\sigma_{SI}^{\text{BestFit}}$ located close to 0 with the $\chi_0^2 - \chi^2_{\min} \sim \mathcal{O}(1)$, therefore equation 8.6 integrates far past the minimum position when calculating the resulting limit $\sigma_{SI}^{90\%}$. As equation 8.6 states, $\sigma_{SI}^{90\%}$ is calculated by integrating from $\sigma_{SI} = 0$ so no negative σ_{SI} χ^2 values are taken into account. Therefore for positive $\sigma_{SI}^{\text{BestFit}}$ values, $\sigma_{SI}^{90\%}$ is calculated by integrating from 0 through the minimum and up the χ^2 curve. Whereas for negative $\sigma_{SI}^{\text{BestFit}}$ values, $\sigma_{SI}^{90\%}$ is calculated by integrating from 0 simply up the χ^2 curve as the minimum is not located within the integral window. Consequently, the more negative a $\sigma_{SI}^{\text{BestFit}}$ value is, the smaller the resulting $\sigma_{SI}^{90\%}$ is. If the 1000 dummy samples have similarly shaped χ^2 curves but with varying $\sigma_{SI}^{\text{BestFit}}$ positions one would expect the resultant $\sigma_{SI}^{\text{BestFit}}$ Vs $\sigma_{SI}^{90\%}$ distributions to have two main features. Firstly they will be steep for large positive $\sigma_{SI}^{\text{BestFit}}$ values, correspondingly shallow at large negative $\sigma_{SI}^{\text{BestFit}}$ values and in the middle for small $\sigma_{SI}^{\text{BestFit}}$ values, due to the minimum position in relation to 0 as discussed above. And secondly the distribution should be thin with no extreme kinks, similarly shaped χ^2 curves with predictable results where $\sigma_{SI}^{\text{BestFit}}$ can virtually predict $\sigma_{SI}^{90\%}$. These features are displayed in Figure 8.9 which means the fitting procedure works similarly well on all the dummy datasets with no apparent mishaps.

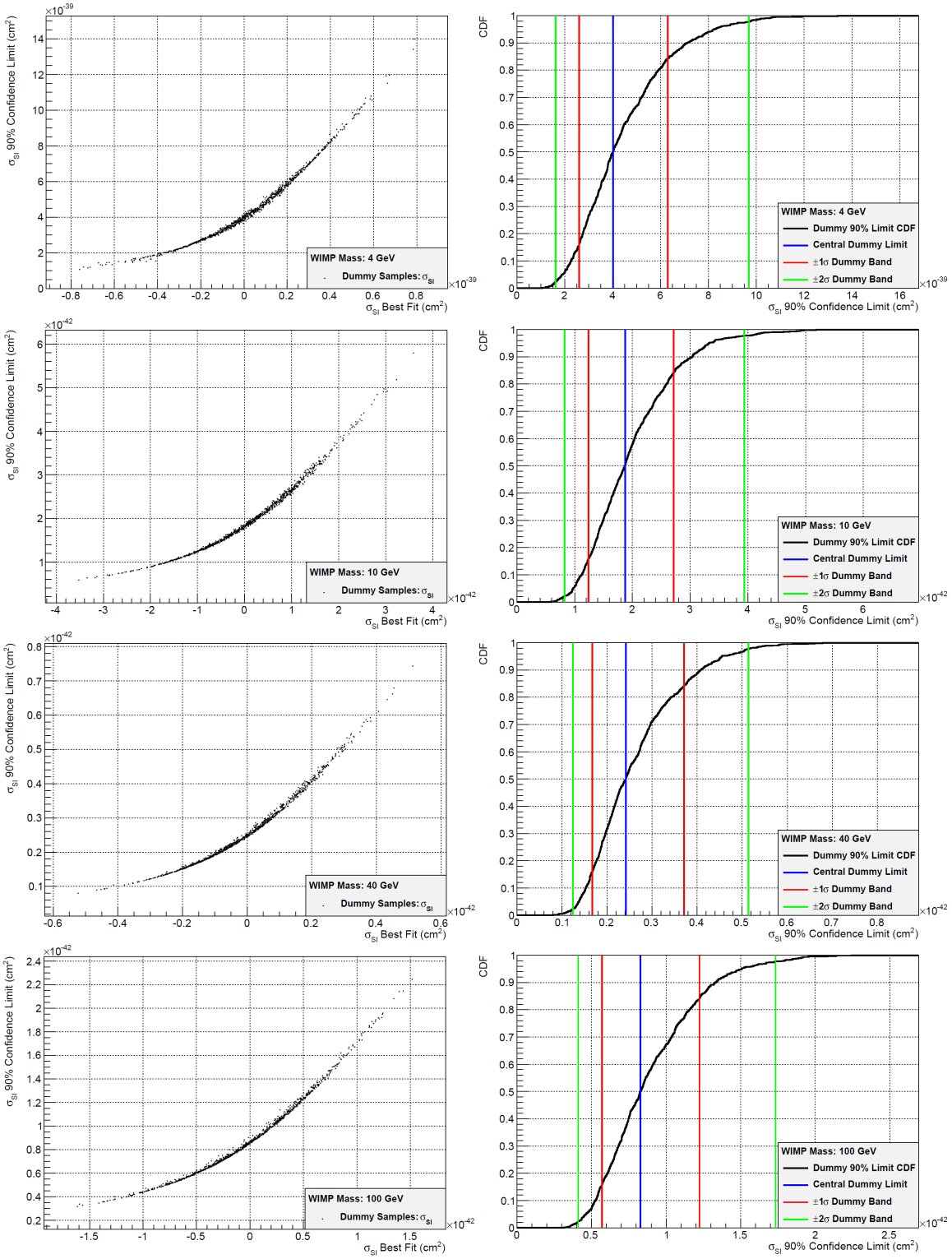


Figure 8.9: 1000 dummy samples σ_{SI} calculations for WIMP masses of 4 GeV, 10 GeV, 40 GeV and 100 GeV. Left: $\sigma_{SI}^{\text{BestFit}}$ Vs $\sigma_{SI}^{90\%}$. Right: $\sigma_{SI}^{90\%}$ CDF with the central value and the $\pm1\sigma$ and $\pm2\sigma$ bands represented by blue, red and green lines respectively. The thin distribution and lack of steps highlights the purely random statistical nature of the dummy datasets and they all perform with similar characteristics.

Chapter 9

Modulation Analyses Results

The results for both the MI and WIMP searches are presented in turn in each of the following sections, one for each analysis. The MI results are presented first as these amplitudes indicate the shape of the resultant 90% confidence level upper limit for the WIMP nucleon spin independent cross section $\sigma_{SI}^{90\%}$ by comparing the measured positive and negative amplitudes with the shape and positioning of the distinct WIMP mass energy spectra. Section 9.1 reports on the previous XMASS modulation analysis results [49, 50] as they represent the baseline for relative improvements, this analysis utilised XMASS data recorded up until June 2017 and applied the likelihood cut. Section 9.2 reports on the complete dataset likelihood cut analysis, this is predominantly an extension of the previous analysis with the same cuts applied and a 50% increase in the dataset. Therefore the amplitudes measured should have smaller error bars and should be statistically compatible with those reported in section 9.1; which they are. The limits set should improve for the entire WIMP mass range however statistical variation of said amplitude have reduced the overall improvement. Section 9.3 presents the stable LY PDF cut analysis results, this analysis implemented some newly developed cuts, restricted the dataset to periods of stable LY and accounted for said LY variation without utilising uncertain BG MC relative efficiency curves. As the cuts applied in this updated analysis result in larger observed event rates, the measured amplitudes and their corresponding error bars will also increase. This effect is exacerbated in the 2^{nd} and 3^{rd} energy bins as these are now considered low

threshold energies with a much reduced dataset. The limits set should improve at high WIMP mass and also at low WIMP mass as depicted in figure 7.6, however the improvements for low mass WIMPs is hindered by the reduction in dataset in the 2nd and 3rd energy bins. The 3 analyses' data $\sigma_{SI}^{90\%}$ results are compared in section 9.4. As stated previously WIMP masses > 20 GeV are only tested for the PDF cut based analysis. The results of a variable phase modulation analysis is reported in section 9.5, no dominant phases are apparent and all amplitudes are consistent with 0.

For each analysis presented below, the MI annual modulation best fit amplitudes of the XMASS data with their respective uncertainties are displayed in black, along with the 1000 dummy samples' $\pm1\sigma$ and $\pm2\sigma$ sensitivity bands in blue and light blue respectively. The DAMA/LIBRA experiment claims to observe an annual modulation in their event rate with a 12.9σ confidence level that is consistent with a DM induced annual modulation signal expected from the Earth's motion around the Sun as the Sun traverses the DM halo [43–45]. Interpreting this modulation signal as resulting from nuclear recoil interactions is ruled out by many DM experiments as is evident in figure 1.15. If the signal is interpreted as a result of electron recoil interactions there are still some DM models that could induce the observed signal in DAMA/LIBRA while not undermining the limits set by many other DM experiments [104]. However, the DM models compatible are rather limited and in addition the ANIAS experiment - designed using the same target material as that used by DAMA/LIBRA - refutes the positive results reported by DAMA/LIBRA, no modulation signal was found and the results are incompatible with those reported by DAMA/LIBRA at 3.3 σ [47]. All of the XMASS data MI amplitudes presented in this chapter are scaled by their respective electron recoil signal efficiency and are also inconsistent with the annually modulated event rates measured by DAMA/LIBRA [45]. If the observed annual modulation of the event rate is caused by DM that doesn't specifically interact strongly with NaI crystals and not Xe, then an observed event rate amplitude by DAMA/LIBRA should also be observed by XMASS. Amplitudes are compared directly in each 0.5 keV$_{ee}$ energy bin, this is reasonable since both experiments are

calibrated with X-ray and γ-ray sources at low energies [105].

All of the $\sigma_{SI}^{90\%}$ limits presented in this chapter use a black line for the data and green and yellow bands for the $\pm1\sigma$ and $\pm2\sigma$ expected sensitivity bands respectively. If no amplitudes were observed in the data, the data's $\sigma_{SI}^{90\%}$ limit would follow the expected sensitivity distribution's central line; however statistical deviations in the data are expected and the resulting non-zero amplitudes affect the shape of the data's $\sigma_{SI}^{90\%}$ limit as a function of WIMP mass. The residual event rate energy spectra displayed in figure 7.5 indicate the important energy bins for each WIMP mass.

The lowest WIMP masses ($\leq$ 7 GeV) are predominantly confined to the lowest energy bin and hence $\sigma_{SI}^{90\%}$ is largely driven by the amplitude measured in this bin alone, a positive amplitude in the lowest energy bin would incur a $\sigma_{SI}^{90\%}$ larger than the expected sensitivity for the lowest WIMP masses. For mid-range WIMP masses (8-20 GeV) the spectra peak at slightly higher energies, ~1 to 1.5 keV$_{ee}$ and the peaks get progressively wider. These surrounding energy bins are important and amplitudes of the same sign can work constructively in increasing or reducing $\sigma_{SI}^{90\%}$, while amplitudes of opposing sign will work destructively in drawing $\sigma_{SI}^{90\%}$ closer to the expected sensitivity. For the higher WIMP masses above 20 GeV the residual event rate flips sign in the lowest energy bins, inducing a negative event rate peak at low energy (1 keV$_{ee}$) and a positive event rate peak at higher energies (~2-3 keV$_{ee}$).

9.1 MI and $\sigma_{SI}^{90\%}$ results for the previous XMASS modulation analysis

Figures 9.1 and 9.2 display the MI and $\sigma_{SI}^{90\%}$ results respectively, obtained previously by utilising XMASS data recorded up until June 2017 and applying the likelihood cut. Negative amplitudes of $\sim -1\sigma$ are observed in the lowest 3 energy bins (0.5-2.0 keV$_{ee}$), these interfere constructively to reduce $\sigma_{SI}^{90\%}$ below the expected sensitivity for the low-mid WIMP masses. The following 3 energy bins are slightly positive and bring $\sigma_{SI}^{90\%}$ closer to the expected sensitivity for WIMP masses of 20 GeV.

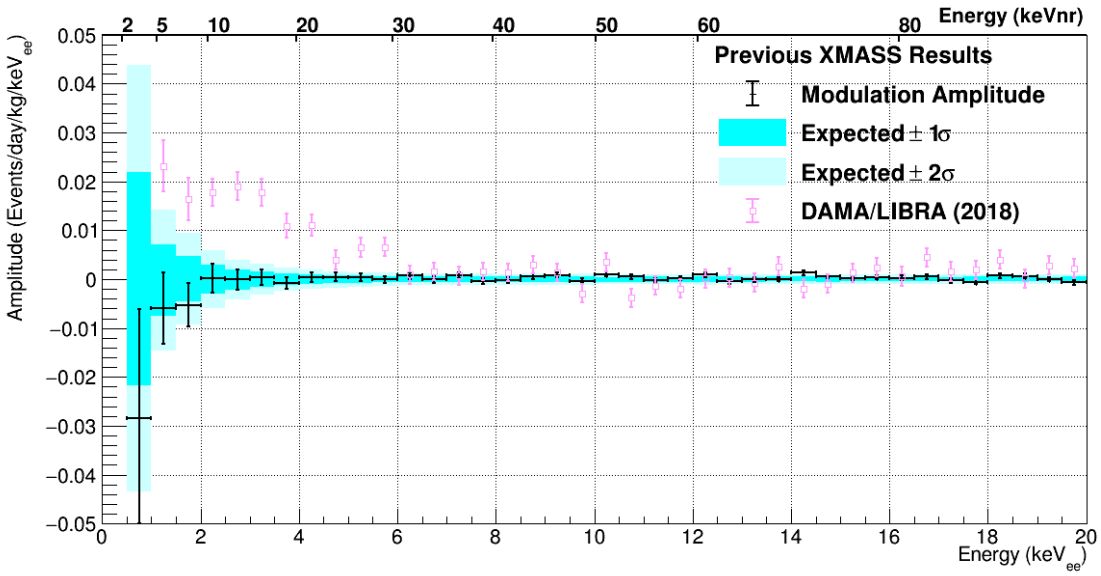


Figure 9.1: Previous XMASS modulation analysis MI amplitude results. Data in black. Expected $\pm 1\sigma$ and $\pm 2\sigma$ sensitivity bands in blue and light blue respectively. DAMA/LIBRA observed modulation amplitudes from [45] in pink. All amplitudes are consistent with 0 within 2σ and do not agree with those observed by DAMA/LIBRA.

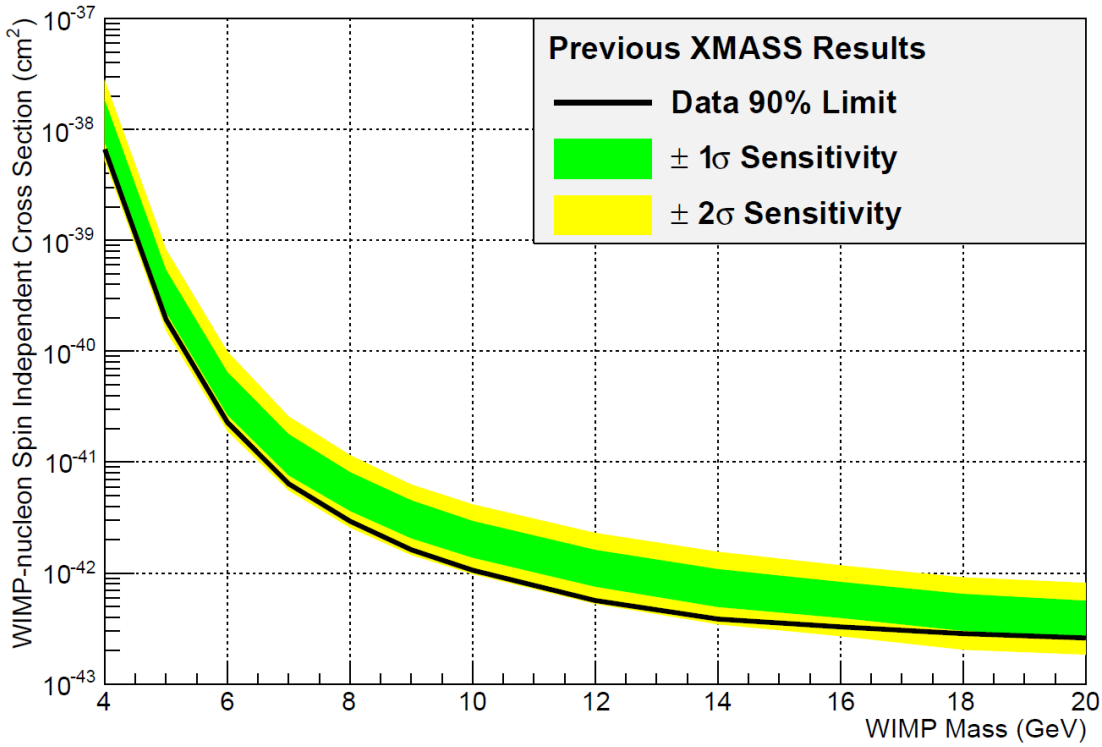


Figure 9.2: Previous XMASS modulation analysis WIMP 90% confidence level results. Data in black. Expected $\pm 1\sigma$ and $\pm 2\sigma$ sensitivity bands in Green and yellow respectively. The limit mostly lies along -1σ due to the observed negative amplitudes.

9.2 MI and $\sigma_{SI}^{90\%}$ results for the complete dataset likelihood cut modulation analysis

Figures 9.3 and 9.4 display the MI and $\sigma_{SI}^{90\%}$ results respectively, obtained by utilising the complete dataset and applying the likelihood cut. The relative livetime increase in low threshold data (276.7 days → 761.96 days) is much larger than in normal threshold data (1045.0 days → 1549.32 days), this reduces the error bar and dummy sensitivity band size in the lowest energy bin. Therefore the expected $\sigma_{SI}^{90\%}$ sensitivity should improve (reduce) more for low-mass WIMPs than for mid-mass WIMPs.

The negative amplitudes present in the lowest 3 energy bins (0.5-2.0 keV_{ee}) are less extreme than observed previously with the increase in the available dataset, hence the data's $\sigma_{SI}^{90\%}$ limit is closer to the expected sensitivity. Additionally the following 3 energy bins register positive amplitudes of ~ $+1\sigma$. These work destructively against the lowest 3 energy bins for the mid-mass WIMPs near 20 GeV. In fact the $\sigma_{SI}^{90\%}$ limit for the data increases above the expected sensitivity and results in a weaker limit than the previous analysis [49, 50].

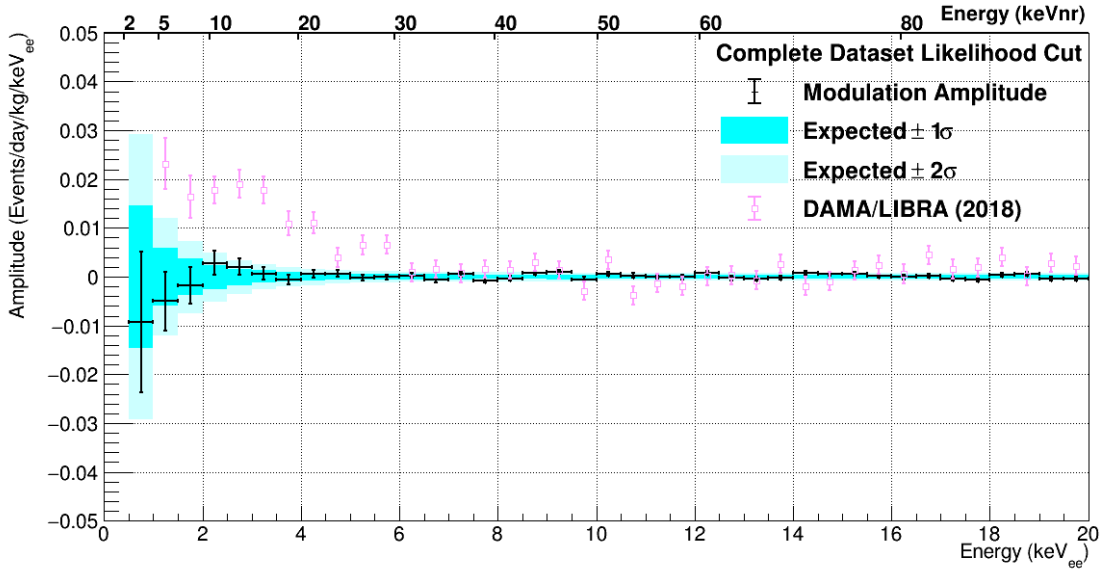


Figure 9.3: Complete dataset likelihood cut modulation analysis MI amplitude results. Data in black. Expected $\pm 1\sigma$ and $\pm 2\sigma$ sensitivity bands in blue and light blue respectively. DAMA/LIBRA observed modulation amplitudes from [45] in pink. All amplitudes are consistent with 0 within 2σ and do not agree with those observed by DAMA/LIBRA.

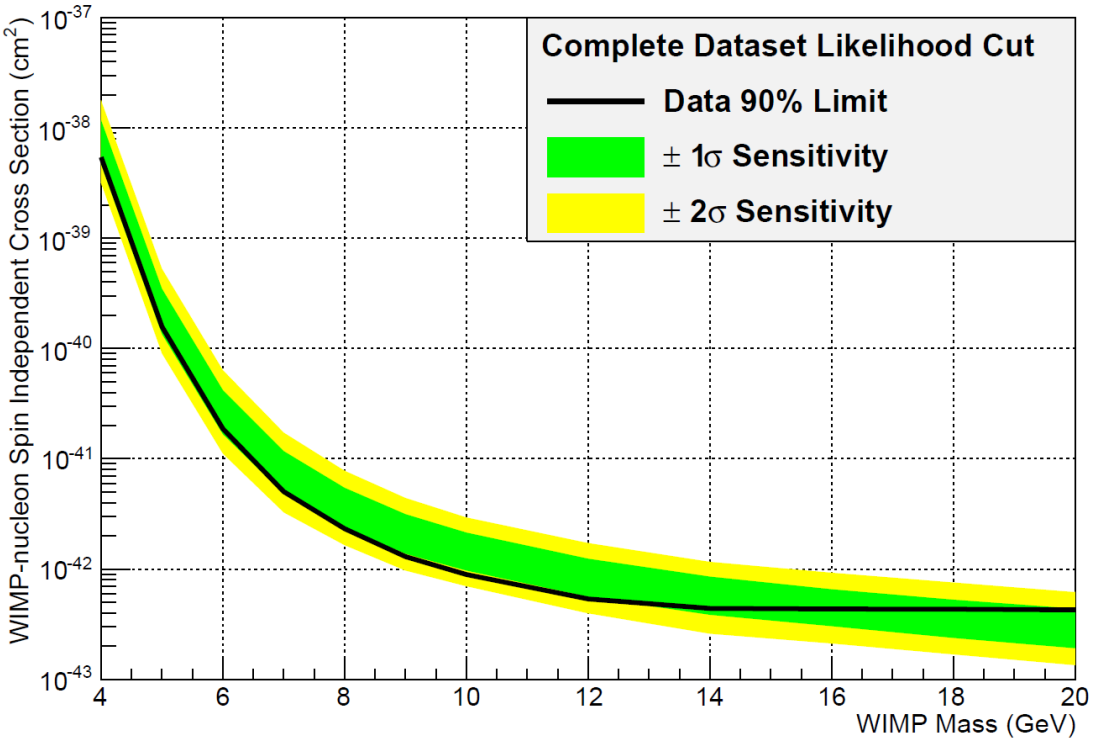


Figure 9.4: Complete dataset likelihood cut modulation analysis WIMP 90% confidence level results. Data in black. Expected $\pm 1\sigma$ and $\pm 2\sigma$ sensitivity bands in Green and yellow respectively. The observed low-energy negative amplitudes and mid-energy positive amplitudes cause the variation in the observed data limit.

Table 9.1 displays the complete dataset likelihood cut modulation analysis fit results for all WIMP masses. All pull terms: α, γ, β_{DC} and $\beta_{\mathrm{L_{Eff}}}$ are $< 1.13\sigma$.

Table 9.1: Complete dataset likelihood cut modulation analysis WIMP fit results. Null signal fit $\chi^2 = 5251.57$ for 4737 n.d.f ($\alpha = 1.11$, $\gamma = -0.36$), WIMP $\sigma_{SI}^{\mathrm{BestFit}}$ has 3 less n.d.f.

Mass (GeV)	$\sigma_{SI}^{90\%}$ (cm^2)	$\sigma_{SI}^{\mathrm{BestFit}}$ (cm^2)	χ^2	α	γ	$\beta_{\mathrm{L_{Eff}}}$	β_{DC}
4	5.4e-39	-1.1e-40	5251.04	1.10	-0.27	0.05	0.003
5	1.6e-40	-1.4e-41	5250.97	1.11	-0.27	0.06	0.005
6	1.9e-41	-4.8e-42	5250.86	1.10	-0.26	0.05	0.006
7	5.0e-42	-2.6e-42	5250.67	1.10	-0.25	0.05	0.010
8	2.3e-42	-1.7e-42	5250.41	1.10	-0.24	0.05	0.013
9	1.3e-42	-1.3e-42	5250.16	1.10	-0.24	0.04	0.011
10	8.9e-43	-9.6e-43	5250.03	1.10	-0.25	0.03	0.008
12	5.4e-43	-5.2e-43	5250.41	1.09	-0.29	-0.03	-0.006
14	4.4e-43	-2.1e-43	5251.21	1.09	-0.34	-0.04	-0.010
16	4.3e-43	-6.4e-49	5251.57	1.11	-0.36	0.00	0.000
18	4.3e-43	1.2e-43	5251.25	1.12	-0.37	0.06	0.012
20	4.3e-43	1.8e-43	5250.56	1.13	-0.38	0.10	0.020

9.3 MI and $\sigma_{SI}^{90\%}$ results for the stable LY dataset PDF cut modulation analysis

Figures 9.5 and 9.6 display the MI and $\sigma_{SI}^{90\%}$ results obtained by utilising the stable LY dataset and applying the newly developed PDF cut. The livetime increase in low threshold data is the same as stated previously however the normal threshold livetime for the stable LY dataset is 1203.72 days, roughly a third of the way between the previously used dataset and the complete dataset. Additionally the second and third energy bins are now limited to only low threshold data and therefore suffer a livetime reduction. This coupled with the fact that the PDF cut was designed to optimise nuclear recoil discrimination at the expense of electron recoil explains the increase in the size of error bars and dummy band expected sensitivities evident in figure 9.5.

Figure 7.6 displays the relative improvement in classification power for each WIMP mass. Improvements in the $\sigma_{SI}^{90\%}$ expected sensitivity are predicted for low-mass and WIMPs with masses > 40 GeV.

Negative amplitudes are observed in the lowest 6 energy bins (0.5-3.5 keV$_{ee}$). However the lowest energy bin is only negative by the tiniest of margins, therefore the low-mass $\sigma_{SI}^{90\%}$ is close to the expected sensitivity and the improvement is less than expected based solely on the relative increase in classification performance. The following 5 energy bins exhibit a larger negative amplitude: ~ -0.7σ to -1.8σ. These work constructively for the mid-mass WIMPs reducing $\sigma_{SI}^{90\%}$ so it is very close to the -2σ sensitivity band - maximally distant at 20 GeV. These negative amplitude interfere destructively for the high-mass WIMPs that have both negative and positive residual event rates. The energy at which the residual event rate sign flips increases with WIMP mass, therefore $\sigma_{SI}^{90\%}$ progressively gets closer to the expected sensitivity.

Table 9.2 displays the stable LY dataset PDF cut modulation analysis fit results for all WIMP masses. Both WIMP pull terms: β_{DC} and $\beta_{\mathrm{L_{Eff}}}$ are < 0.17σ.

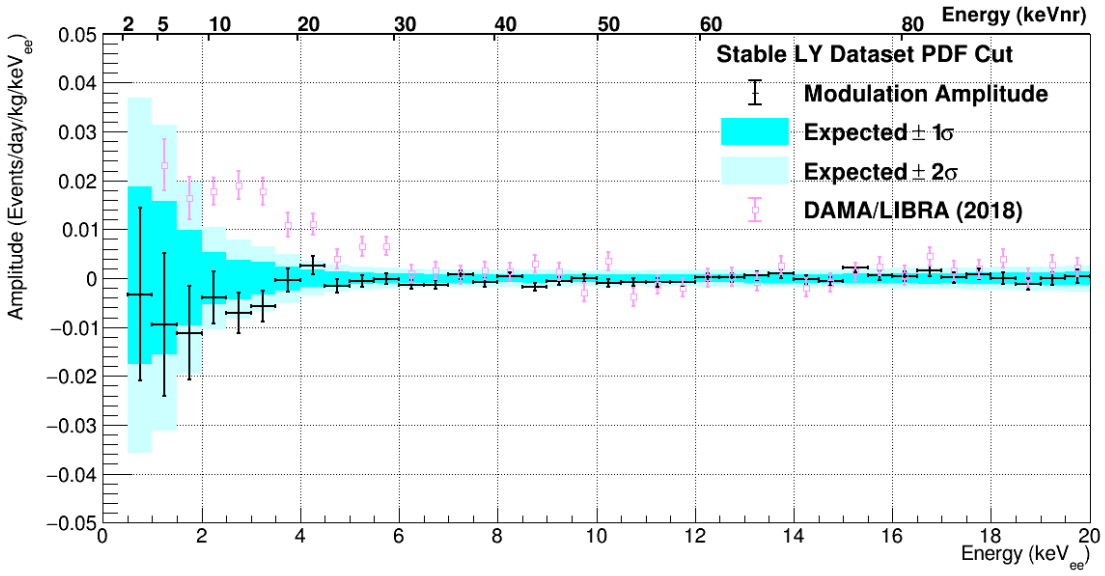


Figure 9.5: Stable LY dataset PDF cut modulation analysis MI amplitude results. Data in black. Expected $\pm 1\sigma$ and $\pm 2\sigma$ sensitivity bands in blue and light blue respectively. DAMA/LIBRA observed modulation amplitudes from [45] in pink. All amplitudes are consistent with 0 within 2σ and do not agree with those observed by DAMA/LIBRA.

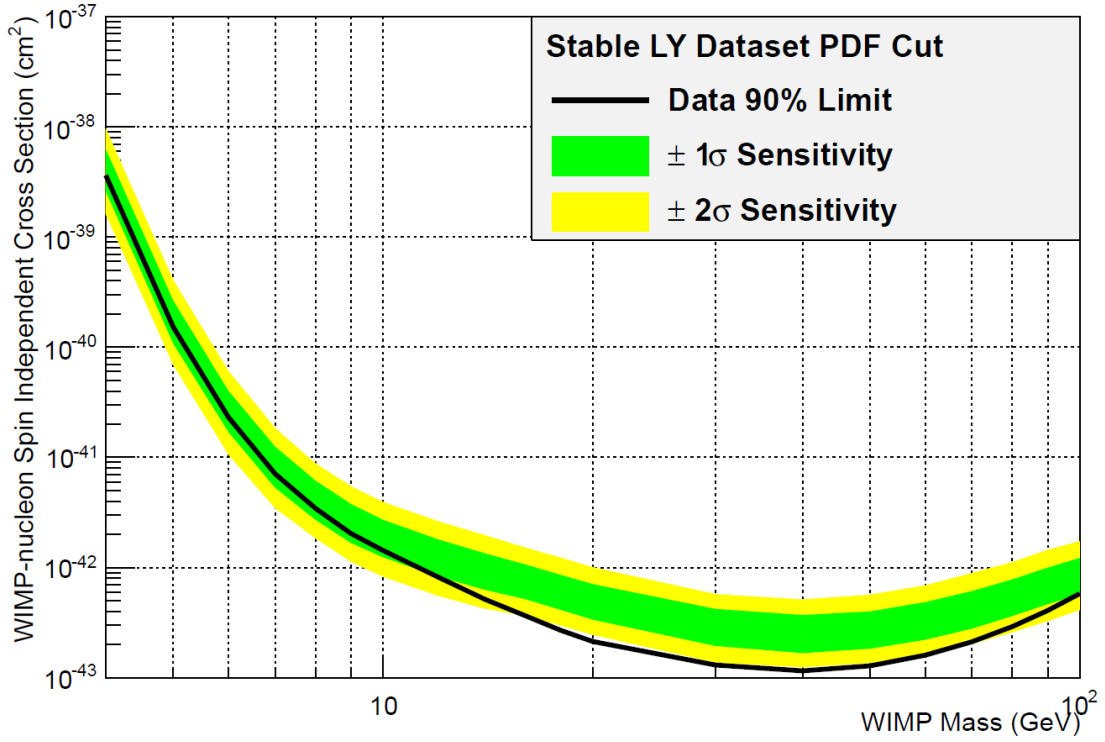


Figure 9.6: Stable LY dataset PDF cut modulation analysis WIMP 90% confidence level results. Data in black. Expected $\pm 1\sigma$ and $\pm 2\sigma$ sensitivity bands in Green and yellow respectively. The observed low-energy negative amplitudes cause the $0\sigma \rightarrow -1\sigma \rightarrow -2\sigma \rightarrow -1\sigma$ observed data limit for the different mass WIMPs.

Table 9.2: Stable LY dataset PDF cut modulation analysis WIMP fit results. Null signal fit χ^2 = 3540.11 for 3540 n.d.f, WIMP $\sigma_{SI}^{\mathrm{BestFit}}$ has 3 less n.d.f.

Mass (GeV)	$\sigma_{SI}^{90\%}$ (cm^2)	$\sigma_{SI}^{\mathrm{BestFit}}$ (cm^2)	χ^2	$\beta_{\mathrm{L_{Eff}}}$	β_{DC}
4	3.6e-39	-5.1e-41	3540.06	-0.00	-0.000
5	1.5e-40	-5.2e-42	3540.06	-0.01	0.000
6	2.3e-41	-1.7e-42	3540.04	-0.00	-0.000
7	7.1e-42	-9.5e-43	3540.01	-0.00	-0.000
8	3.4e-42	-7.2e-43	3539.96	-0.00	-0.000
9	2.0e-42	-6.5e-43	3539.86	-0.02	0.001
10	1.4e-42	-6.6e-43	3539.69	-0.03	0.003
12	8.2e-43	-7.6e-43	3538.97	-0.07	0.010
14	5.1e-43	-8.8e-43	3537.54	-0.16	0.024
16	3.7e-43	-9.1e-43	3535.82	-0.17	0.033
18	2.7e-43	-8.3e-43	3534.61	-0.11	0.024
20	2.1e-43	-7.3e-43	3534.06	-0.04	0.008
30	1.3e-43	-3.9e-43	3534.96	0.13	-0.020
40	1.2e-43	-3.2e-43	3535.49	0.05	-0.004
50	1.3e-43	-3.5e-43	3535.66	0.03	0.006
60	1.6e-43	-4.1e-43	3535.92	-0.02	0.017
70	2.1e-43	-4.9e-43	3536.38	-0.03	0.028
80	2.9e-43	-5.6e-43	3537.13	0.01	0.041
90	4.1e-43	-6.0e-43	3538.04	0.10	0.047
100	5.8e-43	-5.6e-43	3538.97	0.12	0.046

9.4 $\sigma_{SI}^{90\%}$ results comparison

The $\sigma_{SI}^{90\%}$ data limits for all 3 analyses are displayed in the top plot of figure 9.7, the previous XMASS modulation analysis [49, 50], the complete dataset likelihood cut analysis and the stable LY PDF cut analysis are represented by red, black and blue lines respectively. The smaller $\sigma_{SI}^{90\%}$ is, the better the limit. The relative improvement in the $\sigma_{SI}^{90\%}$ data limits is demonstrated in the bottom plot of the same figure, < 1 signifies an improvement. The complete dataset likelihood cut analysis is directly compared with the previous XMASS modulation analysis and the stable LY PDF cut analysis is directly compared with the complete dataset likelihood cut analysis, these are represented by red and blue lines respectively. These comparisons demonstrate the impact on $\sigma_{SI}^{90\%}$, firstly from the increase in statistics (utilising the

complete dataset) and secondly from the variation in classification technique and χ^2 minimisation procedure - fitting the LY rather than utilising MC generated BG LY relative efficiency curves.

There is a relative improvement in $\sigma_{SI}^{90\%}$ due to increased statistics (red line) for the low-mass WIMPs ($\leq$ 12 GeV). This is because the lowest energy bin sees the largest relative increase in statistics. This improvement is less than that expected statistically due to the larger negative amplitudes observed in the previous modulation analysis. The $\sigma_{SI}^{90\%}$ data limit is worse than previously obtained for the mid-mass WIMPs ($>$ 12 GeV) because of the positive amplitudes measured at slightly higher energies (2.0-3.5 keV_{ee}), these displayed close to no amplitude in the previous XMASS modulation analysis.

There is a relative improvement in $\sigma_{SI}^{90\%}$ due to the variation in classification technique and χ^2 minimisation procedure (blue line) for the low-mass and high-mass WIMPs. Improvements were expected for WIMPs with masses $<$ 10 GeV and $>$ 40 GeV. The improvements for low-mass WIMPs were smaller than expected due to the minute amplitude measured in the lowest energy bin. Therefore $\sigma_{SI}^{90\%}$ only improved for WIMPs with masses $\leq$ 5 GeV. The improvements for high-mass WIMPs were larger than expected due to the 6 lowest energy bins all displaying negative amplitudes. This reduced the point at which $\sigma_{SI}^{90\%}$ improved to WIMPs with masses $\geq$ 15 GeV. These consecutive negative amplitude energy bins begin to work destructively for the highest WIMP masses, bringing $\sigma_{SI}^{90\%}$ closer to the expected sensitivity as WIMP mass increases.

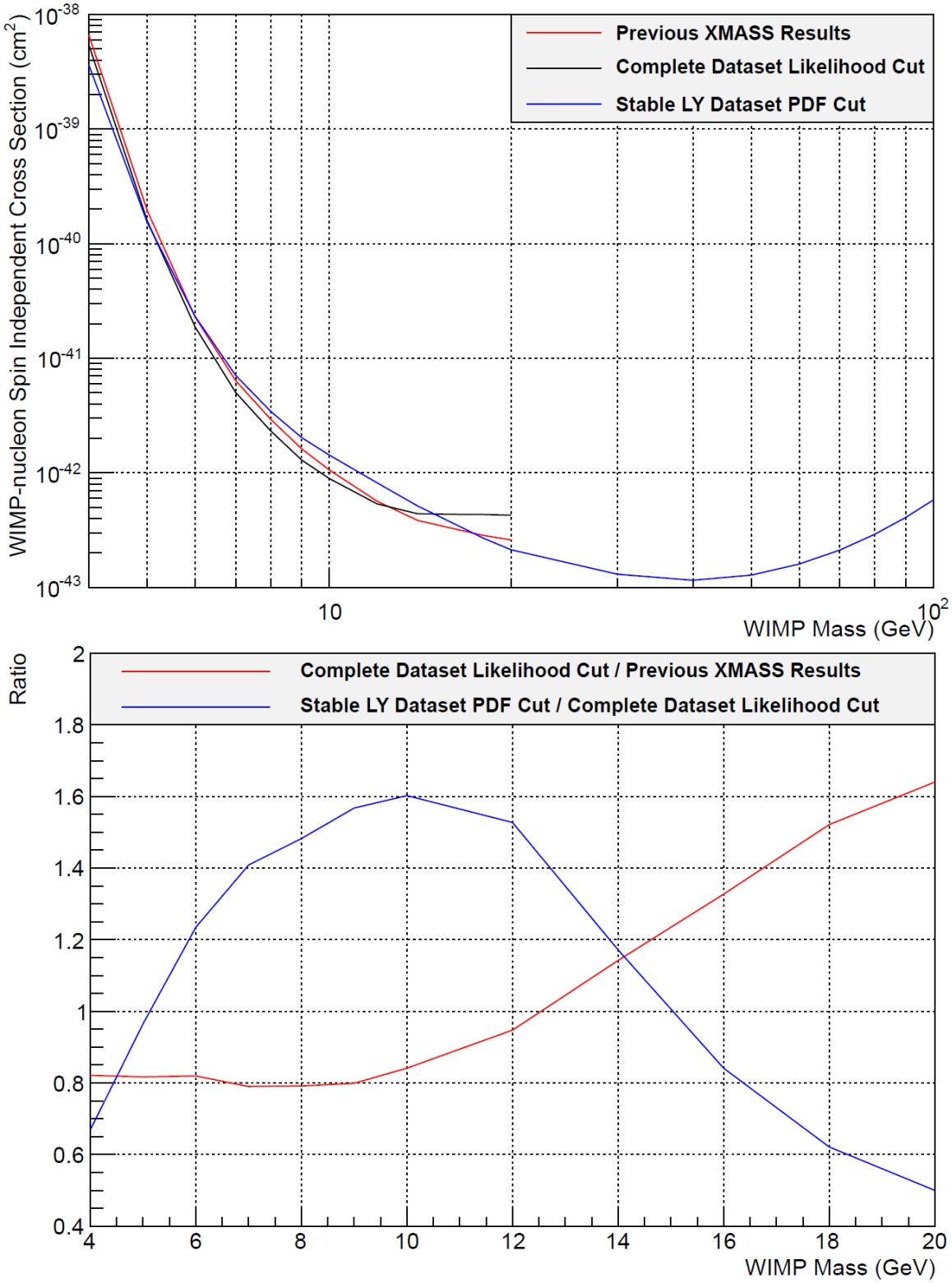


Figure 9.7: $\sigma_{SI}^{90\%}$ data limits comparison. The top plot displays all analyses alongside one another. The bottom plot directly compares the previous XMASS modulation analysis and the stable LY dataset PDF cut analysis against the complete dataset likelihood cut analysis, < 1 represents an improvement. The stable LY dataset PDF cut analysis improves for masses ≤ 5 GeV and ≥ 15 GeV.

9.5 MI variable phase analysis checks

As discussed in section 8.4 an additional MI search was performed for the stable LY dataset PDF cut analysis where the phase and amplitude were varied for each energy bin (i) separately over a gird, the phase (t_0) was varied between 0 and one year (T_{Year}), and the amplitude (A^i_{MI}) from −2% to +2% of each energy bin's BG constant (C^i_{BG}). This was performed to check that no yearly modulation signal was present within the data at a specific phase consistent across energy bins but different from the one predicted by the Earths motion around the Sun within the DM halo. If a modulation signal was present then the analyses outlined in sections 9.2 and 9.3 may not have observed it. If the best fit phase diverged from that predicted, the observable amplitudes would be reduced or removed entirely.

Figures 9.8 and 9.9 display the phase Vs amplitude χ^2 probability $e^{\frac{\chi^2_{\mathrm{min}}-\chi^2}{2}}$ grid for energy bins 0.5 – 4.5 keV$_{ee}$ and 4.5 – 8.5 keV$_{ee}$ respectively. A double peaked distribution is expected and is observed for each energy bin. The two peaks are separated by $\frac{1}{2} \cdot T_{\mathrm{Year}}$ and the amplitudes are of the same magnitude but of opposite sign as expected.

The double peaked maxima are clearly connected for each individual energy bin, none of the observed amplitudes are large enough to fully separate the observed peaks. All of the energy bin distributions are consistent with 0 amplitude within or close to a 90% confidence limit - the probability is rarely < 0.2 at 0 amplitude halfway between the two best fit phase positions. Additionally the best fit phases vary randomly across energy, there is no unanimous best fit phase. Therefore we conclude again that no globally significant modulation signal is observed within the XMASS data.

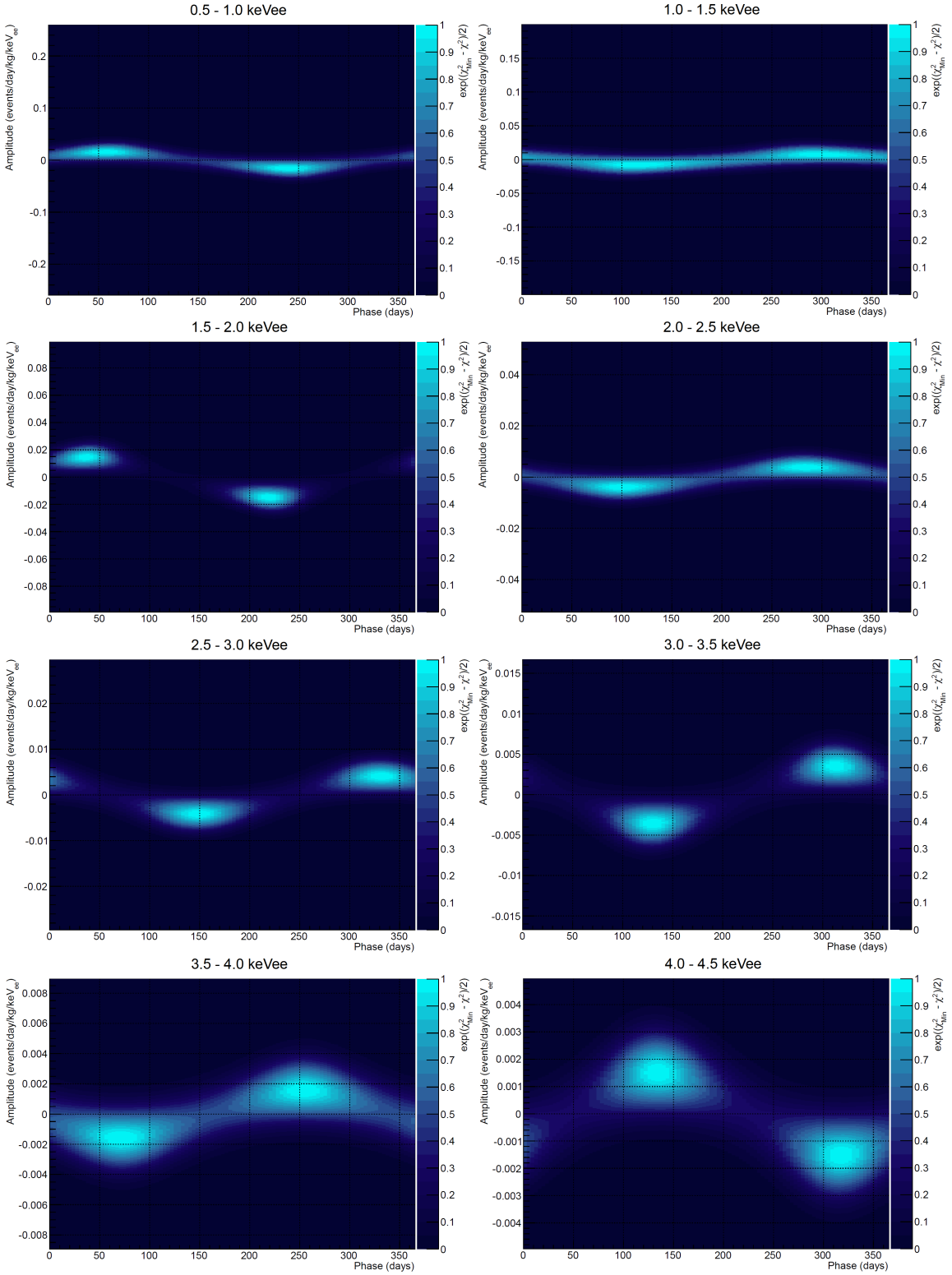


Figure 9.8: Phase Vs amplitude χ^2 probability $e^{\frac{\chi^2_{\text{min}}-\chi^2}{2}}$ grid for the 8 lowest energy bins energy bins $0.5-4.5$ keV$_{ee}$. Double peaked maxima with amplitudes of the same magnitude but of opposite sign separated by $\frac{1}{2}\cdot T_{\text{Year}}$ for all energy bins. No unanimous best fit phase. All amplitudes consistent with 0.

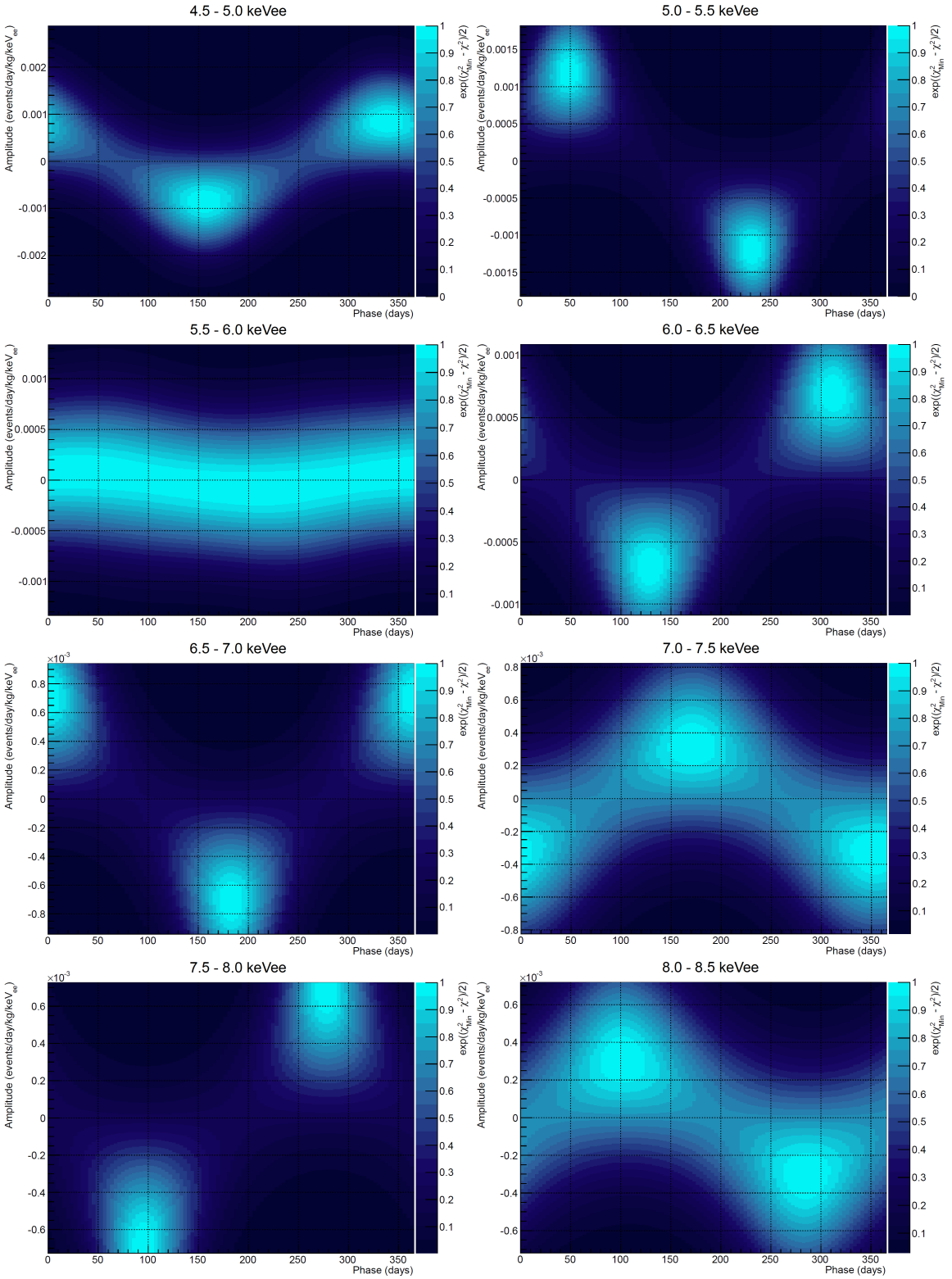


Figure 9.9: Phase Vs amplitude χ^2 probability $e^{\frac{\chi^2_{\text{min}}-\chi^2}{2}}$ grid for 8 energy bins energy bins 4.5 – 8.5 keV$_{ee}$. Double peaked maxima with amplitudes of the same magnitude but of opposite sign separated by $\frac{1}{2} \cdot T_{\text{Year}}$ for all energy bins. No unanimous best fit phase. All amplitudes consistent with 0.

Chapter 10

Conclusion

10.1 Summary of the WIMP search results

Two analyses are presented in this thesis. The first, the complete dataset likelihood cut analysis is an extension of the previously conducted modulation analysis performed by the XMASS collaboration - utilising the complete dataset. The second, the stable LY dataset PDF cut analysis pioneers a new PDF based classification technique that integrates timing, the analysis additionally incorporates LY effects directly into the χ^2 minimisation procedure, which becomes possible if the first 400 days of available data - during which the LXe as well as the newly refurbished detector were still settling into the state of stable operation that this analysis exploits - are discarded. The compromises that are necessitated by including the early data - with its at times abrupt LY changes and the detector's still evolving mix of dissolved impurities that affect it - would outweigh the gain from the additional but lower quality statistics.

The PDF classification technique is the first within XMASS to utilise individual hit timing information rather than just aggregate timing statistics for each event. This boosts performance for nuclear recoil events at high energy where the BG is best understood and at low energy where information is sparse - the new approach systematically incorporates hit timing information.

Removing the data recorded under low LY conditions and the initial few months where LY efficiencies are poorly understood allows for a new approach to χ^2 min-

imisation that doesn't rely on MC generated BG LY relative efficiency curves - an approach beset with systematic uncertainties while averaging over energy bins. The new approach instead uses a linear LY relative efficiency gradient is built into the χ^2 minimisation for each individual energy bin, fitting the data directly.

The 90% confidence level upper limit for the WIMP nucleon spin independent cross section $\sigma_{SI}^{90\%}$ for both analyses were compared against one another in figure 9.6 at the end of the previous chapter, the complete dataset likelihood cut analysis chosen as a benchmark for the newly developed stable LY dataset PDF cut analysis. The $\sigma_{SI}^{90\%}$ limits for the two analyses at different WIMP masses are listed in tables 9.1 and 9.2. The $\sigma_{SI}^{90\%}$ limits are improved by the new approach for WIMPs with masses ≤ 5 GeV and ≥ 15 GeV, there is only a small central window where the complete dataset likelihood cut analysis yields more competitive limits. Extrapolating the smooth sensitivity curves would suggest that this advantage would remain dominant $\ll 5$ GeV and $\gg 15$ GeV. Although comparisons above 20GeV have not been directly tested, by 20GeV the $\sigma_{SI}^{90\%}$ limits are already improved by a factor 2, with the trajectory indicating that this improvement would only increase. The minimal $\sigma_{SI}^{90\%}$ limit set by the new stable LY PDF cut modulation analysis is 1.2×10^{-43} cm^2 occurring at 40 GeV.

As noted in the previous chapter the MI amplitudes measured in the previous modulation analysis [49,50] and the complete dataset likelihood cut analysis are very similar with one another, well within error bars - they apply the same cuts and there is only a 50% increase in the dataset so this is to be expected. The majority of the MI amplitudes measured in the stable LY PDF cut modulation analysis are compatible with those of the complete dataset likelihood cut analysis within error bars. The only noticeable exception are the amplitudes measured within the 2.5-3.5 keV$_{ee}$ energy bins as one can see by comparing figures 9.3 and 9.5. Some differences are to be expected considering that the two analyses apply very different cuts. The event rate energy spectra observed by XMASS over the entirety of data taking is displayed in figure 6.26. The observed event rate is increased by an order of magnitude in the

2.5-3.5 keV$_{ee}$ energy bins when applying the PDF cut compared to the likelihood cut. This statistically large increase in the event rate allows for the observed amplitudes to vary significantly - even flip sign - and still not contradict one another.

Figure 10.1 plots the data's $\sigma_{SI}^{90\%}$ limits for the complete dataset likelihood cut analysis (solid black line) and the stable LY dataset PDF cut analysis (dashed black line) alongside multiple other experiments' limits: XMASS fiducial volume 2018 [51], DAMA NaI 2017 [43–45], CDMS-Si 2013 [52], SuperCDMS 2014 [53], CDMS-Lite 2018 [54], CREST-II 2016 [55], DarkSide 50 2018 [56, 57], PandaX-II 2021 [60], LUX 2017 [61], Xenon1T 2018 [62]. Coherent neutrino scattering (dashed orange line) is a neutrino background that results in a neutrino floor (blocked out yellow) that will hamper direct detection WIMP SI searches.

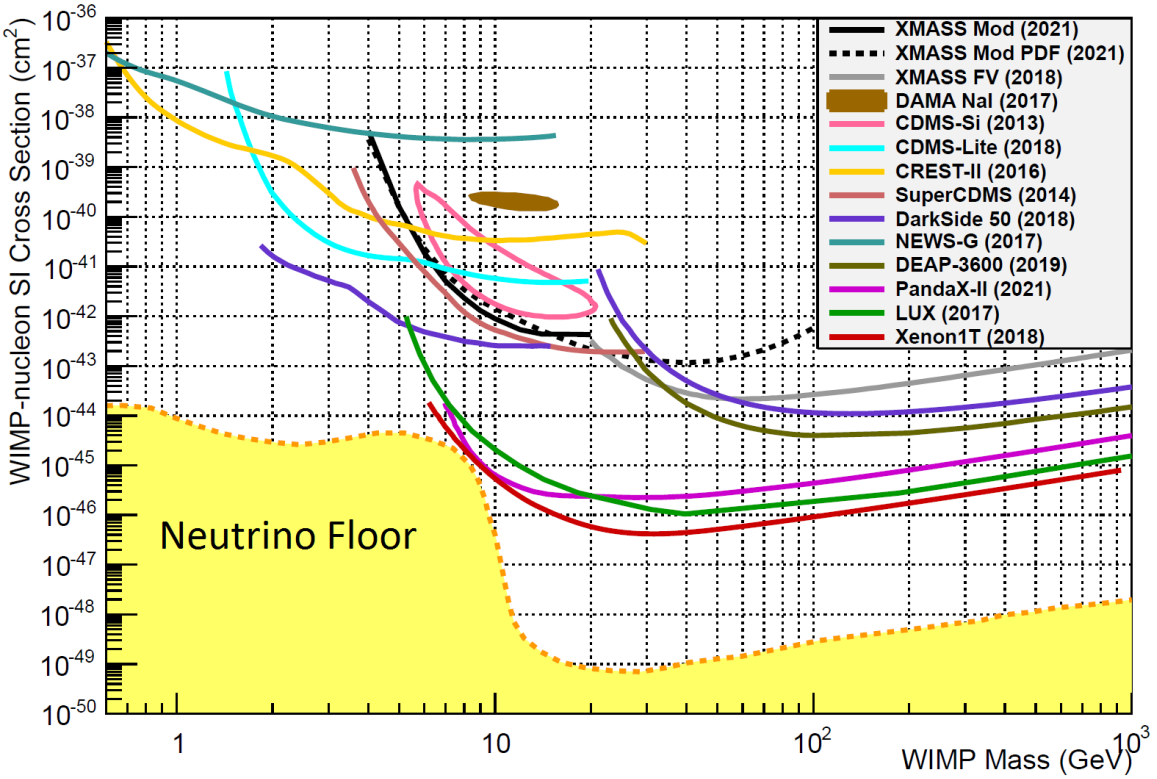


Figure 10.1: WIMP-nucleon SI cross section 90% limits obtained by the two analyses presented in thesis compared to those obtained by multiple other experiments. The Ge and Si semiconductor detectors cover the low WIMP mass region while the noble liquid detectors cover the high WIMP mass region. The largest experiments are getting ever closer to the neutrino floor.

The main non-modulation DM search result by XMASS - the XMASS fiducial volume (FV) 2018 [51] - is included alongside the modulation results in figure 10.1. This analysis applies the FV cut which reconstructs an event's position and only utilises events within the central 20 cm of the ID, but the performance of this cut is poor at low energy. Additionally, whereas the modulation analyses look for period variations in the event rate, the FV analysis directly compares the observed event rate - measured over the entire dataset - with those predicted by MC simulation. Agreement between MC and data is much better at higher energy with large systematic uncertainties at low energy. This results in the approach being heavily optimised for larger mass WIMPs whose energy spectra extend out to higher energies. This is clearly evident from the position of the FV limit with respect to the limits obtained from the Modulation analyses. Additionally if a DM signal is observed within a FV analysis, a modulation analysis would be performed to confirm that these results were indeed a signal and not simply a poor understanding of the BG.

10.2 Discussion for future analyses

XMASS has stopped recording data and the entire available dataset has been investigated for the two analyses presented in this thesis, therefore larger levels of exposure are not an option. Based on the work presented in this thesis there are two possible avenues to explore in the search for possible improvements. The first of which is a progression of the PDF classification technique, either by tuning the cut position on the recorded data to maximise the classification power, or as outlined in section 5.4 the recorded events have a time sequence information structure ideal for input into an RNN. Development of such a machine learning based classifier may observe and employ additional event sub-geometries that are not yet known or utilised within the currently employed classification PDFs. Secondly, the pre low threshold data in the 1.0-1.5 keV_{ee} and 1.5-2.0 keV_{ee} energy bins was not utilised in the stable LY PDF cut analysis. This was to ensure that the use of a single LY relative efficiency gradient

explained the LY effects observed within the raw data event rates. It may be possible to utilise this pre low threshold data (~300 days), fitting it independently from the post low threshold data.

Another avenue to continue pursuing is the proposed high energy alpha event calibration technique detailed in chapter 4. It is very difficult to extract the scattering length in LXe via conventional calibration methods and a precise measurement could aide future experiments for use in their detector MC simulations. The geometry of said alpha events and the fact timing information can be extracted by the novel deconvolution technique could result in the true values of these optical parameters being acquired. As explained in section 4.4 the non-linearity problem can be overcome by using a source of lower energy alpha particles and these lower energy events can be combined by using a redesigned flat planed source holder that simplifies event superposition and reduces the required MC simulation time.

Appendix A

Period Structure and LY Systematics

A.1 Period structure

As mentioned in section 6.1 the period structure divides each calendar month into two halves: 1^{st} – 15^{th} and 16^{th}– month's end. Only normal physics runs are included, calibration runs - which are conducted on a regular basis - were excluded. There are only a few instances where this period structure is adjusted in consideration of interventions or variable operation conditions of the detector. Each of these is outlined below, the first four are the same as in the previous modulation analysis [49, 50].

- **Periods 25-28:** CT Exchange work (2014/12/23-2014/12/25), inner calibration (2015/01/07-2015/01/09) and power outage (2015/01/21-2015/01/29). Period 25 extended (2014/12/01-2014/12/23), Period 26 shifted (2014/12/25-2015/01/07), Period 27 shifted (2015/01/09-2015/01/21) and Period 28 starts early (2015/01/29-2015/02/15).

- **Periods 49-50:** Low threshold DAQ installation (2015/12/08). Period 49 short (2015/12/01-2015/12/08) and Period 50 short (2015/12/08-2015/12/15)

- **Periods 57-58:** LXe distillation and refilling (2016/03/29-2016/04/14), discussed with respect to additional run selection criteria for low threshold data in section 6.1.2. Period 57 ends early (2016/03/16-2016/03/29), a two week gap

and then Period 58 starts early (2016/04/14-2016/04/30).

- **Periods 68-70:** Xe gas flow change to reduce radon concentration (2016/09/27) and (RCK) Xe circulation system exchanged (2016/10/14). Period 68 ends early (2016/09/16-2016/09/27), Period 69 shifted (2016/09/27-2016/10/14) and Period 70 starts early (2016/10/14-2016/10/31).

- **Periods 91-92:** Xe gas flow change (2017/09/28) and (RCK). Period 91 ends early (2017/09/16-2017/09/28) and Period 92 starts early (2017/09/28-2017/10/15).

- **Periods 94-96:** CT Exchange work (2017/11/16) and power outage (2017/11/18-2017/11/24). Period 94 extended (2017/11/01-2017/11/16), additional Period 95 short (2017/11/16-2017/11/18) and Period 96 short (2017/11/24-2017/11/30).

- **Periods 116-117:** CT Exchange work (2018/09/27). Period 116 ends early (2018/09/16-2018/09/27) and Period 117 starts early (2018/09/27-2018/10/15).

A.2 Event rate systematics from LY uncertainties

The LY for each period is outlined in section 6.2.3. Uncertainties on the LY lead to a systematic error on the event rate, this is calculated using equation 6.4. The systematic errors as a proportion of the event rate are displayed for the 8 lowest energy bins in figures A.1 and A.2 for the complete dataset likelihood cut analysis and stable LY dataset PDF cut analysis respectively. At low energy these errors are only a fraction of a percent, even for the larger LY uncertainties induced by the use of the effective Hose LY.

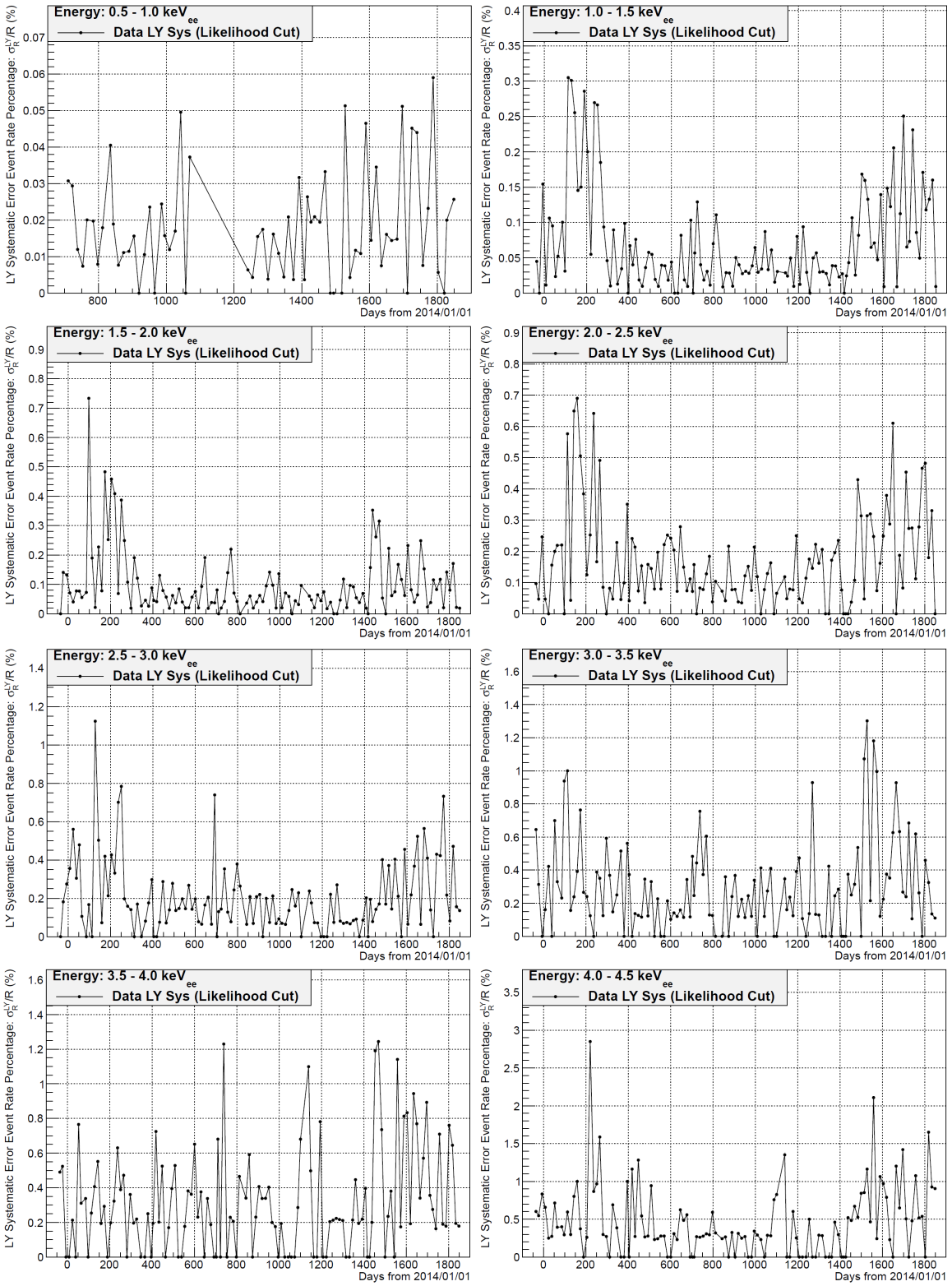


Figure A.1: Complete dataset likleihood cut: LY Systematic error as a percentage of the event rate, 8 lowest energy bins 0.5-4.5 keV$_{ee}$.

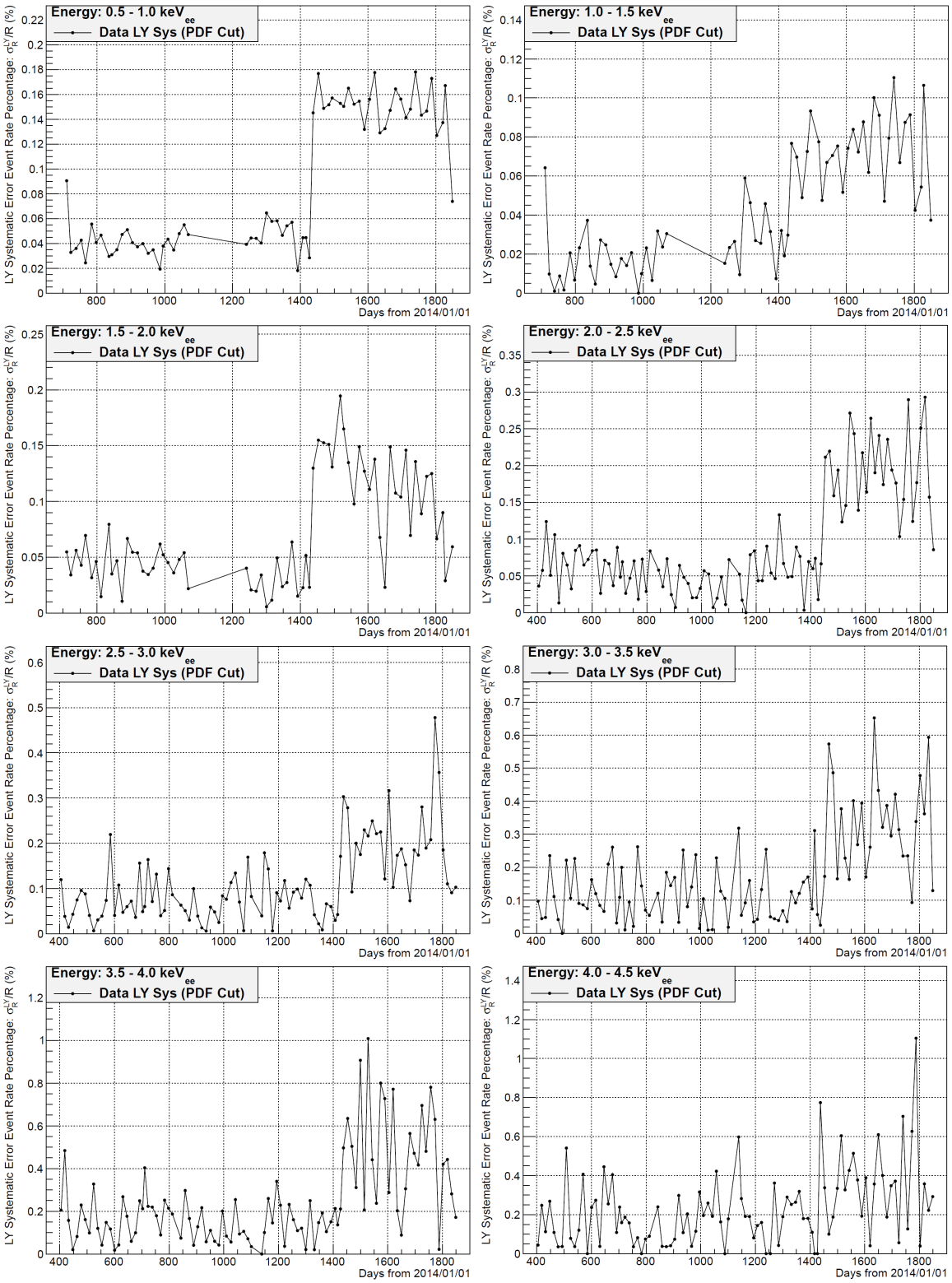


Figure A.2: Stable LY dataset PDF cut: LY Systematic error as a percentage of the event rate, 8 lowest energy bins 0.5-4.5 keV$_{ee}$.

References

[1] F. ZWicky, *Republication of: The redshift of extragalactic nebulae*, General Relativity and Gravitation **41** (2009) 207.

[2] F. ZWicky, *On the Masses of Nebulae and of Clusters of Nebulae*, Astrophysical Journal **86** (1937) 217.

[3] T. S. van Albada, J. N. Bahcall, K. Begeman, and R. Sancisi, *Distribution of dark matter in the spiral galaxy NGC 3198*, Astrophysical Journal **295** (1985) .

[4] NASA and ESA, M. J. Jee and H. Ford, *Galaxy cluster cl 0024+17 (zwcl 0024+1652) gravitational lensing matter map*, `https://www.nasa.gov/content/discoveries-highlights-shining-a-light-on-dark-matter`.

[5] NASA, CXC, CfA, STScI, ESO WFI, M. Markevitch, D. Clowe *et al.*, *Bullet cluster 1e-0657-56*, `https://chandra.harvard.edu/photo/2006/1e0657/`.

[6] P. A. R. Ade *et al.*, *Planck 2013 results. I. Overview of products and scientific results*, AA **571** (2014) .

[7] V. Springel *et al.*, *Simulations of the formation, evolution and clustering of galaxies and quasars*, Nature **435** (2005) 629636.

[8] J. A. Peacock *et al.*, *A Measurement of the Cosmological Mass Density from Clustering in the 2dF Galaxy Redshift Survey*, Nature **410** (2001) 169, `arXiv:astro-ph/0103143`.

[9] D. J. Eisenstein *et al.*, *Detection of the Baryon Acoustic Peak in the Large-Scale Correlation Function of SDSS Luminous Red Galaxies*, The Astrophysical Journal **633** (2005) 560, arXiv:astro-ph/0501171.

[10] N. Aghanim *et al.*, *Planck 2018 results. I. Overview of products and scientific results*, AA **641** (2020) , arXiv:1807.06209.

[11] R. Amanullah *et al.*, *Spectra and Light Curves of Six Type Ia Supernovae at 0.511 ¡ z ¡ 1.12 and the Union2 Compilation*, The Astrophysical Journal **716** (2010) , arXiv:1004.1711.

[12] R. V. Wagoner, *Big-Bang Nucleosynthesis Revisited*, The Astrophysical Journal **179** (1973) 343.

[13] B. D. Fields, *The Primordial Lithium Problem*, Annual Review of Nuclear and Particle Science **61** (2012) 47, arXiv:1203.3551.

[14] M. Milgrom, *A modification of the Newtonian dynamics as a possible alternative to the hidden mass hypothesis*, Astrophysical Journal **270** (1983) 365.

[15] C. Abel *et al.*, *Measurement of the Permanent Electric Dipole Moment of the Neutron*, Phyical Review **124** (2020) .

[16] MACHO collaboration, C. Alcock *et al.*, *The MACHO Project: Microlensing Results from 5.7 Years of LMC Observations*, Astrophysics **124** (2000) , arXiv:astro-ph/0001272.

[17] EROS-2 project, P. Tisserand *et al.*, *Limits on the Macho Content of the Galactic Halo from the EROS-2 Survey of the Magellanic Clouds*, Astrophysics **469** (2007) 387, arXiv:astro-ph/0607207.

[18] s. Hawking, *Gravitationally Collapsed Objects of Very Low Mass*, Monthly Notices of the Royal Astronomical Society **152** (1971) .

[19] A. Barnacka, J. F. Glicenstein, and R. Moderski, *New constraints on primordial black holes abundance from femtolensing of gamma-ray bursts*, Phys. Rev. D **86** (2012) , arXiv:1204.2056.

[20] F. Capela, M. Pshirkov, and P. Tinyakov, *Constraints on primordial black holes as dark matter candidates from capture by neutron stars*, Phys. Rev. D **87** (2013) , arXiv:1301.4984.

[21] P. W. Graham, S. Rajendran, and J. Varela, *Dark Matter Triggers of Supernovae*, Phys. Rev. D **92** (2015) , arXiv:1505.04444.

[22] Y. W. Ali-Hamoud and M. Kamionkowski, *Cosmic microwave background limits on accreting primordial black holes*, Phys. Rev. D **95** (2017) , arXiv:1612.05644.

[23] KATRIN Collaboration, P. Tisserand *et al.*, *Improved Upper Limit on the Neutrino Mass from a Direct Kinematic Method by KATRIN*, Physical Review **123** (2019) , arXiv:1909.06048.

[24] Particle Data Group Collaboration, P. Zyla *et al.*, *Review of Particle Physics PTEP*, .

[25] A. Boyarsky *et al.*, *Sterile Neutrino Dark Matter*, arXiv:1807.07938.

[26] K. Petraki and R. R. Volkas, *Review of asymmetric dark matter*, Mod. Phys. A **28** (2013) , arXiv:1305.4939.

[27] J. E. Kim, *Weak-Interaction Singlet and Strong CP Invariance*, Physical Review Letters **43** (1979) 103.

[28] M. A. Shifman, A. Vainshtein, and V. I. Zakharov, *Can confinement ensure natural CP invariance of strong interactions?*, Nuclear Physics B **166** (1980) 493.

[29] M. Dine, W. Fischler, and M. Srednicki, *A simple solution to the strong CP problem with a harmless axion*, Physics Letters B **104** (1981) 199.

[30] A. R. Zhitnitsky, *A simple solution to the strong CP problem with a harmless axion*, Sov. J. Nucl. Phys **31** (1980) 260.

[31] ADMX Collaboration, T. Braine *et al.*, *Extended Search for the Invisible Axion with the Axion Dark Matter Experiment*, Physical Reviw Letters **124** (2020) , arXiv:1910.08638.

[32] L. J. Rosenberg, *Dark-matter QCD-axion searches*, PNAS **112** (2015) .

[33] DAMPE Collaboration, G. Ambrosi *et al.*, *Direct detection of a break in the teraelectronvolt cosmic-ray spectrum of electrons and positrons*, Nature **552** (2017) 63, arXiv:1711.10981.

[34] P. H. Gu and X. G. He, *Electrophilic dark matter with dark photon: from DAMPE to direct detection*, Physics Letters B **778** (2018) 292, arXiv:1711.11000.

[35] T. S. Virdee, *Beyond the standard model of particle physics*, Phil. Trans. R. Soc. A. **374** (2016) .

[36] ATLAS Collaboration, *Susy searches*, https://atlas.web.cern.ch/Atlas/GROUPS/PHYSICS/CombinedSummaryPlots/SUSY/ATLAS_SUSY_Summary/ATLAS_SUSY_Summary.png.

[37] DES Collaboration, E. O. Nadler *et al.*, *Constraints on Dark Matter Properties from Observations of Milky Way Satellite Galaxies*, Phys. Rev. Lett. **126** (2021) , arXiv:2008.00022.

[38] Fermi-LAT and DES Collaboration, A. Albert *et al.*, *Searching for Dark Matter Annihilation in Recently Discovered Milky Way Satellites with Fermi-LAT*, The Astrophysical Journal. **834** (2016) , arXiv:1611.03184.

[39] AMS Collaboration, A. Albert *et al.*, *The Alpha Magnetic Spectrometer (AMS) on the international space station: Part II Results from the first seven years*, Physics Reports. **894** (2021) .

[40] PAMELA Collaboration, O. Adriani *et al.*, *Ten Years of PAMELA in Space*, Riv. Nuovo Cim. **40** (2017) , arXiv:1801.10310.

[41] Super-Kamiokande collaboration, K. Choi *et al.*, *Search for neutrinos from annihilation of captured low-mass dark matter particles in the Sun by Super-Kamiokande*, Physical Review Letters **114** (2015) , arXiv:1503.04858.

[42] Y. Kim, *Overview of dark matter searches*, https://www.semanticscholar.org/paper/P-o-S-(-I-C-R-C-2-0-1-7-)-1-0-8-5-Overview-of-DM-Kim/fd47f6a18890b8283fa278dab18b9f24316875b1. P o S (I C R C 2 0 1 7) 1 0 8 5.

[43] DAMA/LIBRA Collaboration, R. Bernabei *et al.*, *First results from DAMA/LIBRA and the combined results with DAMA/NaI*, European Physical Journal C **56** (2008) .

[44] DAMA/LIBRA Collaboration, R. Bernabei *et al.*, *Final model independent result of DAMA/LIBRAphase1*, European Physical Journal C **73** (2013) .

[45] DAMA/LIBRA Collaboration, R. Bernabei *et al.*, *First model independent results from DAMA/LIBRA-phase2*, Nuclear Physics (2018) , arXiv:1805.10486.

[46] COSINE-100 Collaboration, G. Adhikari *et al.*, *Search for a Dark Matter-Induced Annual Modulation Signal in NaI(Tl) with the COSINE-100 Experiment*, Phys. Rev. Lett **123** (2019) , arXiv:1903.10098.

[47] J. Amare *et al.*, *Annual modulation results from three-year exposure of ANAIS-112*, Phys. Rev. D **103** (2021) , arXiv:2103.01175.

[48] DARWIN Collaboration, J. Aalbers *et al.*, *DARWIN: towards the ultimate dark matter detector*, Cosmology and Astroparticle Physics (2016) arXiv:1606.07001.

[49] XMASS Collaboration, M. Kobayashi *et al.*, *Search for sub-GeV dark matter by annual modulation using XMASS-I detector*, Physics Letters B **795** (2018) 308, arXiv:1808.06177.

[50] M. Kobayashi, *Search for Sub-GeV WIMP dark matter by annual modulation using XMASS-I detector*, PhD thesis, University of Tokyo, XMASS Collaboration, http://www-sk.icrr.u-tokyo.ac.jp/xmass/_pdf/publist/Dthesis-mkoba.pdf, 2018.

[51] XMASS Collaboration, K. Abe *et al.*, *A direct dark matter search in XMASS-I*, Physics Letters B **789** (2018) 45, arXiv:1804.02180.

[52] CDMS Collaboration, R. Agnese *et al.*, *Silicon Detector Dark Matter Results from the Final Exposure of CDMS II*, Physical Review Letters **111** (2013) , arXiv:1304.4279.

[53] SuperCDMS Collaboration, R. Agnese *et al.*, *Search for Low-Mass Weakly Interacting Massive Particles with SuperCDMS*, Physical Review Letters **112** (2014) , arXiv:1402.7137.

[54] SuperCDMS Collaboration, R. Agnese *et al.*, *Low-mass dark matter search with CDMSlite*, Physical Review D **97** (2018) , arXiv:1707.01632.

[55] CRESST Collaboration, G. Angloher *et al.*, *Results on light dark matter particles with a low-threshold CRESST-II detector*, The European Physical Journal C (2016) , arXiv:1509.01515.

[56] DarkSide Collaboration, P. Agnes *et al.*, *Low-Mass Dark Matter Search with the DarkSide-50 Experiment*, Physical Review Letters **121** (2018) , arXiv:1802.06994.

[57] DarkSide Collaboration, P. Agnes *et al.*, *DarkSide-50 532-day Dark Matter Search with Low-Radioactivity Argon*, Physical Review D **98** (2018) , arXiv:1802.07198.

[58] NEWS-G Collaboration, Q. Arnaud *et al.*, *First results from the NEWS-G direct dark matter search experiment at the LSM*, Astroparticle Physics **97** (2018) 54, arXiv:1706.04934.

[59] DEAP Collaboration, R. Ajaj *et al.*, *Search for dark matter with a 231-day exposure of liquid argon using DEAP-3600 at SNOLAB*, Phys. Rev. D **100** (2019) , arXiv:1902.04048.

[60] PandaX-II Collaboration, Q. Wang *et al.*, *Results of Dark Matter Search using the Full PandaX-II Exposure*, Chinese Physics C **44** (2021) , arXiv:2007.15469.

[61] LUX Collaboration, D. S. Akerib *et al.*, *Results from a search for dark matter in the complete LUX exposure*, Physical Review Letters **118** (2017) , arXiv:1608.07648.

[62] XENON Collaboration, E. Aprile *et al.*, *Dark Matter Search Results from a One Ton-Year Exposure of XENON1T*, Physical Review Letters **121** (2018) , arXiv:1805.12562.

[63] N. E. Bell, G. Busoni, and I. W. Sanderson, *Self-consistent Dark Matter Simplified Models with an s-channel scalar mediator*, JCAP **2017** (2017) , arXiv:1612.03475.

[64] B. A. Kniehl and M. Spira, *Low-Energy Theorems in Higgs Physics*, Zeitschrift fr Physik C **69** (1995) 77, arXiv:hep-ph/9505225.

[65] F. Bishara, J. Brod, B. Grinstein, and J. Zupan, *DirectDM: a tool for dark matter direct detection*, arXiv:1708.02678.

[66] A. De Simone and T. Jacques, *Simplified models vs. effective field theory approaches in dark matter searches*, European Physical Journal C **76** (2016) , arXiv:1603.08002.

[67] M. Bauer, U. Haisch, and F. Kahlhoefer, *Simplified dark matter models with two Higgs doublets: I. Pseudoscalar mediators*, High Energy Physics **138** (2017) , arXiv:1701.07427.

[68] V. Barger, W. Keung, and G. Shaughnessy, *Spin Dependence of Dark Matter Scattering*, Physical Review D **78** (2008) , arXiv:0806.1962.

[69] N. Anand, A. L. Fitzpatrick, and W. C. Haxton, *Weakly interacting massive particle-nucleus elastic scattering response*, Physical Review C **89** (2014) , arXiv:1308.6288.

[70] A. L. Fitzpatrick *et al.*, *The Effective Field Theory of Dark Matter Direct Detection*, JCAP **2013** (2013) , arXiv:1203.3542.

[71] A. Kurylov and M. Kamionkowski, *Generalized analysis of the direct weakly interacting massive particle searches*, Physical Review D **69** (2004) , arXiv:hep-ph/0307185.

[72] D. Baxter *et al.*, *Recommended conventions for reporting results from direct dark matter searches*, arXiv:2105.00599.

[73] XMASS Collaboration, K. Abe *et al.*, *Direct dark matter search by annual modulation in XMASS-I*, Journal of Physics: Conference Series **718** (2016) , arXiv:1511.04807.

[74] K. Hosokawa, *Search for dark matter annual modulation in XMASS-I detector*, PhD thesis, Kobe University, XMASS Collaboration, http://www-sk.icrr.u-tokyo.ac.jp/xmass/_pdf/publist/Hosokawa-dron.pdf, 2016.

[75] A. Bernstein *et al.*, *Report on the Depth Requirements for a Massive Detector at Homestake*, arXiv:0907.4183arXiv:0907.4183.

[76] A. Baldini *et al.*, *Liquid Xe scintillation calorimetry and Xe optical properties*, Trans. Dielectr. Electr. Insul. **13** (2006) , arXiv:physics/0401072.

[77] M. J. Berger *et al.*, *XCOM: Photon Cross Sections Database*, NIST Standard Reference Database 8 (2010) .

[78] EXO Collaboration, N. Ackerman *et al.*, *Observation of Two-Neutrino Double-Beta Decay in Xe-136 with EXO-200*, Physical Review Letters **107** (2011) , arXiv:1108.4193.

[79] PandaX Collaboration, K. Ni *et al.*, *Searching for Neutrino-less Double Beta Decay of Xe-136 with PandaX-II Liquid Xenon Detector*, Chinese Physics C **43** (2019) , arXiv:1906.11457.

[80] A. Hitachi *et al.*, *Effect of ionization density on the time dependence of luminescence from liquid argon and xenon*, Physical Review B **27** (1983) .

[81] S. Kubota, M. Hishida, and J. Raun, *Evidence for a triplet state of the self-trapped exciton states in liquid argon, krypton and xenon*, J. Phys. C: Solid State Phys **11** (1978) .

[82] XMASS Collaboration, K. Ueshima *et al.*, *Scintillation-only Based Pulse Shape Discrimination for Nuclear and Electron Recoils in Liquid Xenon*, NIMA **659** (2011) 161, arXiv:1106.2209.

[83] XMASS Collaboration, K. Abe *et al.*, *A measurement of the scintillation decay time constant of nuclear recoils in liquid xenon with the XMASS-I detector*, JINST **13** (2018) , arXiv:1809.05988.

[84] DEAP Collaboration, P. A. Amaudruz *et al.*, *The liquid-argon scintillation pulseshape in DEAP-3600*, The European Physical Journal C **80** (2020) .

[85] DEAP Collaboration, P. A. Amaudruz *et al.*, *Measurement of the scintillation time spectra and pulse-shape discrimination of low-energy beta and nuclear recoils in liquid argon with DEAP-1*, Astroparticle Physics **85** (2016) , arXiv:0904.2930.

[86] XENON100 Collaboration, E. Aprile *et al.*, *Dark Matter Results from 100 Live Days of XENON100 Data*, Physical Review Letters **107** (2011) , arXiv:1104.2549.

[87] LUX Collaboration, D. S. Akerib *et al.*, *Low-energy (0.7-74 keV) nuclear recoil calibration of the LUX dark matter experiment using D-D neutron scattering kinematics*, arXiv:1608.05381.

[88] XMASS Collaboration, K. Abe *et al.*, *XMASS detector*, Nucl. Instrum. Meth. A **716** (2013) , arXiv:1301.2815.

[89] Y. Suzukia, *The Super-Kamiokande experiment*, Eur. Phys. J. C **79** (2019) .

[90] H. Ikeda *et al.*, *Front-end hybrid circuit for super-KAMIOKANDE*, Nucl. Instrum. Meth. A **320** (1992) .

[91] XMASS Collaboration, H. Takiya *et al.*, *A measurement of the time profile of scintillation induced by low energy gamma-rays in liquid xenon with the XMASS-I detector*, Nucl. Instrum. Meth. A **834** (2016) , arXiv:1604.01503.

[92] XMASS Collaboration, K. Abe *et al.*, *XMASS MC simulation*, JINST **11** (2016) .

[93] S. Agostinelli *et al.*, *GEANT4–a simulation toolkit*, Nucl. Instrum. Meth. A **506** (2002) .

[94] S. Cebrin *et al.*, *Micromegas-TPC operation at high pressure in Xenon-trimethylamine mixtures*, Journal of Instrumentation (2012) , arXiv:1210.3287.

[95] XMASS Collaboration, N. Y. Kim *et al.*, *Micro-source development for XMASS experiment*, Nucl. Instrum. Meth. A **784** (2015) .

[96] Super-Kamiokade Collaboration, Y. Takeuchi *et al.*, *Measurement of radon concentrations at Super-Kamiokande*, Physics Letters B **452** (1999) , arXiv:hep-ex/9903006.

[97] XENON Collaboration, E. Aprile *et al.*, *Analysis of the XENON100 Dark Matter Search Data*, Astroparticle Physics **54** (2014) , arXiv:1207.3458.

[98] Y. Onishi Master's thesis, Kobe University, XMASS Collaboration, 2015.

[99] C. Tan, *Big Gaps and Short Bridges: A Model for Solving the Discontinuity Problem*, Answers Research Journal **9** (2016).

[100] XENON Collaboration, E. Aprile *et al.*, *Observation of Excess Electronic Recoil Events in XENON1T*, Phys. Rev. D **102** (2020) , arXiv:2006.09721.

[101] E. Grace, A. Butcher, J. Monroe, and J. A. Nikkel, *Index of refraction, Rayleigh scattering length, and Sellmeier coefficients in solid and liquid argon and xenon*, Nucl. Instrum. Meth. A **867** (2017) 204, arXiv:1502.04213.

[102] M. F. L'Annunziata, *1 - alpha radiation*, in *Radioactivity* (M. F. L'Annunziata, ed.), pp. 71–84. Elsevier Science B.V., Amsterdam, 2007. doi: https://doi.org/10.1016/B978-044452715-8.50004-9.

[103] Double Chooz collaboration, Y. Abe *et al.*, *Characterization of the Spontaneous Light Emission of the PMTs used in the Double Chooz Experiment*, Journal of Instrumentation **11** (2016) , arXiv:1604.06895.

[104] R. Foot, *DAMA annual modulation from electron recoils*, Physics Letters B **785** (2018) 403, arXiv:1804.11018.

[105] DAMA/LIBRA Collaboration, R. Bernabei *et al.*, *The DAMA/LIBRA apparatus*, Nucl. Instrum. Meth. A **592** (2008) .